THE UNIVERSITY *of* EDINBURGH

Enhanced Carrierless Amplitude and Phase Modulation for Optical Communication Systems

Kabiru Oluwaseun Akande

A thesis submitted for the degree of

Doctor of Philosophy

The University of Edinburgh

2018

THE UNIVERSITY *of* EDINBURGH
School of Engineering

Dedication

To my dear parents,

for their immeasurable care and support.

To my dearest love, **Aa'ishah**,

for all her endless prayers, sacrifice and love.

And to the triple M's,

for the boundless joy they brought to our lives.

Abstract

This thesis develops and investigates enhanced techniques for carrierless amplitude and phase modulation (CAP) in optical communication systems. The CAP scheme is studied as the physical layer modulation technique due to its implementation simplicity and versatility, that enables its implementation as a single carrier (CAP) or multi-carrier technique (m-CAP).

The effect of timing jitter on the error performance of CAP is first investigated. The investigation indicates that synchronization is a critical requirement for CAP receiver and as a result, a novel low-complexity synchronization algorithm is developed with experimental demonstration for CAP-based visible light communication (VLC) systems. To further reduce the overall link complexity, a fractionally-spaced equalizer (FSE) is considered to mitigate the effects of inter-symbol interference (ISI) and timing jitter. The FSE implementation, which eliminates the need for a separate synchronization block, is shown through simulation and VLC experimental demonstration to outperform symbol-spaced equalizers (SSE) that are reported in literature for CAP-based VLC systems.

Furthermore, in this thesis, spectrally-efficient index modulation techniques are developed for CAP. The proposed techniques can be divided into two broad groups, namely spatial index CAP (S-CAP) and subband index CAP (SI-CAP). The proposed spatial index techniques leverage the fact that in VLC, multiple optical sources are often required. The spatial CAP (S-CAP) transmits CAP signal through one of N_{t} available LEDs. It is developed to reduce equalization requirement and improve the spectral efficiency of the conventional CAP. In addition to the bits transmitted through the CAP symbol, the S-CAP encodes additional bits on the indexing/spatial location of the LEDs. The generalised S-CAP (GS-CAP) is further developed to relax the S-CAP limitation of using a single LED per symbol duration. In addition to the S-CAP scheme, multiple-input multiple-output (MIMO) techniques of repetitive-coded CAP (RC-CAP) and spatial multiplexing CAP (SM_{ux}-CAP) are investigated for CAP. Low-complexity detectors are also developed for the MIMO schemes. A key challenge of the MIMO schemes is that they suffer power penalty when channel gains are similar, which occur when the optical sources are

closely located. The use of multiple receivers and power factor imbalance (PFI) techniques are proposed to mitigate this power penalty. The techniques result in significant improvement in the power efficiency of the MIMO schemes and ensure that the spectral efficiency gain is obtained with little power penalty.

Finally, subband index CAP (SI-CAP) is developed to improve the spectral efficiency of m-CAP and reduce its peak-to-average power ratio (PAPR). The SI-CAP encodes additional information bits on the selection of 'active' subbands of m-CAP and only modulate data symbols on these 'active' subbands. The error performance of the proposed SI-CAP is evaluated analytically and verified with computer-based simulations. The SI-CAP technique is also experimented for both VLC and step-index plastic optical fibre (SI-POF) communication links. The experimental results show that for a fixed power efficiency, SI-CAP achieves higher data rate compared to m-CAP. For example, at a representative bit error rate (BER) of 10^{-5}, the SI-CAP achieves a data rate and power efficiency gain of 26.5 Mb/s and 2.5 dB, respectively when compared to m-CAP. In addition, an enhanced SI-CAP (eSI-CAP) is developed to address the complexity that arises in SI-CAP at higher modulation order. The results of the experimental demonstrations in VLC and 10 m SI-POF link shows that when compared with m-CAP, eSI-CAP consistently yields a data rate improvement of between 7% and 13% for varying values of the SNR.

Lay Summary

Carrierless amplitude and phase modulation (CAP) is a high-dimensional modulation technique that is employed for improving the throughput in optical communication systems. However, the CAP technique has many challenges that need to be addressed in order to realize its full potential. The first of the challenges that is addressed in this thesis is the CAP sensitivity to timing variation. A novel technique is developed that suitably correct for the effect of timing variation experienced by CAP in optical communication. In addition, a technique that addresses the distortive effects of both the limited bandwidth and timing variation is implemented to reduce the system complexity. Furthermore, spatial index techniques are developed for the CAP scheme to improve its power and spectral efficiency. The spatial index technique carry additional information, in addition to the information carried by the conventional CAP symbol, on the indices of the multiple LEDs that are employed in optical wireless communication. The spatial index technique is shown through theoretical analysis and computer simulations to substantially improve the power and spectral efficiency of CAP. Similarly, the subband index technique is developed for the multiband version of CAP (m-CAP) by modulating extra information bits on the indices of the m-CAP's subbands. This increases the achievable data rates of the conventional m-CAP and improves its energy efficiency. Using theoretical analyses, computer simulations and proof of concept experiments in both optical fibre and wireless communications, the advantages of the subband index technique are demonstrated. It is shown that between 7% and 13% improvement is achieved in the data rate of m-CAP when the subband index technique is implemented. Finally, this thesis presents a comprehensive development and experimental validation of multiple techniques that enhance the performance of CAP-based optical communication systems.

Acknowledgements

I sincerely acknowledge the special favour bestowed upon me by Almighty Allah that enables me to finish this thesis, despite the circumstances.

My appreciation goes to the school of engineering, university of Edinburgh for funding my PhD program.

I am grateful to my supervisor, Dr W. O. Popoola, for his constant support and guidance as well as his infectious, seemingly boundless enthusiasm. Indeed, several technical contributions in this thesis emanate from his insightful comments and many of the chapters only saw completion due to his drive. I also thank him for granting me the opportunity to carry out my research under his tutelage and as a result, benefit from his knowledge.

I appreciate the entire LiFi team and the immediate members of our research group. Their helpful dispositions create learning opportunities from many difficult moments.

I wish to extend my gratitude to my dear wife, **Aa'ishah**, for her love and sacrifice, especially during those difficult times when our twins were born. And to the triple M's, we all acknowledge the joy and motivation you brought to our lives.

Declaration

I declare that this thesis has been composed solely by myself and that it has not been submitted, either in whole or in part, in any previous application for a degree. Except where otherwise acknowledged, the work presented is entirely my own.

Kabiru O. Akande

Contents

List of Tables

List of Figures

List of Abbreviations

2D . . . . . two dimensional

ADSL . . . . . asynchronous digital subscriber line

APD . . . . . avalanche PD

ATM . . . . . asynchronous transfer mode

AWG . . . . . arbitrary waveform generator

AWGN . . . . . additive white Gaussian noise

BER . . . . . bit error rate

CAP . . . . . carrierless amplitude and phase modulation

CIR . . . . . channel impulse response

CMOS . . . . . complementary metal-oxide-semiconductor

CPC . . . . . compound parabolic concentrator

DCO-OFDM . . direct current biased optical OFDM

DFE . . . . . decision feedback equalizer

DMT . . . . . discrete multitone

E/O . . . . . electrical to optical

EMI . . . . . electromagnetic interference

eSI-CAP . . . . enhanced SI-CAP

EVM . . . . . error vector magnitude

FD . . . . . frequency domain

FEC . . . . . forward error correction

FFE . . . . . feedforward equalizer

FFT . . . . . fast Fourier transform

FIR . . . . . finite impulse response

FSE . . . . . fractionally-spaced equalizer

GaN . . . . . gallium nitride

GS-CAP . . . . generalised S-CAP

HPF . . . . . high pass filter

IFFT . . . . . inverse fast Fourier transform

IM/DD . . . . . intensity modulated and direct detection

IoT . . . . . internet of things

ISI . . . . . intersymbol interference

LD . . . . . laser diode

LED . . . . . light emitting diode

LO . . . . . local oscillator

LOS . . . . . line of sight

LPF . . . . . low pass filter

MED . . . . . minimum Euclidean distance

m**-CAP** . . . . . multiple band CAP

MIMO . . . . . multiple input multiple output

μ**-LED** . . . . . micro LED

MLD . . . . . maximum likelihood detector

MSB . . . . . most significant bit

MSE . . . . . mean square error

MSM . . . . . metal semiconductor metal

NLOS . . . . . non LOS

NRZ . . . . . non return to zero

OFC . . . . . optical fibre communication

OFDM . . . . . orthogonal frequency division multiplexing

OLED . . . . . organic LED

OOK . . . . . on-off keying

OWC . . . . . optical wireless communication

PAM . . . . . pulse amplitude modulation

PAPR . . . . . peak to average power factor

PC-LED . . . . phosphor converted LED

PD . . . . . photodetector

PDF . . . . . probability density function

PEP . . . . . pairwise error probability

PFI . . . . . power factor induced

PIN PD . . . . . p-type n-type intrinsic PD

PLL . . . . . phase locked loop

PMD . . . . . probability of missed detection

POF . . . . . plastic optical fibre

PPM . . . . . pulse position modulation

PWM . . . . . pulse width modulation

QAM . . . . . quadrature amplitude modulation

RC-CAP . . . . repetitive coding with CAP

RC-LED . . . . resonant cavity LED

RF . . . . . radio frequency

RGBY . . . . . red, green, blue and yellow

RLS . . . . . recursive least square

RMS . . . . . root-mean-square

RRC . . . . . raised cosine filter

S-CAP . . . . . spatial modulation with CAP

SCP . . . . . signal constellation points

SI-CAP . . . . . subband index CAP

SI-POF . . . . . step index plastic optical fibre

SIR . . . . . signal-to-interference ratio

SM_{ux}-CAP . . . spatial multiplexing with CAP

SNR . . . . . signal-to-noise ratio

SSE . . . . . symbol-spaced equalizer

SSL . . . . . solid state lighting

TIA . . . . . transimpedance amplifier

VLC . . . . . visible light communication

WDM . . . . . wavelength division multiplexing

List of Mathematical Symbols

b	number of bits to be transmitted
$b_{\mathbf{m}}$	number of symbol bits
$b_{\mathbf{s}}$	number of index bits
$N_{\mathbf{a}}$	number of active LEDs
$N_{\mathbf{t}}$	number of transmitting LEDs
N_0	variance of the AWGN
$N_{\mathbf{r}}$	number of receiving PDs
$N_{\mathbf{u}}$	number of index constellation points used
$f_{\mathbf{s}}$	sampling rate of the system
$h(t)$	channel impulse response
$h_{\mathbf{min}}$	minimum of the channel gains
L	number of samples per symbol
$R_{\mathbf{b}}$	bit rate
$R_{\mathbf{s}}$	symbol rate
T	symbol duration
$T_{\mathbf{b}}$	bit duration
$w(t)$	AWGN
$x(t)$	transmitted signal
$y(t)$	received signal
${}^{N}C_{N_{\mathbf{a}}}$	N combination N_{a}
$\lfloor \cdot \rfloor$	floor function
$\| \cdot \|_{\mathbf{F}}$	Frobenius norm
$\mathcal{N}_H(b_m, \tilde{b}_m)$	Hamming distance between b_m and $\tilde{b}_m$) bits

$D(\cdot)$ . . . . . minimum Euclidean distance metric

d_k . . . . . path traced out by the optical radiation from the source to the receiver

ϕ_k . . . . . angle of incidence

θ_k . . . . . angle of irradiance

$\mathcal{S}$ . . . . . available index constellation

$\tau_{\mathbf{rms}}$ . . . . . channel rms delay spread

$\mathcal{K}$ . . . . . electrical to optical conversion coefficient

$\Phi_{1/2}$ . . . . . half-power LED semiangle

β . . . . . optical modulation index

$\mathcal{O}$ . . . . . order of computational complexity

$\delta_{n_\mathfrak{t}}$ . . . . . PFI weighting factor for $n_\mathfrak{t}^{\text{th}}$ LED

ρ . . . . . reflectivity coefficient

$\mathcal{R}$ . . . . . responsivity of the PD

ξ . . . . . scaling factor to maintain unity power for subband indexing techniques

$\mathcal{S}_{\mathbf{u}}$ . . . . . selected/used index constellation

$\mathcal{M}$ . . . . . set of constellation points

Δ_γ . . . . . SNR per bit penalty

η . . . . . spectral efficiency

Ω . . . . . system configuration

$\mathcal{T}$ . . . . . transmission efficiency

Chapter 1

Introduction

1.1 Background

There has been an exponential increase in the number of devices requiring and assessing wireless connectivity, especially with the growing popularity of Internet of Things (IoT) and ubiquitous connectivity of smart devices [1, 2]. This is coupled with the current trend to enhance mobile broadband experience with innovative data applications and services. This rapid growth in broadband communication and unprecedented demand for high data rate is stretching the limit of the existing network of communication infrastructure. Therefore, supporting this rapid growth requires communication technology with ability to complement the already crowded radio frequency (RF) spectrum. The technologies that are currently being considered as candidate solutions to the spectrum crunch in RF are those utilizing the higher frequency spectrum, such as mm-wave and visible light communications (VLC) [3].

The VLC, which occupies the nano-meter ($\backsim$ 380 nm - 780 nm) wavelength region of the electromagnetic spectrum (EM), is attracting lots of research interest as a suitable technology to augment the RF. It has a unique feature which enables it to combine illumination with high-speed wireless data communication. The main advantages of VLC over RF communication are the availability of huge unused and unlicensed spectrum, its use of inexpensive devices, high security and immunity to electromagnetic interference, among many others [2, 4]. In addition, VLC technology also offers a range of specialized innovative applications and services such as indoor localization and positioning, e-commerce and vehicle-to-vehicle communication [5, 6].

The rapid advancement in the field of solid state light emitting diode (LED) and its wide adoption for lighting purposes are at the core of the heightened interest in VLC . In comparison to the traditional incandescent and fluorescent lighting devices, LEDs are cost effective, long-lasting, energy efficient and can be electronically programmed [2]. Moreover, the fast switching speed of LED enables the possibility of modulating data on its radiated intensity at a rate that is imperceptible to human eye [2]. This gives rise to the combined usage of LEDs for both illumination and VLC. The white LEDs employed in VLC are mainly obtained through two methods. The light from three different chips each emitting red, green and blue light can be mixed together to achieve a single white RGB LED [4, 7]. Alternatively, a blue LED with a yellow phosphor coating can also be employed to realise a white phosphor-converted LED (PC-LED) [7]. The yellow phosphor coating in the PC-LED absorbs part of the emitted blue light to produce a yellow light. The yellow light then combines with the remaining un-absorbed blue light to produce a white PC-LED. However, while the PC-LED is less complex, more cost-effective, energy efficient and offers better colour rendering than the RGB white LED, the use of phosphor coating severely limits the modulation bandwidth of the LED to a few MHz [8, 9]. This is as a result of the slow time response of the phosphor coating in comparison to the blue chip in the LED. Hence, a number of signal processing techniques are employed in improving the bandwidth of PC-LED to achieve a high data rate VLC system. One of the techniques employed in improving the bandwidth of PC-LED is the use of blue filter at the receiver to extract the blue component in the received signal and block the yellow component [10, 11]. This approach results in power penalty as the energy in the yellow component are lost to the filtering process [12]. Other techniques are pre- and post-equalization and the use of advanced modulation techniques [13].

In addition to the VLC technique, step-index plastic optical fibre (SI-POF) is also attracting lots of attention for applications in data communication [14–16]. The use of SI-POF is due to its mechanical flexibility that allows ease of handling and results in fast and inexpensive installation. In addition, it provides immunity to electromagnetic interference (EMI) and offers high data rates [16]. However, SI-POF has implementation challenges such as its limited bandwidth-length product (45 MHz $\times 100$ m) and high attenuation (0.15 dB/m at 650 nm wavelength) [17, 18]. These challenges require adequate solutions in order to fully realise the benefits of SI-POF. The use of advanced modulation techniques is one of the methods that

are adopted to improve the achievable data rate and overcome the challenges encountered in SI-POF implementation [17].

1.2 Research Motivation and Justification

The CAP modulation technique has been widely investigated for optical communication systems [7, 19–22]. This is due to the combination of its high spectral efficiency and implementation simplicity [23]. The CAP modulation scheme also has a special feature in that it can be implemented as a single band or a multi-band scheme [24, 25]. This special feature provides design flexibility as it is easily adaptable to a single or multi-band scenarios. The CAP scheme has previously been adopted by asynchronous transfer mode (ATM) standardization body, ATM Forum, as the standard for ATM LAN physical layer interface and was an early candidate for asymmetric digital subscriber line (ADSL) [26, 27]. It was later discontinued in favour of discrete multitone (DMT) due to its required equalization resources at high throughputs [28]. However, CAP modulation is currently enjoying a resurgence as a result of its special properties that lead to implementation advantages in optical communication. Among these properties is that CAP, as a single carrier modulation, has a low peak-to-average power ratio (PAPR) in comparison to discrete multitone (DMT) whose high PAPR is one of its major issues [29]. The low PAPR factor of CAP modulation is well suited to optical communication since there is a considerable optical power constraint in the transmitter front-end imposed by both the eye safety regulations and design requirements [29]. In addition, the CAP signal is real-valued and as such is suitable for the intensity modulated and direct detection (IM/DD) approach that is employed in optical communication [30, 31]. Furthermore, the CAP transceiver is relatively easy to implement as it uses digital finite impulse response (FIR) filter and avoids the need for carrier modulation and recovery in comparison to its QAM counterpart [23].

However, the CAP modulation scheme is not devoid of challenges. The use of orthogonal filters for pulse-shaping and matched filtering operations in the CAP transceiver significantly increase its sensitivity to timing jitter [22, 23]. Furthermore, CAP performance degrades in channels with a non-flat frequency response, which is typical of VLC systems employing PC-LEDs as the transmitter. Similarly, PC-LEDs suffer from small modulation bandwidth which results in

severe inter-symbol interference (ISI) for systems operating at high throughputs. In addition, just like the DMT approach, the multiband version of CAP (m-CAP) also suffers from high PAPR. When adopted in plastic optical fibre (POF), the limited bandwidth-length product and power attenuation results in performance degradation at high bit rates [30]. These challenges require the development of novel techniques to benefit from the advantages of CAP modulation.

Hence, novel techniques are developed for enhancing the performance of CAP in this thesis. The focus is on developing techniques that have high spectral and energy efficiency coupled with low computational complexity. The developed techniques, which are validated through theoretical analysis, simulations and experimental demonstrations, show that the enhanced CAP is a suitable modulation technique for optical communication systems.

1.3 Research Objectives

This thesis aim to improve the performance of optical systems employing VLC and SI-POF by developing an enhanced CAP modulation schemes. Novel techniques that address the challenges of CAP-based optical communication systems are to be developed and their performances validated through theoretical analysis, simulations and proof-of-concept experimental demonstrations. Fair comparisons with the state-of-the-art techniques are to be performed to quantify the performance gains of the developed techniques. Performance criteria such as bit-error-rate (BER), error vector magnitude (EVM), spectral efficiency (η) and energy efficiency are to be assessed for the developed techniques. In order to achieve the aforementioned goals, the thesis objectives are set as follows:

- To conduct a comprehensive review of the fundamentals of CAP modulation scheme, that leads to firm understanding of the impact of its parameters on the systems performance.
- To investigate the impact of timing jitter on the performance of CAP with a view to developing suitable synchronization algorithm that addresses the jitter effect.
- To investigate multiple-input multiple-output (MIMO) techniques (including spatial modulation and spatial multiplexing) for CAP-based VLC systems as means of improving its spectral efficiency.
- To develop signal processing techniques that improve the performance degradation of

the MIMO CAP-based VLC systems, due to co-located optical sources and non-line of sight (NLOS) propagation.

- To improve the spectral and energy efficiency of m-CAP based VLC and SI-POF systems with subband indexing techniques.
- To ensure low complexity implementation of all the proposed techniques and their validation, where possible, through combination of theoretical analysis, simulations and experimental demonstrations.

1.4 Thesis Contributions

This thesis has made original contributions by:

1. Showing the impact of timing jitter on CAP-based VLC systems, developing a novel synchronization algorithm to address the jitter problem, deriving the theoretical analysis for the algorithm and validating its performance through simulation and experimental demonstration.
2. Achieving low complexity implementation through the use of fractionally spaced equalizer (FSE) for combined equalization and synchronization of CAP-based VLC systems.
3. Enhancing the spectral efficiency of the CAP-based VLC systems through the implementation of spatial modulated and spatial multiplexed CAP (S-CAP and SM$_{ux}$-CAP), deriving the BER analysis of the resulting systems and investigating the performance in LOS and NLOS propagation.
4. Employing signal processing techniques to improve the performance degradation of the S-CAP schemes due to co-located optical sources.
5. Developing low complexity detection algorithms for SM$_{ux}$-CAP, comparing the BER performance of the algorithms and evaluating their computational complexities.
6. Developing spectrally-efficient novel subband index CAP (SI-CAP) schemes and validating their superior spectral efficiencies compared to m-CAP through theoretical analysis, simulation and experimental demonstration.

A synopsis of the thesis contributions, spanning both optical fiber and optical wireless

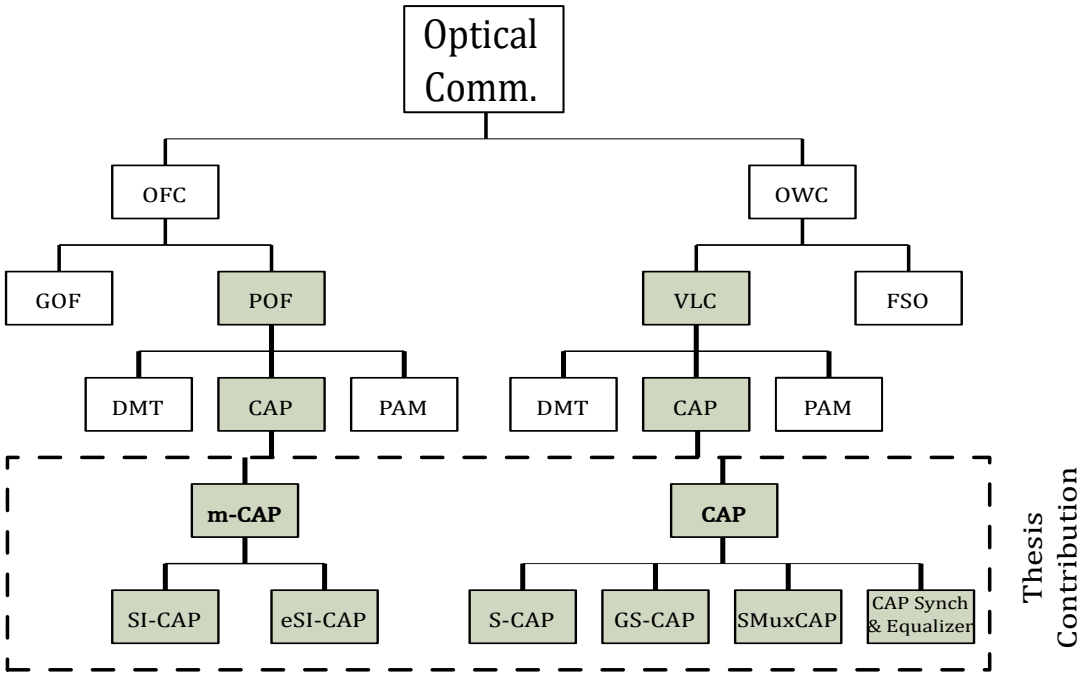

Figure 1.1: A synopsis of the thesis contribution

communications (OFC and OWC), is presented in Fig. 1.1. These contributions have resulted in the following publications:

Publications [J-Journal; C-Conference]

Published

[J1] **K. O. Akande** and W. O. Popoola, "Subband Index Carrierless Amplitude and Phase Modulation for Optical Communications," in *Journal of Lightwave Technology*, vol. 36, no. 18, pp. 4190-4197, 15 Sept.15, 2018.

[J2] **K. O. Akande** and W. O. Popoola, "MIMO Techniques for Carrierless Amplitude and Phase Modulation in Visible Light Communication," in *IEEE Communications Letters*, vol. 22, no. 5, pp. 974-977, May 2018.

[J3] **K. O. Akande**, P. A. Haigh and W. O. Popoola, "On the Implementation of Carrierless Amplitude and Phase Modulation in Visible Light Communication," in *IEEE Access*, vol. 6, pp. 60532-60546, Oct 2018.

[J4] **K. O. Akande** and W. O. Popoola, " Experimental Demonstration of Subband Index Techniques for m-CAP in Short Range SI-POF Links," in *IEEE Photonics Technology Letters*, vol. 30, no. 24, pp. 2155-2158, 15 Dec.15, 2018.

[J5] **K. O. Akande** and W. O. Popoola, " Spatial Carrierless Amplitude and Phase Modulation Technique for Visible Light Communication Systems," in *IEEE Systems Journal*, Jan 2019.

Under review

[J6] **K. O. Akande** and W. O. Popoola, " Enhanced Subband Index Carrierless Amplitude and Phase Modulation in Visible Light Communications," in *Journal of Lightwave Technology*, Feb 2019.

Papers in conference proceedings

[C1] **K. O. Akande** and W. O. Popoola, "Generalised Spatial Carrierless Amplitude and Phase Modulation in Visible Light Communication," 2018 *IEEE International Conference on Communications (ICC)*, Kansas City, MO, USA, 2018, pp. 1-6.

[C2] **K. O. Akande**, F. B. Offiong, H. Alrakah and W. O. Popoola, "Performance Comparison of MIMO CAP Receivers in Visible Light Communication," 2018 11th *International Symposium on Communication Systems, Networks and Digital Signal Processing (CSNDSP)*, Budapest, July 18-20, 2018.

[C3] G. Egecan, **K. O. Akande**, P. A. Haigh, and W. O. Popoola, "Frequency Response Modelling of Cool and Warm White LEDs in VLC Systems," 2018 *The First West Asian Colloquium on Optical Wireless Communications*. Irfan. Iran, 25 April 2018.

[C4] **K. O. Akande**, P. A. Haigh and W. O. Popoola, "Joint equalization and synchronization for carrierless amplitude and phase modulation in visible light communication," 2017 13th *International Wireless Communications and Mobile Computing Conference (IWCMC)*, Valencia, 2017, pp. 876-881.

[C5] **K. O. Akande** and W. O. Popoola, "Synchronization of carrierless amplitude and phase modulation in visible light communication," 2017 *IEEE International Conference on Communications Workshops (ICC Workshops)*, Paris, 2017, pp. 156-161.

[C6] **K. O. Akande** and W. O. Popoola, "Impact of timing jitter on the performance of carrier amplitude and phase modulation," 2016 *International Conference for Students on Applied Engineering (ICSAE)*, Newcastle upon Tyne, 2016, pp. 259-263.

Awards

[1.] **Best poster award** at the first *IEEE International Conference for Students on Applied Engineering (ICSAE 2016)*, Newcastle upon Tyne, UK.

[2.] Recipient of the **IEEE Communication Society (COMSOC) Student Travel Grant** for the *IEEE ICC 2018*, Kansas City, USA.

1.5 Thesis Organization

Following the introductory part contained in this chapter, chapter 1, the remainder of the thesis is organized into seven chapters. Chapter 2 reviews the state-of-the-art by discussing the transmitters and receivers in VLC and SI-POF as well as their pre/post signal processing techniques. In addition, the fundamentals of CAP modulation including its filter parameters, multiband version and challenges are discussed.

The techniques that are employed to mitigate the challenges of CAP-based systems are discussed in chapter 3. Specifically, a low complexity novel synchronization technique is presented along with experimental validation and comparison with the state-of-the-art technique. Furthermore, FSE is shown to be capable of joint synchronization and equalization of CAP signals and its superior performance compared to SSE is experimentally validated.

The S-CAP and its generalised version as well as their BER analytical derivations are presented in chapter 4. The chapter also include the study of their performances in LOS and NLOS conditions along with the performance-enhancing techniques that are developed to improve performance degradation due to closely-spaced optical sources and receivers.

The system model of SM$_{ux}$-CAP, its BER analytical derivation and performance comparison with repetitive-coded CAP (RC-CAP) are presented in chapter 5. Four low-complexity detection algorithms for SM$_{ux}$-CAP, along with their BER performance comparisons and computational complexity analysis, are also detailed in the chapter. Furthermore, it is shown

in chapter 5 how signal processing technique can be employed to improve the performance degradation of SM$_{ux}$-CAP when the optical sources are co-located.

The spectral efficiency of m-CAP is significantly improved by the SI-CAP developed and presented in chapter 6. In addition to the bits transmitted on the signal constellation, the SI-CAP modulates extra bits on the subband indexing of m-CAP, thereby improving its spectral efficiency. Low complexity detection algorithms that ensure the gains of SI-CAP are obtained at comparable complexity with m-CAP are also presented in the chapter. In addition, the chapter contains analytical, simulation and experimental results that validate the gains of SI-CAP compared to m-CAP in both VLC and SI-POF channels.

Enhanced SI-CAP (eSI-CAP) is presented in chapter 7 to solve the complexity challenge in SI-CAP. The complexity arises from the fact that to maintain the same spectral efficiency as m-CAP, the SI-CAP requires increasing number of subbands as constellation size increases. The eSI-CAP developed in chapter 7 resolves this complexity as well as improves the spectral efficiency gain of SI-CAP. The performance gain of eSI-CAP is also validated in the chapter with theoretical analysis, simulations and experimental demonstrations. Furthermore, novel detection algorithm that significantly reduces the detection complexity of eSI-CAP while maintaining the same BER performance as the maximum likelihood detector (MLD) is presented.

Finally, the thesis is concluded in chapter 8 by highlighting the summary of the main contributions in each chapter and their implications. A list of future work that are recommended to improve on the various techniques developed in this thesis is also presented.

Chapter 2

Review of the State of the Art

The background concepts underlining the thesis, such as VLC technology, SI-POF system and the CAP modulation scheme, are covered in this chapter. The state of the art regarding these concepts in the literature are presented to lay a solid background for the performance-enhancing techniques that are later developed in the thesis. The review include the working principles of the optical sources and receivers, modelling of the optical wireless and plastic optical fibre communication channels, signal processing techniques that are adopted for performance improvement, the fundamentals of CAP modulation scheme and its implementation challenges.

2.1 VLC System Model

The first historical reference regarding transmitting information using the visible light medium can be traced back to the demonstration made by Alexander Graham Bell and his assistant Charles Sumner Tainter in 1880 [32]. With their "Photophone" invention, they demonstrated wireless transmission of voice message over a distance of 200 m using the sunbeam as the carrier. However, the intermittent nature of the sunlight coupled with weather conditions such as fog and wind stunted the advancement of Bell's breakthrough and prevents its practical implementation. Subsequent advancement in radio communication further inhibits research in light communication. A combination of several factors is now contributing to a renaissance of communicating using the light beam as conceived by Bell. The radio communication is currently experiencing a spectrum crunch due to bandwidth bottleneck. The overcrowded radio spectrum results from the information revolution and proliferation of smart devices that are accessing the wireless network. Simply put, the demand for bandwidth is far outstripping the network service providers' ability to supply. In addition, the need for higher speed connection

has never been greater due to the current trend of enhancing broadband mobile experience with innovative data applications and services. The combination of all the aforementioned factors has made it imperative to seek alternative and/or complementary technologies with higher capacity than the existing communication network infrastructure. The visible light communication (VLC), which combines illumination with high speed data communication, is one of such technologies with its spectrum ranging from 400 THz to 800 THz (380 nm - 780 nm). Compared to the RF spectrum, VLC provides a higher bandwidth that is up to an order of four as shown in Fig. 2.1. Hence, the VLC represents a vast untapped and unregulated reservoir of free spectrum.

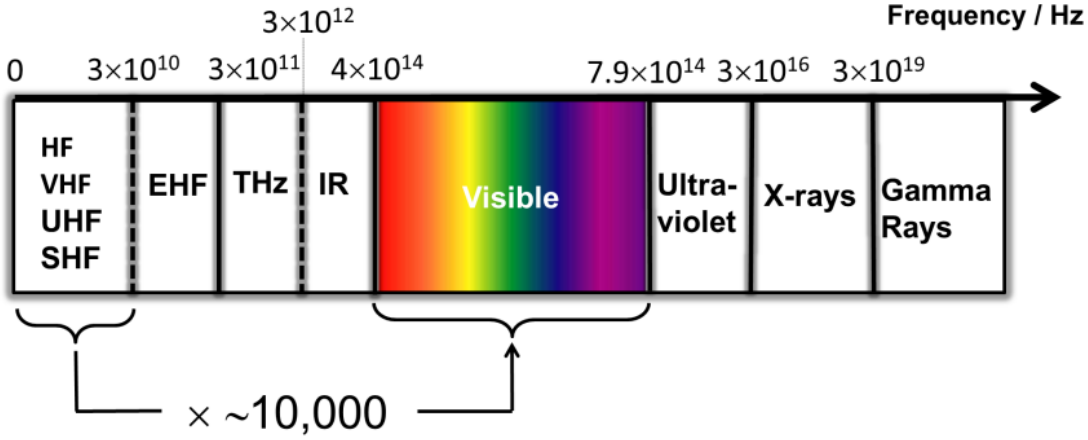

Figure 2.1: The electromagnetic spectrum showing that VLC bandwidth is $\approx \times 10,000$ *larger than that of RF [1].*

The combination of illumination with data communication is another major factor influencing the fast adoption of VLC. Major governmental organizations, institutions, businesses and residential buildings are switching from inefficient conventional lighting sources such as the incandescent and fluorescent lighting devices to the much more efficient solid-state LED. Advancement in the field of solid-state lighting (SSL), the art of producing light through solid-state electroluminescence, has resulted in the production of high-brightness LED with improved luminous efficacy [4]. This improvement has seen the luminous efficacy of LED increasing from 25 lm/W to over 160 lm/W over the last 15 years [33]. This is in addition to the corresponding decrease in the cost of LED packages that has made it competitive to the traditional lighting devices, considering both the initial cost and the operating cost over

the LED life cycle. Furthermore, the best performing conventional lighting devices with the highest luminous efficacy is the high-intensity discharge lamps with around 100 lm/W and usable life of $15,000$ h. This is in comparison to about $100,000$ h operating life cycle of LEDs with up to 250 lm/W. Thus, in comparison to the conventional lighting technologies, SSL offers significant advantage in the energy usage and the associated cost savings. Other advantages of LEDs over the conventional lighting devices include lower heat generation, lower power consumption, smaller and compact size, mercury free and higher tolerance to humidity [2].

While LEDs are steadily gaining popularity due to their associated energy and cost savings properties, their most important property for enabling the widespread of VLC is their fast-switching speed [2, 4]. This property allows data information to be impressed on the LED radiated output by rapid, steady flickering of its intensity and without it being perceived by the human eye. This high frequency switching, which is not available with other lighting technologies, enables the VLC to perform the dual functionality of providing the general illumination and delivering high-speed data communication, simultaneously.

The first reported adoption of LED as a VLC device in the literature is by Pang *et al* [34] who demonstrated the modulation of audio messages on the visible beam of light that is emitted from an LED traffic light. However, full research into VLC for indoor and home network only took-off with the pioneering work of Tanaka *et al* in [35] who proposed the use of high-brighteness LED for wireless home networking. The RONJA (Reasonable Optical Near Joint Access) system later used beam of visible light to established a 10 Mb/s full duplex Ethernet point-to-point free space link that extends up to 1.4 km in 2001 [36]. In 2003, the Visible Light Communication Consortium (VLCC) was established to provide standardization for the now rapidly developing VLC technology and promote its adoption. Following the VLCC establishment, governments, industries and research agencies all provide funds to further the rapid development of VLC technology [2]. Since then, different research groups have reported world record data rates from VLC experimental demonstrations. High-speed VLC links exceeding 10 Gb/s have been established with off-the-shelf LEDs [19].

Apart from the huge bandwidth available in the visible light spectrum, there are other numerous advantages of VLC when compared with RF. Unlike RF, the VLC is unaffected by electromagnetic interference (EMI) which makes it suitable for communication in sensitive

places such as hospitals, military installations, aeroplanes and so on [2, 3]. The inability of the VLC to penetrate opaque objects gives it an inherent security towards eavesdropping/snooping and enables the possibility of spatial reuse. Furthermore, VLC makes use of a relatively simple intensity modulation and direct detection technique as well as inexpensive devices to establish its communication link. Similarly, VLC can easily be incorporated into existing infrastructure at very low cost due to the already wide adoption of energy-efficient LEDs for illumination [37].

In order to fully realize the full benefits of VLC, the challenges encountered in its deployment will need to be addressed. The challenges emanate from the various components of the VLC system as shown in Fig. 2.2. They can be categorized into those relating to the transmitter, the channel and the receiver. Various signal processing techniques are therefore employed to mitigate the challenges in order to obtain a reliable communication link. These challenges and the processing techniques that are employed to mitigate their impact are further discussed.

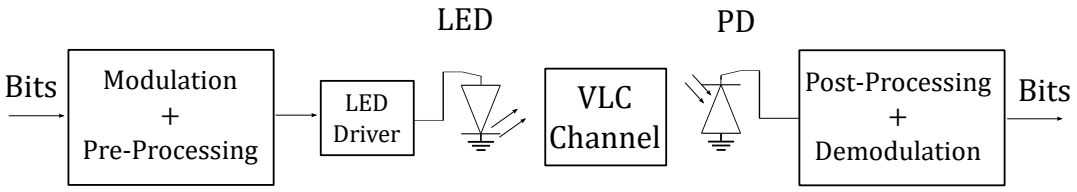

Figure 2.2: The VLC components.

2.1.1 Optical Sources/Transmitters for VLC Systems

In a process referred to as *electroluminescence*, LEDs emit photons of light in response to an applied voltage at its junctions. Though the emitted light is incoherent, it can be functionally regarded as monochromatic from human eye perception. However, white LEDs are the most commonly employed optical source for VLC, mainly to achieve a seamless and low-cost integration of VLC into the existing illumination infrastructure. As a result, the preferred white light is generated through two methods. One widely employed approach is through the application of a yellow phosphor coating to a blue LED, such that the coating absorbed part of the blue light to produce a yellow light [38]. The remaining unabsorbed blue light then combines with the yellow light, resulting in a white phosphor-converted

LED (PC-LED). Though the PC-LED is cost-effective, energy efficient, has low-complexity and good colour rendering index (CRI), it has a low modulation bandwidth due to its slow yellow phosphorescent component. The low modulation bandwidth represents a bottleneck in achieving high speed VLC system.

Another approach to achieving white LED is through the use of multi-chips LED namely red, green and blue LED (RGB LED). The combination of these three colours result in the emission of white light with higher modulation bandwidth than that of PC-LED. However, due to its high cost, relatively complex circuitry and poor quality colour rendering capability, the RGB LED is seldom employed for commercial illumination purposes requiring white lighting [2, 39].

There are other types of LEDs that have been developed. Organic LEDs (OLEDs) are fabricated by using an organic compound as the emissive layer of the LED [38, 40–42]. The resulting LED is suitable for display purposes due to its low-cost and flexible display, wide viewing angle and low driving voltage. However, when compared to inorganic LEDs, it has lower bandwidth on the order of 100's of kHz and has a shorter life span, approximately $50,000$ h. This makes it unsuitable for high-speed data communication and the general illumination purposes. Micro LEDs (μ-LEDs) are another type of LEDs with high bandwidth on the order of 100's of MHz [43–45]. They can be manufactured by reducing LED active area with a corresponding reduction in capacitance and an increase in the current density. With an area of about 100×100 μm^2, they are usually deploy in arrays and thus, very suitable for MIMO systems. There are also resonant cavity LEDs (RC-LEDs) that employed distributed Bragg reflectors to improve the light extraction efficiency of the conventional LEDs and enhance its emitted light [46]. The RC-LEDs have better spectral purity and higher bandwidth than the conventional LEDs [2, 14].

In light of the limited bandwidth of the optical transmitting sources, there have been various experimental and theoretical reports of light sources that can support high speed data communication in the literature. Over 200 Mb/s data rate was first reported by [47] using a single white LED with DMT. This was followed by data rates in the range of Gb/s using CAP and OFDM modulation schemes [48, 49]. Recently, there has been demonstration of 2-Gb/s over a single commercial phosphorescent white LED using OFDM with adaptive bit loading [50]. On the other hand, 10 Gb/s has been demonstrated for RGB LEDs employing a

rate adaptive OFDM with wavelength division multiplexing (WDM) [51, 52]. Using WDM, CAP modulation and equalizers, the use of a commercially available LED having four channels namely red, blue, green and yellow (RGBY LED) has also been experimentally demonstrated to achieve a data rate of 8 Gb/s over a distance of 1 m indoor free space [19]. Similarly, a commercially available RGBY LED has been shown to achieve greater than 5 Gb/s for downlink distance of up to 4 m [53].

For systems employing μ-LED, a high data rate of 1 Gb/s has been experimentally demonstrated in a free space VLC link using on-off keying (OOK) without equalization [45]. Recent demonstrations show an increased data rate of 3 Gb/s and 5 Gb/s with the use of DCO-OFDM and a single blue μ-LED [44, 54]. Despite their low bandwdiths, demonstrations involving organic LEDs including polymer LEDs have reported data rates of more than 50 Mb/s with the use of artificial neuron equalizer and DMT [38, 42].

There have been a number of high data rate experimental demonstrations involving the use of laser diodes (LD) as optical source for free space VLC. The use of an integrated waveguide modulator - laser diode (IWM-LD) with low power consumption was shown to achieve the data rate of 1 Gb/s in [55]. The authors of [56] also demonstrated a high data rate of 9 Gb/s with the use of Gallium Nitride (GaN) blue LD employing OFDM over a 5 m free space link. Furthermore, an off the shelf RGB LD has been experimentally shown to achieve up to 14 Gb/s [57].

To tackle the effect of the slow phosphorescent converter, many experimental demonstrations have employed organic semiconductor colour-converters to improve the limited bandwidth of the PC-LEDs. A novel fast colour-converter using a blend of conjugated polymers has been shown to result in a bandwidth of 200 MHz which is more than 40 times higher than that obtain with the commercially available phosphor colour-converter [58]. Recent work has shown a higher modulation bandwidth of 470 MHz resulting in 140 times improvement in bandwidth and 55 times increase in data rate when compared with that of commercially available phosphor colour converters [59].

2.1.2 Optical Detector/Receiver for VLC Systems

The optical detector/receiver convert the received beam of light into a photocurrent signal. To ensure an efficient conversion, the receiver must have high bandwidth and be highly sensitive at the wavelength of the received signal [60]. The VLC receiver does not need sophisticated and complex circuitry as it directly detects the received optical power. In addition, the area of the optical detector is up to a million times the square of the optical signal wavelength. Because the fluctuation (fading) of the received optical signal occurs at the wavelength scale, this detector size provides 'spatial diversity' and cancels the effect of the fading through averaging [4, 61]. As a result, VLC receivers are broadly based on silicon photodiodes (PDs) and image sensors [62, 63]. The reported high data rates for VLC have been mainly achieved using silicon PDs.

For the silicon PD-based receiver, the two most commonly used are the PIN PD and avalanche PD (APD) [19, 64]. The PIN PD has a lower gain but is more widely adopted due to its low cost and relative stable performance when receiving high intensity photons. There has been experimental demonstrations with data rates of Gb/s for PIN PDs reported in the literature [19, 20, 49, 65]. On the other hand, the APD has a higher gain but requires complex circuitry and is prone to excessive shot noise and thermal runway due to excessive photocurrent produced in response to high intensity photons [62, 66, 67]. The complementary metal-oxide-semiconductor (CMOS) based image sensors that are widely embedded in common devices such as smartphones and laptop can be employed as VLC optical receivers, but their frame rate limits the achievable data rate to less than kb/s [68]. However, a novel CMOS based image sensor capable of receiving high speed optical signals has been reported in a field trial with a data rate of 10 Mb/s [69]. Recent results have also achieved data rate beyond the frame rate by implementing novel demodulation schemes resulting in up to 5.76 kb/s [70, 71].

Optical concentrators are usually employed to enhance the PD receiver collection area, as direct increase of the PD area not only results in high cost but also reduces the electrical bandwidth. However, the field of view (FOV) and gain of the conventional compound parabolic concentrator (CPC) are limited by the conservation of 'Entendue' [72]. This limitation has been addressed with the recent proposed fluorescent optical concentrators that exceed the limit

of entendue and achieve gain of up to 50 times that of an entendue conserving concentrator [72–75]. There are also various VLC receiver configurations proposed to improve performance. The simplest and most commonly adopted is the single element PD that has been reported in many demonstrations. Apart from this, selection/diversity combiners are reported in [76] as a way to improve performance. However, some of the results only show marginal improvement in spite of the significant increase in complexity. Imaging receiver is another configuration that has been reported in [77–79]. The configuration uses multiple optical lens to decompose received signal based on their sources and focus each on separate photodetector. This removes interference and is very useful for MIMO scenarios [79]. Angle diversity receiver have also been reported in [77]. This receiver configuration uses a wide FOV to improve the area covered by the PD.

2.1.3 Modelling of VLC Channels

The power that is radiated by the VLC optical source is not coherent which makes it impossible to employ a coherent receiver. As a result, intensity modulation (IM), where the modulating waveform $(x(t))$ is impressed upon the instantaneous radiated intensity of the optical source, is mostly adopted in VLC systems. The radiated intensity is then directly detected (DD) to generate a proportional photocurrent with the aid of a photodetector. Thus, the VLC channel is referred to as *intensity modulation and direct detection* (IM/DD) channel.

Figure 2.3 shows a baseband linear system model of the VLC channel where $s(t)$ and $y(t)$ represent the channel input and output waveforms. The $s(t)$ and $y(t)$ correspond to the instantaneous optical radiated power by the optical source and the instantaneous generated photocurrent by the receiving PD, respectively. The $y(t)$ is obtained by integrating the received instantaneous power all over the surface of the PD. Since the PD area is million of square of the optical wavelength, the integration over the PD surface provides spatial diversity that eliminates multipath fading effect [61]. However, the receiver still experiences multipath-induced distortion, especially in a NLOS medium where the radiated power propagates over different paths with varying lengths.

The VLC baseband model in Fig. 2.3 can be expressed as

$$y(t) = \mathcal{R}h(t) \otimes s(t) + w(t) \tag{2.1}$$

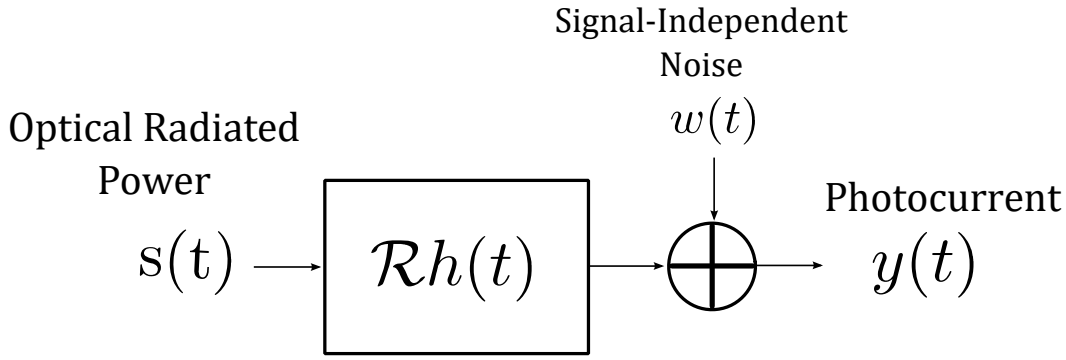

Figure 2.3: The baseband linear system model of VLC channel.

where $h(t)$ is the channel impulse response of the OWC, $\mathcal{R}$ is the responsivity (A/W) of the PD and '$\otimes$' symbol represents the convolution operation. The $w(t)$ is the signal-independent noise component consisting of the shot and ambient noise, and modelled as white additive Gaussian noise (AWGN). In contrast to the RF system where the channel input $s(t)$ is the signal amplitude, the $s(t)$ represents the instantaneous power in optical system. As a result, there are some fundamental differences due to this distinction. The first is that $s(t)$ is non-negative $x(t) \geq 0$ and also, the average radiated optical power P_t is given by

$$P_t = \lim_{T\to\infty} \frac{1}{2T} \int_{-T}^{T} s(t)dt. \tag{2.2}$$

2.1.3.1 VLC Link Modelling for LOS Propagation

The VLC system usually adopts an LED as its optical source while using a PD to detect the radiated intensity. A typical path profile for the ray tracing indoor optical channel model, used to model the VLC link [61], is shown in Fig.2.4. Using a generalized Lambertian radiant intensity, the angular distribution of the radiation intensity pattern can be modelled as [4]:

$$R_0 = \begin{cases} \frac{m_1+1}{2\pi} \cos^{m_1}(\theta), & \text{for } \theta \in [-\pi/2, \pi/2] \\ 0 & \text{for } \theta \geq \pi/2 \end{cases} \tag{2.3}$$

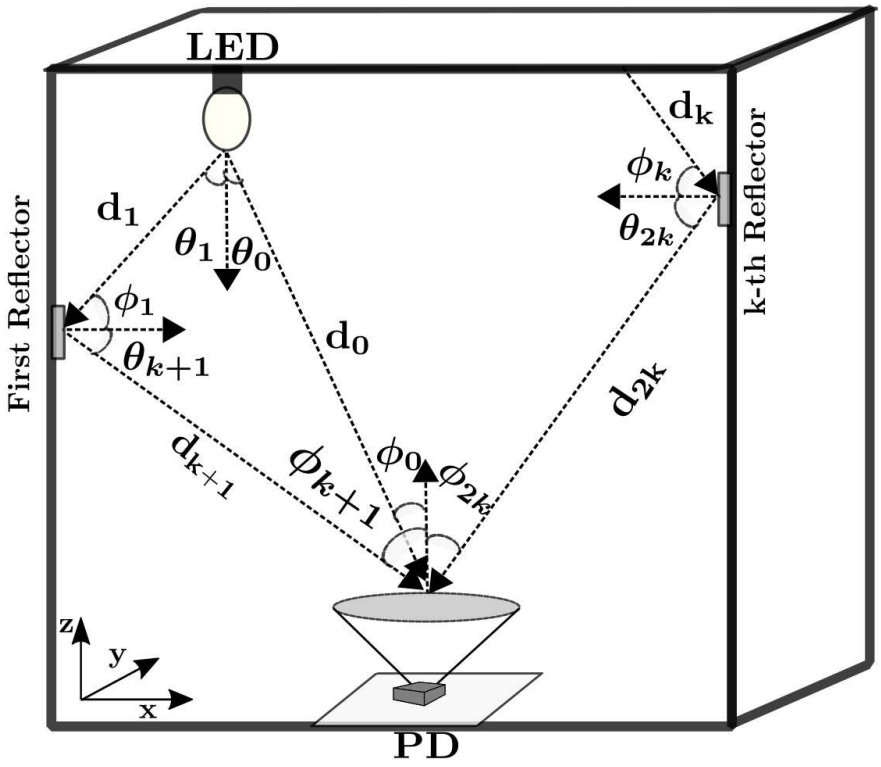

Figure 2.4: The path profile for the ray tracing indoor optical wireless channel model.

where θ is the irradiance angle and m_1 is the Lambert's mode denoting the directivity of the source beam. The m_1 can be expressed in terms of the LED semiangle at half-power $\Phi_{1/2}$ as

$$m_1 = \frac{-\ln(2)}{\ln(\cos \Phi_{(1/2)})} \tag{2.4}$$

An optical concentrator is usually employed in practise to focus a large part of the radiated intensity on the PD. Though using a large-area PD will also increase the amount of power detected, the associated challenges such as reduced bandwidth and increased noise make it not as practicable. The optical gain of an ideal non-imaging concentrator with a refractive index n is expressed as:

$$g(\phi) = \begin{cases} \frac{n^2}{\sin^2 \phi_c}, & 0 \leq \phi \leq \phi_c \\ 0 & \text{for } \phi > \phi_c \end{cases} \tag{2.5}$$

where ϕ is the incidence angle and $\phi_c \leq \pi/2$ is the FOV of the receiver. For a VLC link employing an optical source with Lambertian radiation, an optical filter with gain $T_s(\phi)$ and a concentrator with a gain of $g(\phi)$, the LOS impulse response for the receiver having an area

$A_{(PD)}$ and located at distance d is given as

$$h_{\text{LOS}}(t) = \frac{A(m_1+1)}{2\pi d^2} \cos^{m_1}(\theta) T_s(\phi) g(\phi) cos(\phi) \delta\left(t - \frac{d}{c}\right) \tag{2.6}$$

where $\delta(\cdot)$ is the dirac delta function, $\delta\left(t - \frac{d}{c}\right)$ represents the propagation delay while c is the speed of light in free space. The expression in (2.6) assumes that $\theta < 90°$, $\phi <$ FOV and that $d \gg \sqrt{A}$.

Alternatively, the VLC channel can be characterized in frequency domain by taking the Fourier transform (FT) of the channel impulse response to obtain the frequency response of the channel, $H(f)$. The $H(f)$ can be expressed as:

$$H(f) = \int_{-\infty}^{\infty} h(t) e^{(-j2\pi ft)} dt. \tag{2.7}$$

From (2.7), the channel DC gain can be obtained as

$$H(0) = \int_{-\infty}^{\infty} h(t) dt. \tag{2.8}$$

while the DC gain for the LOS configuration can be approximated as:

$$H_{\text{LOS}}(0) = \begin{cases} \frac{A(m_1+1)}{2\pi d^2} \cos^{m_1}(\theta) T_s(\phi) g(\phi) cos(\phi) & 0 \leq \phi \leq \phi_c \\ 0 & \text{elsewhere} \end{cases} \tag{2.9}$$

Using (2.9), the received power for an LOS channel can be expressed as:

$$P_{r-\text{LOS}} = H_{\text{LOS}}(0) P_t \tag{2.10}$$

2.1.3.2 VLC Link Modelling for Non-LOS (NLOS) Propagation

The optical channel modelling for NLOS link is more complex as it depends on many factors such as the room dimensions, the reflectivity of the ceiling, floor and walls of the room as well as those of the various objects in the room, the relative placement of the optical source and detector, the window size and so on [4]. In general, the received optical power for non-LOS (NLOS) link can be expressed as [4]:

$$P_{r-\text{NLOS}} = \left(H_{\text{LOS}}(0) + H_{\text{NLOS}}(0)\right) P_t \tag{2.11}$$

$$= \left(H_{\text{LOS}}(0) + \sum_{refl} H_{\text{refl}}(0)\right) P_t \tag{2.12}$$

where $\sum_{refl} H_{\text{refl}}(0)$ represents the gain of the reflected path. The radiated intensity that passes through NLOS link arrive at the receiver through multiple paths, at varying time and with different gains. As a result, the impulse response is obtained by integrating the power of all the components that propagate through the different paths (multipath) and are received by the detector. The received optical power distribution for NLOS link has been investigated in [80] using a single reflection only. However, the power associated with higher order reflections can not be ignored as they arrive at the receiver much later than the first order reflection. In order to incorporate the effect of higher order reflections in the channel modelling of NLOS link, Barry et al. [61] developed a framework for evaluating the path loss and time delay of every components arriving at the receiver for a given number of reflections. These are then added together to get the impulse response. The Barry et al. recursive algorithm for evaluating the impulse response $h^{(k)}(t; S, R)$, for a given source S, receiver R and small j^{th} elemental surface of area ΔA, after k reflections is given by [4, 61]

$$h_{\text{nlos}}(t; S, R) = \frac{m_1 + 1}{2\pi} \sum_{j=1}^{K} \rho_j \cos^{m_1}(\theta_j) \frac{\cos(\phi)}{d_{Sj}^2} \text{rect}\left(\frac{2\phi}{\pi}\right) \times h_{\text{nlos}}^{(k-1)}\left(t - \frac{d_{Sj}}{c}; S, R\right) \Delta A \tag{2.13}$$

where ρ_j is the reflectivity of the j^{th} reflecting surface given for indoor VLC in [81]. The d_{Sj} represents the distance from S to the j^{th} reflecting surface while

$$\text{rect}(x) = \begin{cases} 1, & \text{for } \|x\| \leq 1 \\ 0 & \text{for } \|x\| > 1. \end{cases} \tag{2.14}$$

The time-dispersive property of multipath propagation is quantified using the RMS channel delay spread, τ_{rms} defined as [4, p. 85]:

$$\tau_{\text{rms}} = \left[\frac{\int (t - \mu)^2 h^2(t) dt}{\int h^2(t) dt}\right]^{1/2} \tag{2.15}$$

where μ is the mean delay spread given by :

$$\mu = \frac{\int t h^2(t) dt}{\int h^2(t) dt} \tag{2.16}$$

2.1.4 Signal Processing Techniques for Impairments in VLC systems

Despite the many benefits of VLC systems, it has its limiting challenges. The limited bandwidth of the white PC-LED is one of the major challenges of VLC systems. In addition, the LED has a limited linear operating region as shown in its I-V curve of Fig. 2.5. This limited range puts a constraint on the maximum amplitude swing of the transmitted signal and can result in clipping of signals with high PAPR. Furthermore, the transmission range is limited due to significant attenuation of the radiated power with distance. Other sources of challenge include the significant noise contribution of ambient light that reduces the signal SNR, resulting in BER degradation. The signal processing techniques that are adopted to address the VLC challenges and improve the received signal quality are further discussed.

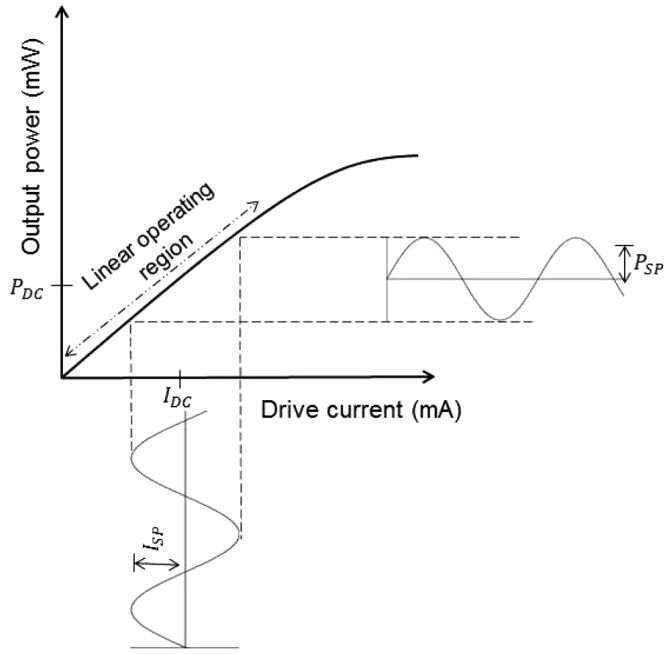

Figure 2.5: The current-power output curve of an LED with the swinging current I_{SP} [2].

2.1.4.1 Enhancing the Bandwidth of VLC Systems

To enhance the limited bandwidth of VLC systems that result from the use of white PC-LEDs, the following processing techniques are usually employed:

- Blue filtering: The low modulation bandwidth of the PC-LED is due to the slow time response of the yellow phosphor coating. In comparison to the blue chip in the LED, the

yellow phosphor is very slow at high frequency and becomes a bottleneck to achieving high speed data communication. This bottleneck can be removed by the use of blue filter at the receiver. The blue filter is used to extract the blue component of the received signal while the yellow component is blocked [10, 11]. Though, this filtering out results in power penalty due to the lost energy of the yellow component, the approach substantially improve the available bandwidth from less than 5 MHz to ~ 20 MHz.

- Pre-Equalization: Analog RLC circuit have been employed at the transmitter to provide frequency response equalization [82]. The multiple-resonant equalization, implemented at the transmitter, are reported in [10, 82] to result in up to 25 MHz bandwidth improvement. The pre-equalization approach requires an initial measurement of the LED frequency response followed by designing adequate resonant frequencies for the equalization. A pre-equalization approach reported in [10] uses a driving technique that utilizes a group of LEDs to form a single link. It achieves an improved aggregate bandwidth by independently tuning the frequency response of each LED using a resonant driving technique. Employing 16 LEDs, the technique successfully improve bandwidth from 2.5 MHz to 25 MHz. In addition to the analog pre-equalization, optimal power and bit loading have also been implemented for optical systems employing multicarrier modulation schemes at the transmitter. To achieve a specified BER, the subcarriers of a multicarrier technique like OFDM are adaptively allocated power and loaded with bits under the constraints of the channel state information (CSI) [83, 84]. In this way, the optimum QAM symbol level and power are allocated to subcarriers in order to achieve a specified aggregate BER performance [84].

- Post-Equalization: Analog post-equalization has also been considered for indoor VLC systems in [85]. The proposed system uses a first-order equalizer followed by an amplifier and improved the bandwidth of the VLC system from 3 MHz to 50 MHz [85]. However, this technique is prone to noise enhancement at the amplification stage. In contrast, adaptive equalizers are not prone to noise amplification and generally have better performance, especially for high-speed VLC systems. Adaptive equalizers employ stochastic gradient descent algorithms such as recursive least squares (RLS) and least mean squares (LMS) to automatically adapts to the time-varying properties of the VLC channel. Decision feedback and feedforward equalizers (DFE and FFE) are examples of

adaptive equalizers that have been implemented to achieve high data rate in VLC systems [20, 86]. As adaptive equalizers use training symbols for their weights adaptation, this lead to spectral efficiency loss especially for mobile terminals requiring frequent training. It also leads to high computational complexity for channels with large delay spread that require long training sequences for adequate performance. Hence, there is a trade-off between the performance gain of the adaptive equalizers and the associated spectral loss and/or computational complexity.

2.1.4.2 Compensating LED-Nonlinearity

The I-V characteristics of the LED, shown in Fig.2.5, places a constraint on the amplitude swing of the signal that can be used to modulate the LED radiated power. An LED with low dynamic range will have a non-linear output when the modulating signal have a large negative swing that goes below its turn on voltage (TOV) or a large positive swing that extends to its saturation region [2]. This is a problem with multicarrier techniques such as OFDM and m-CAP as the symbols modulated on their subcarriers have high probability of adding up to a large peak [87]. This increases intercarrier interference and results in BER degradation. As a result, it is imperative to employ an LED with a large dynamic range and operate the device within its linear region and around an optimum bias point. The most common method to deal with LED non-linearity is through signal clipping [88–90]. Other techniques have been proposed in the literature with the aim of achieving good balance between BER improvement and computational complexity [29].

2.1.4.3 Mitigating Interference from Optical Background Noise in VLC

There are multiple sources of optical noise that degrades the performance of VLC receiver. Shot noise arises from the random/fluctuating arrival of photons at the receiver and the flow of dark current in the PD even when no input photons is received [4]. In receiver employing APD, there is an additional gain-dependent excess noise that emanates from the cascaded flow of electrons as a result of the APD internal random multiplicative process [64]. Furthermore, background/ambient noise exists in VLC receiver due to the excited electrons by the photons received from surrounding optical sources such as fluorescent light and sun radiation. Additionally, the resistive element of the receiver circuit generates heat which

causes thermal fluctuation of electrons that results in thermal noise [4]. The use of Manchester coding to mitigate optical background noise has been investigated in [91] using theoretical analysis and experimental demonstrations. The experimental results shows that Manchester coding can significantly reduce the optical noise with frequency below 500 kHz and those from fluorescent light. The use of adaptive filtering to improve the signal-to-interference ratio (SIR) that are contributed by light sources of different wavelengths have also been investigated in [92], resulting in an improved performance.

2.2 Description of Step-Index Plastic Optical Fibre (SI-POF)

The first demonstration of a low-loss optical fibre in 1970, by engineers at the Corning Glass Company, heralded the era of optical fibre communication [93, 94]. The engineers demonstrated an optical fibre with attenuation of 20 dB/km in comparison to the approximately 1000 dB/km attenuation existing at the time. Despite the development of the low-loss fibre, the first set of fibres had bandwidth limitation resulting from multi-mode dispersion. This was later overcome by the development of single-mode fibres [14]. Further advancement in optical fibre necessitates improvement in electronics which has become the system limiting factor at high frequency transmission. As a result, technologies such as WDM, optical amplifiers, coherent detection, polarization multiplexing and spatial division multiplexing were all developed to achieve high frequency data transmission through optical fibre [14].

The use of optical fibre for data communication has revolutionized the communication landscape as they are deployed in virtually all the core and metro networks and serve as the backbone for high-speed switching in large networks [16]. They are also increasingly being used closer to the end user due to the proliferation of fibre-to-the-home (FTTH) technologies. The optical fibre technology has replace the traditional copper transmissions due to many of its advantages. It is immune to electromagnetic interference (EMI), has lower attenuation, possesses higher bandwidth and data rates [14]. In home networks, the plastic optical fibre (POF) represents an attractive medium of communication due to its ease of installation and lower cost [15].

The first available POF had very high attenuation of up to 1000 dB/km and was later reduced to 125 dB/km. Despite the advancement, the use of POF for data communication only started

gaining foothold due to the coming of digitization age [16]. Copper cables were the preferred medium for computer networks and in fibre, the use of glass fibre is much preferred due to its superiority at longer distances. With data digitization, POF steadily gained popularity due to its resilience and immunity to EMI. As a result, several standards have been developed for POF and consumer products are now available. A typical system model for POF transmission is

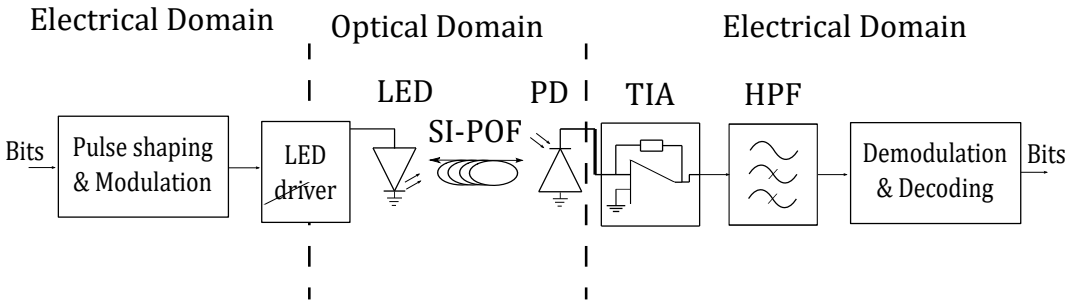

Figure 2.6: An SI-POF system model for data transmission.

shown in Fig.2.6. The processing for optical transmission are mainly done in electrical domain and only the data transmission takes place in the optical domain. This means there is conversion from electrical to optical domain (E/O conversion) at the transmitter typically achieved by an optical source and optical to electrical conversion (O/E) at the receiver which is achieved by a PD. As discussed in VLC case, this process is mostly done by intensity modulation (IM) at the transmitter and the direct detection (DD) of the radiated intensity at the receiver. A coherent detection, where the received light intensity is proportional to the electric field as opposed to the photocurrent in IM/DD can also be employed, but is not usually used as complicated and precise optics are required to realize a reliable detection.

2.2.1 Transmitters/Receivers for SI-POF

The optical sources that are mostly employed for SI-POF are the LED, the RC-LED and the semiconductor LD. The choice of which to use depends on the design objectives as each of the optical sources has its advantages and disadvantages. The conventional luminescence LED is the simplest and the most common light emitting semiconductor. The LED is widely adopted due to its simplicity and cost-effectiveness. The RC-LED is developed by modifying the emission and modulation characteristics of the conventional LED to achieve an improved optical source. Using photo quantization in micro-cavities, key performance parameters of the

conventional LED such as spontaneous emission properties, directionality, intensity and purity are enhanced in RC-LED [46]. Specifically, the enhancement by the RC effect may shorten the spontaneous emission lifetime and results in a higher modulation bandwidth for RC-LED compared to the regular LEDs [14, 95]. RED RC-LED are very important as SI-POF exhibit minimal absorption for optical sources operating at the 650 nm wavelength [16].

In contrast to the LED which operates on the principle of spontaneous emission, the semiconductor LD uses stimulated emission. Though the LD results in higher modulation bandwidth which translates to high data rate transmission, it requires more complex circuitry than the LEDs. The use of a green LD operating at 520 nm has been shown to offer lower attenuation than the traditional 650 nm red LD in [96].

As with the optical sources, there are mainly three types of optical receivers for the SI-POF system. The PIN PD is the most commonly employed receiver for POF systems [97]. The APD contains an extra highly doped layer, in comparison to PIN PD, which gives it ability to generate high number of electrons in response to the impinging photons [98]. The electrons produced in the APD doped layer are multiplied and rapidly accelerated by a local electrical field. This gives the APD higher sensitivity and faster response when compared with the PIN PD [14, 16]. Metal-semiconductor-metal (MSM) PD is a type of PD which has no p-n junction like the APD and PIN PD [99, 100]. It offers a large photo-detecting area with low device capacitance per area [101]. Its large area makes it useful for characterization of large-core POF and its low capacitance per area ensures high bandwidth. High data rate of ≥ 10 Gb/s has been reported in [100] for large area MSM-based photo receivers.

2.2.2 Modelling of SI-POF channel

The SI-POF transmission channel can be approximated by combining the optical transmitter, SI-POF and optical receiver models using the approach in [102]. In developing the models, the transmission channel is assumed to be linear and any non-linearities are neglected. The optical transmitter is modelled as a first-order low-pass filter (LPF) with a frequency response given as [102]:

$$H_{\text{POFtx}}(f) = \left(1 + j\frac{f}{f_{\text{POFtx}}}\right)^{-1} \tag{2.17}$$

where f_{POFtx} is the -3 dB bandwdith of the SI-POF transmitter.

The SI-POF effect can be modelled as a first-order Butterworth LPF with a frequency response [102]:

$$H_{\text{POF}}(f) = \left(1 + j\frac{f}{f_{\text{POF}}}\right)^{-1} \tag{2.18}$$

where the f_{POF} is the -3 dB bandwidth of the POF and is given as the bandwidth-length product divided by the length of the POF link.

The receiver is a photodetector followed by a TIA and can be designed as a two-stage amplifier. The amplifier can be modelled as a second-order LPF with frequency response [102]:

$$H_{\text{POFrx}}(f) = \left(1 + j\frac{f}{f_{\text{POFrx}}\sqrt{\sqrt{2}-1}}\right) \tag{2.19}$$

where the -3 dB of the receiver is given as [14]:

$$f_{\text{POFrx}} = \frac{f_{\text{s}}}{\sqrt{8}} \tag{2.20}$$

with f_{s} being the sampling rate of the system. Therefore the effective SI-POF transmission channel can be realised by combining the models of the transmitter, POF and the receiver as:

$$H_{\text{POFeff}}(f) = H_{\text{POFtx}}(f).H_{\text{POF}}(f).H_{\text{POFrx}}(f) \tag{2.21}$$

2.2.3 Impairments and Signal Processing Techniques in SI-POF

The major impairments in SI-POF transmission can be categorized as attenuation, dispersion, system noise and non-linearity. The non-linearity is encountered mainly at the transmitter when the dynamic range of the optical source is exceeded by the modulating signal [17, 18]. It is less often experienced both during transmission through the fibre and at the receiver.

The signal transmitted through the POF experiences loss of optical power which reduces the received signal SNR as the receiver noise power remains constant. The power attenuation is an exponential function of the fiber length, L and can be expressed as:

$$P_{\text{POFrx}} = 10^{-\gamma L} P_{\text{POFtx}} \tag{2.22}$$

where P_{POFrx} and P_{POFtx} are the received and transmitted power, respectively. The γ is the attenuation coefficient of the POF. Other than the POF attenuation, the signal power can also be attenuated due to the use of splitters and connectors [103].

The different paths or modes that are available in SI-POF create differing path lengths for a propagating signal. As a result, the propagating signal suffers from modal dispersion which leads to broadening of the received signal. The dispersion effect is more pronounced in SI-POF as modal path lengths are directly related to the propagation angle. The maximum delay that is introduced in SI-POF can be calculated as [14]:

$$\delta t_{\text{POF}} = \frac{L n_1^2}{c n_2^2} \left(\frac{n_1 - n_2}{n_1} \right) \tag{2.23}$$

where n_1 and n_2 are the refractive indices of the core and the cladding.

The shot and thermal noise are the two main sources of noise which degrades system performance at the SI-POF receiver. The shot noise arises from the random generation of photoelectrons when the photons impinge on the receiver while thermal noise is due to the temperature of the receiver.

Different equalization techniques have been proposed in [17, 18, 104] to compensate for the transmitter non-linearity, link attenuation, distortion and modal dispersion in SI-POF system. Multilayer perceptron (MLP) based equalizer has been shown in [17] to provide the best performance for nonlinearity and dispersion compensation in SI-POF systems when compared with Volterra and transversal equalizer. It has been experimentally demonstrated in [18] that data rate of more than 10 Gb/s can be achieved using a 10 m SI-POF and an MLP equalizer.

2.3 Modulation Techniques for Optical Communication

The modulation technique employed to impress information on the radiated light intensity, for the purpose of data transmission, depends on several factors such as the intrinsic characteristics of optical sources, the nature of the data-carrying optical signal and the envisioned application. With regards to the characteristics of the optical sources, the non-linear intensity/voltage response must be considered to ensure that the time-domain signal generated by the applied modulation technique lies within the limited dynamic range of the sources. Since the IM/DD approach is adopted in optical communication considered in this thesis, the modulating signal needs to be both real-valued and unipolar non-negative. Due to these factors/constraints, the well-researched traditional modulation schemes from the field of RF communications must be adapted to make them suitable for optical communication.

Single carrier modulation techniques such as OOK, pulse position modulation (PPM), pulse width modulation (PWM), and pulse amplitude modulation (PAM) are typically used for low-to-moderate data rate applications. An OOK scheme for VLC using organic LED with a 93 kHz bandwidth to achieve a data rate of 2.2 Mb/s is demonstrated in [40]. Using an OOK non-return-to-zero (NRZ) modulation with post-equalization and blue filtering, data rates of 100 Mb/s and 340 Mb/s were achieved in [8] and [105], respectively. Pulse position modulation (PPM) based scheme has been shown to require less average power than OOK but is more complex and has higher bandwdith requirement [4, 106].

Multilevel modulations such as PAM can offer high spectral efficiency for VLC applications. The use of multiple intensity levels means that the PAM scheme could be affected by the LED's non-linear characteristics and colour temperature (chromaticity) shift because of variation in drive current [107]. With PAM-4 modulation and use of pre-equalization, a 2 Gb/s data rate has been experimentally demonstrated in [108] over a 0.6 m VLC link employing μ-LED and APD. In [109], bit rates of 5 and 5.4 Gb/s over 20 m SI-POF have been achieved using PAM-4 and PAM-8, respectively. Furthermore, with the use of LED and APD in [110], a 5 Gb/s data rate has been achieved over 25 m SI-POF link.

Typically, the performance of single carrier modulation techniques deteriorates as the data rates increase due to the increase in ISI. Hence, complex equalization techniques are applied to achieve good error performance at high data rates. On the contrary, multicarrier modulation techniques such as OFDM or DMT utilizes multiple orthogonal sub-carriers to send parallel data streams concurrently, thereby reducing ISI and avoiding the use of complex equalizers [111]. A 10 Gb/s data rate has been experimentally demonstrated for OFDM based VLC system in [43] using a micro-LED. Similarly, [112] achieved 10 Gb/s bit rate over a 2.5 mm DMT-based SI-POF system.

2.4 Description of CAP Modulation Scheme

This section explores the details of the CAP modulation scheme, including its generation, the design of its digital filters, comparison to other modulation techniques, reported performance in experimental demonstrations and its implementation challenges.

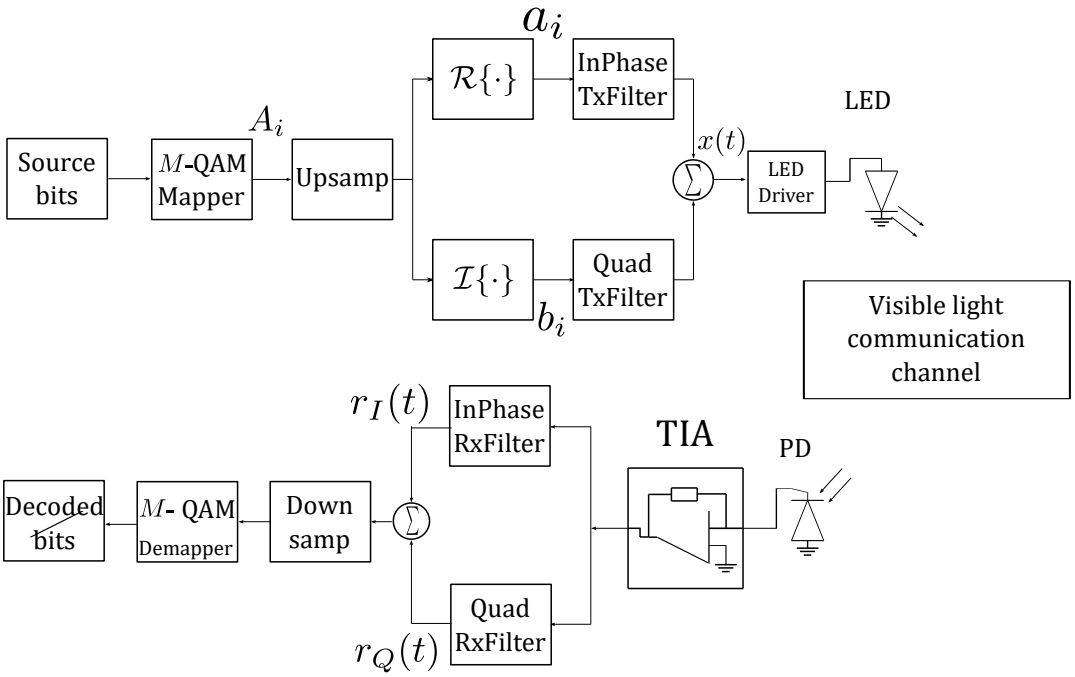

Figure 2.7: Schematic block diagram of the CAP modulation scheme.

2.4.1 Fundamentals of CAP Implementation

The block diagram of a CAP transceiver is depicted in Fig. 2.7. The stream of incoming bits are grouped in blocks of b bits and mapped into one of $M = 2^b$ different complex symbols by the M-QAM mapper. Each complex symbol from the mapper output can be represented as $A_i = a_i + jb_i$ where a_i and b_i are the real and imaginary part of the i^{th} symbol, respectively. The outputs of the mapper are upsampled sufficiently to match the overall system sampling frequency, f_s. The in-phase (a_i) and quadrature (b_i) components are then fed, respectively, into the in-phase ($p(t)$) and quadrature ($\tilde{p}(t)$) digital pulse-shaping filters. The $p(t)$ and $\tilde{p}(t)$ are realized as the product of a root raised cosine filter (RRC) with a cosine and a sine function, respectively. The filters are orthogonal to each other and form a Hilbert pair having the same amplitude response but differing in phase by 90° [113]. The output of the filters are then summed with a suitable DC bias to make it non-negative. The resulting signal is used to modulate the intensity of the LED for onward transmission through the optical channel. The radiated optical signal, $s(t)$, can be represented as:

$$s(t) = \mathcal{K}(\beta x(t) + x_{\text{dc}}) \tag{2.24}$$

where $\mathcal{K}$ is the electrical-to-optical conversion coefficient, β is the optical modulation intensity, x_{dc} is the DC bias and $x(t)$ is the transmitted electrical CAP signal which can be written as:

$$x(t) = \sum_{i=-\infty}^{\infty} [a_i p(t - iT) - b_i \tilde{p}(t - iT)]. \tag{2.25}$$

The pulse-shaping filters are given by:

$$p(t) = g(t)\cos(\omega_c t) \tag{2.26}$$

and

$$\tilde{p}(t) = g(t)\sin(\omega_c t) \tag{2.27}$$

where $g(t)$ is the RRC, $\omega_c = 2\pi f_c$ is the center frequency of the CAP signal and T is the symbol duration. At the receiver, the transmitted signal $x(t)$ is recovered from the incoming optical radiation by a photodetector (PD) and converted to a voltage signal using a transimpedance amplifier (TIA). The DC component of the recovered electrical signal is suppressed with a high pass filter (HPF). This is then passed to the matched filters that consist of the conjugated, time reversed versions of the transmit pulse-shaping filters. The output of the matched filters are then passed through the M-QAM demapper for the receiver estimates of the transmitted symbols.

The received electrical signal, with the DC component suppressed, can be represented as:

$$y(t) = \mathfrak{R}\mathcal{K}\beta h(t) \otimes x(t) + w(t) \tag{2.28}$$

where $\mathfrak{R}$ is the responsivity of the PD and $h(t)$ is the channel attenuation. The $w(t)$ represents the ambient and thermal noise, modelled as AWGN with mean of zero and double-sided spectral density of $N_0/2$ [61].

2.4.2 Design of Digital Pulse-shaping Filters for CAP

The pulse-shaping filter for CAP is often designed in the digital domain. This way, the problem of electronic component drift and tolerance are eliminated, the spectrum characteristics are reproducible without variation and importantly, the digital designs can easily be translated to hardware implementation [114]. Furthermore, the filters are designed as FIR, which are desirable for phase-sensitive applications like data communication.

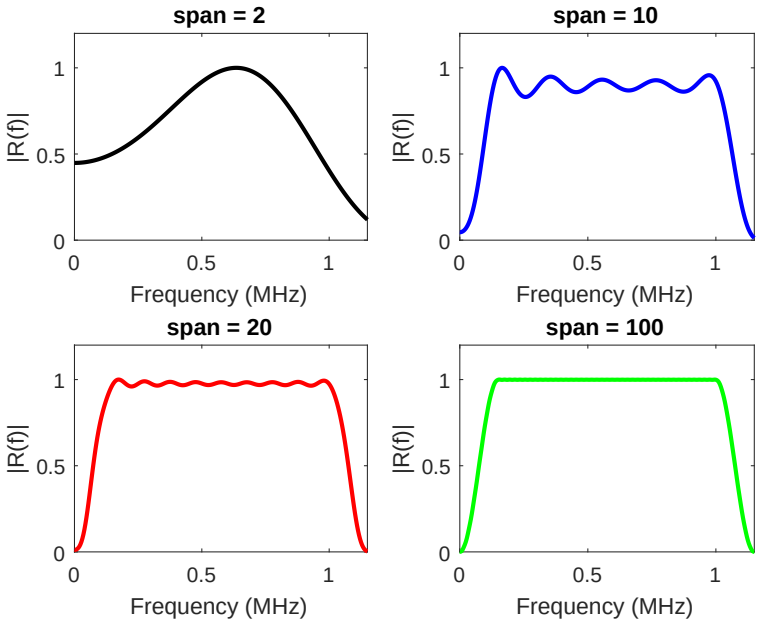

Figure 2.8: Magnitude response of the combined in-phase transmit and receive CAP filters for varying values of the filter span, $R_s = 1$ MHz, excess bandwidth, $\alpha = 0.15$ and samples/symbol, $L = 4$.

However, careful selection of the RRC filter parameters is essential to the performance of CAP signal. The main parameters to be designed are the excess bandwidth occupied by the filter pulse (the roll-off factor, α), the length of the filter symbol span and the sampling rate, f_s [24, 113]. A high value of α results in more bandwidth usage but leads to better performance [115]. The choice of α in the literature generally varies between 0.1 and unity, but the value of $\alpha = 0.15$ is widely used for CAP modulation in optical communication [24, 113]. An ideal transmit filter requires an infinite symbol span to give zero ISI at the sampling instant when combined with the matched filter at the receiver. However, for practical systems, the span is finite and the filter is truncated. Therefore, the span of the filter is chosen based on the trade-off between computational complexity and performance. The frequency response of the combined transmit and receive in-phase CAP filters is shown in Fig. 2.8, using samples per symbol $L = 4$ and $\alpha = 0.15$, to highlight the effect of the filter span. It can be observed from the figure that the magnitude response of the combined transmit and receive CAP filters, $|R(f)|$, becomes flat over its spectrum with an increase in the filter span. A span of 10 has been shown to give satisfactory performance for the filter design [24]. The sinusoids frequency, f_c, is chosen as

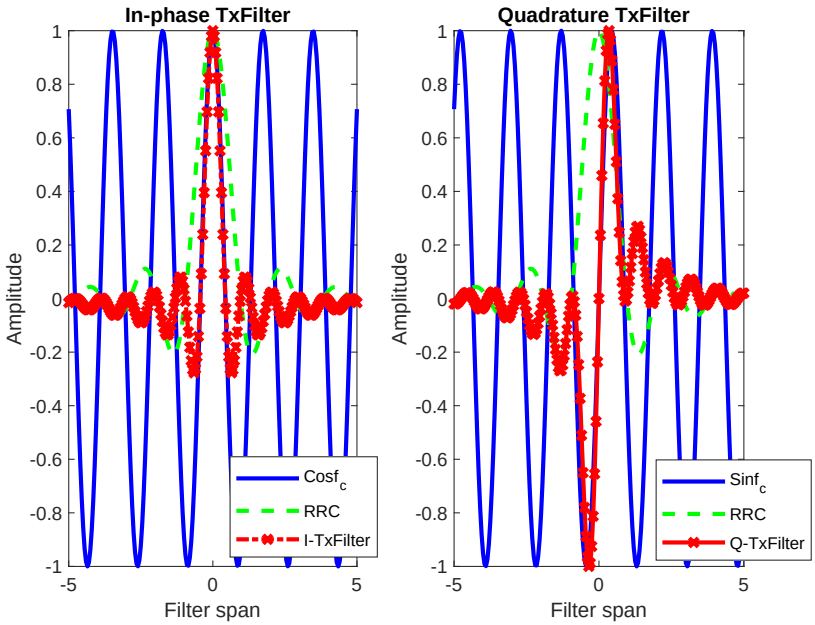

Figure 2.9: The impulse response of the I and Q transmit filters for CAP with a span of 10*,* $\alpha = 0.15$*,* $L = 20$*,* $f_s = 20$ *MSa/s.*

the center frequency of the transmitted spectrum and is given as:

$$f_{\mathrm{c}} = \frac{1+\alpha}{2T}. \tag{2.29}$$

From (2.29), the upper and lower boundary of the transmitted spectrum can be written as:

$$f_{\mathrm{u}} = f_{\mathrm{c}} + \frac{(1+\alpha)R_{\mathrm{s}}}{2} \tag{2.30}$$

and

$$f_{\mathrm{l}} = f_{\mathrm{c}} - \frac{(1+\alpha)R_{\mathrm{s}}}{2} \tag{2.31}$$

respectively where R_s is the symbol rate. In line with the Nyquist sampling requirement, the sampling rate, f_{s}, has to be chosen as:

$$f_{\mathrm{s}} \geq 2f_{\mathrm{u}}. \tag{2.32}$$

It can be deduced from (2.32) that the sampling rate is a function of α. As α increases from 0 to 1, f_s goes from a minimum of $2R_s$ to $4R_s$. The in-phase and quadrature transmit filters together with their corresponding sinusoids and RRC are presented in Fig. 2.9 for illustration purposes.

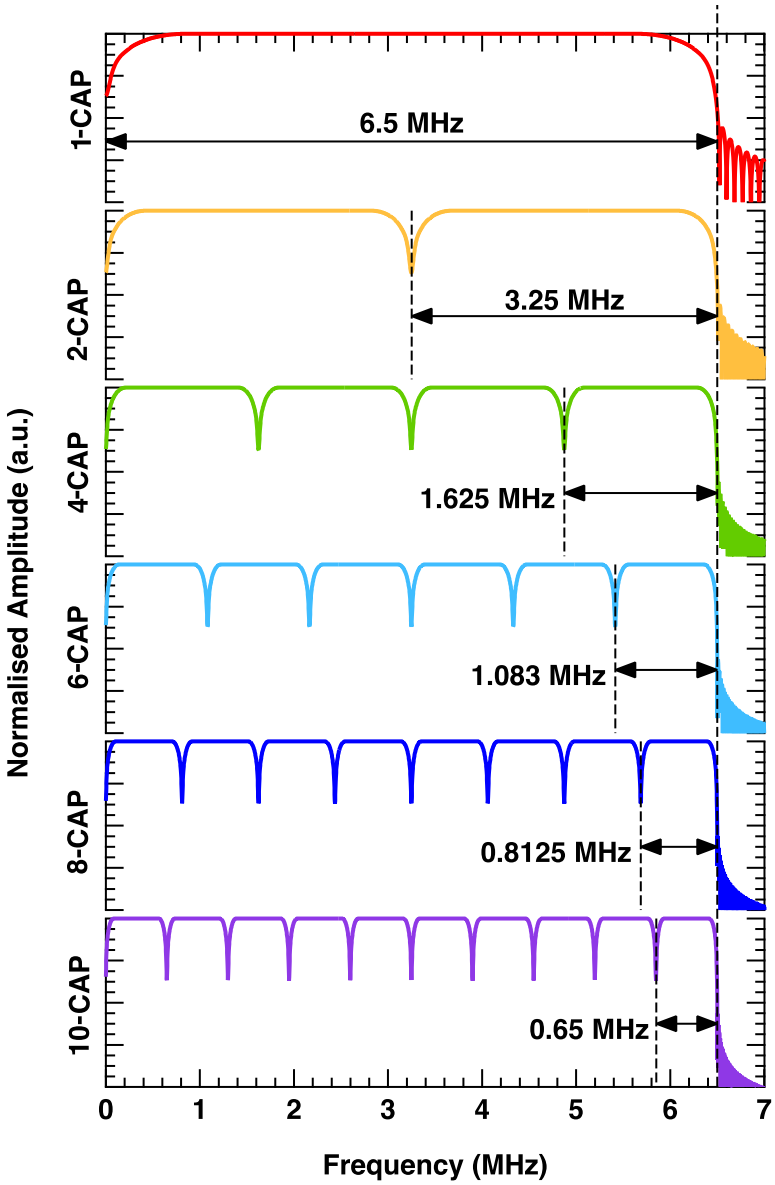

Figure 2.10: Frequency responses of the subbands for different configurations of m-CAP [116].

2.4.3 Multiband CAP (m-CAP)

The CAP modulation technique can be implemented as a multiband scheme by placing CAP signals on multiple subbands to realize m-CAP [24, 25, 116–118]. The main advantage of m-CAP is its improved tolerance to channel impairments compared to the single band CAP [24]. By dividing the single wideband CAP into multiple narrow subbands, an approximation of a flat frequency response can be realized in each subband for m-CAP when transmitted over a frequency selective channel. Furthermore, it circumvents the problem of generating wideband

filters and leads to improved bit error rate (BER) performance [24]. The center frequency of the n^{th} subband can be expressed as:

$$f_{\text{c},n} = (2n-1)f_{\text{c}} \qquad n = 1, 2, \cdots, N \tag{2.33}$$

where the $\{f_{c,n}\}$ are chosen to prevent overlap between the subbands and are harmonics of the fundamental subband f_c. This observation is very important as it explains the increasing PAPR of m-CAP that is discussed in Section 2.5.3. The frequency responses of the subbands for different configurations of m-CAP are shown in Fig. 2.10 [116]. Other benefits of m-CAP include the possibility of achieving the Nyquist sampling rate as shown in [24].

2.4.4 Comparison of CAP with other Modulation Schemes

The simplicity of the physical implementation of CAP is derived from its use of digital FIR filters to realize orthogonal channels, which eliminate the need for explicit modulation and demodulation blocks. This is unlike its passband QAM counterpart that requires a local oscillator (LO) to generate the sine and cosine functions needed for its modulation and demodulation blocks. In addition, the LO signal at the QAM coherent receiver must be aligned with that of the transmitter, both in phase and frequency, using a phase-locked loop (PLL) to ensure a successful carrier recovery. Failure to do this results in lack of synchronization in the QAM transceiver and leads to BER performance degradation. However, as shown in Fig. 2.7, the modulation/demodulation blocks have been integrated into the pulse-shaping/match filtering blocks in the CAP transceiver. This removes the necessity of having to modulate the CAP baseband signal onto quadrature carriers, hence eliminating the need for carrier recovery, LO and PLL at the receiver. In addition, since the symbol rate and carrier frequency are usually of the same order, the CAP filters can be realised with a reasonably small number of taps [119]. Hence, the main advantage of CAP over QAM is its simpler implementation [23, 60].

The PAPR of CAP has been compared to that of PAM and DMT in the literature [13, 30, 115, 120]. It is shown that the PAPR of CAP is lower when compared with that of DMT but higher in comparison to PAM. This results in advantage when LED non-linearity and the effect of signal clipping are taken into consideration, especially at high modulation orders. Furthermore, the BER performance of CAP has also been compared to that of DMT and PAM [121–124]. Apart

Table 2.1: Summary of the results of CAP performances in optical experimental demonstrations.

Year	Data rate	Transmitter	Equalization	BER	Distance	Ref
2015	8 Gb/s	RGBY LED with WDM	Pre and Post	$< 3.8 \times 10^{-3}$	1 m	[19]
2015	4.5 Gb/s	RGB LED with WDM	Pre and Post	$< 3.8 \times 10^{-3}$	1.5 m	[126]
2015	4.5 Gb/s	RGB LED with WDM	Pre and Post	$< 3.8 \times 10^{-3}$	1.1 m	[127]
2014	1.35 Gb/s	RGB LED with WDM	Pre and Post	$< 3.8 \times 10^{-3}$	0.3 m	[128]
2013	3.22 Gb/s	RGB LED with WDM	Pre and Post	$< 1 \times 10^{-3}$	0.25 m	[129]
2013	1.32 Gb/s	Blue LED	Pre and Post	$< 1 \times 10^{-3}$	0.25 m	[129]
2013	5 Gb/s	LD	DFE	$< 1 \times 10^{-3}$	50 m	[109]
2013	2.1 Gb/s	DVD LD	DFE	$< 1 \times 10^{-3}$	100 m	[130]
2012	1.1 Gb/s	White LED	Pre and Post	$< 1 \times 10^{-3}$	0.23 m	[131]
2012	2.1 Gb/s	LED	DFE	$< 1 \times 10^{-3}$	50 m	[124]

from the implementation simplicity and lower PAPR, CAP also has better BER and data rate performance in comparison to DMT in the same physical link [122, 123]. Employing only the blue chip of an RGB-LED at a BER of 10^{-3}, CAP demonstrates a superior data rate of 1.32 Gb/s in comparison to 1.08 Gb/s for DMT [123]. With all the three chips employed, CAP demonstrates a superior data rate of 3.22 Gb/s in comparison to 2.93 Gb/s for DMT [123]. Also, DMT has been found to exhibit a substantially worse performance than CAP in a VLC link employing a white phosphorescent LED and an SI-POF link using a red DVD laser [30, 122]. Some of the main reasons for the DMT performance are its low tolerance to the non-linearity of LED and signal clipping [122]. However, at very high data rates, CAP requires complex equalization techniques that increase its complexity in comparison to DMT, which requires a simple single-tap equalizer [125].

The summary of the performance of CAP in various experimental demonstrations, as reported in optical communication literature, is presented in Table 2.1.

2.5 CAP Implementation Challenges

The challenges that are encountered in the implementation of CAP modulation technique are discussed in this section. The focus is directed at four major aspects of the modulation technique. These are: (*i*) sensitivity to timing jitter, (*ii*) effect of limited modulation bandwidth of the LED, (*iii*) power requirement and (*iv*) computational complexity.

2.5.1 CAP Sensitivity to Timing Jitter

Timing jitter, one of the challenges of CAP modulation, has been identified as a major impediment to achieving high data rates in optical systems [132–135]. It can be defined as the deviation of the receiver clock from the ideal sampling instant. The reasons for the jitter sensitivity exhibited by the CAP modulation technique can be found in the analysis of its receiver architecture [23, 136]. The matched filter output at the receiver has two components corresponding to the in-phase (in-phase Rx filter) and the quadrature (quadrature Rx filter) arms. In the absence of noise and link attenuation, referring to Fig. 2.7, the in-phase arm of the matched filter output can be expressed as follows [23]:

$$r_I(t) = x(t) \otimes q(t) \tag{2.34}$$

where

$$q(t) = p(T - t). \tag{2.35}$$

Then, it follows that:

$$r_I(t) = \sum_{i=-\infty}^{\infty} a_i r_{II}(t - iT) + \sum_{i=-\infty}^{\infty} b_i r_{IQ}(t - iT) \tag{2.36}$$

where the desired and the interference parts are respectively given as:

$$r_{II}(t) = p(t) \otimes p(T - t) \text{ and } r_{IQ}(t) = \tilde{p}(t) \otimes p(T - t). \tag{2.37}$$

From (2.37), the desired part can be further expanded as:

$$r_{II}(t) = \int_{-\infty}^{\infty} g(\tau)\cos(\omega_c\tau)\cdot g(\lambda+\tau)\cos(\omega_c(\lambda+\tau))\,d\tau \tag{2.38}$$

$$= 0.5\cos(\omega_c\lambda)\int_{-\infty}^{\infty} g(\tau)g(\lambda+\tau)\,d\tau + 0.5\int_{-\infty}^{\infty} g(\tau)g(\lambda+\tau)\cos(\omega_c(\lambda+2\tau))\,d\tau \tag{2.39}$$

$$\therefore r_{II}(t) \cong \cos(\omega_c(T-t))r_{ii}(t) \tag{2.40}$$

where $\lambda = T - t$ and

$$r_{ii}(t) = 0.5[g(t) \otimes g(T-t)]. \tag{2.41}$$

The second term in (2.39) can be neglected as it is analogous to filtering a high frequency signal modulated on a sinusoid of frequency ($2\omega_c$) with a LPF ($g(t)$). Following the same procedure,

$$r_{IQ}(t) \cong \sin(w_c(T-t))r_{ii}(t). \tag{2.42}$$

The in-phase arm of the matched filter output ($r_I(t)$), the desired ($r_{II}(t)$) and the interference ($r_{IQ}(t)$) parts are depicted in Fig. 2.11(a)–(c) respectively for a single transmitted symbol. It can be observed that the desired part, though has its peak at the sampling time $n = 0$, has a very narrow lobe. Also, the interference part contributes no distortion at the sampling instant, but has significant values between sampling instances. This combination increases the sensitivity of CAP signal to timing jitter error and channel impairments as any deviation from the ideal sampling instant leads to taking samples containing significant distortions. Hence, a synchronization technique is a key requirement in the CAP transceiver. A detailed comparison of the CAP and QAM architectures showing that QAM suffers less distortion from the effects of sampling jitter in comparison to CAP has been presented in [23].

2.5.2 CAP Performance under Limited LED Modulation Bandwidth

The frequency response of the PC-LED employed in VLC systems is non-flat over its spectrum. Also, the phosphor coating that is used to convert the emitted light spectrum from blue to white further limits the available modulation bandwidth. The combination of these factors leads to ISI in VLC receivers for high data rate transmission. Additionally, the CAP modulation technique is very sensitive to ISI and requires complex equalizers to achieve good performance

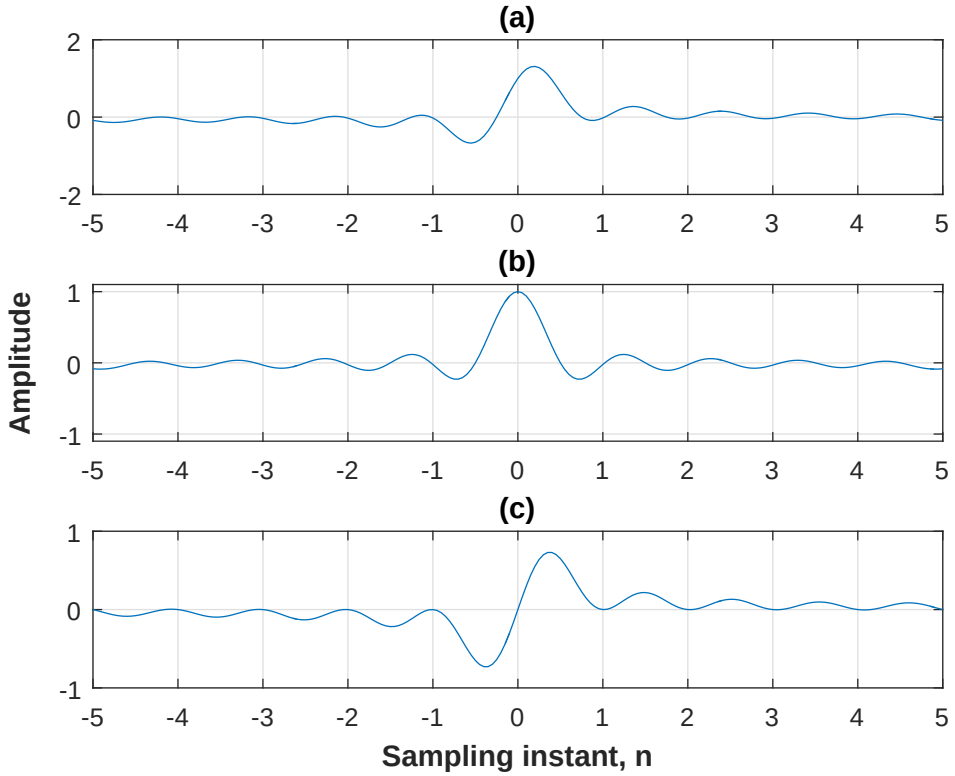

Figure 2.11: (a) In-phase arm of the matched filter output of CAP. (b) The desired part; (c) The interference part.

in channels with non-flat spectrum [24, 137]. The reason for the high sensitivity of CAP modulation to ISI might be linked to its receiver structure as shown in Fig. 2.11, which shows that the distortion in a CAP symbol is due to contributions from both its desired and the interference parts. This is in contrast to its QAM counterpart which has a negligible interference part for all t [23]. Therefore, the use of CAP modulation in high throughput LED-based VLC systems requires complex processing techniques to eliminate the effects of the resulting ISI in the received symbols. However, as previously mentioned, m-CAP can be conveniently used to mitigate this non-flat response. Techniques such as bit/power loading can be integrated with m-CAP to further improve performance.

2.5.3 m-CAP Power Requirement

The PAPR of an m-CAP system merits an important consideration, given its multi-band nature. One of the advantages of single band CAP is its low PAPR. However, for an m-CAP

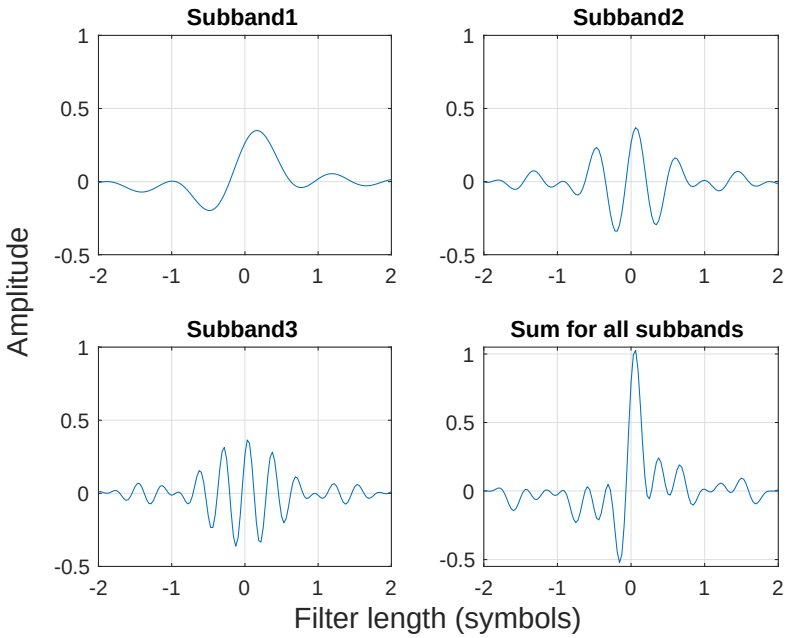

Figure 2.12: The quadrature transmit filters of an m-CAP scheme and their additions for $m = 3$.

modulation scheme, the probability of high peak occurrence increases with increase in the number of subbands. The center frequencies of the m-CAP subbands are harmonics of $f_{c,1}$, as such, the subband signals will periodically add up in amplitude during the modulation process. To illustrate this, Fig. 2.12 shows the transmit filters of an m-CAP scheme with three subbands ($m = 3$). It can be observed that the addition of the transmit filters produces a larger amplitude at the sampling instant in comparison to the individual transmit filters. This will increase the likelihood of the occurrence of high PAPR as a result of the coherent addition of the signals in the individual subbands. In order to investigate the m-CAP PAPR, we define the PAPR per each transmitted symbol as:

$$PAPR \triangleq \frac{\max\limits_{0 \leq i \leq L-1} |x_i|^2}{E[|x_i|^2]} \tag{2.43}$$

where x_i is the i^{th} transmitted m-CAP sample while $E[\cdot]$ denotes the statistical expectation. Figure 2.13 shows the complimentary cumulative distribution function (CCDF) of the m-CAP PAPR. The CCDF is defined as the probability that the PAPR exceeds a certain reference value PAPR_0 [29]. As can be inferred from the figure, the probability that the PAPR will exceed 10 dB is 1.2×10^{-3} for $m = 4$ and this increases to 6×10^{-2} and 3×10^{-1} for $m = 16$ and

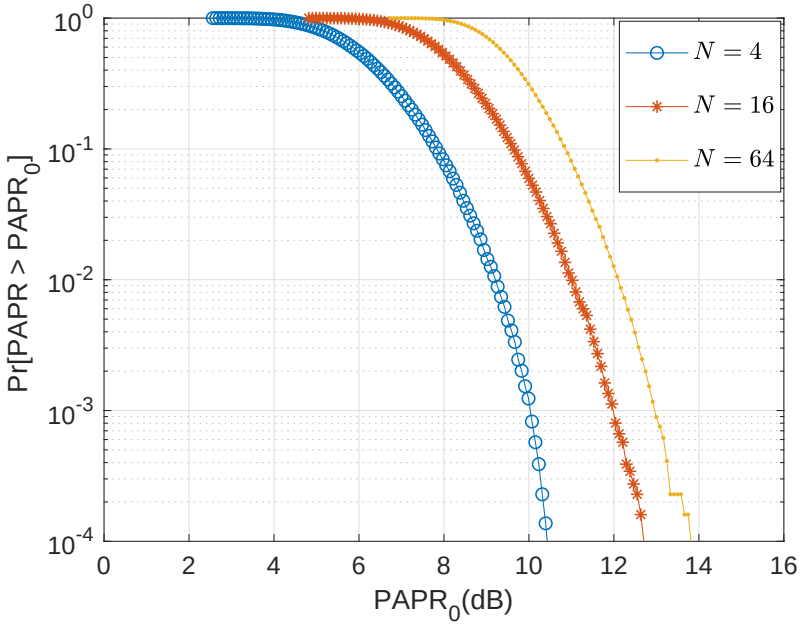

Figure 2.13: The CCDF of PAPR of m-CAP for different number of subbands using CAP-64.

64, respectively. This means that out of every 1000 symbols, only 15 are likely to have their PAPR exceeding 10 dB for $m = 4$ as compared to 40 and 700 for $m = 16$ and 64, respectively. Expectedly, the PAPR of the m-CAP increases with increasing number of subbands. Thus, the PAPR of m-CAP will be an important factor to monitor given the power and dynamic range constraints in VLC systems.

2.5.4 m-CAP Computational Complexity

The CAP modulation scheme uses 4 FIR filters in its transceiver (FIR filter 'quads'), a pair each for pulse-shaping at the transmitter and matched filtering at the receiver [138, 139]. So there is a need to consider the number of computations involved in a CAP transceiver, especially considering the growing popularity of m-CAP. For a CAP system using a filter of length G, the number of real multiplications require for its implementation per each transmitted symbol can be calculated from (2.25), (2.26), (2.27) and Fig. 2.7 as follows:

- The evaluation of either (2.26) and (2.27) requires G real multiplications since it involves element-wise multiplication.
- The pulse-shaping convolution operation of either of the terms on the right hand side of

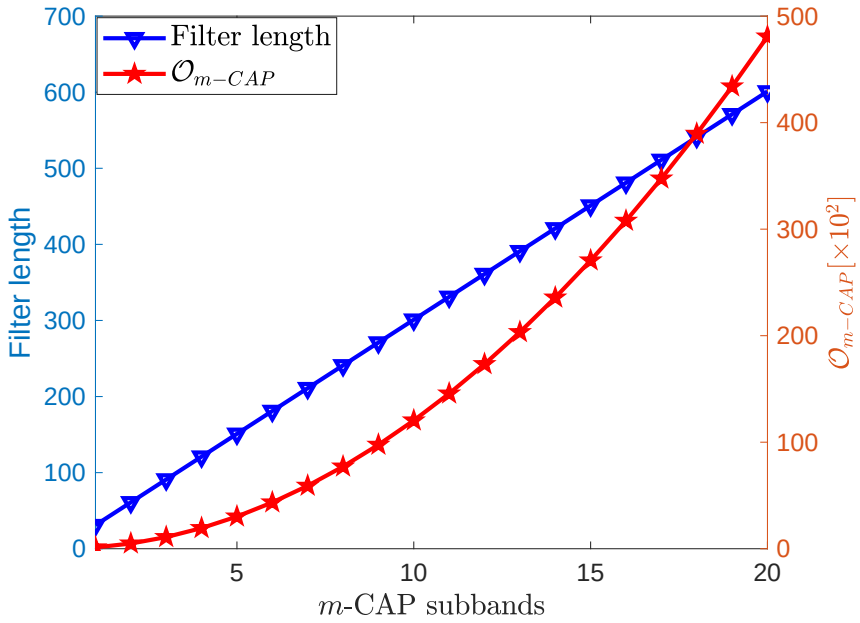

Figure 2.14: Complexity dynamics of an m-CAP system showing the filter length and the required number of computations as a function of the number of subbands, N.

(2.25) involves another G real multiplications.

- While the matched filtering convolution operation at the receiver in either of the in-phase or quadrature Rx filter of Fig. 2.7 also involves G real multiplications.

However, the complexity contribution of (2.26) or (2.27) is only incurred once and can be done as part of the pre-processing. Hence, the total real multiplications required for the implementation of CAP transceiver is $2(2G)$ per symbol and this can be generalized for an m-CAP system as:

$$\mathcal{O}_{m\text{-CAP}} = 4GN. \tag{2.44}$$

The filter length G is given as:

$$G = G_{\text{s}}L + 1 \tag{2.45}$$

where G_{s} is the filter span and $L > 2N(1+\alpha)$ [24]. For the typical values of $G_s = 10$, $\alpha = 0.15$ ($L = 3N$) as proposed in [24], then

$$G = 30N + 1. \tag{2.46}$$

Substituting (2.46) for G in (2.44), the required computational cost per symbol in an m-CAP system can be expressed in terms of m as:

$$\mathcal{O}_{m\text{-CAP}} = 120N^2 + 4N. \tag{2.47}$$

Therefore, for a fixed value of G_s and α, (2.46) and (2.47) respectively provide insight into the complexity dynamics of an m-CAP system with regards to the filter length and the required number of computations as more subbands are added. The complexity dynamics is presented in Fig. 2.14 using (2.46) and (2.47). While (2.46) shows that the filter length of m-CAP increases as a linear function of N, (2.47) shows that the $\mathcal{O}_{m\text{-CAP}}$ increases as a quadratic function of N. This means that $\mathcal{O}_{m\text{-CAP}}$ will quickly ramp up as more subbands are added. It follows from (2.47) that as N increases from 2 to 4 and 16, the $\mathcal{O}_{m\text{-CAP}}$ increases in order of magnitude from 3 to 4 and 5, respectively. A compromise is thus needed between increasing the subbands to improve performance and the resulting system complexity.

2.6 Summary of Chapter 2

A detailed review of the state of the art in VLC and OFC has been conducted in this chapter. The review covers the varieties of optical sources and receivers that are employed along with their characteristics. It also include the channel modelling, link impairments as well as the signal processing techniques that are deployed to improve performance. Furthermore, different modulation techniques are also discussed with a focus on CAP modulation technique. The chapter is concluded by identifying the challenges that are experienced in a CAP-based optical communication system.

The performance enhancing techniques that are developed for CAP scheme, including their theoretical analyses, simulation results and experimental demonstrations, will now be discussed in the rest of the thesis.

Chapter 3

Synchronization and Equalization for CAP Implementation Challenges

Novel techniques that are developed to mitigate the highlighted challenges of CAP modulation are discussed in this chapter along with their analytical, simulation and experimental performances. The main design consideration in developing the mitigation techniques is to ensure that the implementation simplicity of the CAP modulation scheme is maintained.

3.1 Description of the CAP Mitigation Techniques

Two novel techniques are developed to mitigate the timing jitter and improve the limited bandwidth effect encountered by CAP modulation scheme in optical communication systems.

3.1.1 Mitigating Timing Jitter with the 'CAP Filter' Synchronization Technique

There are two broad categories of solutions for addressing the timing jitter challenge in CAP modulation. One way is to modify the filter structure of CAP while the other maintains the structure and creates a separate synchronization block. The modified receiver structures from the first set are less-sensitive to timing jitter but results in higher complexity. Examples of this are the sets of two-dimensional (2D) CAP pulses and a set of frequency domain (FD) 3D CAP pulses that are proposed in [22]. The proposed 2D pulses result in improved tolerance to timing jitter but the corresponding BER is worse in the absence of timing jitter. In addition, the FD 3D pulses are more sensitive to timing jitter than the existing CAP pulses. Furthermore, the timing sensitivity solution demonstrated in [140] considered a modified QAM receiver. The receiver, though has low timing sensitivity, results in the loss of the simple linear CAP receiver.

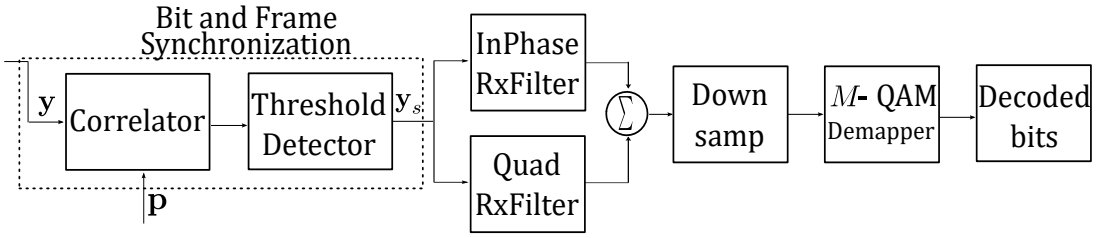

Figure 3.1: Schematic block diagram of a simplified CAP receiver showing the location of the synchronizer and its components.

A novel solution, termed the 'CAP filter' synchronization technique, that retains the simplicity of CAP by not modifying its generic receiver is developed in this thesis [136]. The technique uses a synchronization sequence that is derived from the CAP filter with some inherent benefits. The 'CAP filter' synchronization technique maintains the mean value of the transmitted signal and enjoys the benefits of the Nyquist sampling rate of CAP together with the interference elimination of the RRC filter [136]. The maintenance of the average value of the transmitted signal is very important in OWC due to eye safety regulations. A schematic block diagram of the CAP receiver showing both the location of the synchronizer and its components is presented in Fig. 3.1.

3.1.1.1 The Proposed Synchronization Technique

Let a vector of length W be represented by bold face symbol, $\mathbf{x}$ and $x(w)$ be its w^{th} element for $w = 1, \cdots, W$. The proposed synchronization sequence, $\mathbf{g}$, for CAP synchronization is obtained by taking the samples of the pulse shaping RRC filter whose expression is given by [141]:

$$g(t) = \begin{cases} 1-\alpha+4\dfrac{\alpha}{\pi}, & t=0 \\ \dfrac{\alpha}{\sqrt{2}}[(1+\dfrac{2}{\pi})\cos\dfrac{4}{\pi}+(1-\dfrac{2}{\pi})\sin\dfrac{4}{\pi}], & t=\pm\frac{T}{4\alpha} \\ \dfrac{\sin(\pi(1-\alpha)\frac{t}{T})+4\alpha\frac{t}{T}\cos(\pi(1+\alpha)\frac{t}{T})}{\pi\frac{t}{T}(1-(4\alpha\frac{t}{T})^2)}, & \text{elsewhere} \end{cases} \tag{3.1}$$

and $\mathbf{g}$ is the sequence obtained from $g(\frac{i}{f_s})$, for $i = 1, \cdots, L$ where L is the number of samples per symbol and f_s is the sampling rate. The proposed synchronization pattern for CAP symbols, $\mathbf{p}$, is then derived as a P-array of Barker sequence [142]. For example, when

$P = 3$;

$$\mathbf{p} = \chi \begin{bmatrix} \mathbf{g} & \mathbf{g} & -\mathbf{g} \end{bmatrix} \tag{3.2}$$

where χ is a design parameter defined as:

$$\chi = \frac{\max\limits_{0 \le m < M} \{|c(m)|\}}{\max\limits_{0 \le l \le L-1} \{|g(l)|\}} \tag{3.3}$$

and $c(m)$ is from the M-QAM constellation:

$$c(m) = \frac{-(M-1) + 2m}{\sqrt{(M^2-1)/3}} \tag{3.4}$$

Therefore, the length of $\mathbf{p}$ becomes PL. A typical single frame can be defined as $\mathbf{f} = [\mathbf{p}, \mathbf{s}]$ where $\mathbf{s}$ contains the sequence of transmitted data with length S and $\mathbf{f}$ has length $K = PL + S$. The received sequence can be written as:

$$\mathbf{y} = \mathbf{f} + \mathbf{w} \tag{3.5}$$

where the elements of $\mathbf{w}$ are statistically independent and identically distributed (i.i.d.) AWGN samples. The sliding correlator output at the receiver is:

$$v(k) = \sum_{i=0}^{PL-1} p(i) \cdot y(i + k - (PL-1)) \tag{3.6}$$

$$= \sum_{i=0}^{PL-1} p(i) \cdot f(i + k - (PL-1)) + \sum_{i=0}^{PL-1} p(i) \cdot w(i + k - (PL-1)) \tag{3.7}$$

$$= v_f(k) + v_w(k), \qquad k = 0, 1, \cdots, K-1 \tag{3.8}$$

The correlator output, $\mathbf{v}$, has its maximum value at index $k = k_p$ which means that $\max\limits_{0 \le k \le K-1} \{v(k)\} = v(k_p)$. Hence, the maximum value $v(k_p)$ occurs at the index k_p. It is worthy of mention that since the system parameters are usually known at the receiver, $\mathbf{p}$ can easily be generated. Therefore, the objective now is to locate the peak of the correlator output and obtain a clock signal which is in alignment with it.

3.1.1.2 Performance Analysis of the Proposed Synchronization Technique

A good correlation sequence should have high autocorrelation value only at the zero lag point and small autocorrelation values at the non-zero lag points. Therefore, an intrinsic measure

of performance can be defined based on the peak-to-sidelobe distance of the correlator output. Consequently, it is desired that $v_f(k_p) > \max_{\forall k<k_p}\{v_f(k)\}$ and a threshold γ can be set which satisfy the following condition:

$$v_f(k_p) > \gamma > \max_{\forall k<k_p}\{v_f(k)\} \tag{3.9}$$

The expression in (3.9) seeks to determine an optimum threshold value that is set between the peak and its nearest value. Also, the correlator output sequence in (3.8), $\mathbf{v}$, is a Gaussian random variable since $\mathbf{v}_w$ is an additive Gaussian noise vector with variance of $K\sigma^2_{v_w}$ where $\sigma^2_{v_w} = \|\mathbf{p}\|^2 \cdot \sigma^2$ and $\|\cdot\|$ is the Euclidean norm.

Probability of missed detection (PMD) is defined as the probability that the synchronization sequence is not flagged as detected at the expected instant, and this definition is adopted in this study for the performance evaluation of the proposed technique [143]. To derive the PMD for the proposed scheme, in the presence of AWGN, recall that the expected detection instant is $k_p = PL - 1$. From (3.8),

$$v(k_p) = v_f(k_p) + v_w(k_p) \tag{3.10}$$

where $v(k_p) \sim \mathcal{N}(v_f(k_p), \sigma^2_{v_w})$. The PDF of $v(k_p)$ can then be expressed as:

$$f(v(k_p) \mid v_f(k_p), \sigma^2_{v_w}) = \frac{1}{\sqrt{2\sigma^2_{v_w}\pi}}\, e^{-\frac{(v(k_p)-v_f(k_p))^2}{2\sigma^2_{v_w}}} \tag{3.11}$$

The threshold detector in Fig. 3.1 flags synchronization whenever the correlator output sequence exceeds the threshold level, γ. Since elements of $\mathbf{v}$ are i.i.d. and it is desired that (3.9) is satisfied, the optimum threshold γ is therefore:

$$\gamma = (v_f(k_p) - \max_{\forall k<k_p}\{v_f(k)\})/2. \tag{3.12}$$

The PMD is then obtained by evaluating (3.11) for the region below γ. Therefore,

$$\text{PMD} = \frac{1}{\sqrt{2\sigma^2_{v_w}\pi}} \int_{-\infty}^{\gamma} e^{-\frac{(v(k_p)-v_f(k_p))^2}{2\sigma^2_{v_w}}}\, dv(k_p). \tag{3.13}$$

Using a change of variable, (3.13) can be evaluated as:

$$\text{PMD} = \frac{1}{\sqrt{2\pi}} \int_{-\infty}^{\frac{\gamma - v_f(k_p)}{\sigma_{v_w}}} e^{-\frac{(x)^2}{2}} dx \tag{3.14}$$

$$= \frac{1}{\sqrt{2\pi}} \int_{-\infty}^{\frac{-(v_f(k_p)-\gamma)}{\sigma_{v_w}}} e^{-\frac{(x)^2}{2}} dx \tag{3.15}$$

$$= \frac{1}{\sqrt{2\pi}} \int_{\frac{(v_f(k_p)-\gamma)}{\sigma_{v_w}}}^{\infty} e^{-\frac{(x)^2}{2}} dx \tag{3.16}$$

$$= Q\left(\frac{D}{\|\mathbf{p}\| \cdot \sigma}\right), \tag{3.17}$$

where the peak-to-sidelobe mid-point, D, is expressed as:

$$D = (v_f(k_p) + \max_{\forall k < k_p} \{v_f(k)\})/2 \tag{3.18}$$

It can be observed from (3.17) that the performance of the correlator receiver improves as the system SNR increases because this reduces the effect of the noise contribution, σ and increases the detection distance, D.

3.1.2 Mitigating the Effect of Limited Bandwidth and Timing Jitter with a Fractionally-Spaced Equalizer (FSE)

The majority of the work reported in CAP modulation literature are based on the use of equalization techniques for improving the achievable data rate in LED-based VLC systems [19, 144, 145]. The reported works have concentrated on using symbol-spaced equalizer (SSE) which samples the equalizer inputs at symbol rate and thus have symbol-spaced taps. The SSE is susceptible to the effect of timing jitter which causes spectrum nulls that result in noise enhancement and potential performance degradation [146]. In contrast, fractionally-spaced equalizers (FSE) circumvent the potential noise enhancement and the resulting performance degradation in SSE by sampling its input at a higher rate of $T^{'} = T/Q$ for $Q > 1$ [146]. Hence, considering the high sensitivity of CAP to timing jitter, SSE is not the best equalization technique to adopt. Therefore, a comparative performance evaluation of FSE and SSE in joint mitigation of the effects of timing jitter and limited bandwidth on CAP in LED-based VLC system is investigated [147].

It is shown that FSE implementation not only results in a higher achievable data rate and spectral efficiency, but also reduces the complexity of the overall system by eliminating the need for a separate synchronization block, such as the one considered in section 3.1.1.

Furthermore, as a proof of concept, an experimental LED-based VLC demonstration is performed to show the advantage of FSE over SSE.

The main difference between FSE and SSE is that the input sampling rate of SSE is the same as the symbol rate while that of FSE is at least the Nyquist rate. This results in the summation of aliased components in SSE. In the event of cancellation of aliased components with similar phase delay, this could lead to occurrence of null in the frequency spectrum of the SSE inputs. Consequently, SSE results in a high gain to compensate for this null which could result in noise enhancement and subsequent degradation in performance [148]. However, FSE avoids this potential pitfall by using no less than the Nyquist sampling frequency to avoid aliasing [146]. Thus, FSE is able to compensate directly for channel distortion before aliasing and mitigate the effect of any phase error in the equalizer input. As such, it is well suited to address the severe ISI and timing jitter sensitivity of the CAP modulation technique in VLC systems.

3.1.2.1 Fractionally Spaced Equalizer (FSE)

An optimum receiver for a signal corrupted by AWGN is a filter matched to that signal and whose output are sampled periodically at the symbol rate. If the channel introduces ISI then an equalizer is required to remove the ISI effect from the samples of the matched filter output. An SSE is designed by taking the samples of the matched filter output at the symbol rate while FSE samples its inputs faster than the symbol rate. The usual choice for FSE in the literature is twice the sampling rate resulting in $T/2$-spaced equalizer taps. The equalizer's output is then taken at the symbol rate which makes the FSE a decimating filter [146, 149–151].

The frequency response of an SSE equalizer can be expressed as [146]:

$$W_T(f) = \sum_{k=0}^{K-1} w_k e^{-j2\pi fkT} \tag{3.19}$$

where $\{w_k\}$ are the weights of the equalizer and K is the number of equalizer taps. The equalized spectrum can then be expressed as [146]:

$$H_T(f) = W_T(f) \sum_i Y\left(f - \frac{i}{T}\right) e^{j2\pi(f-i/T)\tau} \tag{3.20}$$

where $Y(f)$ is the spectrum of the received corrupted signal and τ is a timing delay. The transmitter and receiver clock frequencies should be perfectly synchronized ideally but there

is usually some offset τ in practice due to mismatch in the transceiver clock rate. It can be observed that the summation term in (3.20) is a folded spectrum consisting of the sum of the aliased components and that the presence of a phase factor can result in potential noise enhancement due to spectral nulls.

However, FSE circumvents this potential noise enhancement in SSE by sampling its input at a higher rate of $T^{'} = T/Q$. Hence, (3.19) and (3.20) can be expressed for FSE as:

$$W_{T'}(f) = \sum_{k=0}^{K-1} w_k e^{-j2\pi f k T^{'}} \tag{3.21}$$

and

$$H_{T'} = W_{T'}(f) \sum_{i} Y\left(f - \frac{i}{T'}\right) e^{j2\pi(f - i/T^{'})\tau} \tag{3.22}$$

respectively. If Q is chosen appropriately to prevent aliasing in the folded spectrum, then (3.22) becomes [148]:

$$H_{T'}(f) = W_{T'}(f) Y(f) e^{j2\pi(f)\tau}, \quad |f| \leq \frac{1}{2T'} \tag{3.23}$$

and the spectrum of FSE output can be expressed as:

$$H_{T'}(f) = \sum_{i} W_{T'}\left(f - \frac{i}{T}\right) Y\left(f - \frac{i}{T}\right) e^{j2\pi(f - i/T)\tau} \tag{3.24}$$

since the output is sampled at the symbol rate (because the decisions on the received data are made at T-interval) and $\{w_k\}$ are adjusted only once for every Q inputs (Q/T rate adjustment does not result in faster convergence [146]).

The main difference in the performance of SSE and FSE can be seen by comparing their outputs given by (3.20) and (3.24), respectively. It is seen that while (3.20) is the equalization of sum of aliased components, (3.24) is the aliased sum of equalized components. Therefore, the FSE is able to compensate directly for the received signal spectrum and any resulting timing jitter before aliasing due to symbol rate sampling at the equalizer output. This characteristic enables the FSE to avoid potential noise enhancement due to occurrence of null in the received spectrum and thus the possibility of performance degradation resulting from timing jitter error. Another intuitive explanation is that since the SSE takes one sample for every symbol, the sampling requirement is very strict such that the sampling clock needs to be adjusted to ensure the samples are taken at the peak, the "top dead center" [149], of the received pulses. FSE

relaxes this strict sampling requirement by taken at least two samples for each received symbol. Hence, the FSE is more suitable to mitigate the timing jitter sensitivity of CAP and the severe ISI introduced by the bandlimited VLC system.

The two equalizers under test have been implemented as an adaptive FIR filter using the LMS algorithm for training and adaptation of the equalizer taps. Equalizers generally require a training phase during which the equalizer tap coefficients are adaptively computed to mimic the channel through which the corrupted signal has traversed. In this work, the LMS algorithm is used due to its simplicity of implementation and lower computational complexity [148, 152]. During the training phase, known transmitted symbols are compared to the equalizer outputs to generate an error signal which is used to adaptively update the equalizer weights.

The error signal at the i^{th} iteration is given as [152]:

$$e_i = d_i - \boldsymbol{W}_i^T \boldsymbol{Y}_i \tag{3.25}$$

where d is the desired symbol, $\boldsymbol{Y}$ is a vector that represents the input samples to the equalizer and $\boldsymbol{W}^T$ is the transpose of the equalizer weight vector given as [152]:

$$\boldsymbol{W}_{i+1} = \boldsymbol{W}_i + \mu e_i \boldsymbol{Y}_i \tag{3.26}$$

where μ is the step size used to adjust the equalizer convergence. The training phase lasts until the weights converge and the equalizer settles into steady state. The optimum weights, obtained after the equalizer convergence, are then used to equalize the received symbols in a decision-directed mode. In this mode, the decisions made on the equalizer outputs are used to guide the weights update as opposed to the known pattern that was used during the training phase. A simplified CAP transceiver showing the location of the equalizer component, as considered in this work, is presented in Fig. 3.2.

3.2 Results and Discussions on the Performance of CAP Mitigation Techniques

In this section, the performances of the developed mitigation techniques are evaluated through simulations and validated using experimental demonstrations. The techniques are also compared with the state of the art in CAP literature to highlight the performance improvement.

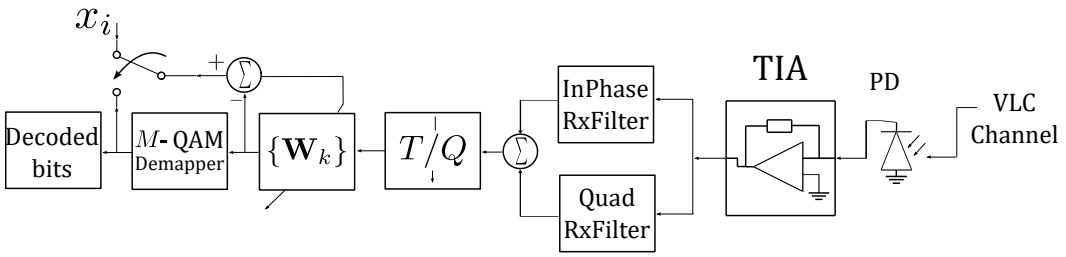

Figure 3.2: Schematic block diagram of a simplified CAP transceiver showing the location of the equalizer component.

3.2.1 Results and Discussions on the Performance of 'CAP Filter' Synchronization Technique

Simulations are carried out to investigate the impact of timing jitter on the CAP performance and the effectiveness of the proposed technique in mitigating this impact in VLC system. The simulations are performed for different scenarios involving varying constellation sizes and timing jitter. The performance criteria employed are BER, the derived PMD, constellation diagram and error vector magnitude (EVM). The parameters for CAP modulation are set as $L = 4$, $\alpha = 0.15$ and $f_c = 1.15$ MHz.

In the experimental demonstration, CAP signal with an header consisting of the proposed 'CAP-filter' algorithm is transmitted from a laptop to an Agilent E4428C signal generator and the signal from the generator is used to drive an OSRAM OSTAR LED. The intensity emitted from the LED is then passed through an optical lens to concentrate most of the power on the VLC receiver placed 1 m away and consisting of a silicon PD (S6967) with a trans-impedance amplifier. The received signal, acquired by an oscilloscope (MS07104B), is then captured for offline processing. The back-to-back (B2B) transmission is achieved by connecting the signal generator directly to the oscilloscope without passing the signal through the LED. The 'greedy' synchronization algorithm is obtained by using a long random bipolar sequence (span of 160 symbols) as the header of the transmitted signal and the performance is compared to that of the proposed, shorter sequence 'CAP-filter' algorithm which spans a mere 11 symbols. The 'greedy' algorithm is implemented with a long sequence in order to ensure perfect synchronization.

Figure 3.3 shows the BER performance of CAP for a range of timing jitter at SNR of 20 dB.

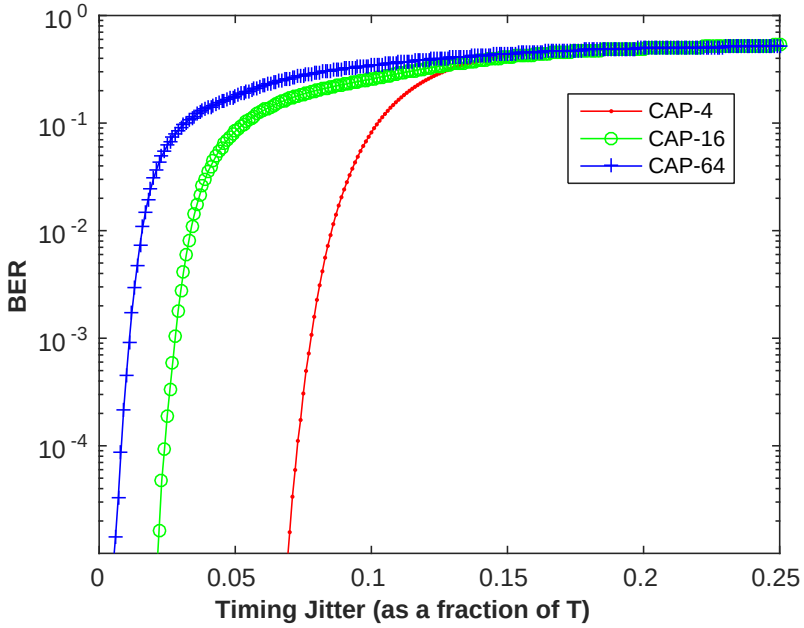

Figure 3.3: BER performance of CAP for a range of timing jitter, SNR $= 20$ *dB.*

The result confirms the fact that higher constellation order incurs more SNR penalty from the sampling time error, which results in more degradation as the jitter increases. It is also shown that, for the 20 dB SNR under consideration and a timing jitter of $0.15T$, all the constellation orders have BER of 0.5 indicating a total failure of the communication link. Therefore, an effective synchronization algorithm will be required to achieve a reliable communication especially in high-speed data applications which rely on high order modulation schemes.

The PMD derived in (3.17) is used to investigate the effect of varying the length of the synchronization sequence on the performance of the proposed 'CAP-filter' synchronization scheme and the result is presented in Fig. 3.4. The synchronization sequence to noise ratio is defined as $\text{SNR}_{\text{ss}} = \|\mathbf{p}\|^2 / PL\sigma^2$. It can be inferred from the figure that the probability of synchronization error greatly improves with an increase in SNR_{ss} and the sequence length. This is due to the fact that an increase in SNR_{ss} reduces the effect of noise variance, while increasing the sequence length leads to increase in detection distance. For instance, at an SNR_{ss} of 20 dB, the probability of missed detection is 10^{-4} for $P = 3$, which greatly improves to 10^{-9} for $P = 7$. Thus, increasing sequence length reduces the probability of loss of synchronization but results in increasing number of computations.

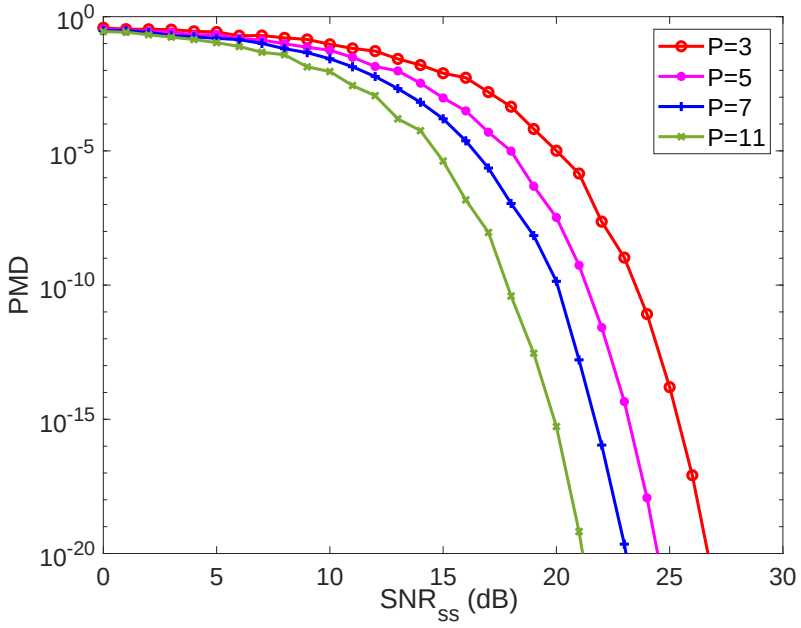

Figure 3.4: Probability of missed detection for the 'CAP filter' synchronization technique for different sequence length.

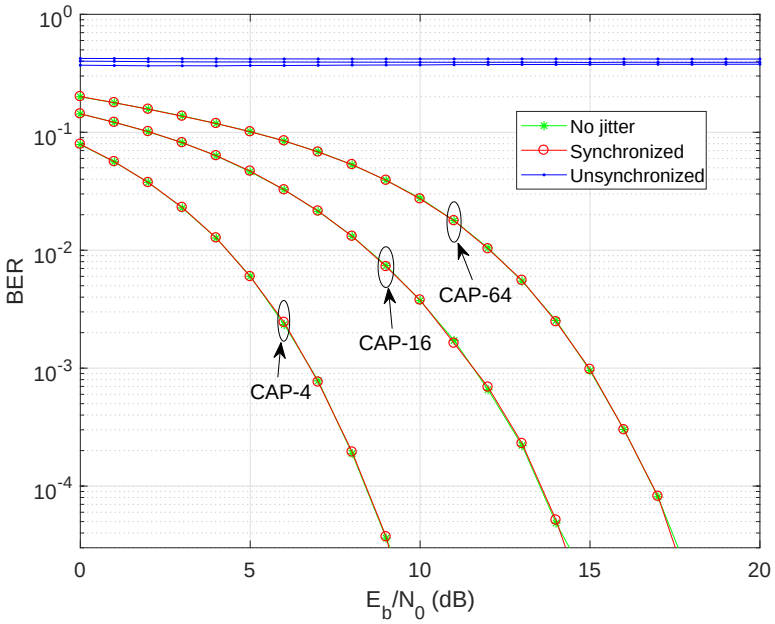

Figure 3.5: Comparison of BER performance of CAP with no jitter, with and without synchronization for different constellation sizes in VLC system, $\tau = 0.25T$ and $P = 11$.

In order to further quantify the performance of the proposed 'CAP-filter' technique, the BER of the synchronized CAP in VLC system is simulated. In the set-up, the white LED is represented

as a first-order LPF [116]. Figure 3.5 shows the BER of CAP with no jitter (ideal), along with the BER performance before and after synchronization in VLC system for a timing jitter of $0.25T$. The simulation of CAP with no jitter refers to the performance of CAP with the assumption of perfect synchronization. Without synchronization, a BER of 0.5 is obtained for both low and high constellation order at the 25% jitter considered. This performance leads to failure of the communication link and shows the severity of the timing jitter effect on the BER performance of CAP. However, with the proposed 'CAP-filter' technique, synchronization is achieved with the BER matching perfectly with that of the CAP with no jitter. This means that the 'CAP-filter' algorithm is able to adequately remove the effect of the timing jitter. The result also shows the effectiveness of the proposed 'CAP-filter' technique in low SNR region, which is a very significant result.

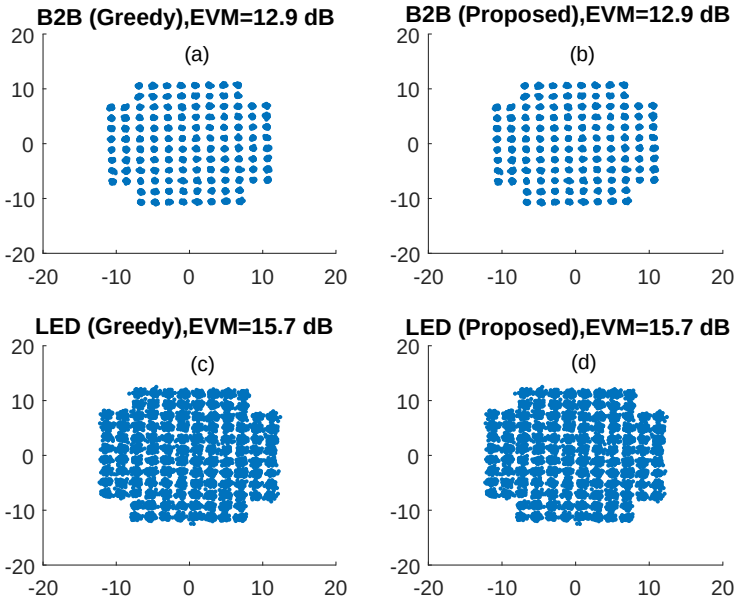

Figure 3.6: Constellation diagrams and EVM of the experimental demonstration in VLC for both the 'greedy' and the 'CAP-filter' synchronization algorithm.

Finally, the viability of the proposed 'CAP-filter' algorithm in VLC system is demonstrated through a laboratory experiment and the result is depicted for high order CAP-128 in Fig. 3.6. Figures 3.6 (a) and (b) show the received constellation for both the 'greedy' and the proposed 'CAP-filter' synchronization algorithm respectively in a back-to-back transmission. As expected, both synchronization algorithms have the same EVM of 12.9 dB. This shows

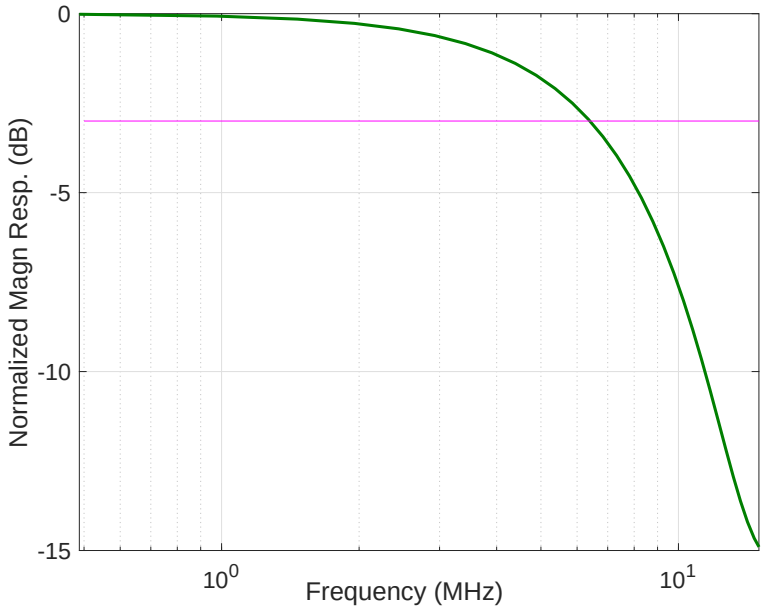

Figure 3.7: The normalized frequency response of the overall measured VLC channel with a line through the -3 dB point.

that the proposed 'CAP-filter' algorithm achieves the same performance as the 'greedy' synchronization algorithm. Furthermore, the received constellation after transmission through a 1 m LED link is shown for the 'greedy' and the proposed 'CAP-filter' algorithms in Fig. 3.6 (c) and (d), respectively. It is seen that the proposed 'CAP-filter' algorithm achieves the same EVM performance of 15.7 dB as the 'greedy' synchronization algorithm in LED transmission as well. This shows that the proposed algorithm is able to completely remove the effect of timing jitter. Therefore, the experimental results confirmed the viability of the proposed 'CAP-filter' synchronization technique in VLC systems.

3.2.2 Results and Discussions on the Performance of FSE

The performance of both FSE and SSE for CAP modulation in VLC system is investigated through extensive simulations. An experimental VLC channel with a non-flat frequency response whose -3 dB frequency cut-off is approximately 6.5 MHz as shown in Fig. 3.7 is used for the simulations. The two equalizer types are evaluated with regards to their performance for different data rate, SNR and varying constellation sizes. The sampling rate of the system is fixed as $f_s = 2$ GHz. The tap-spacing for FSE is set to $T/2$ to conform with the literature [146].

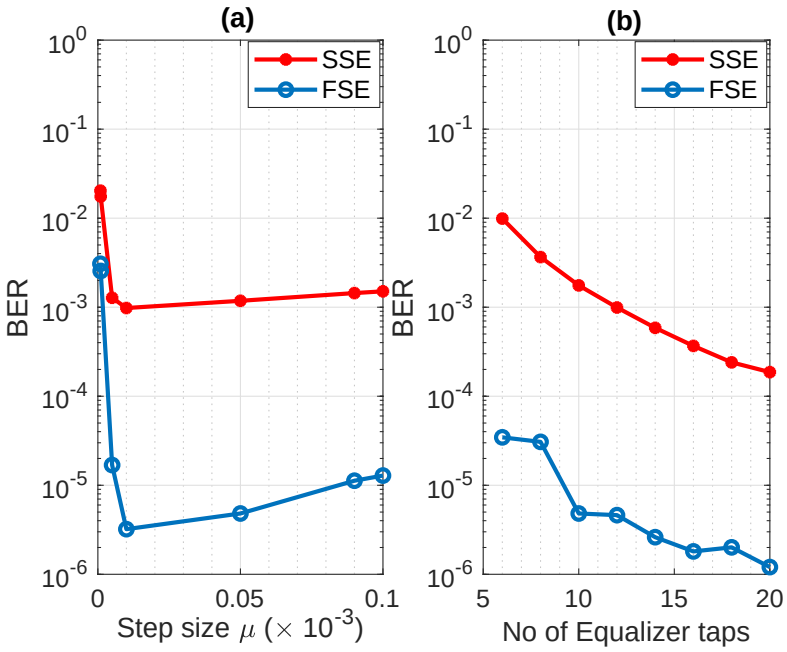

Figure 3.8: Sensitivity of the performance of the equalizers to varying step sizes and number of taps, SNR $= 15$ *dB and* $R_b = 30$ *Mb/s.*

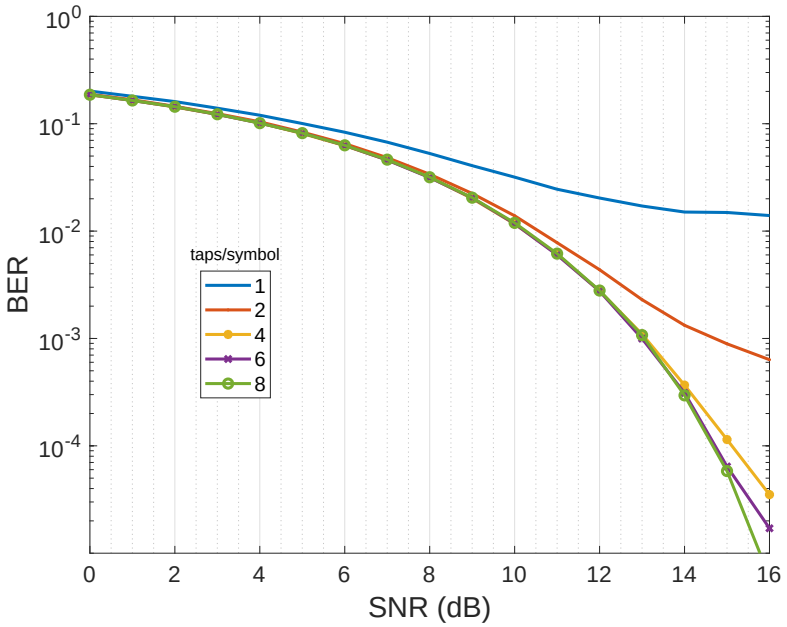

Figure 3.9: Performance of FSE with increasing number of taps/symbol for a high data rate of 700 *Mb/s, equalizer length of* 100 *and link bandwidth of* 16 *MHz.*

In all cases, the received electrical SNR is used in the simulations.

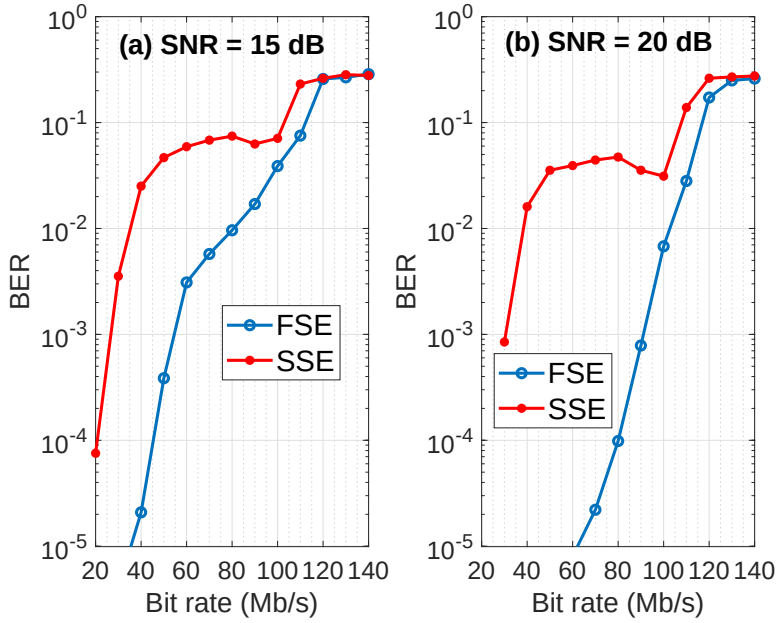

Figure 3.10: BER performance of CAP-16 for different data rates at SNR of 15 dB and 20 dB.

After a preliminary sensitivity study presented in Fig. 3.8 (a), an optimum step size of 1×10^{-5} is chosen. Similarly, Fig. 3.8 (b) shows that the performance of both equalizers increases with increasing number of taps. Therefore, both equalizers have been implemented using 12 taps to maintain the same computational cost. Figure 3.9 shows the performance of FSE for varying number of taps/symbol at a high data rate of 700 Mb/s and link bandwidth of 16 MHz. It is shown that the performance gain of FSE reduces with increasing number of taps/symbol while the computational complexity increases. Hence, the choice of two taps/symbol (i.e $T/2$ tap-spacing) represents a compromise between complexity and performance.

Figures 3.10 and 3.11 show the performance comparison of the $T/2$ FSE and the SSE in a LED-based VLC system. At an SNR of 15 dB and below the forward error correction (FEC) BER limit of 3×10^{-3}, Fig. 3.10 (a) shows that FSE is able to achieve a bit rate of 65 Mb/s while SSE only achieves 30 Mb/s resulting in a spectral efficiency (η) gain of 5.4 bits/s/Hz using CAP-16. For the same constellation size and FEC BER limit, the η gain for FSE in comparison to SSE increases to 9.2 bits/s/Hz at an SNR of 20 dB as depicted in Fig. 3.10 (b).

Furthermore, for a higher constellation size of CAP-64 and at an SNR of 20 dB, Fig. 3.11 shows that FSE achieves a bit rate of 95 Mb/s compared to 30 Mb/s achieved by SSE. This results

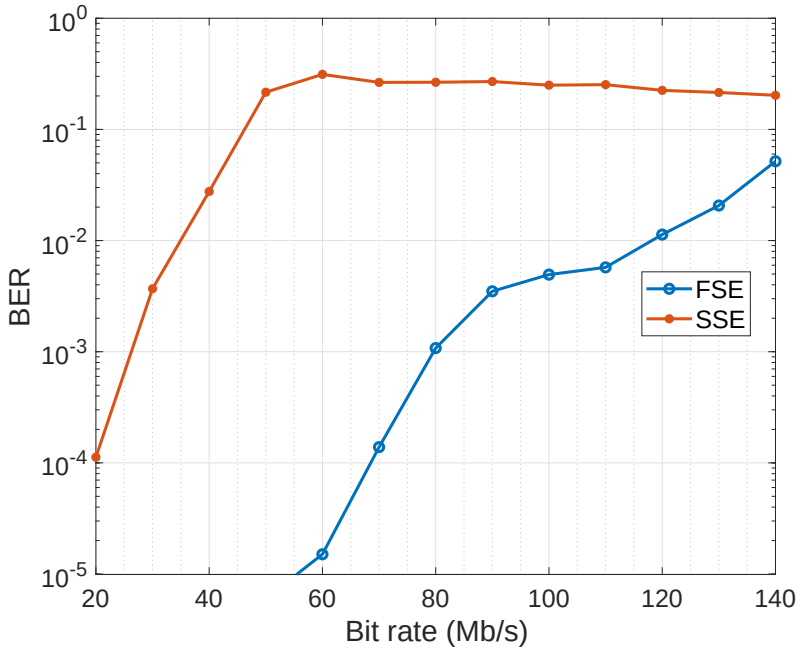

Figure 3.11: BER performance of CAP-64 for different data rates at SNR of 20 dB.

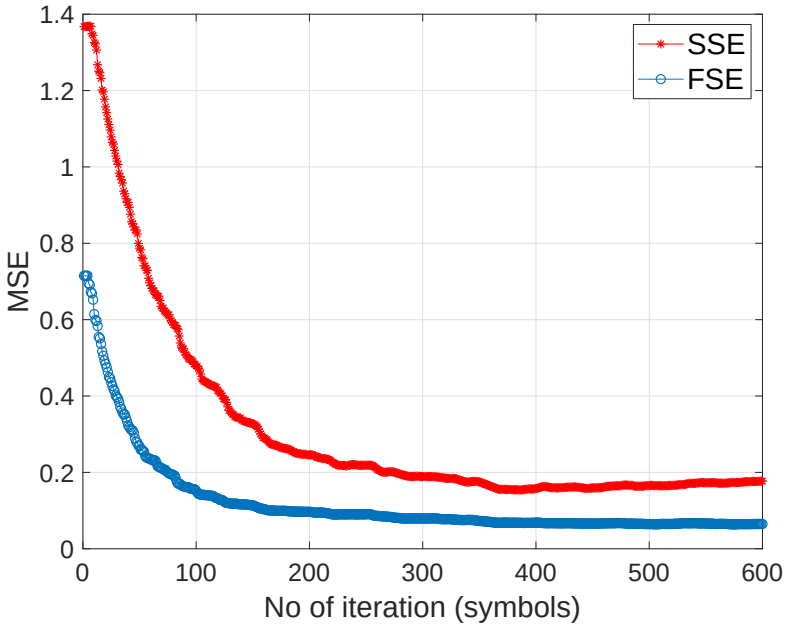

Figure 3.12: MSE convergence rate of FSE and SSE for CAP-16 at $R_b = 30$ Mb/s and SNR=20 dB.

in a η gain of 10 bits/s/Hz from using FSE. It can therefore be concluded that for the same transmission bandwidth, FSE achieves better data rate and spectral efficiency in comparison to

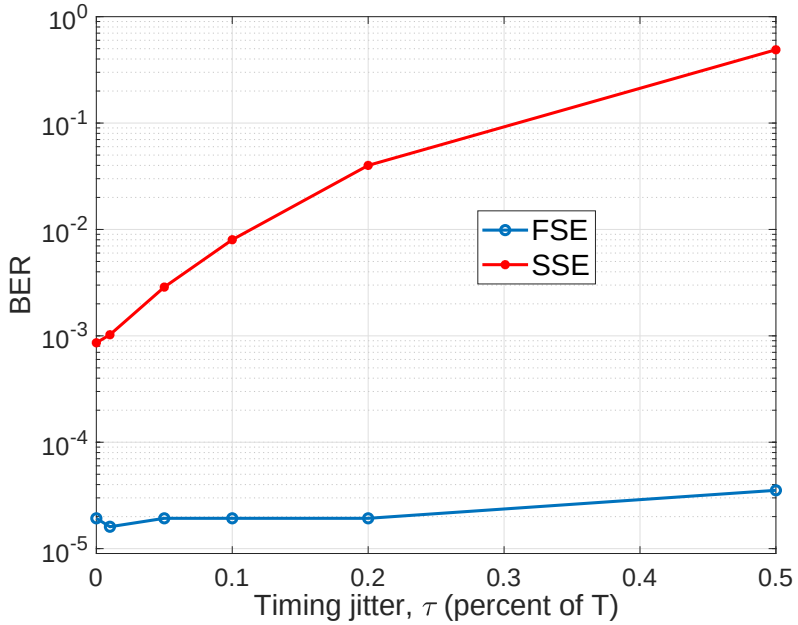

Figure 3.13: Comparison of timing jitter mitigation by FSE and SSE using CAP-16 at R_b = 10 Mb/s and SNR = 10 dB.

SSE and that the performance advantage increases with increase in SNR and constellation size.

The mean square error (MSE) convergence rate for the two equalizers is shown in Fig. 3.12 at an SNR of 20 dB and $R_b = 30$ Mb/s. The FSE offers faster convergence rate and a lower MSE. Faster MSE convergence also implies that a shorter training sequence is required in FSE implementation. It is shown in the figure that the required training sequence for FSE is about 200 symbols while that of SSE is twice that at about 400 symbols.

A further advantage of FSE over SSE for LED-based VLC systems employing CAP modulation is shown in Fig. 3.13. This figure depicts the performance comparison of FSE and SSE for varying timing jitter using CAP-16. It is shown that FSE performance remains stable while that of SSE suffers severe degradation with increasing timing jitter. These characteristics of FSE to maintain its good performance in the presence of timing jitter is especially desired for CAP modulation. Hence, it can be argued that FSE implementation is more appropriate to address the timing jitter sensitivity of CAP, as it does not require an extra synchronization block.

An important observation is that both the FSE and SSE have been implemented with the same

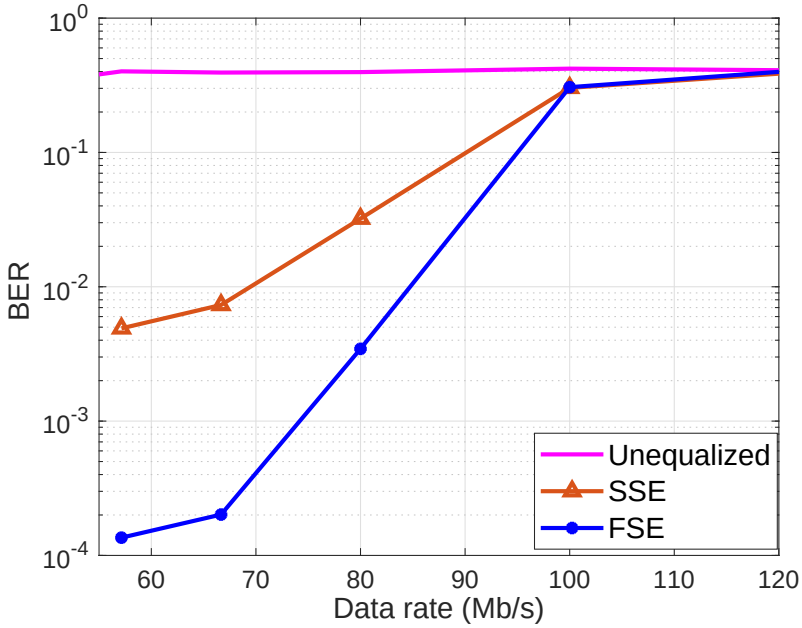

Figure 3.14: Experimental demonstration of the BER performance comparison of FSE and SSE using CAP-16 with an OSRAM OSTAR LED that has a -3 dB bandwidth of 6.5 MHz.

number of taps (to maintain the same number of computations for both equalizers) and yet, FSE has better performance. Thus, FSE implementation maintains the simplicity of CAP transceiver in LED-based VLC systems, leading to higher achievable spectral efficiency and reduction in both cost and complexity. In addition, since the other techniques such as QAM do not suffer from the effect of timing jitter as much as CAP, the performance gain of FSE will be lower in such techniques.

Finally, as a proof of concept, an experimental LED-based VLC demonstration is carried out to validate the performance advantage of a $T/2$ FSE over SSE for CAP modulation. The transmission distance is 1 m using an OSRAM OSTAR LED with a -3 dB cut-off bandwidth of 6.5 MHz as shown in Fig. 3.7 and employing a silicon PD (s6967) receiver. The experimental result is presented in Fig. 3.14 using CAP-16. For the data rates of over 55 Mb/s considered, there is a breakdown of the communication link when no equalization is implemented as depicted in the figure. More importantly, at the FEC BER limit, SSE is only able to achieve a data rate of 55 Mb/s in contrast to 80 Mb/s achieved by FSE. This further validates the conclusion that an FSE is preferred to SSE for CAP-based optical communication systems.

3.3 Summary of Chapter 3

Two novel techniques that address the effects of timing jitter and limited LED bandwidth, encountered by CAP-based optical communication systems, have been presented along with evaluation of their performances. It is shown that the 'CAP filter' synchronization technique is able to correct for the effect of timing jitter suffered by the CAP modulation scheme. For the 25% timing jitter considered in the simulation, the 'CAP filter' synchronization technique is shown to completely correct for the effect of the timing jitter. To reduce complexity, it is shown that both the timing jitter and the limited LED bandwidth effects can be addressed with the use of FSE thereby eliminating the need for a separate synchronization block. At the FEC BER limit of 3×10^{-3}, it is experimentally demonstrated that the FSE achieves a 45% data rate improvement when compared to the SSE. Furthermore, it is shown that the performance of FSE remain constant while that of SSE suffers degradation as the timing jitter increases. Additional techniques that improve on the spectral and energy efficiency of the CAP modulation scheme are developed and presented in subsequent chapters of the thesis.

Chapter 4

Spatial-Multiplexing with CAP (SM_{ux}-CAP) in VLC Systems

Due to the implementation challenges of CAP, the main focus in the literature is the designing of various equalization techniques to improve its throughput in VLC applications [21, 126–128, 145]. However, these equalization techniques significantly increase the complexity of the resulting system. Therefore, a novel approach is proposed in this chapter that exploits the spatial domain to improve the spectral efficiency and BER performance of CAP, while maintaining its low-complexity transceiver.

Multiple LEDs are often deployed to achieve sufficient illumination in VLC, due to the limited luminous flux of the individual LED. The availability of these multiple LEDs have been exploited in the literature to achieve improved throughput using MIMO techniques [153]. Therefore, this chapter exploits the use of spatial domain to realise diversity and multiplexing gain for CAP modulation scheme in VLC applications. Spatial multiplexed CAP (SM_{ux}-CAP), which simultaneously transmit streams of independent CAP signals through multiple LEDs, is developed to realise significant improvement in the data rate of conventional CAP. Repetitive coded CAP (RC-CAP), with parallel transmission of the same CAP signal over multiple LEDs, is also proposed to improve the BER performance of CAP through spatial diversity. The proposed techniques are novel implementations of CAP in MIMO systems and demonstrate its potential as a suitable modulation technique for VLC applications.

The BER performance analysis of the proposed schemes are derived based on the optimum maximum likelihood (ML) detector. However, the complexity of ML detection scheme increases exponentially with increase in the number of transmitter, N_{t} and symbol modulation

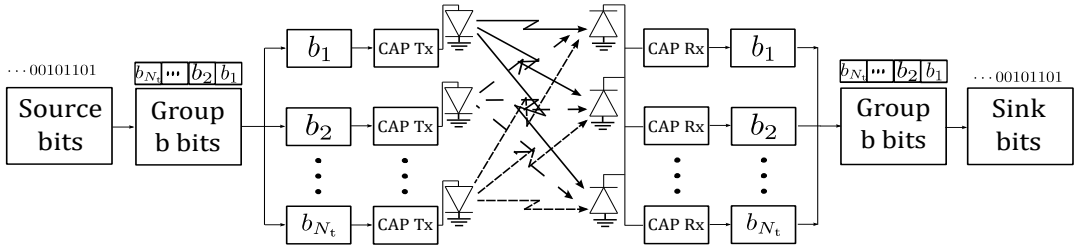

Figure 4.1: The schematic block diagram of the MIMO CAP transceiver.

order, M. This makes ML detector infeasible for practical implementation. Hence, four practical, low-complexity detectors are further investigated for SM$_{ux}$-CAP and their performances compared with that of the optimum ML detector.

Zero-forcing (ZF) and minimum mean squared error (MMSE) linear detectors are implemented and their performances are improved by combining them with optimally-ordered successive interference cancellation (OSIC). The resulting detectors, ZF-OSIC and MMSE-OSIC, have significant improvement in BER performance with significant reduction in computational complexity.

4.1 Model Description

The major difference between SM$_{ux}$-CAP and RC-CAP is that while independent data symbols are transmitted in SM$_{ux}$-CAP, the data symbols in RC-CAP are identical. Hence, SM$_{ux}$-CAP improves the data rate of the conventional CAP while RC-CAP offers spatial diversity gain.

4.1.1 Description of SM$_{ux}$-CAP Model

For an SM$_{ux}$-CAP, at each transmitting instant, the incoming information bits are grouped into blocks of b bits as shown in Fig. 4.1 where $b = N_{\mathrm{t}}\log_2 M$ and M represents the constellation size of an M-QAM scheme. The block of b bits is then divided into parallel streams, each of $\log_2 M$ bits, that are simultaneously passed into CAP modulators. The outputs are then sent over the VLC channel. In this way, N_{t} streams of independent CAP signals, each conveying $\log_2 M$ bits, are simultaneously transmitted resulting in total transmission of $N_{\mathrm{t}}\log_2 M$ bits per symbol duration. Thus, SM$_{ux}$-CAP improves the bandwidth efficiency of the conventional CAP by a factor of N_{t}, provided $N_{\mathrm{r}} \geq N_{\mathrm{t}}$ where N_{r} is the number of receivers.

4.1.2 Description of RC-CAP Model

Repetitive coding (RC) is a MIMO technique in which the same symbol is simultaneously transmitted over multiple LEDs. This results in full transmit diversity of N_{t} in optical MIMO systems employing IM/DD approach [154]. For RC-CAP, identical CAP signals are transmitted through the N_{t} LEDs which significantly improve the BER of the conventional CAP. Due to the transmission of identical symbols in RC-CAP, its detection is simpler compared to that of SM$_{ux}$-CAP. As will be shown, its BER expression can be derived as a scaled version of that of the conventional CAP.

4.2 BER Performance Analysis

The received electrical signal can be written, for an $N_{\mathrm{r}} \times N_{\mathrm{t}}$ MIMO configuration shown in Fig. 4.1, as:

$$\mathbf{y} = \mathfrak{R}\mathcal{K}\beta\mathbf{H}\mathbf{x} + \mathbf{w} \tag{4.1}$$

where $\mathbf{y}$ is an $N_{\mathrm{r}} \times 1$ received signal vector, $\mathbf{H}$ is an arbitrary $N_{\mathrm{r}} \times N_{\mathrm{t}}$ channel matrix with component $\mathbf{h}_{n_{\mathrm{r}}}$ representing the column vector of channel gains at the $n_{\mathrm{r}}^{\mathrm{th}}$ receiver, $\mathbf{x}$ is an $N_{\mathrm{t}} \times 1$ transmitted vector and $\mathbf{w}$ is an $N_{\mathrm{r}} \times 1$ noise components with each component having zero mean and double-sided power spectral density, $N_0/2$. Both N_{t} and N_{r} represent the number of transmitting LEDs and the number of receiving PDs, respectively. The task of the detector is to recover the multiple transmitted symbols from the received multiplexed signal at each PD. The BER performance of the detectors have been derived by considering LOS propagation under the assumption that channel state information (CSI) is perfectly known at the receiver. The CSI can be acquired with the aid of a training sequence [155].

4.2.1 BER Expression for SM$_{ux}$-CAP

At the $n_{\mathrm{r}}^{\mathrm{th}}$ receiver, given that symbol $\mathbf{x}_m$ has been transmitted, the received electrical signal can be expressed as:

$$y_{n_{\mathrm{r}}}(t) = r_{n_{\mathrm{r}}}^{m}(t) + w_{n_{\mathrm{r}}}(t) \qquad n_{\mathrm{r}} = 1, 2, \cdots, N_{\mathrm{r}} \tag{4.2}$$

where $r_{n_\mathrm{r}}^m(t) = \Re\mathcal{K}\beta\mathbf{h}_{n_\mathrm{r}}^T\mathbf{x}_m(t)$. Hence, the output of SM$_{ux}$-CAP demodulators is written as:

$$\mathbf{y} = \mathbf{r}^m + \mathbf{w} \tag{4.3}$$

where y_{n_r}, $r_{n_\mathrm{r}}^m$ and w_{n_r} are the components of vectors $\mathbf{y}$, $\mathbf{r}^m$ and $\mathbf{w}$, respectively.

The optimum SM$_{ux}$-CAP detector decides on the estimated symbol using ML detection criterion [156, p. 242–247]. This is because the $\{\mathbf{x}_m\}_{m=1}^{M^{N_\mathrm{t}}}$ are equiprobable with $p(\mathbf{x}_m) = 1/M^{N_\mathrm{t}}$. Thus, the SM$_{ux}$-CAP optimum detector decides on the $\mathbf{x}_m$ that maximizes the probability of $\mathbf{y}$ conditioned on $\mathbf{r}^m$ as:

$$\hat{\mathbf{x}}_m = \arg\max_m p(\mathbf{y}, \mathbf{r}^m) \tag{4.4}$$

where the conditional PDF, given the AWGN corrupted channel, is expressed as:

$$\begin{aligned} p(\mathbf{y}, \mathbf{r}^m) &= \frac{1}{(2\pi N_0)^{N_\mathrm{r}/2}} \exp\left[-\sum_{n_\mathrm{r}=1}^{N_\mathrm{r}} \frac{\left|y_{n_\mathrm{r}} - r_{n_\mathrm{r}}^m\right|^2}{2N_0}\right] \\ &= \frac{1}{(2\pi N_0)^{N_\mathrm{r}/2}} \exp\left[\frac{-1}{2N_0}\,||\mathbf{y} - \mathbf{r}^m||_{\mathbf{F}}^2\right] \end{aligned} \tag{4.5}$$

where $\|\cdot\|_{\mathbf{F}}$ is the Frobenius norm. The ML detection criterion reduces to finding the $\mathbf{x}_m$ that results in the minimum Euclidean distance (MED), i.e.

$$\hat{\mathbf{x}}_m = \arg\min_m D(\mathbf{y}, \mathbf{r}^m) \tag{4.6}$$

and the distance metrics is given by:

$$D(\mathbf{y}, \mathbf{r}^m) = ||\mathbf{y} - \mathbf{r}^m||_{\mathbf{F}}^2 \tag{4.7}$$

In the case of correct decision, the decision metrics is given as

$$D(\mathbf{y}, \mathbf{r}^m) = ||\mathbf{w}||_{\mathbf{F}}^2 \tag{4.8}$$

otherwise,

$$D(\mathbf{y}, \tilde{\mathbf{r}}^m) = ||\mathbf{r}^m - \tilde{\mathbf{r}}^m + \mathbf{w}||_{\mathbf{F}}^2 \tag{4.9}$$

Therefore, the pairwise error probability (PEP) of SM$_{ux}$-CAP, which is defined as the probability that the SM$_{ux}$-CAP detector decides in favour of vector $\tilde{\mathbf{x}}$ given that $\mathbf{x}$ has actually

$$\text{BER}_{\text{SM}_{ux}\text{-CAP}} \leq \frac{1}{M^{N_\text{t}}\log_2(M^{N_\text{t}})} \sum_{m=1}^{M^{N_\text{t}}} \sum_{\tilde{m}=1}^{M^{N_\text{t}}} \mathcal{N}_H(b_m, \tilde{b}_m) \; Q\left(\sqrt{\frac{(\Re\mathcal{K}\beta)^2}{2N_0}\left|\left|\mathbf{H}\left(\mathbf{x}_m - \tilde{\mathbf{x}}_m\right)\right|\right|_\mathbf{F}^2}\right). \tag{4.11}$$

$$\text{BER}_{\text{RC-CAP}} \leq \frac{1}{M\log_2(M)} \sum_{m=1}^{M} \sum_{\tilde{m}=1}^{M} \mathcal{N}_H(b_m, \tilde{b}_m) \; Q\left(\sqrt{\frac{(\Re\mathcal{K}\beta)^2}{2N_0}\sum_{n_\text{r}=1}^{N_\text{r}}\left(\sum_{n_\text{t}=1}^{N_\text{t}} h_{n_\text{r}n_\text{t}}\right)^2 |x_m - \tilde{x}_m|}\right). \tag{4.12}$$

been transmitted, can be obtained as:

$$\begin{aligned}\text{PEP}_{\text{SM}_{ux}\text{-CAP}} &= p(\mathbf{x} \to \tilde{\mathbf{x}}|\mathbf{H}) \\ &= p(D(\mathbf{y}, \mathbf{r}^m) > D(\mathbf{y}, \tilde{\mathbf{r}}^m)) \\ &= Q\left(\sqrt{\frac{(\Re\mathcal{K}\beta)^2}{2N_0}\left|\left|\mathbf{H}\left(\mathbf{x}_m - \tilde{\mathbf{x}}_m\right)\right|\right|_\mathbf{F}^2}\right).\end{aligned} \tag{4.10}$$

An upper bound BER expression, shown in (4.11), is then derived for SM$_{ux}$-CAP from (4.10) by considering all possible M^{N_t} signal combinations using the union bound technique [156, p. 261–262], [157]. The $\mathcal{N}_H(b_m, \tilde{b}_m)$ in (4.11) represents the number of bit in error when the receiver decides for the symbol $\tilde{\mathbf{x}}_m$ instead of the transmitted symbol $\mathbf{x}_m$.

4.2.2 BER Expression for RC-CAP

For RC-CAP, since $x_1 = x_2 = \cdots = x_{N_\text{t}}$, $(\mathbf{x}_m - \tilde{\mathbf{x}}_m) = (x_m - \tilde{x}_m)\,\mathbf{1}_{\mathbf{N_t}\times\mathbf{1}}$ where $\mathbf{1}_{\mathbf{N_t}\times\mathbf{1}}$ is an $N_\text{t} \times 1$ vector that has all its entries to be unity. Thus, an upper bound for the BER of RC-CAP can be obtained from (4.11) as shown in (4.12).

However, the upper bound expression in (4.12) can be reduced to an approximation by noting that the argument of the Q-function is the transmitted SNR of a single-input single-output (SISO) system scaled by the summation of the channel gains. Therefore, substituting for the SNR (γ) in the BER expression for a SISO M-ary square QAM shown in (4.13) [158], an approximation for the BER of RC-CAP can be obtained as expressed in (4.14). The erfc$(\cdot)$ is

the cumulative error function and is related to the Q-function by $Q(x) = \text{erfc}(\frac{x}{\sqrt{2}})$.

$$\text{BER} \cong \frac{\sqrt{M}-1}{\sqrt{M}\log_2\sqrt{M}}\text{erfc}\left[\sqrt{\frac{3\log_2\sqrt{M}\cdot\gamma}{2(M-1)}}\right]. \tag{4.13}$$

$$\text{BER}_{\text{RC-CAP}} \cong \frac{2(\sqrt{M}-1)}{\sqrt{M}\log_2\sqrt{M}}Q\left(\sqrt{\frac{3(\Re\mathcal{K}\beta)^2}{(M-1)N_0}\sum_{n_\text{r}=1}^{N_\text{r}}\left(\sum_{n_\text{t}=1}^{N_\text{t}}h_{n_\text{r}n_\text{t}}\right)^2}\right). \tag{4.14}$$

4.3 Low Complexity Detection Algorithms for SM$_{ux}$-CAP

The ML detector (MLD) derived in section 4.2.1 is the optimum detector for SM$_{ux}$-CAP. However, the MLD computes the MED between each received symbol and all the possible M^{N_t} symbols in order to make a decision. Thus, its computational complexity is exponential of the order M^{N_t} which makes it infeasible for large number of transmitting LEDs or high constellation orders. Hence, four alternative low-complexity detection schemes are presented in this section.

4.3.1 Zero Forcing (ZF) Detector

Zero forcing (ZF) is a linear detection scheme that seeks to suppress the ISI between the received multiplexed symbols by forcing the ISI to zero. If the effect of noise is ignored, the linear detection problem represented by (4.1) is solved by the ZF scheme. The ZF solution is realized by using the Moore-Penrose pseudo inverse of the channel matrix which is represented as [159]:

$$\mathbf{G}_{\text{ZF}} = \mathbf{H}^\dagger = (\mathbf{H}^T\mathbf{H})^{-1}\mathbf{H}^T \tag{4.15}$$

where $(\cdot)^\dagger$ represents the Moore-Penrose pseudo-inverse operation. Using (4.15), the output of the ZF detector can be expressed as:

$$\hat{\mathbf{x}} = \mathbf{G}\mathbf{y} = \alpha\mathbf{x} + \tilde{\mathbf{w}} \tag{4.16}$$

where α is one and $\tilde{\mathbf{w}} = \mathbf{G}\mathbf{w}$. A decision can then be made on $\hat{\mathbf{x}}$ by mapping it to the nearest level in the M-ary QAM constellation set. The post-detection SNR of each symbol at the

output of the ZF detector is obtained from (4.16) as:

$$\gamma_{\text{ZF},n_\text{t}} = \frac{\mathbb{E}\left[\mathbf{x}\mathbf{x}^T\right]_{n_\text{t}n_\text{t}}}{\mathbb{E}\left[\tilde{\mathbf{w}}\tilde{\mathbf{w}}^T\right]_{n_\text{t}n_\text{t}}} = \frac{E_s/N_0N_\text{t}}{[\mathbf{H}^T\mathbf{H}]^{-1}_{n_\text{t}n_\text{t}}}, \quad n_\text{t} = 1, 2, \ldots, N_\text{t} \tag{4.17}$$

where $[\cdot]_{n_\text{t}n_\text{t}}$ denotes the (n_t, n_t) element of $[\cdot]$ and E_s is the average transmitted electrical energy per symbol. Therefore, an approximate BER expression can be obtained for SM$_{ux}$-CAP with ZF detector by substituting (4.17) for the SNR in the AWGN BER expression of CAP. Hence, using (4.13), the approximate BER expression for SM$_{ux}$-CAP with ZF detector is derived as:

$$\text{BER}_\text{ZF} \cong \frac{2(\sqrt{M}-1)}{N_\text{t}\sqrt{M}\log_2\sqrt{M}} \sum_{n_\text{t}=1}^{N_\text{t}} Q\left(\sqrt{\frac{3\gamma_{\text{ZF},n_\text{t}}}{(M-1)}}\right). \tag{4.18}$$

The performance of ZF is impacted in cases where the channel matrix is ill-conditioned. It is clear from (4.17) that small eigenvalues of $\mathbf{H}^T\mathbf{H}$ will reduce the post-detection SNR due to noise amplification. This will lead to error in the detection process. Therefore, the MMSE detection scheme addresses this ZF shortcoming by including the noise term in its design criteria.

4.3.2 Minimium Mean Square Error (MMSE) Detector

The MMSE detection scheme minimizes the error between the output of the linear detector and the actually transmitted symbol [160]. It seeks to improve on the performance of ZF by including the noise variance in its design. Thus, similar to ZF, (4.15), (4.17) and (4.18) can be respectively expressed for MMSE as :

$$\mathbf{G}_\text{MMSE} = (\mathbf{H}^T\mathbf{H} + \gamma_s^{-1}\mathbf{I}_{N_\text{t}})^{-1}\mathbf{H}^T, \tag{4.19}$$

$$\gamma_{\text{MMSE},n_\text{t}} = \frac{\gamma_s^{-1}}{\left[\mathbf{H}^T\mathbf{H} + \gamma_s^{-1}\mathbf{I}_{N_\text{t}}\right]^{-1}_{n_\text{t}n_\text{t}}} - 1, \quad n_\text{t} = 1, 2, \ldots, N_\text{t} \tag{4.20}$$

and

$$\text{BER}_\text{MMSE} \cong \frac{2(\sqrt{M}-1)}{N_\text{t}\sqrt{M}\log_2\sqrt{M}} \sum_{n_\text{t}=1}^{N_\text{t}} Q\left(\sqrt{\frac{3\gamma_{\text{MMSE},n_\text{t}}}{(M-1)}}\right). \tag{4.21}$$

where $\gamma_s = E_s/N_0N_\text{t}$.

Algorithm 1 MMSE-OSIC

Initialization:

$\mathbf{H}^{\dagger} = [\mathbf{H}^T\mathbf{H} + \gamma_s^{-1}\mathbf{I}_{N_\mathrm{t}}]^{-1}\mathbf{H}^T$

$\mathbf{G} = \mathbf{H}^{\dagger}$

$k_1 = index(\underset{j}{\operatorname{argmin}}\|\mathbf{G}_j\|^2)$; {$\mathbf{G}_j$ returns the j^{th} row of $\mathbf{G}$; *index(·) returns the position of the element (·)* }

Recursion:

for $i = 1$ to N_t **do**

  $\mathbf{g} = \mathbf{G}_{k_i}$; {$\mathbf{g}$ is the k^{th} row of $\mathbf{G}$}

  $\hat{x}_{k_i} = \mathbf{g}\mathbf{y}$

  $\tilde{x}_{k_i} = Q(\hat{x}_{k_i})$; {quantizing $\hat{x}_{k_i}$ to the closest M-ary QAM level}

  $\mathbf{y} = \mathbf{y} - \mathbf{H}_{k_i}\tilde{x}_{k_i}$; {$\mathbf{H}_{k_i}$ is the k^{th} column of $\mathbf{H}$}

  if $(i < N_\mathrm{t})$ **then**

    $\mathbf{H} = \mathbf{H} - \mathbf{H}_{k_i}$; {the k^{th} column of $\mathbf{H}$ is zeroed}

    $\mathbf{G} = \mathbf{H}^{\dagger}$

    $k_{i+1} = index(\underset{j \notin \{k_1,\cdots,k_i\}}{\operatorname{argmin}}\|\mathbf{G}_j\|^2)$

  end if

end for

4.3.3 Optimally-Ordered Successive Interference Cancellation (OSIC)

Though the linear ZF and MMSE detectors have acceptable performance, their error performance can be improved by combining them with some non-linear techniques. The OSIC is a recursive, symbol-cancellation based technique that can be combined with either ZF (ZF-OSIC) or MMSE (MMSE-OSIC) for performance improvement [155]. In order to detect the symbol from the n_tth transmitter at the receiver, OSIC approaches the detection process by considering all the remaining $N_\mathrm{t} - 1$ symbols as 'interferers'. Thus, it proceeds to the detection of the signal of interest by cancelling the interference effect of the other signals.

During each symbol duration, OSIC first detects the component of $\mathbf{y}$ with the highest post-detection SNR ('the strongest') and makes a decision on its detection. It then uses the decision to cancel the interference contribution of the detected symbol from $\mathbf{y}$, effectively leaving $\mathbf{y}$ with reduced number of 'interferers'. It proceeds to detect the next 'strongest' of the remaining symbols in $\mathbf{y}$ and recursively carry out this operation till all the transmitted symbols are detected. In this manner, OSIC-based detectors encounter increasing reduction in the number of 'interferers' at successive iteration due to the recursive interference cancellation. On the other hand, ZF and MMSE always detect each symbol in the presence of all other 'interferers' which increases the probability of error of the detection process. Furthermore,

Table 4.1: Simulation parameters for the channel configuration.

TX coordinates (m)	LED1 - (1.25,1.25,3), LED2 - (1.25,3.75,3), LED3 - (3.75,1.25,3), LED4 - (3.75,3.75,3)
$\mathbf{H}_1$ coordinates (m)	PD1 - (2.4,2.4,0), PD2 - (2.4,2.6,0), PD3 - (2.6,2.4,0), PD4 - (2.6,2.6,0)
$\mathbf{H}_2$ coordinates (m)	PD1 - (1.2,1.2,0), PD2 - (1.2,3.8,0), PD3 - (3.8,1.2,0), PD4 - (3.8,3.8,0)

OSIC avoids error propagation by ensuring the symbol with the highest probability of being correctly detected (symbol with the highest post-detection SNR) is detected at each iteration. The MMSE-OSIC algorithm is given in algorithm 1 from which its ZF version can easily be derived by discarding the noise term.

4.4 Simulation Results and Discussions

In the results presented in this section, the electrical SNR per bit is defined as $\gamma_b = \frac{(\mathcal{R}\mathcal{K}\beta)^2}{\eta N_0}$ where $(\mathcal{R}\mathcal{K}\beta)^2$ denotes the average received electrical energy per symbol, E_s and $\mathop{\mathbb{E}}_{\forall t}\{x^2(t)\} = 1$. The spectral efficiency, η, is $\log_2(M^{N_\mathrm{t}})$ and $\log_2 M$ for SM$_{ux}$-CAP and RC-CAP, respectively. For a fair comparison, the emitted intensity from each transmitting LEDs has been scaled by a factor N_t to preserve the total transmit power for the two schemes, irrespective of the number of LEDs employed.

4.4.1 Performance Comparison of SM$_{ux}$-CAP and RC-CAP

Two receiver position arrays are investigated for the proposed MIMO techniques. The first array, $\mathbf{H}_1$, is realised by symmetrical arrangement of the PDs at the centre of the room. The second array is realised by direct placement of the PDs under the LEDs to maximize the received LOS signal. The channel gains corresponding to the two arrays are obtained using the ray tracing channel modelling technique in a room that is 3 m in height and 5 m in length and width [161]. The LED half angle, $\varphi_{1/2}$ is 60°, the Field of view of PD is 85° while the PD area, A_PD is given as 1 cm^2. Other configuration parameters are given in Table 4.1. The

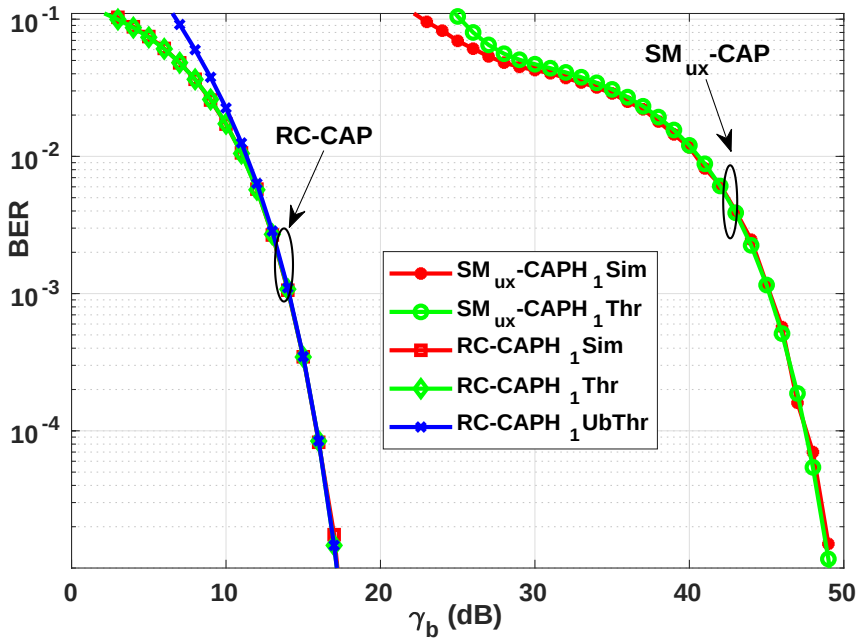

Figure 4.2: BER performance comparison of SM_{ux}-CAP ($M = 4$ and $\eta = 8$ bits/s/Hz) and RC-CAP ($M = 256$ and $\eta = 8$ bits/s/Hz) using channel matrix $\mathbf{H}_1$.
Sim : Simulation; Thr: Theory; UbThr: Upper bound Theory

channel gains, normalized such that the $\max\{h_{n_r n_t}\} = 1$, are given as:

$$\mathbf{H}_1 = \begin{bmatrix} 1.0000 & 0.8481 & 0.9194 & 0.9194 \\ 0.8481 & 1.0000 & 0.9194 & 0.9194 \\ 0.9194 & 0.9194 & 1.0000 & 0.8481 \\ 0.9194 & 0.9194 & 0.8481 & 1.0000 \end{bmatrix} \tag{4.22}$$

and

$$\mathbf{H}_2 = \begin{bmatrix} 1.0000 & 0.1675 & 0.3373 & 0.3373 \\ 0.1675 & 1.0000 & 0.3373 & 0.3373 \\ 0.3373 & 0.3373 & 1.0000 & 0.1675 \\ 0.3373 & 0.3373 & 0.1675 & 1.0000 \end{bmatrix} \tag{4.23}$$

The performance comparison of SM_{ux}-CAP and RC-CAP in a 4×4 MIMO set up with channel matrix $\mathbf{H}_1$ and $\eta = 8$ bits/s/Hz is presented in Fig. 4.2. The results validate the derived analytical expressions for both SM_{ux}-CAP and RC-CAP as the various theoretical analysis curves show excellent agreement with the simulation results at the low BER region where meaningful communication takes place. The slight disagreement at BER $> 10^{-2}$ is however

due to the union bound technique adopted in the analytical derivation. The SNR required for SM$_{ux}$-CAP to achieve the spectral efficiency of 8 bits/s/Hz, at a representative BER of 10^{-4}, is 48.5 dB for the channel configuration considered. This high SNR is due to the high similarity of the channel gains at this receiver position as evident from (4.22). Thus, SM$_{ux}$-CAP suffers BER degradation since it requires sufficient channel gain dissimilarity to separate the received signals.

On the other hand, RC-CAP benefits from spatial diversity due to the high channel gains similarity. It achieves a representative BER of 10^{-4} at an SNR of 16 dB. The RC-CAP BER performance improvement due to similarity in the channel gains can be explained by the factor $\sum_{n_{\mathrm{t}}=1}^{N_{\mathrm{t}}} h_{n_{\mathrm{r}}n_{\mathrm{t}}}$ in (4.14). This factor increases with increasing channel gain similarity. This in turn increases the argument of the Q-function leading to a reduction in BER. Also, the RC-CAP performance gain can be viewed from the fact that it assigns the total transmit power to the transmitted symbol while SM$_{ux}$CAP equally divide the power among all the transmitted symbols. Hence, it can be concluded that RC-CAP is a better choice than SM$_{ux}$-CAP in highly correlated channels. However, to achieve the same spectral efficiency as SM$_{ux}$-CAP with M = 4, RC-CAP requires a much higher constellation order of M = 256 which translates to higher PAPR at the transmitter [122]. The foregoing depicts the trade-off between multiplexing and diversity techniques for MIMO CAP in VLC applications in terms of BER performance, power penalty and spectral efficiency.

When the PDs are directly placed under the LEDs, the LOS gains become pronounced leading to highly dissimilar channel gains and a nearly diagonal channel matrix as shown in (4.23). Thus in Fig. 4.3, RC-CAP loses some of its diversity gain as it achieves the representative BER of 10^{-4} at an SNR of 22 dB. This is a power penalty of 6 dB in comparison to the performance in $\mathbf{H}_1$ and is due to the channel dissimilarity as previously discussed. However, SM$_{ux}$-CAP benefits from the channel dissimilarity to improve its performance by achieving the representative BER of 10^{-4} at an SNR of 14.5 dB. Thus, while still maintaining its spectral efficiency, SM$_{ux}$-CAP achieves a substantial SNR gain of 34 dB in comparison to its performance in $\mathbf{H}_1$. Thus, it can be inferred that SM$_{ux}$-CAP should be deployed in channels with dissimilar gains.

It is not always possible to achieve a dissimilar channel gains due to receiver mobility.

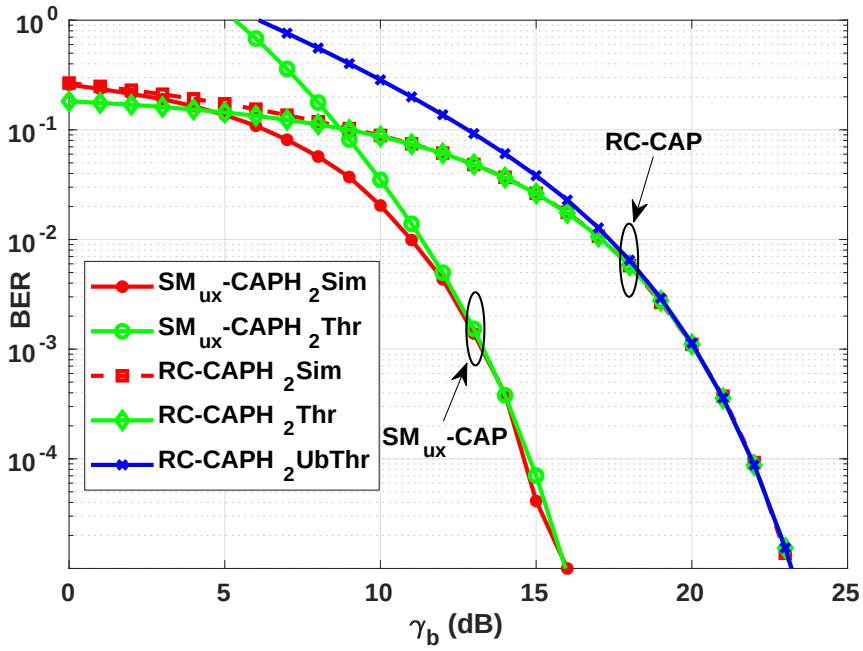

Figure 4.3: BER performance comparison of SM_{ux}-CAP ($M = 4$ and $\eta = 8$ bits/s/Hz) and RC-CAP ($M = 256$ and $\eta = 8$ bits/s/Hz) using channel matrix $\mathbf{H}_2$.
Sim : Simulation; Thr: Theory; UbThr: Upper bound Theory

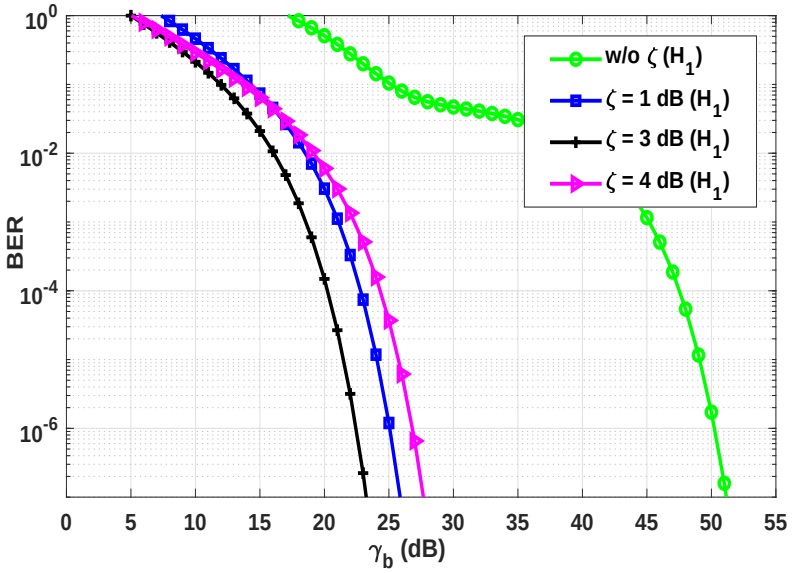

Figure 4.4: Improving the power efficiency of SM_{ux}-CAP using PFI precoding technique when channel gains are highly similar or the transmitters are co-located.

In such cases where preliminary channel estimation shows highly similar channel gains, a precoding technique can be implemented to infuse dissimilarity and improve the power efficiency. Power factor imbalance (PFI) is a simple and very effective precoding technique.

The PFI is implemented by scaling the emitted intensity from each LEDs with a weighting factor, δ_{n_t}. The weighting factor for each LED, derived such that the total transmit power is preserved, is given as:

$$\delta_{n_\mathrm{t}} = \left(\frac{1}{N_\mathrm{t}} \sum_{i=1}^{N_\mathrm{t}} 10^{0.1(i-n_\mathrm{t})\lambda} \right)^{-1} \tag{4.24}$$

where λ is a user-defined PFI in dB. For example, if $\lambda = 2$ dB in (4.24) and $N_\mathrm{t} = 4$, the emitted optical power from LEDs 1 to 4 are scaled by $\delta_1 = 0.4406$, $\delta_2 = 0.6984$, $\delta_3 = 1.1068$ and $\delta_4 = 1.7542$, respectively. It should be noted that the λ implementation neither increases the total transmit power nor the complexity of the decoder [162]. Also, the performance of RC-CAP is unaffected by λ due to the preservation of the total transmit power and it is not necessary to apply λ when the channel gains are similar. Hence, the effect of λ is only shown on the performance of SM$_{ux}$-CAP in $\mathbf{H}_1$ as depicted in Fig. 4.4. It is seen that the λ of 1 dB and 3 dB lead to substantial SNR gain of 26 dB and 28.5 dB, respectively when compared to the case of no λ at the representative BER of 10^{-4}. This shows that λ is an effective precoding technique for the improvement of the power efficiency of SM$_{ux}$-CAP. However, an optimum scaling factor is $\lambda = 3$ dB. Beyond 3 dB, λ results in reduced SNR on the channels with smaller gains which leads to performance degradation. This is reflected by the result of $\lambda = 4$ dB.

4.4.2 Performance Comparison of the Detection Algorithms

The performance analysis of the various SM$_{ux}$-CAP detectors are also investigated and verified through simulation using channel matrix $\mathbf{H}_3$ as shown in (4.25).

The performance comparison of ML detector with linear ZF and MMSE detectors is shown in Fig. 4.5 for a 4×8 SM$_{ux}$-CAP with $M = 4$ and $\eta = 8$ bits/s/Hz. The figure shows the accuracy of the derived analysis for SM$_{ux}$-CAP with ZF and MMSE in (4.18) and (4.21) as the simulation results perfectly match the derived analytical expressions. The slight deviation observed in the ML results at low BER region is due to the union bound technique considered in its derivation. As expected, the ML detector is shown to outperform the linear detectors as it only requires an γ_b of 18 dB to achieve BER of 10^{-4} in comparison to 28 dB and 28.2 dB required by MMSE and ZF, respectively. Also, the MMSE performs better than ZF at low γ_b

where the noise effect dominates.

$$\mathbf{H}_3 = \begin{bmatrix} 1.00 & 0.73 & 0.35 & 0.35 & 0.29 & 0.18 & 0.73 & 0.29 \\ 0.73 & 1.00 & 0.73 & 0.29 & 0.35 & 0.29 & 0.55 & 0.55 \\ 0.35 & 0.73 & 1.00 & 0.18 & 0.29 & 0.35 & 0.29 & 0.73 \\ 0.35 & 0.29 & 0.18 & 1.00 & 0.73 & 0.35 & 0.73 & 0.29 \\ 0.29 & 0.35 & 0.29 & 0.73 & 1.00 & 0.73 & 0.55 & 0.55 \\ 0.18 & 0.29 & 0.35 & 0.35 & 0.73 & 1.00 & 0.29 & 0.73 \\ 0.73 & 0.55 & 0.29 & 0.73 & 0.55 & 0.29 & 1.00 & 0.35 \\ 0.29 & 0.55 & 0.73 & 0.29 & 0.55 & 0.73 & 0.35 & 1.00 \end{bmatrix} \tag{4.25}$$

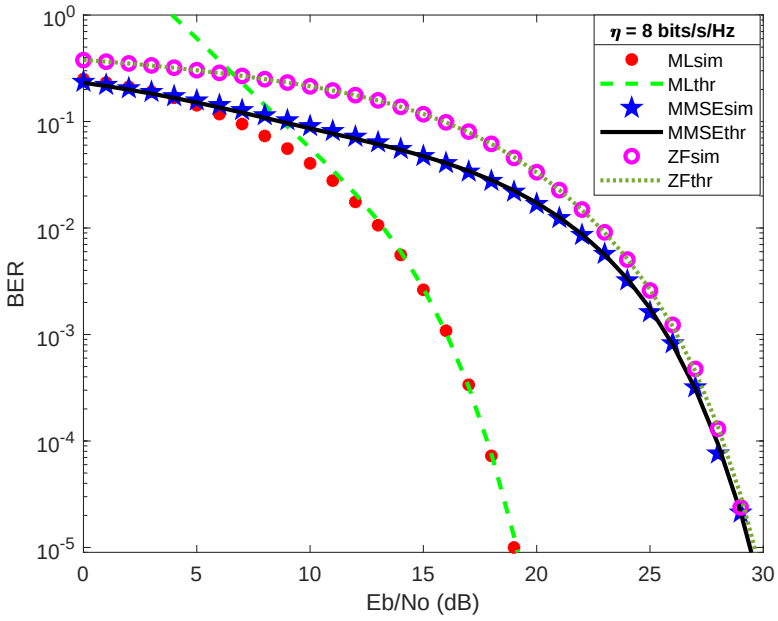

Figure 4.5: Performance comparison of ML and the linear receivers for a 4×8 SM_{ux}-CAP with $M = 4$ and $\eta = 8$ bits/s/Hz. Sim: Simulation; Thr: Theoretical Analysis

However, both have identical performance at high γ_b due to reduction in the noise effect. The performance gain of ML in comparison to the linear detectors at BER of 10^{-4} is approximately 10 dB but as mentioned earlier, its exponential complexity makes it infeasible for practical implementation. Hence, other techniques with feasible complexity are implemented to improve the performance of the linear detectors.

Figure 4.6 shows the performance improvement of the linear detectors combined with OSIC. The BER plot is shown for a 4×8 SM_{ux}-CAP system with $M = 16$ and $\eta = 16$ bits/s/Hz.

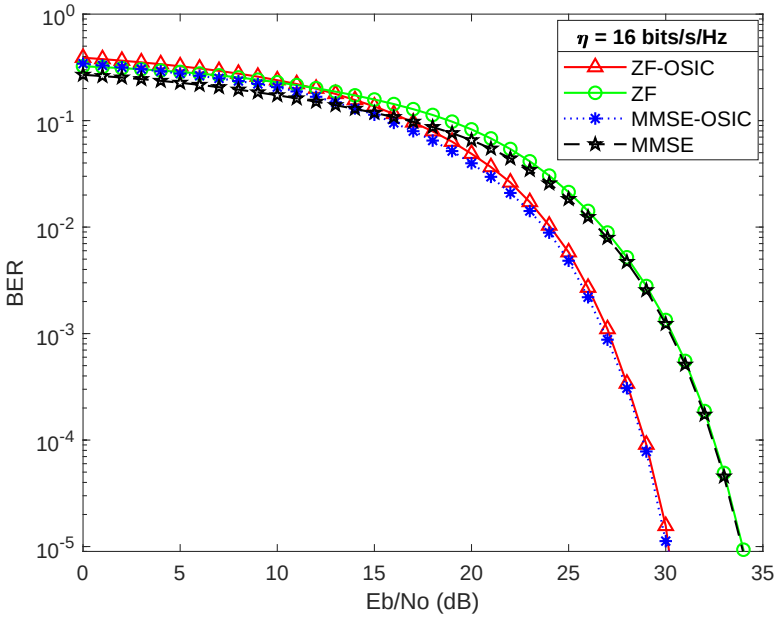

Figure 4.6: Performance improvement of the linear detectors using ordered successive interference cancellation for a 4×8 *SM$_{ux}$-CAP with* $M = 16$ *and* $\eta = 16$ *bits/s/Hz.*

The combination of OSIC with the linear detectors improve the performance by about 3 dB at BER of 10^{-4} for the considered configuration. Specifically, while ZF and MMSE respectively require a γ_b of 32.5 dB and 32.4 dB to achieve a BER of 10^{-4}, both ZF-OSIC and MMSE-OSIC require 28.9 dB and 28.8 dB, respectively.

The γ_b required to achieve a BER of 10^{-4} for all the detectors are compared over a range of spectral efficiencies and different SM$_{ux}$-CAP configurations in Fig. 4.7. The ML has a superior performance of all the detectors as it maintains a performance gain of approximately 5 dB and 10 dB over the OSIC-based and the linear detectors, respectively for η ranging from 6 to 10 bits/s/Hz. Thus, the OSIC implementation significantly improves the performance of the linear detectors. Furthermore, the OSIC addition enhances the performance of MMSE better than that of ZF resulting in performance gap of 1.5 dB between MMSE-OSIC and ZF-OSIC in comparison to the 0.5 dB observed between the two without OSIC implementation. Therefore, MMSE-OSIC presents an acceptable BER performance compromise between the linear detectors and the ML.

The computational complexity of all the detectors is presented in Table 4.2. The complexity

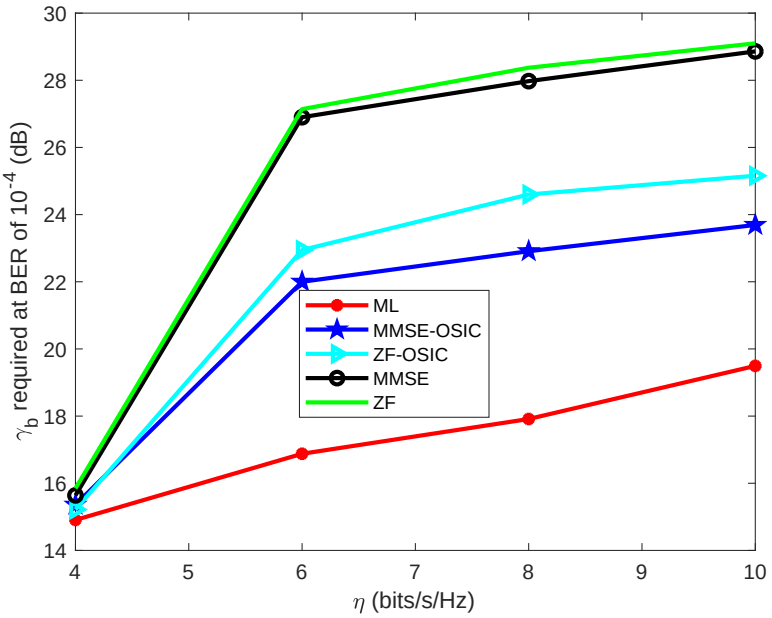

Figure 4.7: Comparison of the required γ_b to achieve BER of 10^{-4} for all SM$_{ux}$-CAP detectors at varying spectral efficiency with $N_r = 8$ and $M = 4$.

Table 4.2: Computational complexity of SM$_{ux}$-CAP detectors.

SM$_{ux}$-CAP Detectors	**Complexity (Number of flops)**
ZF	$18N_{\mathrm{t}}^3 + 16N_{\mathrm{r}}N_{\mathrm{t}}^2 + 4N_{\mathrm{r}}N_{\mathrm{t}} + 2N_{\mathrm{t}} - 2$
MMSE	$18N_{\mathrm{t}}^3 + 16N_{\mathrm{r}}N_{\mathrm{t}}^2 + 4N_{\mathrm{r}}N_{\mathrm{t}} + 4N_{\mathrm{t}} - 2$
ZF-OSIC	$\frac{9}{2}N_{\mathrm{t}}^4 + 9N_{\mathrm{t}}^3 + \frac{11}{2}N_{\mathrm{t}}^2 + N_{\mathrm{r}}(\frac{8}{3}N_{\mathrm{t}}^3 + 6N_{\mathrm{t}}^2 + \frac{22}{3}N_{\mathrm{t}}^2 - 4) - N_{\mathrm{t}}$
MMSE-OSIC	$\frac{9}{2}N_{\mathrm{t}}^4 + 9N_{\mathrm{t}}^3 + \frac{13}{2}N_{\mathrm{t}}^2 + N_{\mathrm{r}}(\frac{8}{3}N_{\mathrm{t}}^3 + 6N_{\mathrm{t}}^2 + \frac{22}{3}N_{\mathrm{t}}^2 - 4)$
ML	$M^{N_{\mathrm{t}}}(3N_{\mathrm{r}}N_{\mathrm{t}} + 9N_{\mathrm{r}} - 1)$

of the algorithms is given in terms of the required number of floating point operations (flops) [163, 164]. The required number of computations is evaluated by taking into account the fact that the optical channel $\mathbf{H}$ is real while the received CAP signal vector $\mathbf{y}$ is complex. As a result, real multiplication and addition are counted as one flop each while either multiplication or addition between a complex and real value is counted as 2 flops. Table 4.2 shows that ML has a prohibitive exponential complexity of $\mathcal{O}(M^{N_{\mathrm{t}}})$ while both the OSIC-based and the linear detectors have computational complexity of order $\mathcal{O}(N_{\mathrm{t}}^4)$ and $\mathcal{O}(N_{\mathrm{t}}^3)$, respectively.

As an illustration, for a 4×8 SM$_{ux}$-CAP configuration with $M = 4$ and $\eta = 8$ bits/s/Hz,

the number of flops required to implement ML, MMSE-OSIC, ZF-OSIC, MMSE and ZF are respectively 42752, 4168, 4148, 3342 and 3334. Also, for the same spectral efficiency and SM$_{ux}$-CAP configuration, the MMSE-OSIC has an γ_b gain of 1.7 dB over ZF-OSIC with a penalty of just 8 flops. Furthermore, the MMSE-OSIC has an γ_b penalty of 5 dB with a savings of 38584 flops (an order of magnitude reduction in complexity) in comparison to the practically-infeasible ML. In addition, the complexity of the MMSE-OSIC can be significantly reduced to the order of $\mathcal{O}(N_{\mathrm{t}}^3)$ based on many available computationally-efficient algorithms [163, 164]. Therefore, it can be concluded that MMSE-OSIC detector offers the best performance-complexity trade-off for SM$_{ux}$-CAP system.

4.5 Summary of Chapter 4

MIMO techniques have been proposed in this work to realise a low-complexity implementation of carrierless amplitude and phase modulation (CAP) with improved spectral efficiency and BER performance in visible light communication (VLC). It is found that RC-CAP is most suitable for highly correlated channels while SM$_{ux}$-CAP should be deployed in channels with dissimilar gains. A precoding technique is also implemented to improve the power efficiency of the MIMO scheme leading to an SNR gain of 28.5 dB. The resulting schemes represent a novel implementations of CAP in MIMO schemes and demonstrate its potential as a suitable modulation technique for VLC applications. To address the high complexity of the optimum ML detector, low-complexity detection schemes are also investigated for SM$_{ux}$-CAP. The OSIC detection schemes, ZF-OSIC and MMSE-OSIC, are found to offer significant performance improvement over their corresponding linear detectors, ZF and MMSE. Furthermore, for the configuration considered, the MMSE-OSIC is found to outperform the ZF-OSIC with an γ_b gain of 1.5 dB at the expense of few extra computations. In addition, the MMSE-OSIC has only 5 dB extra SNR per bit requirement in comparison to the practically-infeasible ML detector. However, the ML detector has a higher computational complexity of an order of magnitude. Thus, MMSE-OSIC represents the best detection scheme in terms of performance-complexity trade-off for SM$_{ux}$-CAP system. In addition to the PFI proposed in this work, the use of singular value decomposition (SVD) and multiple wavelengths can also be adopted to improve the MIMO channel capacity. This is because the PFI is not optimal and has to be implemented through exploratory process.

Chapter 5

Spatial-CAP (S-CAP) in VLC Systems

The spatial modulation (SM) technique is another MIMO transmission technique that has been studied in optical wireless communication. Only one out of N_{t} LEDs is active at any instant in an SM system. The index/position of this active LED is then used to encode data [165, 166]. In SM, a block of information bits to be transmitted is divided into two subblocks. One subblock is mapped to symbols in the signal domain corresponding to the regular modulation scheme while the other is used to activate one of the LED transmitters in the spatial domain. Therefore, the signal domain bits are transmitted through the activated LED while other LEDs remain inactive [157]. Unlike spatial multiplexing, the SM technique avoids inter-carrier/inter-channel interference at the receiver while improving the spectral efficiency of the system. The SM technique has been studied and compared with other modulation schemes in [153, 167]. Experimental demonstrations of SM techniques have also been reported for optical wireless systems in [168]. These studies conclude that SM offers a low complexity approach to improving the throughput of optical wireless communication systems.
As a result, a spatial modulation-based CAP (S-CAP) is proposed to improve the spectral efficiency of CAP while maintaining its low complexity. The BER analysis of S-CAP is derived and its performance is investigated in both LOS and NLOS scenarios. Furthermore, performance enhancing techniques are proposed to improve on its performance.

Though S-CAP avoids ICI with significant reduction in receiver complexity, it only offers logarithmic increase in spectral efficiency and requires that the number of transmitting LEDs be a power of two. These limitations means that a large number of LEDs is required to achieve similar throughput as SM$_{ux}$-CAP. Therefore, generalised S-CAP (GS-CAP) is developed to retain the benefits of S-CAP while improving its spectral efficiency. The GS-CAP

error rate performance is derived and validated via simulation. In addition, various system configurations and parameters are investigated for the developed GS-CAP using the derived analytical expression.

5.1 System Model Description

In S-CAP, only one LED transmits CAP signal of the N_{t} available in each symbol duration. An extra $\log_2(N_{\mathrm{t}})$ information bits can then be encoded on the index of the transmitting LED. Thus, by transmitting extra bits in the spatial domain, S-CAP achieves higher throughput compared to the conventional CAP. The benefits of S-CAP can be illustrated in two ways: (*i*) for a fixed number of transmitted bits/symbol, S-CAP requires lower bandwidth in comparison to CAP. (*ii*) For a fixed bandwidth requirement, S-CAP transmits more bits/symbol thus achieving a higher spectral efficiency. For a bit duration T_{b} and modulation order M, the S-CAP symbol duration can be expressed as:

$$T_{\text{S-CAP}} = T_{\mathrm{b}} \log_2 M N_{\mathrm{t}} \tag{5.1}$$

while CAP symbol duration is expressed as:

$$T_{\text{CAP}} = T_{\mathrm{b}} \log_2 M \tag{5.2}$$

Using (5.1) and (5.2), the spectral efficiency improvement factor of S-CAP over the conventional CAP can be derived as:

$$\eta_f = \frac{T_{\text{S-CAP}}}{T_{\text{CAP}}} = \log_M (M N_{\mathrm{t}}) \tag{5.3}$$

Similarly, during each symbol duration, the GS-CAP transmits copies of the same CAP symbol over N_{a} active LEDs out of the total N_{t} transmitting LEDs. As a result, there are $N = \binom{N_{\mathrm{t}}}{N_{\mathrm{a}}}$ possible number of symbols in the spatial constellation of GS-CAP with a maximum spectral efficiency of $\log_2(N)$ bits/s/Hz. The S-CAP can be viewed as a special case of GS-CAP with $N_{\mathrm{a}} = 1$.

5.1.1 S-CAP System Model

The block diagram illustrating the modulation process of S-CAP is shown in Fig. 5.1. The stream of information bits is grouped into blocks of b bits, where $b = \log_2(N_{\mathrm{t}}) + \log_2(M)$. The

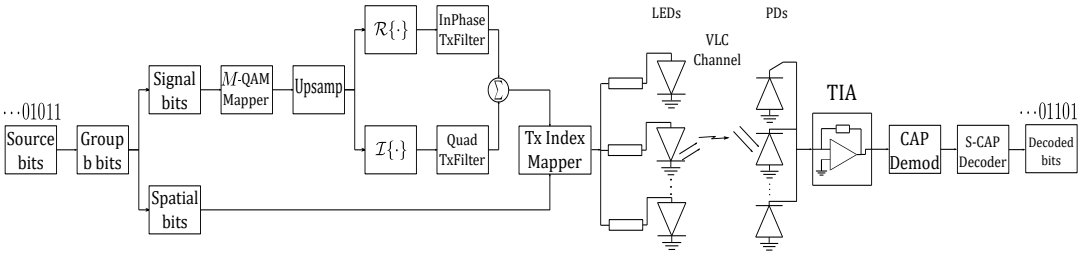

Figure 5.1: The schematic block diagram of the proposed S-CAP transceiver for VLC link.

Table 5.1: S-CAP mapping illustration, $N_{\mathrm{t}} = 2$ and $M = 4$.

Input b bits	LED index	Signal constellation
000	1	$+1 + j$
001	1	$-1 + j$
010	1	$-1 - j$
011	1	$+1 - j$
100	2	$+1 + j$
101	2	$-1 + j$
110	2	$-1 - j$
111	2	$+1 - j$

$\log_2(N_{\mathrm{t}})$ bits is taken as the spatial bits and mapped to a transmitter index while the remaining $\log_2(M)$ bits, taken as the signal bits, is passed to the CAP modulator. The signal bits are mapped to the corresponding M-QAM symbol to generate a CAP signal. In order to select the appropriate transmitter, the $\log_2(N_{\mathrm{t}})$ spatial bits are mapped to an index which corresponds to one of the available N_{t} transmitting LEDs.

The mapping process for the proposed S-CAP is illustrated in Table 5.1 for the case of $N_{\mathrm{t}} = 2$ and $M = 4$. Starting with the most significant bit (MSB), $\log_2(N_{\mathrm{t}})$ bits are mapped to the LED index to activate the transmitter while the remaining $\log_2(M)$ bits are mapped to the CAP signal amplitude to be sent on the activated transmitter. For example, when the input bits is 011, the MSB '$0'$ is mapped to the LED1 while the remaining bits '$11'$ are mapped to the signal symbol $+1 - j$ where $+1$ and -1 become the amplitudes of the in-phase and quadrature filters, respectively.

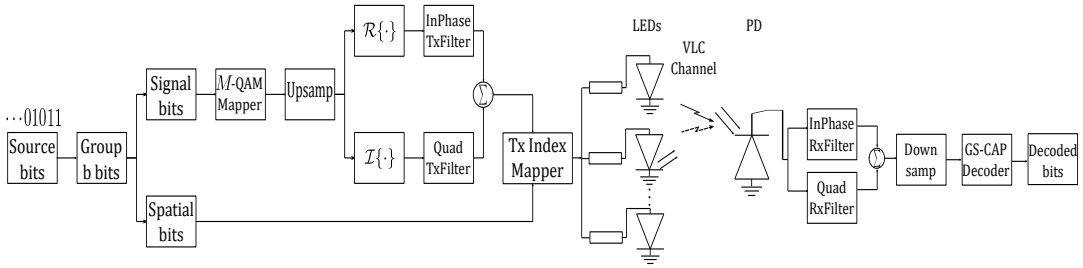

Figure 5.2: The schematic block diagram of the proposed GS-CAP system.

5.1.2 Generalised S-CAP (GS-CAP) System Model

The GS-CAP system configuration is denoted as $\Omega = \left\langle {N_\mathrm{t} \atop N_\mathrm{r}} \right\rangle_{N_\mathrm{a}}^{M}$ where N_t, N_r, N_a and M respectively represent the number of transmitter, number of receiver, number of active LED and M-QAM symbol. Whenever $N_\mathrm{t} = N_\mathrm{r}$, N_r is omitted from the argument of $\langle\cdot\rangle$. Though GS-CAP removes the restriction of the conventional SM where N_t has to be a power of two, the number of symbols employed in the spatial constellation must still satisfy this requirement. This implies that out of the possible $N = \binom{N_\mathrm{t}}{N_\mathrm{a}}$ LED combinations available for spatial signalling, only $N_\mathrm{u} = 2^{\lfloor \log_2(N) \rfloor}$ combinations are used, where $\lfloor\cdot\rfloor$ represents the floor function. Thus, the total bits b encoded in the GS-CAP system consists of both the spatial bits, $b_\mathrm{s} = \lfloor \log_2(N) \rfloor$ and the signal constellation bits, $b_\mathrm{m} = \log_2(M)$. It can therefore be seen that the proposed GS-CAP improves the spectral efficiency of the conventional CAP by an additional b_s bits without requiring any extra channel bandwidth.

The schematic block diagram of the proposed GS-CAP is presented in Fig. 5.2 with two active transmitting LEDs and one PD receiver. The stream of information bits are first grouped into b bits and then separated into b_s and b_m bits. The b_m bits is encoded on one of the M-QAM symbols to generate a CAP signal. The resulting CAP signal is transmitted by all the N_a active LEDs appropriately chosen by the b_s bits. The b_s bits are mapped to one of the N_u spatial constellations.

An illustration of the mapping process for $\Omega = \left\langle {4 \atop 1} \right\rangle_{2}^{4}$ is presented in Table 5.2 where the first N_u spatial constellation points have been selected for spatial signalling. For example, if the bits to be transmitted is 1001 and starting with the most significant bits (MSB), the first b_s MSB '$10'$ are used to activate LEDs 1 and 4. The last b_m bits '$01'$ are then mapped to the symbol

$-1+j$.

5.2 BER Performance Analysis

5.2.1 BER Expression for S-CAP

The received S-CAP signal on the $n_{\mathrm{r}}^{\mathrm{th}}$ receiver given that symbol m has been transmitted on the $n_{\mathrm{t}}^{\mathrm{th}}$ transmitter can be written as:

$$y_{n_{\mathrm{r}}}(t) = r^{m}_{n_{\mathrm{r}}n_{\mathrm{t}}}(t) + w_{n_{\mathrm{r}}}(t) \qquad n_{\mathrm{r}} = 1, 2, \cdots, N_{\mathrm{r}} \tag{5.4}$$

where $r^{m}_{n_{\mathrm{r}}n_{\mathrm{t}}}(t) = \Re\mathcal{K}\beta h_{n_{\mathrm{r}}n_{\mathrm{t}}} x_m(t)$. At each receiver, the S-CAP demodulator uses a pair of linear filters that are, respectively, matched to the pair of the transmit orthogonal filters. From (5.4), the output of the S-CAP demodulators can be expressed as:

$$\mathbf{y} = \mathbf{r}^{m}_{n_{\mathrm{t}}} + \mathbf{w} \tag{5.5}$$

where $y_{n_{\mathrm{r}}}$, $r^{m}_{n_{\mathrm{r}}n_{\mathrm{t}}}$ and $w_{n_{\mathrm{r}}}$ are the components of $\mathbf{y}$, $\mathbf{r}^{m}_{n_{\mathrm{t}}}$ and $\mathbf{w}$, respectively. The S-CAP detector will then make a decision on the transmitted signal in each signal interval based on the demodulator output such that the probability of a correct decision is maximized. Assuming perfect synchronization and full knowledge of the channel matrix $\mathbf{H}$, the S-CAP optimum detector employs ML criterion since $\{x_m\}_{m=1}^{M}$ are equiprobable with $p(x_m) = 1/M$. Thus, the S-CAP optimum detector decides on the $x_{mn_{\mathrm{t}}}$, which is the m^{th} symbol transmitted on the $n_{\mathrm{t}}^{\mathrm{th}}$ transmitter, that maximizes the probability of $\mathbf{y}$ conditioned on $\mathbf{r}^{m}_{n_{\mathrm{t}}}$ as:

$$\hat{x}_{mn_{\mathrm{t}}} = \arg\max_{n_{\mathrm{t}},m} p(\mathbf{y}|\mathbf{r}^{m}_{n_{\mathrm{t}}}) \tag{5.6}$$

where the conditional PDF, given the AWGN corrupted channel, is expressed as:

$$p(\mathbf{y}|\mathbf{r}^{m}_{n_{\mathrm{t}}}) = \frac{1}{(2\pi N_0)^{N_{\mathrm{r}}/2}} \exp\left[-\sum_{n_{\mathrm{r}}=1}^{N_{\mathrm{r}}} \frac{\left|y_{n_{\mathrm{r}}} - r^{m}_{n_{\mathrm{r}}n_{\mathrm{t}}}\right|^2}{2N_0}\right] \tag{5.7}$$

The ML criterion reduces to finding the $x_{mn_{\mathrm{t}}}$ that results in the minimum Euclidean distance, i.e.

$$\hat{x}_{mn_{\mathrm{t}}} = \arg\min_{n_{\mathrm{t}},m} D(\mathbf{y}, \mathbf{r}^{m}_{n_{\mathrm{t}}}) \tag{5.8}$$

Table 5.2: GS-CAP constellation mapping process for $\Omega = \left\langle {4 \atop 1} \right\rangle_2^4$

Possible Spatial constellation	b_{s} bits	Selected spatial constellation	b_{m} bits	Signal constellation
$1,2$	00	$1,2$	00	$+1+j$
$1,3$	01	$1,3$	01	$-1+j$
$1,4$	10	$1,4$	10	$-1-j$
$2,3$	11	$2,3$	11	$+1-j$
$2,4$				
$3,4$				

and the distance metrics is given by:

$$D(\mathbf{y}, \mathbf{r}_{n_{\mathrm{t}}}^{m}) = \sum_{n_{\mathrm{r}}=1}^{N_{\mathrm{r}}} \left| y_{n_{\mathrm{r}}} - r_{n_{\mathrm{r}} n_{\mathrm{t}}}^{m} \right|^2 \tag{5.9}$$

To find the error probability of S-CAP, we consider a joint detection of both the transmitter index and the transmitted symbol using PEP. The PEP of S-CAP is defined as the probability that the S-CAP detector decides in favour of vector $\tilde{\mathbf{x}}$ given that $\mathbf{x}$ has actually been transmitted. If the detector makes the correct decision, the decision metrics become

$$D(\mathbf{y}, \mathbf{r}_{n_{\mathrm{t}}}^{m}) = \sum_{n_{\mathrm{r}}=1}^{N_{\mathrm{r}}} |w_{n_{\mathrm{r}}}|^2 \tag{5.10}$$

otherwise,

$$D(\mathbf{y}, \tilde{\mathbf{r}}_{n_{\mathrm{t}}}^{m}) = \sum_{n_{\mathrm{r}}=1}^{N_{\mathrm{r}}} \left| r_{n_{\mathrm{r}} n_{\mathrm{t}}}^{m} - \tilde{r}_{n_{\mathrm{r}} n_{\mathrm{t}}}^{m} + w_{n_{\mathrm{r}}} \right|^2 \tag{5.11}$$

Thus, the PEP for S-CAP can be obtained as:

$$\begin{aligned} \mathrm{PEP}_{\text{S-CAP}} &= p(\mathbf{x} \to \tilde{\mathbf{x}} | \mathbf{H}) \\ &= p(D(\mathbf{y}, \mathbf{r}_{n_{\mathrm{t}}}^{m}) > D(\mathbf{y}, \tilde{\mathbf{r}}_{n_{\mathrm{t}}}^{m})) \\ &= Q\left(\sqrt{\frac{(\Re \mathcal{K} \beta)^2}{2N_0} \sum_{n_{\mathrm{r}}=1}^{N_{\mathrm{r}}} |x_m h_{n_{\mathrm{r}} n_t} - x_{\tilde{m}} h_{n_{\mathrm{r}} \tilde{n}_{\mathrm{t}}}|^2} \right). \end{aligned} \tag{5.12}$$

The BER performance of S-CAP can be derived from (5.12) by considering all possible MN_{t} signal combinations and using the union bound technique [156, p. 261–262], [157]. Hence, the BER of S-CAP is upper-bounded as shown in (5.13) where $\mathcal{N}_H(\tilde{b}_{mn_{\mathrm{t}}}, b_{mn_{\mathrm{t}}})$ is the number of bit in error when the receiver decides for the symbol $\tilde{x}_{mn_t}$ instead of the transmitted symbol $x_{mn_{\mathrm{t}}}$. Alternatively, $\mathcal{N}_H(\tilde{b}_{mn_{\mathrm{t}}}, b_{mn_{\mathrm{t}}})$ refers to the number of positions in which the

$$\text{BER}_{\text{S-CAP}} \leq \frac{1}{MN_{\text{t}}\log_2(MN_{\text{t}})} \sum_{m=1}^{M} \sum_{n_t=1}^{N_{\text{t}}} \sum_{\tilde{m}=1}^{M} \sum_{\tilde{n}_{\text{t}}=1}^{N_{\text{t}}} \mathcal{N}_H(\tilde{b}_{mn_t}, b_{mn_{\text{t}}}) \; Q\left(\sqrt{\frac{(\Re\mathcal{K}\beta)^2}{2N_0} \sum_{n_{\text{r}}=1}^{N_{\text{r}}} |x_m h_{n_{\text{r}}n_t} - x_{\tilde{m}} h_{n_{\text{r}}\tilde{n}_{\text{t}}}|^2}\right). \tag{5.13}$$

bits corresponding to symbol $\tilde{x}_{mn_{\text{t}}}$ and $x_{mn_{\text{t}}}$ differ (Hamming distance). For example, if a symbol corresponding to bits '100' is transmitted and the S-CAP detector erroneously detect the symbol corresponding to bits '000', '001' or '011', the $\mathcal{N}_H(\tilde{b}_{mn_t}, b_{mn_{\text{t}}})$ term becomes 1, 2 or 3, respectively.

5.2.2 BER Expression for GS-CAP

Since the same copies of the CAP signal x_{m} are transmitted over N_{a} active LEDs in GS-CAP, the received signal at the n_{r}^{th} receiver is given as

$$y_{n_{\text{r}}}(t) = \psi^m_{n_{\text{r}}n_{\text{u}}}(t) + w_{n_{\text{r}}}(t) \qquad\qquad n_{\text{r}} = 1, 2, \cdots, N_{\text{r}} \tag{5.14}$$

where $\psi^m_{n_{\text{r}}n_{\text{u}}}(t) = \Re\mathcal{K}\beta\vartheta_{n_{\text{r}}n_{\text{u}}}x_{\text{m}}$ and $\vartheta_{n_{\text{r}}n_{\text{u}}} = \sum_{n_{\text{a}}}^{N_{\text{a}}} h^{n_{\text{u}}}_{n_{\text{r}}n_{\text{a}}}$. The $\vartheta_{n_{\text{r}}n_{\text{u}}}$ is the sum of the channel gains that correspond to the N_{a} active LEDs from the n_{u}^{th} spatial constellation to the n_{r}^{th} receiver. Therefore, $\vartheta_{n_{\text{r}}n_{\text{u}}}$ is the effective channel gain of the GS-CAP system. The output of the GS-CAP demodulators can then be expressed as:

$$\mathbf{y} = \boldsymbol{\psi}^m_{n_{\text{u}}} + \mathbf{w} \tag{5.15}$$

where $y_{n_{\text{r}}}$, $\psi^m_{n_{\text{r}}n_{\text{u}}}$ and $w_{n_{\text{r}}}$ are the entries of $\mathbf{y}$, $\boldsymbol{\psi}^m_{n_{\text{u}}}$ and $\mathbf{w}$, respectively. Given that $\{\boldsymbol{\psi}^m_{n_{\text{u}}}\}$ are equiprobable, the optimum GS-CAP detector employs maximum ML decision criterion. The ML criterion decides on the $x_{mn_{\text{u}}}$, which is the m^{th} signal transmitted on the n_{u}^{th} LED combination, that maximizes the probability of $\mathbf{y}$ conditioned on $\boldsymbol{\psi}^m_{n_{\text{u}}}$ as:

$$\hat{x}_{mn_{\text{u}}} = \arg\max_{n_{\text{u}},m} p(\mathbf{y}, \boldsymbol{\psi}^m_{n_{\text{u}}}) \tag{5.16}$$

where $p(\mathbf{r}, \boldsymbol{\psi}^m_{n_{\text{u}}})$, considering the AWGN channel, is given by

$$p(\mathbf{y}, \boldsymbol{\psi}^m_{n_{\text{u}}}) = \frac{1}{(2\pi N_0)^{N_{\text{r}}/2}} \exp\left[-\sum_{n_{\text{r}}=1}^{N_{\text{r}}} \frac{\left|y_{n_{\text{r}}} - \psi^m_{n_{\text{r}}n_{\text{u}}}\right|^2}{2N_0}\right] \tag{5.17}$$

$$\text{BER}_{\text{GS-CAP}} \leq \frac{1}{MN_{\text{u}}\log_2(MN_{\text{u}})} \sum_{m=1}^{M} \sum_{n_u=1}^{N_{\text{u}}} \sum_{\tilde{m}=1}^{M} \sum_{\tilde{n}_{\text{u}}=1}^{N_{\text{u}}} \mathcal{N}_H(b_{mn_{\text{u}}}, \tilde{b}_{mn_u}) \\ Q\left(\sqrt{\frac{(\Re\mathcal{K}\beta)^2}{2N_0} \sum_{n_{\text{r}}=1}^{N_{\text{r}}} |x_m \vartheta_{n_{\text{r}}n_{\text{u}}} - x_{\tilde{m}} \vartheta_{n_{\text{r}}\tilde{n}_{\text{u}}}|^2}\right). \quad (5.23)$$

The ML criterion of (5.16) is equivalent to finding the $x_{mn_{\text{u}}}$ that minimizes the minimum Euclidean distance as:

$$\hat{x}_{mn_{\text{u}}} = \arg\min_{n_{\text{u}},m} D(\mathbf{y}, \boldsymbol{\psi}_{n_{\text{u}}}^m) \quad (5.18)$$

where the distance metric $D(\mathbf{y}, \boldsymbol{\psi}_{n_{\text{u}}}^m)$ is given by

$$D(\mathbf{y}, \boldsymbol{\psi}_{n_{\text{u}}}^m) = \sum_{n_{\text{r}}=1}^{N_{\text{r}}} \left|y_{n_{\text{r}}} - \psi_{n_{\text{r}}n_{\text{u}}}^m\right|^2 \quad (5.19)$$

A joint detection of the LED combination index n_{u} and the transmitted symbol x_{m} is considered in finding the error probability of GS-CAP using the PEP. When the GS-CAP detector makes the correct decision, the distance metric becomes

$$D(\mathbf{y}, \boldsymbol{\psi}_{n_{\text{u}}}^m) = \sum_{n_{\text{r}}=1}^{N_{\text{r}}} |w_{n_{\text{r}}}|^2 \quad (5.20)$$

otherwise,

$$D(\mathbf{y}, \tilde{\boldsymbol{\psi}}_{n_{\text{u}}}^m) = \sum_{n_{\text{r}}=1}^{N_{\text{r}}} \left|\psi_{n_{\text{r}}n_{\text{t}}}^m - \tilde{\psi}_{n_{\text{r}}n_{\text{t}}}^m + w_{n_{\text{r}}}\right|^2 \quad (5.21)$$

Therefore, the PEP of GS-CAP can be obtained as:

$$\begin{aligned} \text{PEP}_{\text{GS-CAP}} &= p(\mathbf{x} \to \tilde{\mathbf{x}}|\mathbf{H}) \\ &= p(D(\mathbf{y}, \boldsymbol{\psi}_{n_{\text{u}}}^m) > D(\mathbf{y}, \tilde{\boldsymbol{\psi}}_{n_{\text{u}}}^m)) \\ &= Q\left(\sqrt{\frac{(\Re\mathcal{K}\beta)^2}{2N_0} \sum_{n_{\text{r}}=1}^{N_{\text{r}}} |x_m \vartheta_{n_{\text{r}}n_{\text{u}}} - x_{\tilde{m}} \vartheta_{n_{\text{r}}\tilde{n}_{\text{u}}}|^2}\right). \end{aligned} \quad (5.22)$$

An upper bound expression for the BER performance of GS-CAP, shown in (5.23), can be derived from (5.22) by considering all possible MN_{u} combinations of GS-CAP symbol using the union bound technique [156, p. 261–262], [157]. The $\mathcal{N}_H(\tilde{b}_{mn_u}, b_{mn_{\text{u}}})$ in (5.23) is the number of bits in error when the GS-CAP detector decides in favour of symbol $\tilde{\mathbf{x}}$ instead of the transmitted symbol $\mathbf{x}$.

Table 5.3: Configuration parameters for S-CAP channel modelling.

Parameter	Value	Parameter	Value
LED half angle, $\varphi_{1/2}$	60°	ρ_{ceiling}	0.48
Field of view of PD	85°	ρ_{floor}	0.63
Temporal resolution : Δt	0.2 ns	ρ_{wall}	0.83
Spatial resolution : ΔA_{PD}	0.04 m^2	PD area, A_{PD}	1 cm^2

5.3 Simulation Results and Discussions

In the results presented in this section, the electrical SNR per bit is defined as $\gamma_b = \frac{(\Re\mathcal{K}\beta)^2}{\eta N_0}$ where $(R\mathcal{K}\beta)^2$ denotes the average received electrical energy per symbol, E_s with $\underset{\forall t}{\mathbb{E}}\{x^2(t)\} = 1$. The η is $\log_2(N_{\text{t}}M)$ for S-CAP and $\log_2(MN_{\text{u}})$ for GS-CAP.

5.3.1 Performance of S-CAP in Line-of-Sight (LOS) Channel

The impulse response of the indoor optical channel is obtained using the ray-tracing algorithm reported in [61, 161]. The simulation is carried out by considering four LED positions whose coordinates, along with other simulation parameters, are given in Table 5.3. It can be seen from Table 5.3 that the LEDs' coordinates have been chosen to realize a symmetrical arrangement. The path profile for the ray-tracing algorithm for an LED and PD is depicted in Fig. 2.4 while the channel impulse response (CIR) simulation procedure is detailed in [161]. The angle of incidence and irradiance are denoted by ϕ_k and θ_k, respectively while d_k represents the path traced out by the optical radiation from the source to its destination. The room dimension is configured to be 5 m in length and width (along x- and y- axis) and 3 m in height (along z-axis), but can be extended to any arbitrary dimension. The PD receiver position is varied across the dimension of the room floor to account for user mobility. Typical values of the reflectivity, ρ, adopted for the surfaces of the room in the simulation are reported in [81]. The z-axis coordinate for both LEDs and PDs have been fixed at 3 m and 0 m as they are considered attached to the ceiling and floor of the room, respectively. As a result, only the x and y coordinates are reported for the PDs. In the LOS channel simulation, the channel gain values are normalized such that the $\max\{h_{n_{\text{r}}n_{\text{t}}}\} = 1$ and $\min\{h_{n_{\text{r}}n_{\text{t}}}\} = h_{\text{min}}$. The coordinates of all the PDs employed in the simulation, along with their configurations, are given in Table 5.4.

The spectral efficiency/bandwidth improvement, η_f, provided by S-CAP over the conventional

Table 5.4: Coordinates of the PDs and LEDs employed in the simulations with the datum or origin chosen as the room corner shown in Fig. 5.7.

Figure	PD1	PD2	PD3	PD4	LED
Fig. 5.5	$(0.8, 3.2)$	$\times$	$\times$	$\times$	$1-4$
Fig. 5.6	$(0.8, 3.2)$	$(0.8, 0.8)$	$(3.2, 3.2)$	$(3.2, 0.8)$	$1-4$
Fig. 5.10	$(0.8, 2.6)$	$(0.8, 0.8)$	$(2.6, 2.6)$	$(2.6, 0.8)$	$1\,\&\,4$
Fig. 5.11	$(0.8, 4.2)$	$(0.8, 0.8)$	$(4.2, 4.2)$	$(4.2, 0.8)$	$1\,\&\,4$
Fig. 5.16	$(1.0, 1.0)$	$\times$	$\times$	$\times$	$1\,\&\,4$
Fig. 5.17	$(2.6, 2.6)$	$\times$	$\times$	$\times$	$1\,\&\,4$
Fig. 5.18 (C)	$(1.0, 1.0)$	$(3.0, 1.4)$	$(1.4, 3.0)$	$(2.0, 2.6)$	$1\,\&\,4$
Fig. 5.18 (D)	$(2.6, 2.6)$	$(3.0, 1.4)$	$(1.4, 3.0)$	$(2.0, 2.6)$	$1\,\&\,4$
TX coordinates (m)	LED1 - $(1.25, 1.25, 3)$, LED2 - $(1.25, 3.75, 3)$, LED3 - $(3.75, 1.25, 3)$, LED4 - $(3.75, 3.75, 3)$				
PD arrangement	1 PD $\triangleq$ PD1;	2 PDs $\triangleq$ PD1 & PD4;		4 PDs $\triangleq$ All PDs.	

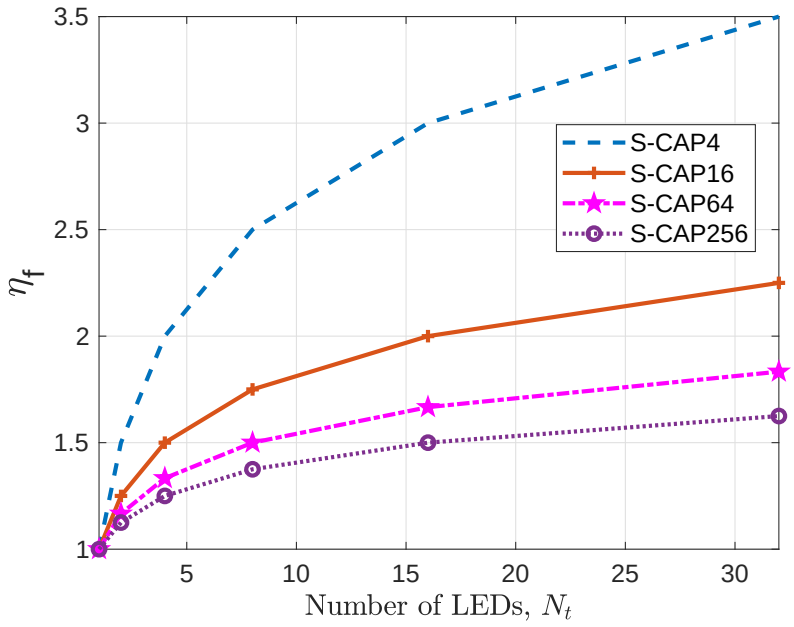

Figure 5.3: Spectral efficiency improvement of S-CAP over the conventional CAP scheme for different number of LEDs and constellation sizes.

CAP is illustrated in Fig. 5.3 using the derived expression in (5.3). Furthermore, Fig. 5.4 shows the BER performance comparison and spectral/power efficiency trade-off of the two schemes for the same constellation order. Compared to CAP at the same constellation order, S-CAP achieves a higher spectral efficiency but its power efficiency is lower. For example, to achieve

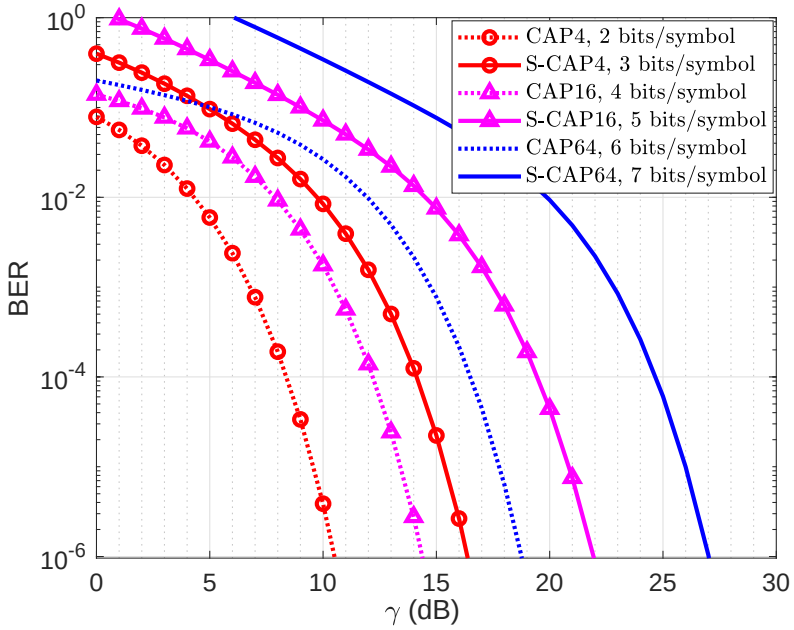

Figure 5.4: Spectral/power efficiency trade-off of S-CAP compared to CAP for the same constellation order using two transmitting LEDs and one PD.

the same BER of 10^{-4} as CAP-4 with $M = 4$, S-CAP4 incurs a 6 dB power penalty but transmits an extra 1 bit/symbol which results in a spectral efficiency improvement factor of 1.5. This trend is also observed for $M = 16$ and 64. The power penalty incurred by S-CAP is due to its distinct channel gains requirement and the penalty can be substantially reduced by performance-enhancing techniques which are presented in later results.

The derived analytical expression for S-CAP is validated in Fig. 5.5 for different M and multiple LEDs. The figure shows that at the lower BER region where meaningful communication can be established, the derived expression shows excellent agreement with the simulation results in LOS propagation. The slight deviation at the high BER region is however due to the union bound technique considered in the analysis. The results of Fig. 5.5 also depicts the BER performance comparison of S-CAP for different constellation sizes. For example, it is shown that for $M = 4, 16$ and 64 and using 2 LEDs, S-CAPM requires γ_b of 15 dB, 19 dB and 25 dB, respectively to achieve a representative BER of 10^{-4}. This γ_b increases to 28 dB, 37.5 dB and 48 dB respectively in the case of four LEDs. This shows that, at the BER and PD location considered, S-CAP4, S-CAP16 and S-CAP64 respectively requires a power penalty of 13 dB, 18.5 dB and 23 dB for a corresponding increase of 33.3%,

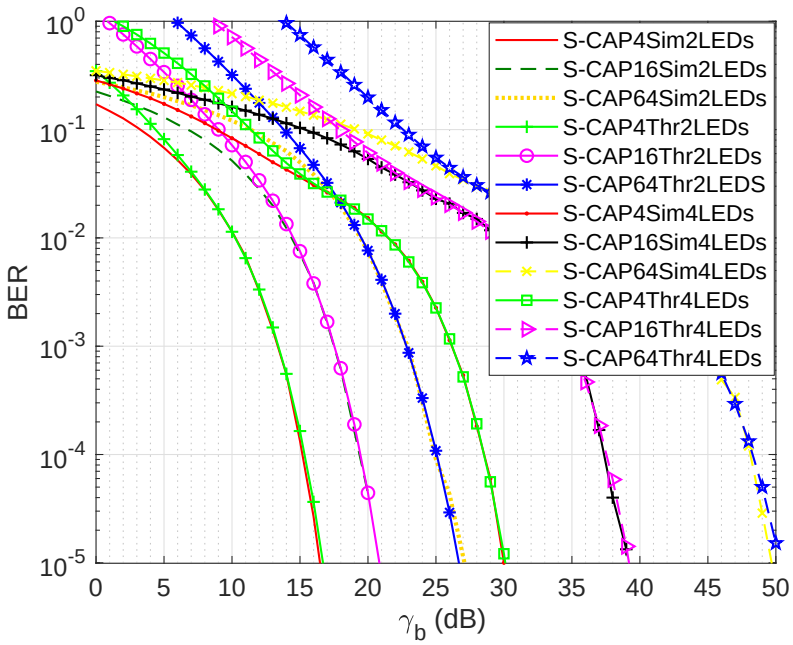

Figure 5.5: BER performance comparison of S-CAP using simulation and the derived analytical expression for multiple LEDs and one PD with LOS channel gain. Sim: Simulation and Thr: Analysis

20% and 14.1% in spectral efficiency. This illustration depicts the trade-off between the power and spectral efficiency of an S-CAP system. Henceforth, as a result of the validation, only S-CAP16 is used for further investigation.

Figure 5.6 shows the performance of S-CAP16 in LOS propagation using multiple LEDs and PDs (MIMO). The result confirms the tightness of the derived analytical upper bound for MIMO S-CAP. The effectiveness of using multiple PDs to improve performance, which is exploited in later results, is also reflected. In comparison to the performance of one PD, the use of two and four PDs result in γ_b improvement of 17 dB and 24 dB, respectively at a representative BER of 10^{-4}.

The γ_b required for S-CAP LOS propagation to achieve a BER of 10^{-4} at each PD location across the room is presented in Fig. 5.7 using two LEDs. The corresponding values of h_{min} is shown in Fig. 5.8. For the case of the two LEDs considered, $\{h_{n_t}\}_{n_t=1}^{N_t} = \begin{bmatrix} 1 & h_{\text{min}} \end{bmatrix}$. In addition to the effect of γ_b, the performance of S-CAP depends on the interaction of three factors. These are: (i) signal constellation points (SCP); (ii) the channel dissimilarity, $(|\Delta h|)$; and (iii) the minimum value of the channel gains (h_{min}). This is evident from the expression

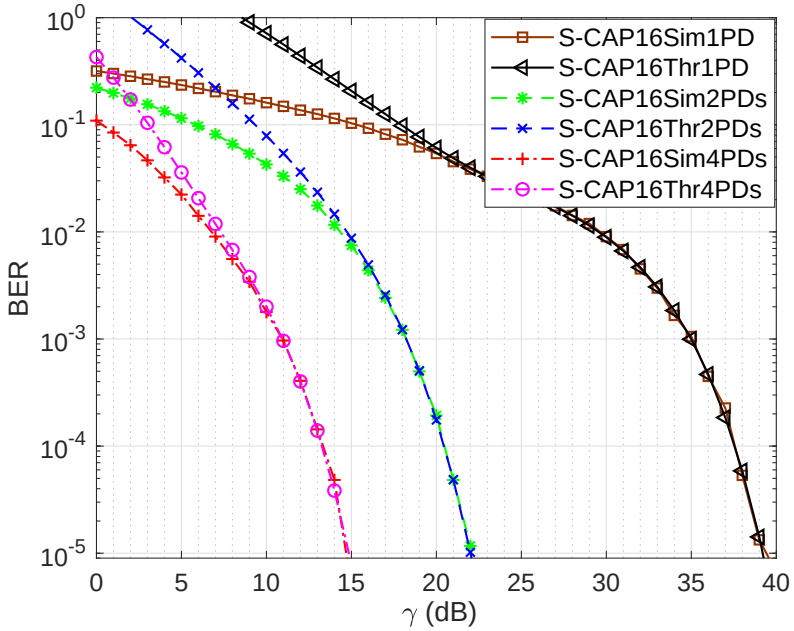

Figure 5.6: BER performance comparison of S-CAP16 using simulation and the derived analytical expression for four LEDs and varying number of PDs with LOS channel gain. Sim: Simulation and Thr: Analysis

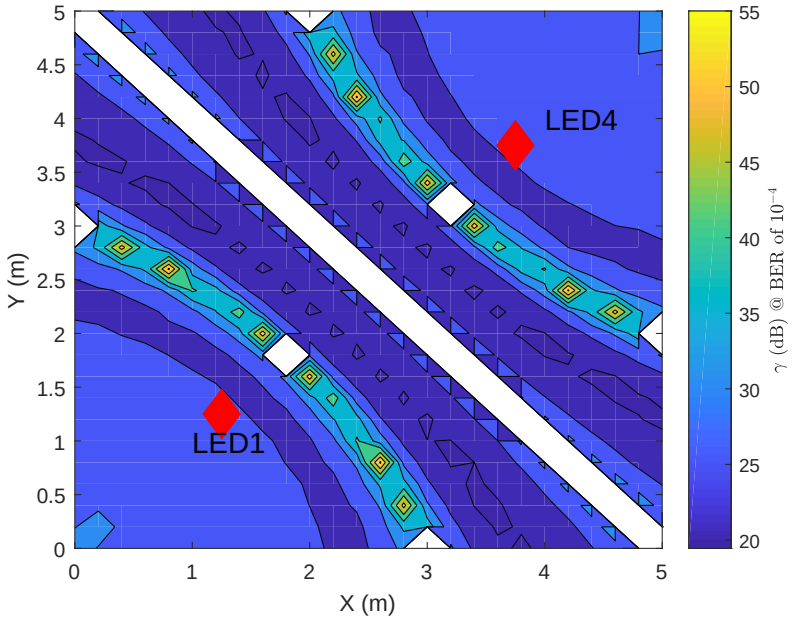

Figure 5.7: The required γ_b for S-CAP16 LOS propagation to achieve BER of 10^{-4} at each PD location across the room using LED1 and LED4 whose positions are shown by the red stars. The white region shows area of BER $> 10^{-4}$.

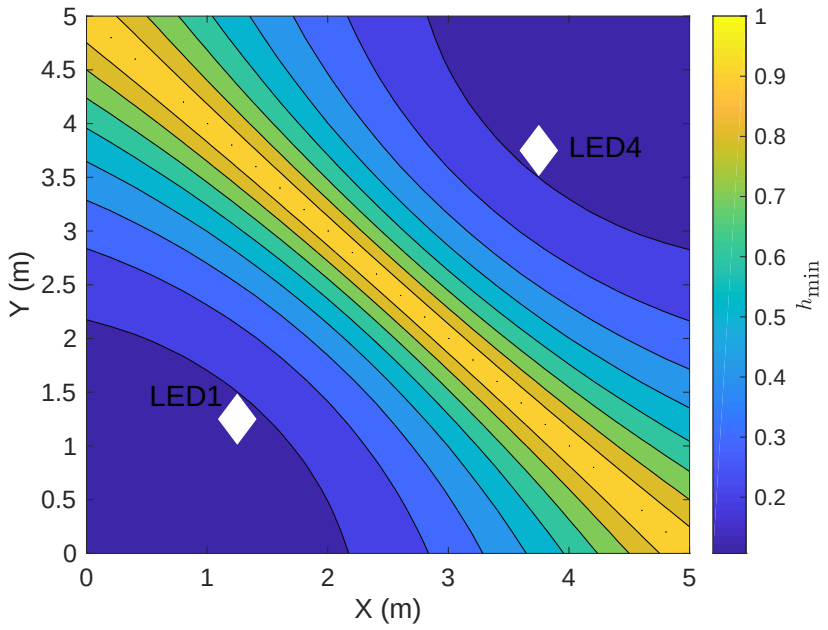

Figure 5.8: Distribution of h_{min} across the room for S-CAP16 considering LED1 and LED4 whose positions are shown by the white stars.

in (5.13). At low values of $h_{\min}$ in the range $0 \leq Y(m) \leq 2$, the required γ_b is moderate despite the fact that the channel gains are completely dissimilar ($|\Delta h| \rightarrow 1$). This means the performance is solely dictated by the small value of $h_{\min}$. Hence, as $h_{\min}$ increases the required γ_b reduces. However, the required γ_b momentarily becomes high in the range $2 < Y(m) < 2.8$ as SCP becomes the dominating factor. Beyond the range of SCP influence, $h_{\min}$ value continues to dictate the performance until $|\Delta h|$ becomes the dominating factor where $0.9 \leq h_{\min} \leq 1$ and $|\Delta h| \rightarrow 0$. Within this range, the channel gains become perfectly identical leading to an irreducible BER region.

In order to further highlight the effect of the performance-determining factors, a 2-D plot is extracted from Fig. 5.7 by fixing the value on x-axis at 0.8 m and varying the PD position across the y-axis. The resulting plot, overlaid by the plot of $h_{\min}$ across the same region, is depicted in Fig. 5.9. Within the range of $0 \leq Y(m) \leq 2$, as the value of $h_{\min}$ increases from 0.1 to 0.22, the required γ_b decreases which shows an improving performance as the BER in this region is dictated by the increasing value of $h_{\min}$. However, SCP becomes the determining factor within the range of $2 < Y(m) < 2.8$ even though the value of $h_{\min}$ continue to increase from 0.22 to 0.35. The increasing value of $h_{\min}$ together with high $|\Delta h|$ should lead to performance

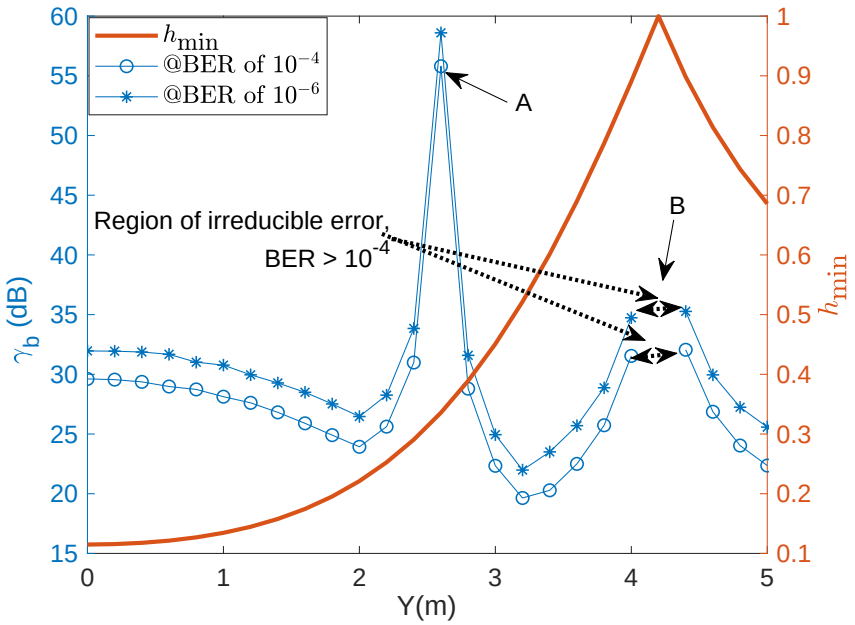

Figure 5.9: SNR per bit penalty for S-CAP16 LOS propagation using LED1 and LED4 by considering a fixed location on x-axis ($x = 0.8$ m) and varying the PD's location across the y-axis overlaid by the corresponding h_{min} values.

improvement but SCP dictates the performance degradation in this range. This explains the high γ_b at location A which requires 24 dB more than the neighbouring locations to achieve the same BER of 10^{-4}. Finally, the effect of channel gains dissimilarity can be seen from the range $3.2 < Y(m) < 4.4$ where $|\Delta h| \to 0$ as the value of $h_{\min}$ increases from 0.52 to 1. At location B, where both channel gains have a value of unity ($|\Delta h| = 0$) and are thus perfectly identical, the decoder is unable to differentiate between symbols from the two LEDs. The same pattern is also recorded at lower BER of 10^{-6}.

Similar to other SM techniques, the performance of S-CAP is affected by the aforementioned performance determining factors as demonstrated in Fig. 5.9. To improve the performance of S-CAP in such scenarios, PFI and multiple PDs are employed. Inducing PFI redistributes the transmit power from the LEDs non-uniformly and thereby restoring dissimilarity among the channel gains [162].

Figures 5.10 and 5.11 depict the influence of the two performance-enhancing techniques on the performance of S-CAP LOS propagation at location A and B in Fig. 5.9, respectively. It is shown that the BER performance can be significantly improved using these techniques. A

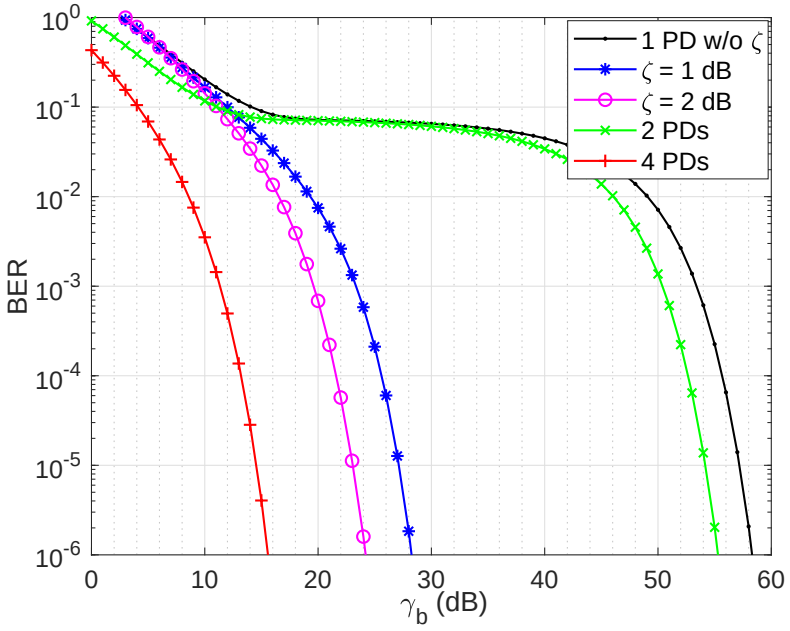

Figure 5.10: Improving the BER performance of S-CAP16 through power redistribution with PFI and the use of multiple PDs at Location A in Fig. 5.9.

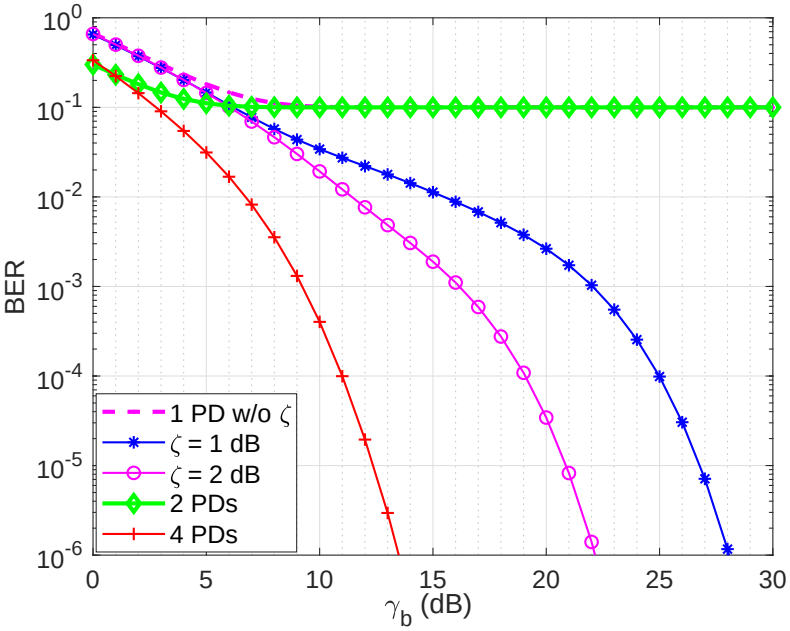

Figure 5.11: Improving the BER performance of S-CAP16 through power redistribution with PFI and the use of multiple PDs at location B in Fig. 5.9.

gain of 30 dB and 33.5 dB can be realised at BER of 10^{-4} using PFI of 1 dB and 2 dB, respectively at location A as shown in Fig. 5.10. Similarly, at the same location A, the use of

multiple PDs results in performance gain of 3 dB and 43 dB corresponding to two and four PDs, respectively. Using multiple PDs increases the performance since receiving the same symbol in multiple locations increases the probability of correctly detecting that symbol.
However, the diversity gain due to multiple PDs is a function of the PD positions. To illustrate this, the use of two PDs at locations $(0.8, 4.2)$ and $(4.2, 0.8)$, both with channel gain of 1, in Fig. 5.11 lead to no improvement. However, using four PDs significantly reduces the BER to 10^{-4} at an γ_b of 13 dB. Also, Fig 5.11 shows that the use of 1 dB and 2 dB PFI improve the irreducible BER at location B to 10^{-4} at γ_b of 28 dB and 22 dB, respectively. Therefore, both multiple PDs and PFI are effective in significantly improving the BER performance of S-CAP in indoor LOS propagation.

5.3.2 Performance of S-CAP in Non-LOS (Multipath) Channel

The majority of the studies on optical SM have been in LOS indoor propagation [153, 162]. For high-speed indoor optical communication however, the presence of multiple reflections impair the link performance [4]. The multiple reflections of the transmitted signal that arrive at the receiver much later than the LOS, though carry much smaller power, can not be ignored due to their time-dispersive properties especially when considering high-speed indoor optical communication. These reflections constitute non-line of sight (NLOS) propagation which reduces the quality of the received signal. Therefore, the performance of S-CAP in multipath indoor optical communication is studied considering CIR with second-order reflections. The maximum data rate that can be transmitted in a diffuse channel without the need for equalization is given as $R_b \leq 0.1/\tau_{\text{rms}}$ [4, p. 465]. Hence, normalizing the τ_{rms} by bit duration, the maximum normalized τ_{rms} for an equalizer-free transmission can be obtained as $\bar{\tau}_{\text{rms}} = 0.1$. Therefore, for the multipath study, the range of $0.1 \leq \bar{\tau}_{\text{rms}} \leq 0.4$ is considered across the room.

The impact of indoor multipath propagation with second-order reflections on the BER performance of S-CAP is presented in Fig. 5.12 at two different locations with $\bar{\tau}_{\text{rms}}$ of 0.4 (PD1) and 0.28 (PD2). At PD1 location where $\bar{\tau}_{\text{rms}} = 0.4$, S-CAP is able to achieve a BER of 10^{-4} with an SNR of 29.5 dB in LOS propagation in comparison to the error floor of 8×10^{-2} it achieved in multipath. Similarly, it reaches error floor of 7×10^{-4} in multipath propagation at PD2 location while it is able to achieve a BER of 10^{-4} in LOS with an SNR

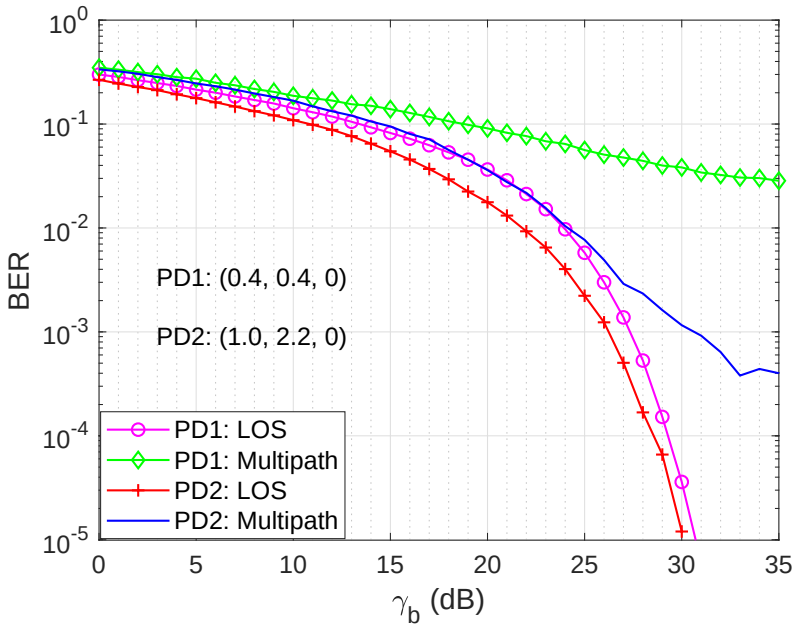

Figure 5.12: Comparison of the BER performance of S-CAP16 in LOS and multipath indoor optical communication.

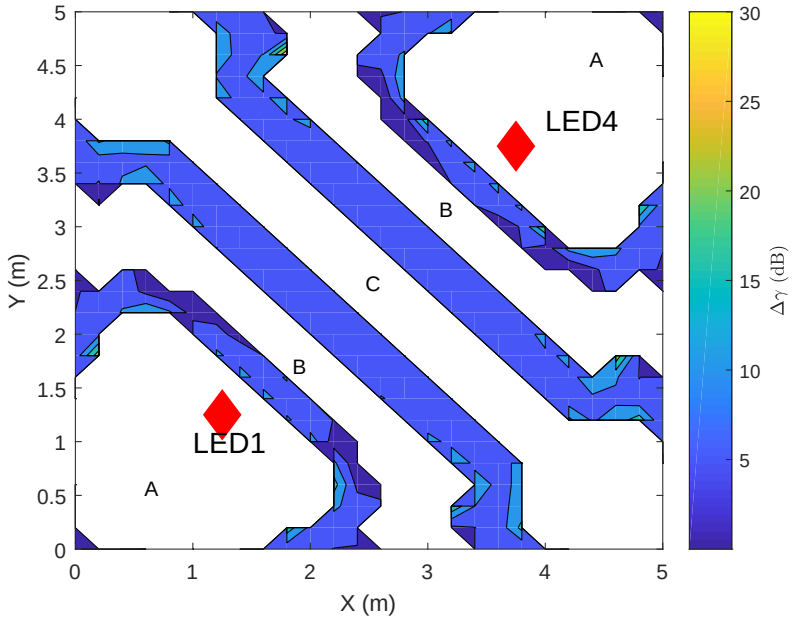

Figure 5.13: The γ_b penalty incurred by S-CAP16 to achieve the FEC BER limit of 3×10^{-3} in an optical indoor multipath propagation with second-order reflections in comparison to LOS propagation. The white regions indicate region where BER $> 3 \times 10^{-3}$.

of 28.5 dB. This shows the impact of indoor multipath propagation on the BER performance of S-CAP. This figure also indicates that the S-CAP performance in multipath will depend on the particular location in the room hence, the effect of user mobility across the room is further investigated.

The γ_b penalty (Δ_γ) incurred due to the multipath propagation effect in comparison to the LOS scenario is shown in Fig. 5.13. It is seen that the penalty could be up to 30 dB in γ_b to achieve a BER of 3×10^{-3} in some parts of the room due to the effect of multipath. The regions marked A, B and C in Fig. 5.13 correspond to the earlier mentioned three factors influencing S-CAP performance. However, in contrast to the case of LOS where h_{min} is the dominant factor in region A, it is the τ_{rms} that dominates the BER performance in this region in multipath propagation.

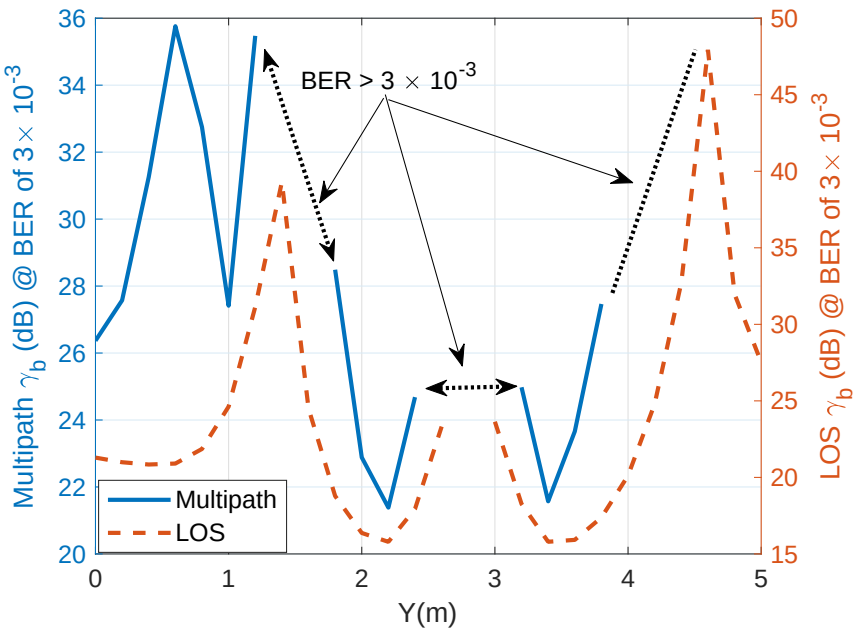

Figure 5.14: Comparison of the BER performance trend of S-CAP16 in multipath and LOS propagation across the room for a fixed location on x-axis ($x = 2.2$ m) and at the FEC BER limit of 3×10^{-3}.

In order to show the influence of these factors, the performance of S-CAP in LOS and multipath propagation is compared and presented in Fig. 5.14 at the forward error correction (FEC) BER limit of 3×10^{-3} and location $x = 2.2$ m. The corresponding values of h_{min} and τ_{rms} are shown in Fig. 5.15. Within the range $0 \leq Y(m) \leq 1$, Fig. 5.14 shows that the multipath performance

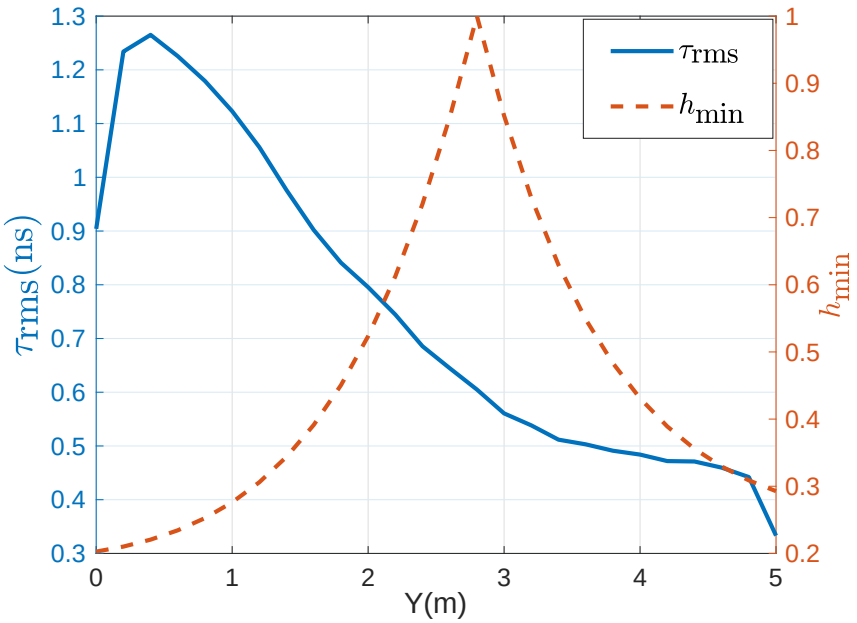

Figure 5.15: Comparison of the trend followed by τ_{rms} and hmin across the room for a fixed location on x-axis ($x = 2.2$ m).

follows exactly the trend of τ_{rms} in Figs. 5.15 while LOS performance follows that of h_{min}. However, between $1 < Y(m) \leq 5$, both the performance of S-CAP in LOS and multipath follow the same trend though the BER in the multipath case is higher. Therefore it can be deduced that while h_{min}, SCP and $|\Delta h|$ dominate S-CAP performance in LOS propagation, it is the τ_{rms}, SCP and $|\Delta h|$ that dictate performance in multipath scenario. This is due to the fact that τ_{rms} overrides the influence of h_{min} especially where the latter has small values $(0 < h_{\text{min}} < 0.3)$ and the former has high values $(0.9 \leq \tau_{\text{rms}} \leq 1.3)$.

The results discussed above indicate that the BER performance in multipath propagation can be divided into two regions. The region dominated by the multipath factor, τ_{rms} and the region dominated by LOS factors, SCP and $|\Delta h|$. Hence two locations in Fig. 5.13, one each from the multipath and LOS region where there is irreducible BER, have been selected in investigating the performance of PFI and multiple PDs in multipath propagation.

The results of the PFI are presented in Figs. 5.16 and 5.17. Location C with $\bar{\tau}_{\text{rms}} = 0.31$ and location D with $\bar{\tau}_{\text{rms}} = 0.13$ belong to the multipath and LOS region, respectively and S-CAP performance suffers irreducible error floor at both locations. The PFI is found to be

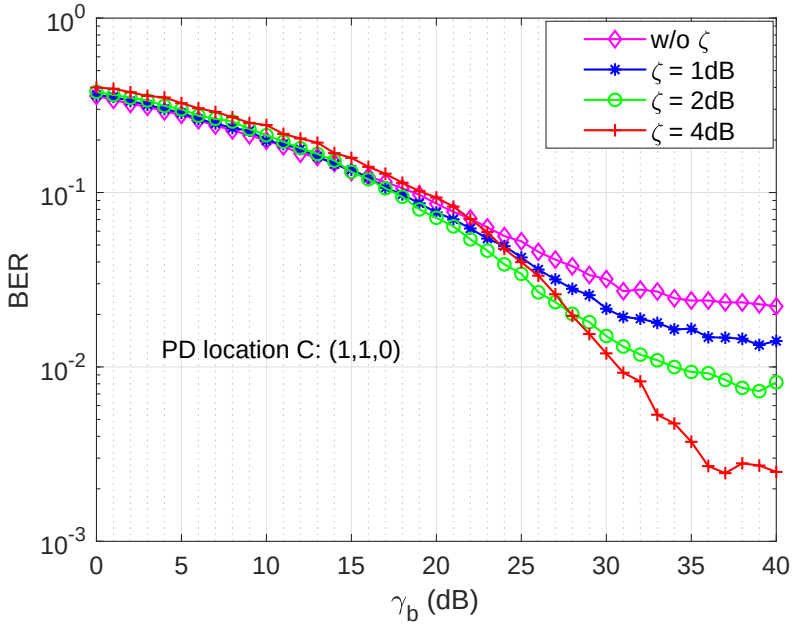

Figure 5.16: BER performance improvement for S-CAP16 using PFI in a multipath propagation with second-order reflections at a location dominated by τ_{rms}.

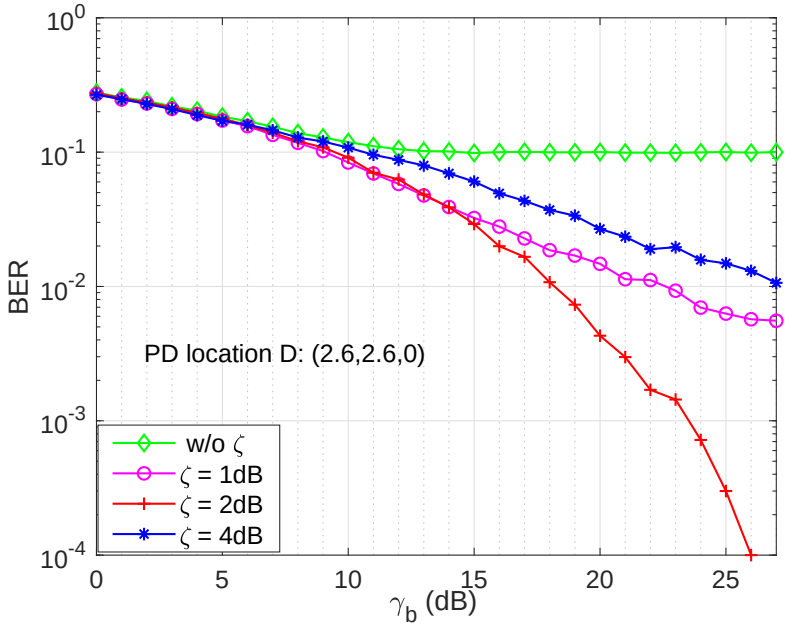

Figure 5.17: BER performance improvement for S-CAP16 using PFI in multipath propagation with second-order reflections at a location dominated by h_{min}.

ineffective in improving the BER performance degradation in the region with high τ_{rms} as shown in Fig. 5.16. However, PFI is able to improve the performance in region dominated by

SCP and $|\Delta h|$ to achieve BER of 10^{-4} at γ_b of 28 dB using $\lambda = 2$ dB. This confirms the earlier results regarding the effectiveness of PFI in LOS scenario. It can thus be said that PFI does not significantly improve the BER performance in multipath propagation in the region dominated by high τ_{rms}. Also, it can be deduced from Fig. 5.17 that the value of PFI should not be too high as $\lambda = 4$ dB results in performance degradation. While PFI increase results by increasing channel gain dissimilarity, it also reduces the emitted optical power on some of the LEDs. This results in low SNR on these LEDs and hence, the consequent degradation in BER performance.

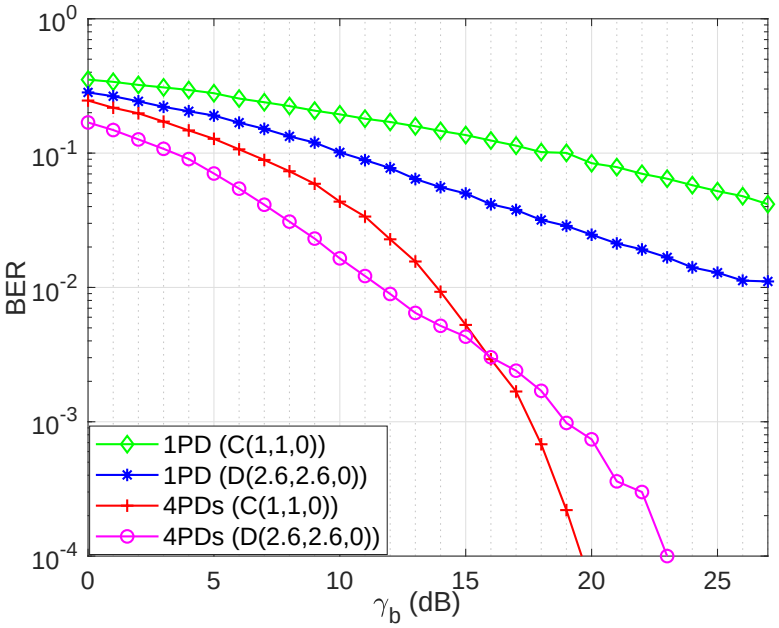

Figure 5.18: BER performance improvement for S-CAP16 using multiple PDs in multipath propagation with second-order reflections.

Multiple PDs are also employed to improve performance of S-CAP in multipath channel. The results, as presented in Fig. 5.18, show that the performance can be significantly improved with the use of multiple PDs. In comparison to the previous irreducible error performance, BER of 10^{-4} is achieved in location C and D at γ_b of 19.5 dB and 23 dB, respectively using 4 PDs. This shows that multiple PDs can be employed to significantly improve the performance of S-CAP in both LOS and multipath propagation.

5.3.3 Performance of GS-CAP in LOS Channel

For the GS-CAP simulation results, two channel gain matrices, $\mathbf{H}_1$ in (5.3.3) and $\mathbf{H}_2$ in (5.3.3), corresponding to coordinates R_1 and R_2 in Table 5.5 are employed. The $\mathbf{H}_1$ has been used for the various simulation results while $\mathbf{H}_2$ is only employed when investigating the impact of receiver mobility.

Table 5.5: System configuration for GS-CAP channel modelling.

LED Transmitter	Coordinate (x, y, z) m	PD Receiver	R_1 Coordinate (x, y, z) m	R_2 Coordinate (x, y, z) m
LED1	$(1.25, 1.25, 3)$	PD1	$(1.25, 1.25, 0)$	$(2.50, 0.55, 0)$
LED2	$(1.25, 2.50, 3)$	PD2	$(1.25, 2.50, 0)$	$(1.25, 1.10, 0)$
LED3	$(1.25, 3.75, 3)$	PD3	$(1.25, 3.75, 0)$	$(1.25, 1.65, 0)$
LED4	$(3.75, 1.25, 3)$	PD4	$(3.75, 1.25, 0)$	$(1.25, 2.20, 0)$
LED5	$(3.75, 2.50, 3)$	PD5	$(3.75, 2.50, 0)$	$(1.25, 2.75, 0)$
LED6	$(3.75, 3.75, 3)$	PD6	$(3.75, 3.75, 0)$	$(1.25, 3.30, 0)$
LED7	$(2.50, 1.25, 3)$	PD7	$(2.50, 1.25, 0)$	$(1.25, 3.85, 0)$
LED8	$(2.50, 3.75, 3)$	PD8	$(2.50, 3.75, 0)$	$(1.25, 4.40, 0)$

$$\mathbf{H}_1 = \begin{bmatrix} 1.00 & 0.73 & 0.35 & 0.35 & 0.29 & 0.18 & 0.73 & 0.29 \\ 0.73 & 1.00 & 0.73 & 0.29 & 0.35 & 0.29 & 0.55 & 0.55 \\ 0.35 & 0.73 & 1.00 & 0.18 & 0.29 & 0.35 & 0.29 & 0.73 \\ 0.35 & 0.29 & 0.18 & 1.00 & 0.73 & 0.35 & 0.73 & 0.29 \\ 0.29 & 0.35 & 0.29 & 0.73 & 1.00 & 0.73 & 0.55 & 0.55 \\ 0.18 & 0.29 & 0.35 & 0.35 & 0.73 & 1.00 & 0.29 & 0.73 \\ 0.73 & 0.55 & 0.29 & 0.73 & 0.55 & 0.29 & 1.00 & 0.35 \\ 0.29 & 0.55 & 0.73 & 0.29 & 0.55 & 0.73 & 0.35 & 1.00 \end{bmatrix}$$

$$\mathbf{H}_2 = \begin{bmatrix} 0.66 & 0.39 & 0.19 & 0.66 & 0.39 & 0.19 & 0.90 & 0.22 \\ 0.72 & 0.52 & 0.26 & 0.72 & 0.52 & 0.26 & 1.00 & 0.32 \\ 0.71 & 0.64 & 0.36 & 0.71 & 0.64 & 0.36 & 0.97 & 0.45 \\ 0.62 & 0.72 & 0.48 & 0.62 & 0.72 & 0.48 & 0.83 & 0.62 \\ 0.49 & 0.72 & 0.61 & 0.49 & 0.72 & 0.61 & 0.64 & 0.81 \\ 0.37 & 0.65 & 0.70 & 0.37 & 0.65 & 0.70 & 0.47 & 0.96 \\ 0.27 & 0.53 & 0.73 & 0.27 & 0.53 & 0.73 & 0.33 & 1.00 \\ 0.19 & 0.40 & 0.67 & 0.19 & 0.40 & 0.67 & 0.23 & 0.91 \end{bmatrix}$$

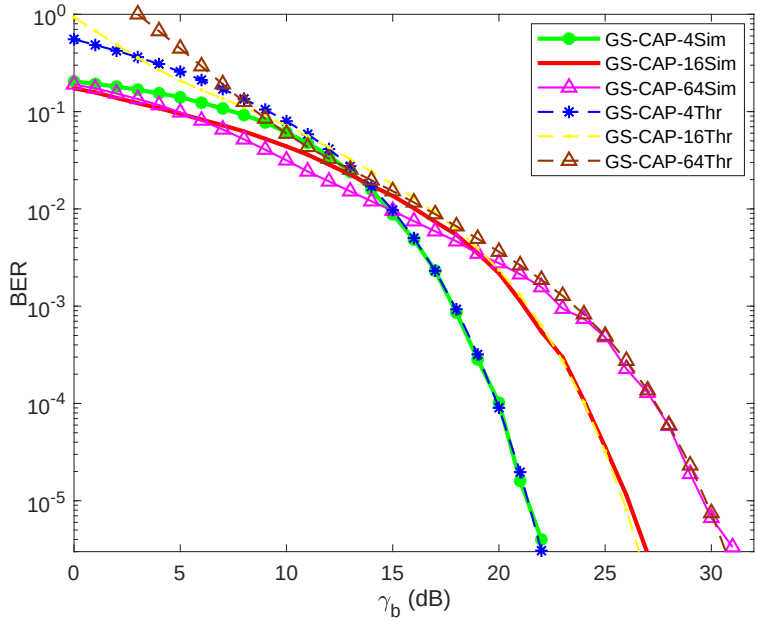

Figure 5.19: BER performance of GS-CAP with system configuration $\Omega = \langle 5 \rangle_2^M$ *for* $M = 4, 16$ *and* 64*. Sim: Simulation results; Thr: Theoretical results.*

The BER performance of GS-CAP for $\Omega = \langle 5 \rangle_2^M$ with $M = 4, 16$ and 64 is presented in Fig. 5.19. The results obtained from the simulations are in excellent agreement with those of the theoretical expressions in the low BER region where communication takes place. This validates the performance analysis derived for the GS-CAP for various values of M. It is seen that at a representative BER of 10^{-5}, $\Omega = \langle 5 \rangle_2^M$ requires SNR of 21.5 dB, 25.5 dB and 29.5 dB for $M = 4, 16$ and 64, respectively. This means that the γ_b penalty for using the symbol domain (M) to increase the spectral efficiency by 2 bits/s/Hz is 4 dB.

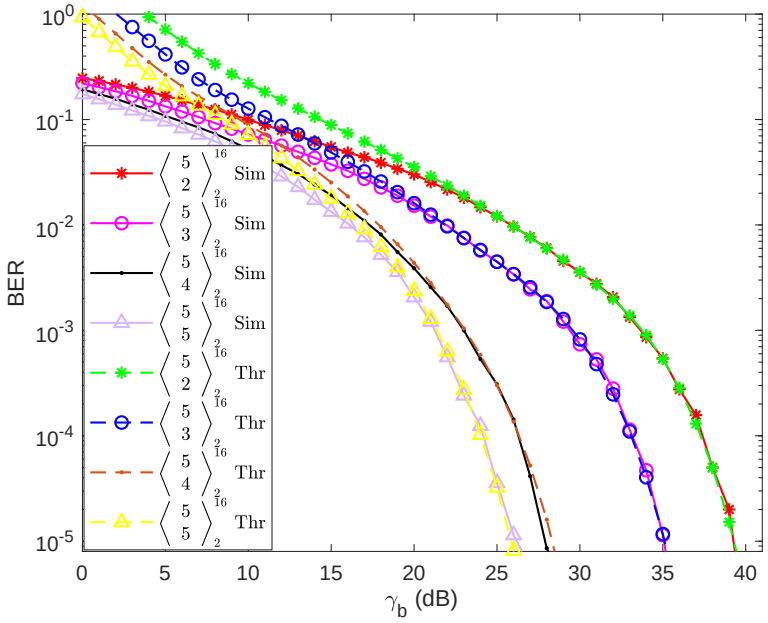

Figure 5.20: BER performance of GS-CAP with system configuration $\Omega = \left\langle \begin{smallmatrix} 5 \\ N_r \end{smallmatrix} \right\rangle_2^{16}$ *for* $N_r = 2, 3, 4$ *and* 5. *Sim: Simulation results; Thr: Theoretical results.*

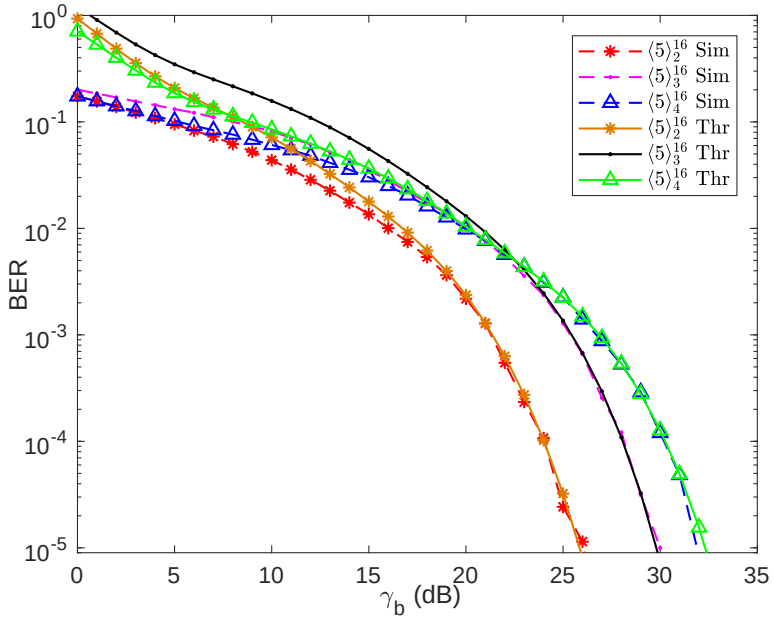

Figure 5.21: BER performance of GS-CAP with system configuration $\Omega = \langle 5 \rangle_{N_a}^{16}$ *for* $N_a = 2, 3$ *and* 4. *Sim: Simulation results; Thr: Theoretical results.*

The BER performance of GS-CAP for $\Omega = \left\langle \begin{smallmatrix} 5 \\ N_r \end{smallmatrix} \right\rangle_2^{16}$ with $N_r = 2, 3, 4$ and 5 is shown in Fig. 5.20. The figure shows that the performance of the proposed GS-CAP can be greatly

enhanced by using multiple receivers. At a representative BER of 10^{-5}, the SNR gain for increasing the number of receivers from 2 to 3, 4 and 5 are 4 dB, 11 dB and 13 dB, respectively. The results also validate the derived analytical expression for various values of N_{r}.

Figure 5.21 depicts the performance of GS-CAP for $\Omega = \langle 5 \rangle_{N_{\mathrm{a}}}^{16}$ for $N_{\mathrm{a}} = 2, 3$ and 4. It shows that to maintain a fixed BER performance, additional power is required when the number of active LEDs is increased. For example, at a representative BER of 10^{-5}, increasing N_{a} from 2 to 3 and 4 requires extra SNR of 4 dB and 6 dB, respectively.

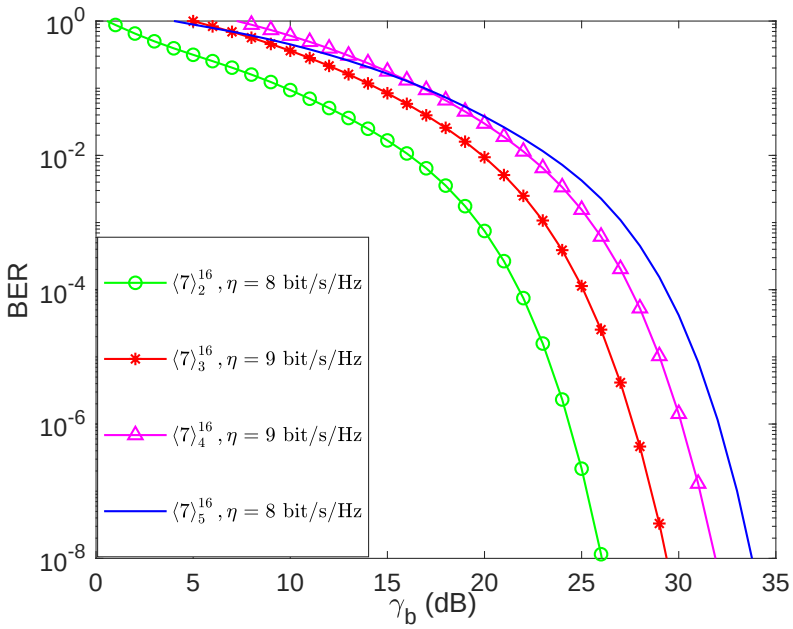

Figure 5.22: Choosing the number of active LEDs, N_a, for a target spectral efficiency, η in a GS-CAP system.

However, since the spectral efficiency (η) of GS-CAP can only be enhanced through spatial domain by increasing N_{a}, the optimum N_{a} should be used to achieve high power efficiency. The results of Fig. 5.22 shows the optimum N_{a} for a particular η. For configurations $\Omega = \langle 7 \rangle_2^{16}$ and $\Omega = \langle 7 \rangle_5^{16}$, even though both have the same $\eta = 8$ bits/s/Hz, the case of $N_{\mathrm{a}} = 5$ has a power penalty of 8 dB in comparison to $N_{\mathrm{a}} = 2$ at a representative BER of 10^{-5}. Similarly, for $\eta = 9$ bits/s/Hz and at the same representative BER of 10^{-5}, the Ω with $N_{\mathrm{a}} = 4$ has power penalty of 2.5 dB in comparison to Ω with $N_{\mathrm{a}} = 3$. Therefore, it can be concluded that to achieve optimum power efficiency for a target BER and η, the Ω with the smaller N_{a} should be

implemented.

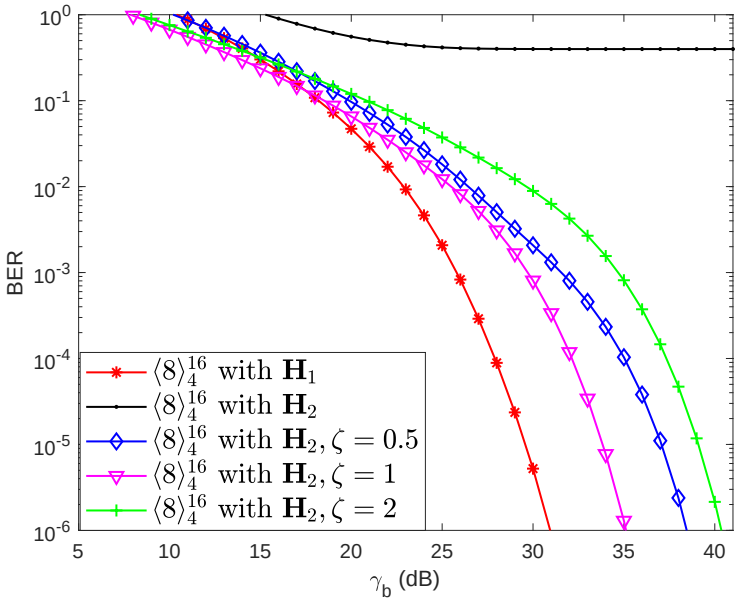

Figure 5.23: Impact of channel gain similarity of the BER performance of GS-CAP and the use of PFI to restore dissimilarity.

In order to investigate the impact of receiver mobility on the BER performance of GS-CAP, the channel gain matrix $\mathbf{H}_2$ is obtained by placing all the receivers along the centre of the room. This results in weak received signals from the transmitters. The results of Fig. 5.23 depict the performance comparison of GS-CAP in $\mathbf{H}_1$ and $\mathbf{H}_2$ using configuration $\Omega = \langle 8 \rangle_4^{16}$. While GS-CAP requires an SNR of 29.5 dB to achieve a BER of 10^{-5} in $\mathbf{H}_1$, the receiver positions that correspond to $\mathbf{H}_2$ result in complete breakdown of the communication link with an error floor of 0.5. To improve performance in this situation, PFI can be employed for redistributing power on the channel links. The result of applying PFI is also shown in Fig. 5.23 where GS-CAP achieves the BER of 10^{-5} at an SNR of 37 dB with $\mathbf{H}_2$ using $\lambda = 0.5$ dB. Further improvement is achieved using $\lambda = 1$ dB as GS-CAP only requires 34 dB for the same BER of 10^{-5}. This is a significant improvement in comparison to the error floor previously achieved without the use of PFI. Therefore, PFI is an effective precoding technique for improving the performance of GS-CAP in poor channel conditions. No further improvement is achieved by increasing the λ beyond 1 dB as shown by the result of $\lambda = 2$ dB. This is because further increase in PFI leads to disproportionate induced power imbalance which reduces the SNR on

Table 5.6: Channel gains for different constellation points.

LED Transmitter	Channel gains $\mathbf{h}$	$\mathcal{S}_{\mathrm{u}}^{\mathrm{sub}}$	ϑ^{sub}	$\mathcal{S}_{\mathrm{u}}^{\mathrm{opt}}$	ϑ^{opt}
LED1	1	$1,2$	1.6931	$1,2$	1.6931
LED2	0.6931	$1,3$	1.3268	$2,3$	1.0199
LED3	0.3268	$1,4$	1.3486	$3,4$	0.6758
LED4	0.3486	$2,3$	1.0199	$1,3$	1.3268

some of the links thus resulting in BER degradation.

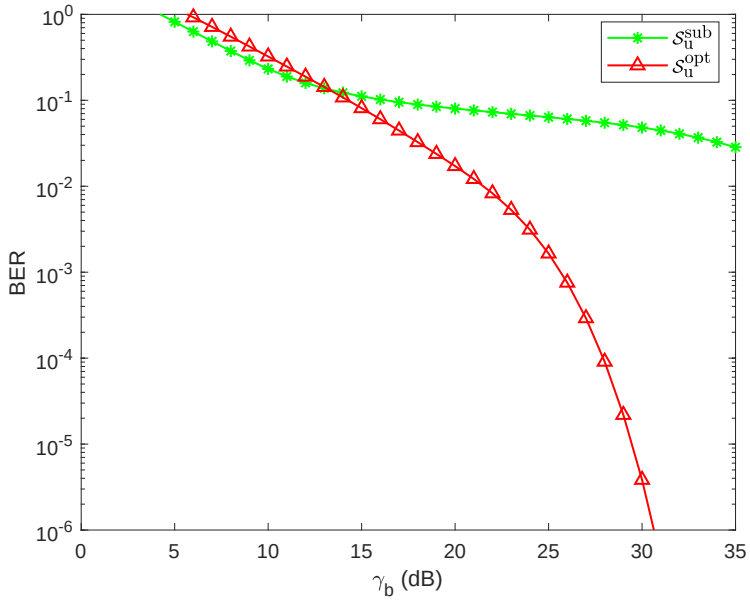

Figure 5.24: BER performance of GS-CAP using the optimal ($\mathcal{S}_u^{opt}$) and sub-optimal ($\mathcal{S}_u^{sub}$) constellation set with $\Omega = \left\langle {4 \atop 1} \right\rangle_2^{16}$.

Since the performance of GS-CAP depends on the channel gains, the specific set of used spatial constellations denoted as $\mathcal{S}_{\mathrm{u}}$ selected from the total possible set $\mathcal{S}$ will also influence performance. The size of $\mathcal{S}$ and $\mathcal{S}_{\mathrm{u}}$ are N and N_{u}, respectively. Using $\Omega = \left\langle {4 \atop 1} \right\rangle_2^{16}$, an optimal and a sub-optimal approach of selecting the entries of $\mathcal{S}_{\mathrm{u}}$ are shown in Table 5.6. The sub-optimal selection, which results in the constellation set $\mathcal{S}_{\mathrm{u}}^{\mathrm{sub}}$ with the corresponding effective channel gain ϑ^{sub}, is done without giving any consideration to the similarities in the effective channel gains. On the other hand, the entries of the optimum set $\mathcal{S}_{\mathrm{u}}^{\mathrm{opt}}$ with the corresponding effective channel gain ϑ^{opt} are selected by choosing the constellation points whose effective channel gains are dissimilar. The performance of GS-CAP using the two sets

is presented in Fig. 5.24. The figure shows that while GS-CAP performance results in error floor when using the sub-optimal set, the use of the optimal set results in a BER of 10^{-5} at an SNR of 29 dB. This result highlights the importance of selecting an optimal constellation set for GS-CAP system.

5.4 Summary of Chapter 5

Spatial carrierless amplitude and phase modulation (S-CAP) has been developed as a low-complexity, spectrally-efficient scheme for visible light communication system. The S-CAP improves the spectral efficiency of the conventional CAP scheme by a factor of $\log_M(MN_{\mathrm{t}})$. An analytical expression for the BER performance of S-CAP in LOS propagation is derived and verified via simulation. It is found that the BER performance of S-CAP in LOS propagation is dictated by the minimum of the channel gains $h_{\min}$, the signal constellation points, SCP and the channel dissimilarity, $\Delta|h|$. While in multipath propagation, the channel RMS delay spread τ_{rms} overrides the influence of $h_{\min}$. The impact of multipath propagation due to second-order reflections on the performance of S-CAP is also reported. Considering user mobility across the room at the FEC BER limit of 3×10^{-3}, multipath propagation results in up to 30 dB SNR penalty in some parts of the room. Both power factor imbalance (PFI) and the use of multiple photodiode receivers (multiple PDs) are then introduced as performance enhancing techniques. PFI is found to be very effective in improving performance for LOS scenario resulting in SNR gain of 33.5 dB for PFI $=$ 2 dB while it is largely ineffective in multipath scenario when the performance is dominated by high τ_{rms}. In contrast, multiple PDs are able to significantly improve the performance of S-CAP in both LOS and multipath channels leading to 43 dB SNR gain with the use of four PDs.

Generalised spatial carrierless amplitude and phase modulation (GS-CAP) is also developed to improve on the spectral efficiency of S-CAP. The theoretical analysis for the BER performance of the GS-CAP is presented and shown to be in excellent agreement with the simulation results for various system parameters. It is found that for different GS-CAP system configurations with the same spectral efficiency, the configuration with the lowest number of active LEDs results in optimum power efficiency (SNR) and BER performance. It is also shown that while the GS-CAP performance degrades due to receiver mobility, PFI precoding technique can be employed to significantly improve its performance.

Chapter 6

Subband Index CAP Modulation (SI-CAP)

The challenge with the MIMO and spatial approaches that are developed in chapters 4 and 5 for CAP modulation is that they require distinct channel gains for optimal performance and this might not be available especially for mobile VLC systems [169]. As an alternative, the available link bandwidth can be subdivided to realise multi-band CAP (m-CAP) with improved tolerance towards channel non-linearity effect [24, 116]. The m-CAP scheme has been experimentally demonstrated to offer improved BER performance for optical communication systems [24, 25]. Despite its BER improvement, the m-CAP scheme does not improve the spectral efficiency of the conventional CAP system. In addition, m-CAP suffers the same high PAPR problem inherent in multi-carrier systems. Therefore, subband index CAP (SI-CAP) is introduced in this chapter to improve on the spectral and energy efficiency of the m-CAP system.

The SI-CAP works by modulating some of the subbands (termed active subbands) of m-CAP with data symbols. It then make up on the lost spectral efficiency by encoding additional bits in the selection of the active/inactive subband indices. Additionally, a detection scheme is developed for SI-CAP that achieves maximum likelihood (ML) performance at lower complexity. Furthermore, as will be shown, a proper configuration of the SI-CAP system parameters results in higher throughput beyond the maximum $\log_2(M)$ bits per channel use (bpcu) possible in m-CAP. The performance gain of SI-CAP is demonstrated using theoretical analysis, simulations and experimental demonstrations in both VLC and SI-POF. An adaptive equalization technique is further implemented which results in higher gain for the proposed SI-CAP.

During each symbol duration, the SI-CAP scheme transmits unique M-QAM symbol on each N_{a} active subbands out of the total N subbands available. Though, there are ${}^{N}C_{N_{\text{a}}}$ possible

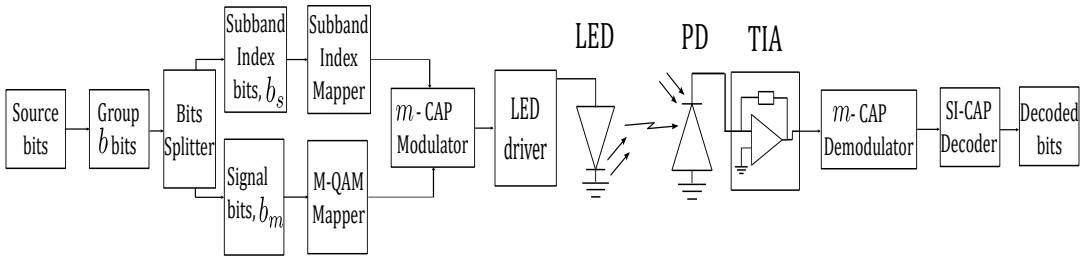

Figure 6.1: The schematic block diagram of the proposed SI-CAP transceiver for VLC link.

combinations/ways for selecting N_{a} out of N, only $N_{\mathrm{u}} = 2^{\lfloor \log_2 \left({}^{N}C_{N_{\mathrm{a}}} \right) \rfloor}$ combinations can be employed for carrying information bits where $\lfloor \cdot \rfloor$ is the floor function. Thus, the total number of bits that can be encoded in the subband domain of the proposed SI-CAP is $\log_2(N_{\mathrm{u}})$. The performance gain of the developed SI-CAP is investigated through analysis and validated using simulation and experimental demonstrations in optical communication systems.

6.1 Model Description of SI-CAP

The proposed SI-CAP system configuration is represented as $\Omega = \left\langle {N \atop N_{\mathrm{a}}} \right\rangle_{M}^{\mathcal{T}}$ where N, N_{a}, M and $\mathcal{T}$ respectively represent the total number of subbands, number of active subbands, QAM constellation order, and the transmission efficiency of the system in bpcu. The transmission efficiency $(\mathcal{T})$ is defined as the number of bits per symbol divided by the number of subbands. The previously described m-CAP can be regarded as a special case of SI-CAP where N_{a} = N. In order to generate the SI-CAP signal, the total b bits to be transmitted is split into two groups consisting of the symbol bits, $b_{\mathrm{m}} = N_{\mathrm{a}} \log_2(M)$ and the subband bits, $b_{\mathrm{s}} = \log_2(N_{\mathrm{u}})$ as shown in Fig. 6.1. The b_{s} bits are then used to select the appropriate subband indices, $S_{n_{\mathrm{u}}}$, out of the total possible set, $\mathcal{S}$. The set $\mathcal{S} = \{S_{n_{\mathrm{u}}}\}_{n_{\mathrm{u}}=1}^{N_{\mathrm{u}}}$ can also be referred to as the subband constellation while $S_{n_{\mathrm{u}}} = \left\{S_{n_{\mathrm{u}}}^{n_{\mathrm{a}}}\right\}_{n_{\mathrm{a}}=1}^{N_{\mathrm{a}}}$ can be referred to as the subband symbol. The b_{m} bits are then mapped to the subbands corresponding to $S_{n_{\mathrm{u}}}$ while zeros are placed on the remaining subbands i.e the remaining subbands are not modulated with data symbols.

The process of generating SI-CAP signal is illustrated with an example as follows: consider a total of 4 subbands in which 2 are active. There are 6 (that is, ${}^{4}C_{2}$) different ways or combinations of selecting the 2 active subbands, out of which only $N_{\mathrm{u}} = 4$ (that is, $2^{\lfloor \log_2 \left({}^{4}C_{2} \right) \rfloor}$) can be chosen. Thus, $b_{\mathrm{s}} = 2$ bits can be encoded in the selection of the $N_{\mathrm{u}} = 4$ subband

Table 6.1: SI-CAP mapping process for $\Omega = \left\langle {4 \atop 2} \right\rangle_4^{1.5}$

Possible subband constellation	b_{s} bits	Selected subband constellation, $\mathcal{S}$	Signal bits	Signal constellation, $\mathcal{M}$
$1,2$	00	$1,2$	00	$+1+j$
$1,3$	01	$1,3$	01	$-1+j$
$1,4$	10	$1,4$	10	$-1-j$
$2,3$	11	$2,3$	11	$+1-j$
$2,4$				
$3,4$				

combinations. The active subbands corresponding to the chosen combination are then encoded with data symbols from QAM constellation. For this example, the system configuration is $\Omega = \left\langle {4 \atop 2} \right\rangle_4^{1.5}$. To transmit bits $b = \text{`}011001'$, the first $b_{\text{s}}$ bits, `$01'$, is used for selecting the $S_{n_{\text{u}}}$ which corresponds to $S_2 = \{1,3\}$ using Table 6.1. This means that only the 1st and 3rd subbands will carry information while no information will be carried on the 2^{nd} and 4^{th} subbands. Notice that the entries of $\mathcal{S}$ have been arbitrarily selected from the total number of possible combinations. The remaining b_{m} bits, `$1001'$, is then used to select the appropriate QAM symbols from the QAM constellation, $\mathcal{M}$, which in this case correspond to symbol $-1-j$ and $-1+j$. Thus, the signal sent to the m-CAP modulator is

$$\mathbf{x} = \begin{bmatrix} -1-j & 0 & -1+j & 0 \end{bmatrix}^T. \tag{6.1}$$

The transmission efficiency of SI-CAP can thus be expressed as:

$$\mathcal{T}_{\text{SI-CAP}} = \frac{b_{\text{s}} + b_{\text{m}}}{N} \tag{6.2}$$

$$= \frac{\left\lfloor \log_2 \left({}^4C_2 \right) \right\rfloor + N_{\text{a}} \log_2(M)}{N}. \tag{6.3}$$

Both the transmission efficiency of SI-CAP and m-CAP are compared and shown in Fig. 6.2 for $M = 4$ and 16. The figure shows that $\mathcal{T}_{\text{SI-CAP}}$ exceeds the maximum limit of $\log_2(M)$ possible for $\mathcal{T}_{m\text{-CAP}}$. It can also be deducted from the Fig. 6.2 that the condition $N \geq M$ has to be satisfied for $\mathcal{T}_{\text{SI-CAP}}$ to be equal to $\mathcal{T}_{m\text{-CAP}}$. This is shown by circles in Fig. 6.2 for $M = 4$ and 16. Due to the condition $N \geq M$, the number of subbands required for SI-CAP to improve on $\mathcal{T}_{m\text{-CAP}}$ increases with increasing M. This requirement increases the complexity of the resulting system for high value of M.

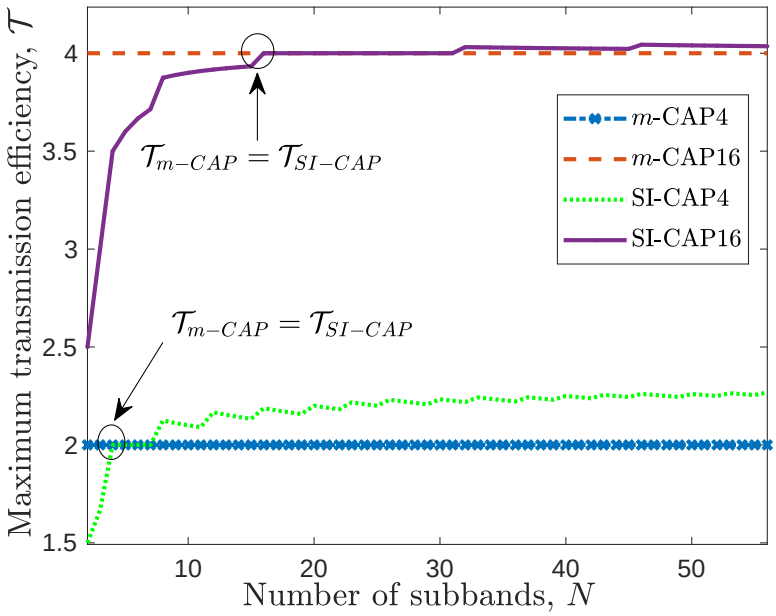

Figure 6.2: The maximum transmission efficiency, $\mathcal{T}$, in bpcu achievable by SI-CAP and m-CAP as number of subbands, N, increases.

6.2 Performance Analysis of Detection Schemes for SI-CAP

Due to the extra bits carried by the index of the SI-CAP subbands, the conventional m-CAP detector can not be successfully applied. Therefore, three detectors are investigated for the proposed SI-CAP scheme. The received SI-CAP signal at the output of the m-CAP demodulator, considering line-of-sight (LOS) channel gain h, can be expressed as:

$$\mathbf{y} = \xi \mathfrak{R} \mathcal{K} \beta h \mathbf{x}_{n_\mathrm{u}}^m + \mathbf{w} \tag{6.4}$$

where y_n, $x_{n_\mathrm{u},n}^m$ and w_n are the components of the $N \times 1$ vectors $\mathbf{y}$, $\mathbf{x}_{n_\mathrm{u}}^m$ and $\mathbf{w}$, respectively. The $x_{n_\mathrm{u},n}^m$ is the symbol transmitted on the n^{th} subband and is either zero or belongs to one of the M-QAM symbols as shown in (6.1). The $\xi = N/N_\mathrm{a}$ is the scaling factor required to keep the total transmit optical power constant irrespective of the system configuration. The received signal in (6.4) can be re-written as

$$\mathbf{y} = \boldsymbol{\zeta}_{n_\mathrm{u}}^m + \mathbf{w} \tag{6.5}$$

where $\boldsymbol{\zeta}_{n_\mathrm{u}}^m = \xi \mathfrak{R} \mathcal{K} \beta h \mathbf{x}_{n_\mathrm{u}}^m$.

6.2.1 BER Derivation for Maximum Likelihood Detector (MLD)

The performance analysis of the proposed SI-CAP is derived based on the ML detector. The MLD is the optimum detector for SI-CAP considering the fact that its symbols, $\left\{\mathbf{x}_{n_\mathrm{u}}^m\right\}$, are equiprobable with $p(\mathbf{x}_{n_\mathrm{u}}^m) = 1/N_\mathrm{u}M^{N_\mathrm{a}}$. As a result, the decision criteria for MLD can be expressed as [170]:

$$\hat{\mathbf{x}}_{n_\mathrm{u}}^m = \arg\max_{n_\mathrm{u},m} p(\mathbf{y}, \boldsymbol{\zeta}_{n_\mathrm{u}}^m) \tag{6.6}$$

where

$$p(\mathbf{y}, \boldsymbol{\zeta}_{n_\mathrm{u}}^m) = \frac{1}{(2\pi N_0)^{N/2}} \exp\left[-\frac{\left\|\mathbf{y} - \boldsymbol{\zeta}_{n_\mathrm{u}}^m\right\|^2}{2N_0}\right] \tag{6.7}$$

due to the AWGN channel. The criterion in (6.6) can be reduced to

$$\hat{\mathbf{x}}_{n_\mathrm{u}}^m = \arg\min_{n_\mathrm{u},m} D(\mathbf{y}, \boldsymbol{\zeta}_{n_\mathrm{u}}^m) \tag{6.8}$$

where

$$D(\mathbf{y}, \boldsymbol{\zeta}_{n_\mathrm{u}}^m) = \left\|\mathbf{y} - \boldsymbol{\zeta}_{n_\mathrm{u}}^m\right\|^2. \tag{6.9}$$

The MED criterion of (6.8) becomes

$$D(\mathbf{y}, \boldsymbol{\zeta}_{n_\mathrm{u}}^m) = \|\mathbf{w}\|^2 \tag{6.10}$$

in case the detector makes the correct decision, otherwise

$$D(\mathbf{y}, \tilde{\boldsymbol{\zeta}}_{n_\mathrm{u}}^m) = \left\|\boldsymbol{\zeta}_{n_\mathrm{u}}^m - \tilde{\boldsymbol{\zeta}}_{n_\mathrm{u}}^m - \mathbf{w}\right\|^2. \tag{6.11}$$

Using (6.10) and (6.11), the PEP of SI-CAP can be derived as:

$$\begin{aligned}
\mathrm{PEP}_{\text{SI-CAP}} &= p(\mathbf{x}_{n_\mathrm{u}}^m \to \tilde{\mathbf{x}}_{n_\mathrm{u}}^m) \\
&= p(D(\mathbf{y}, \boldsymbol{\zeta}_{n_\mathrm{u}}^m) > D(\mathbf{y}, \tilde{\boldsymbol{\zeta}}_{n_\mathrm{u}}^m)) \\
&= Q\left(\sqrt{\frac{(\xi\Re\mathcal{K}\beta)^2}{2N_0}\left\|h\left(\mathbf{x}_{n_\mathrm{u}}^m - \tilde{\mathbf{x}}_{n_\mathrm{u}}^m\right)\right\|^2}\right).
\end{aligned} \tag{6.12}$$

The PEP of (6.12) is used to obtain an upper bound on the BER of SI-CAP, as shown in (6.13), by considering all possible $N_\mathrm{u}M^{N_\mathrm{a}}$ symbol combinations using union bound technique.

Though the optimum detector for SI-CAP is MLD, its computational complexity is prohibitive as it searches $N_\mathrm{u}M^{N_\mathrm{a}}$ symbol combinations in order to make decision. As a result, two lower

$$\text{BER}_{\text{SI-CAP}} \leq \frac{1}{N_{\text{u}} M^{N_{\text{a}}} \log_2(N_{\text{u}} M^{N_{\text{a}}})} \sum_{n_{\text{u}}=1}^{N_{\text{u}}} \sum_{m=1}^{M^{N_{\text{a}}}} \sum_{\tilde{n}_{\text{u}}=1}^{N_{\text{u}}} \sum_{\tilde{m}=1}^{M^{N_{\text{a}}}} \mathcal{N}_H(b_{mn_{\text{u}}}, \tilde{b}_{mn_u}) \\ Q\left(\sqrt{\frac{(\xi \Re \mathcal{K} \beta)^2}{2N_0} \left\| h\left(\mathbf{x}_{n_{\text{u}}}^m - \tilde{\mathbf{x}}_{n_{\text{u}}}^m\right)\right\|^2}\right). \quad (6.13)$$

complexity detectors are further investigated.

6.2.2 SI-CAP with Log-Likelihood Ratio Detector (LLR)

The LLR computes the logarithm of the ratio between the a *posteriori* probabilities of the SI-CAP symbols in each subband considering the fact that they are either zero or drawn from $\mathcal{M}$. Thus, the LLR is formulated as [170]:

$$\chi_n = \ln \frac{\sum_{i=1}^{M} \text{Pr}(x_n = \mathfrak{m}_i | y_n)}{\text{Pr}(x_n = 0 | y_n)} \quad (6.14)$$

where $\mathfrak{m}_i \in \mathcal{M}$. Using Bayes' theorem, (6.14) can be written as:

$$\chi_n = \ln \frac{\sum_{i=1}^{M} \text{Pr}(y_n | x_n = \mathfrak{m}_i) \text{Pr}(x_n = \mathfrak{m}_i)}{\text{Pr}(y_n | x_n = 0) \text{Pr}(x_n = 0)}. \quad (6.15)$$

Given the AWGN corrupted channel,

$$\text{Pr}(y_n | x_n = \mathfrak{m}_i) = \frac{1}{(2\pi N_0)^{1/2}} \exp\left[-\frac{|y_n - \mathfrak{m}_i h_n|^2}{2N_0}\right] \quad (6.16)$$

while

$$\text{Pr}(y_n | x_n = 0) = \frac{1}{(2\pi N_0)^{1/2}} \exp\left[-\frac{|y_n|^2}{2N_0}\right]. \quad (6.17)$$

Therefore, considering the fact that $\text{Pr}(y_n | x_n = \mathfrak{m}_i) = N_{\text{a}}/N$ and $\text{Pr}(y_n | x_n = 0) = (N - N_{\text{a}})/N$, the expression in (6.15) can be expressed as:

$$\chi_n = \ln\left(\frac{N_{\text{a}}}{N - N_{\text{a}}}\right) + \frac{|y_n|^2}{N_0} + \ln\left(\sum_{i=1}^{M} \exp\left[-\frac{|y_n - \mathfrak{m}_i h_n|^2}{2N_0}\right]\right). \quad (6.18)$$

To avoid computational overflow when computing the last term of (6.18), the Jacobian logarithm is employed [171, 172]. The indices of the first N_{a} entries of the computed $\{\chi_n\}$ when sorted in descending order correspond to the indices of the active subbands, $S_{n_{\text{u}}}$. Thereafter, M-QAM decoder is used to decode the symbols on the detected active subbands.

It can be seen from (6.18) that the complexity of LLR is of $\mathcal{O}(NM)$, the same as the

conventional m-CAP. In addition, though the LLR is a near-ML decoder as it does not use all the possible combinations of symbols, it will be shown in the results section that it does achieve the same error rate performance as the MLD.

Finally, it is possible for LLR to detect some $S_{n_\text{u}} \notin \mathcal{S}$ when the noise variance is very high. In such cases, the detected indices can be randomly mapped to any entry of $\mathcal{S}$ since it is already an error event.

6.2.3 SI-CAP with Low Complexity Detector (LCD)

In comparison to MLD, the LLR achieves the same solution at significantly lower complexity. However, LLR requires the knowledge of the noise variance and is susceptible to computational overflow [170, 172]. In order to address these concerns, a novel low complexity detection (LCD) scheme is proposed. The LCD makes use of prior knowledge of the constellation by directly comparing the received symbol in each subband to the entries of $\mathcal{M}$. The formulation for LCD can be expressed as:

$$\boldsymbol{\lambda}_{n,i} = \min_{i} |y_n - \mathfrak{m}_i h_n|^2. \tag{6.19}$$

The expression in (6.19) stores both the minimum value, λ_n and its corresponding index, $\lambda_{n,i}$. Consequently, the subbands corresponding to the first N_a entries of $\{\lambda_n\}$ when sorted in ascending order are chosen as the active subbands. In addition, the $\{\mathfrak{m}_i\}$ with $\{\lambda_{n,i}\}$ that correspond to those N_a entries are chosen as the symbols on the active subbands. Thus, it can be seen that the complexity of LCD is also of $\mathcal{O}(NM)$ but with less number of computations in comparison with LLR. This is because the LCD of (6.19) only computes a part of the last term of (6.18) to complete its detection process. Whereas, the LLR detection still require M-QAM decoding after evaluating all the terms in (6.18). Furthermore, the LCD is not susceptible to computational overflow like LLR and does not contain the noise variance in its expression. In addition, LCD achieves the same performance as the ML and LLR detectors.

However, the LCD is also liable to decide on some $S_{n_\text{u}} \notin \mathcal{S}$. In such cases, the random mapping solution employed for LLR is implemented.

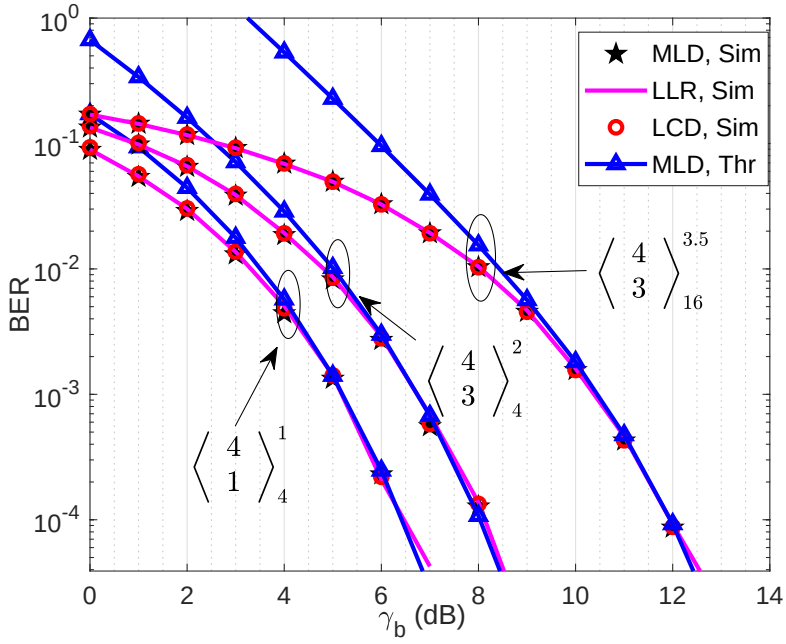

Figure 6.3: Comparison of the performance of SI-CAP detectors and validation of the derived analysis using different system configurations. Sim: Simulation; Thr: Theoretical analysis

6.3 Simulation Results and Discussions

In the results presented in this section, the electrical SNR per bit is defined as $\gamma_b = \frac{(\xi \Re\mathcal{K}\beta)^2}{\mathcal{T} N_0}$ where $\mathcal{T}$ is $\log_2(M)$ for m-CAP and it is as defined in (6.3) for SI-CAP [153].

The theoretical expression obtained for SI-CAP is validated in Fig. 6.3 using different M-QAM constellations and system configurations. The analysis shows excellent match with the simulation for both $\mathcal{T} = 1$, 2 and 3.5 bpcu. At BER of 10^{-4}, the proposed SI-CAP requires γ_b of 6.5, 8 and 12 dB to achieve transmission efficiencies of 1, 2 and 3.5 bpcu, respectively. It is also shown that the LLR achieves the same performance as the MLD at a reduced complexity. Similarly, the LCD also achieve the same performance as the MLD but at reduced number of computations in comparison to LLR. Furthermore, the LCD is not susceptible to computational overflow and does not require the knowledge of the noise variance. Hence, it can be concluded that the LCD is the best detection scheme in terms of performance and complexity considerations for the proposed SI-CAP. Also, it can be inferred that the same analysis for MLD is valid for both LLR and LCD since both detectors achieve

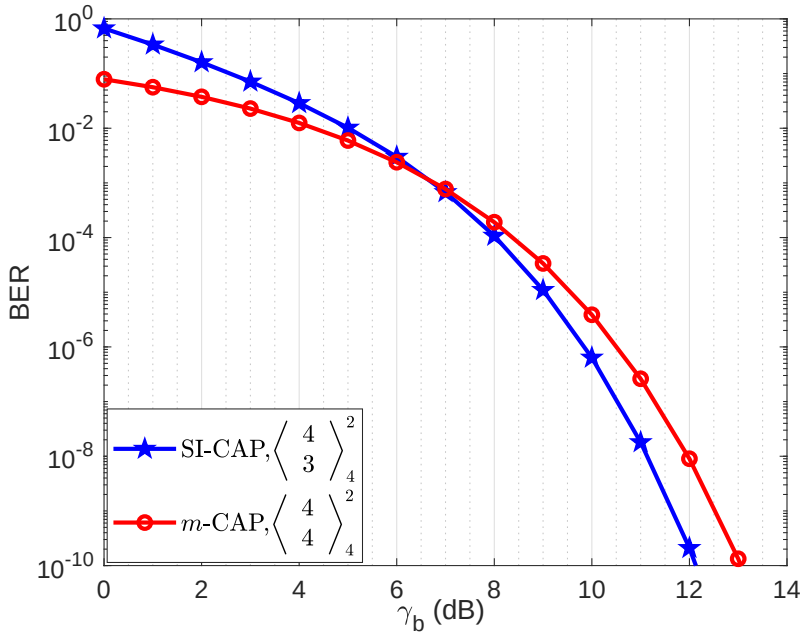

Figure 6.4: The BER performance comparison of SI-CAP and m-CAP in AWGN channel, $\mathcal{T} = 2$ bpcu.

the same performance as MLD.

The BER performance of the proposed SI-CAP and the conventional m-CAP in AWGN channel is shown in Fig. 6.4 for $\mathcal{T} = 2$ bpcu. The SI-CAP has a performance gain of about 1 dB over m-CAP at high SNR. This shows the power efficiency of SI-CAP over the conventional m-CAP. The figure also shows that SI-CAP has a slight performance loss at low SNR which might be attributed to its joint detection of both the subband index and symbol bits as compared to only the symbol bits in m-CAP. The joint detection might result in error propagation as an erroneous detection of the active subband will most likely result in symbol bits error. However, SI-CAP achieves better performance at high SNR when the likelihood of error propagation reduces.

The effect of bandwidth-limited LED employed in VLC on SI-CAP and m-CAP is investigated using a first-order low pass filter (LPF) model for the LED response [25]. The 3 dB cut-off frequency of the LPF is set as 10 MHz. The result is shown in Fig. 6.5 by comparing the γ_b required to achieve BER of 10^{-5} for a range of data rate, R_b. It is shown that the proposed SI-CAP has better performance than the conventional m-CAP as it requires lower γ_b

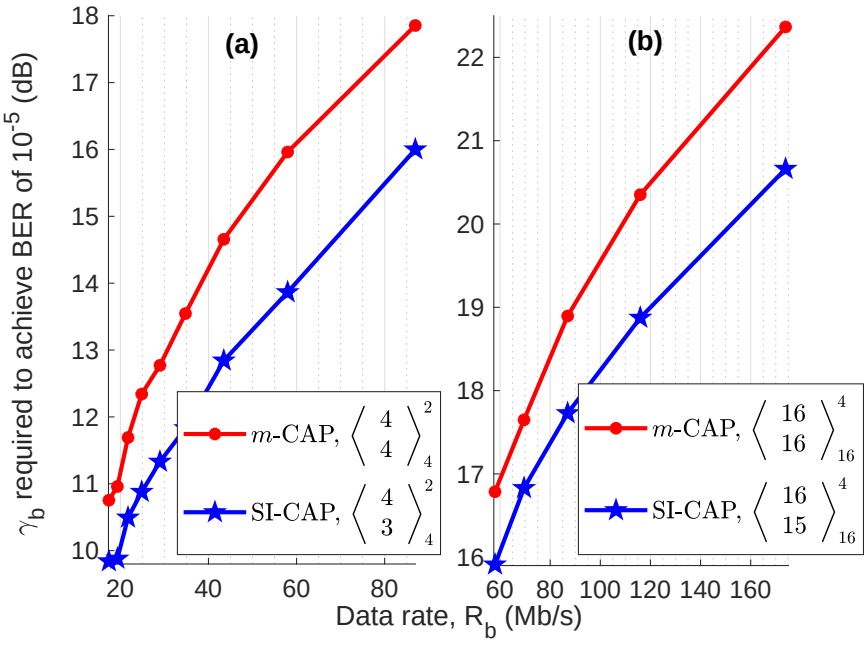

Figure 6.5: Comparison of the γ_b required by SI-CAP and m-CAP to achieve BER of 10^{-5} at varying R_b in a VLC system modelled using a first-order low pass filter with a 10 MHz 3 dB cut-off frequency, $\mathcal{T} = 2$ and 4 bpcu.

to achieve the same data rate. For example, to achieve BER of 10^{-5} at $R_\mathrm{b} = 50$ Mb/s, SI-CAP requires about 13.2 dB compare to 15.7 dB required by m-CAP as shown in Fig. 6.5 (a). This results in an γ_b gain of 2.5 dB for SI-CAP over m-CAP. Alternatively, with an γ_b of 15 dB, SI-CAP achieves R_b of 74 Mb/s in comparison to 47.5 Mb/s achieved by m-CAP which leads to 26.5 Mb/s improvement in R_b. The SI-CAP maintains its performance gain at higher constellation and data rate as shown in Fig. 6.5 (b) using $M = 16$ to achieve $\mathcal{T} = 4$ bpcu. From the Fig. 6.5 (b), the γ_b required by SI-CAP to achieve $R_\mathrm{b} = 150$ Mb/s is 1.6 dB less than that of m-CAP. This illustration shows the power/spectral efficiency gain of SI-CAP over the conventional m-CAP. The performance gain shown by the simulations is further validated through experimental demonstrations in section 6.4.

The CCDF of the electrical PAPR of SI-CAP and m-CAP is investigated and shown in Fig. 6.6. Though Fig. 6.6 shows that both SI-CAP and m-CAP exhibit comparable PAPR, a closer observation reveals that the PAPR of SI-CAP is marginally better especially in the region of interest for m-CAP. For example, the probability that the PAPR will exceed 9 dB is 6×10^{-4} and 3.5×10^{-3} respectively for SI-CAP and m-CAP using 4-QAM with $N = 4$ and $\mathcal{T} = 2$ bpcu.

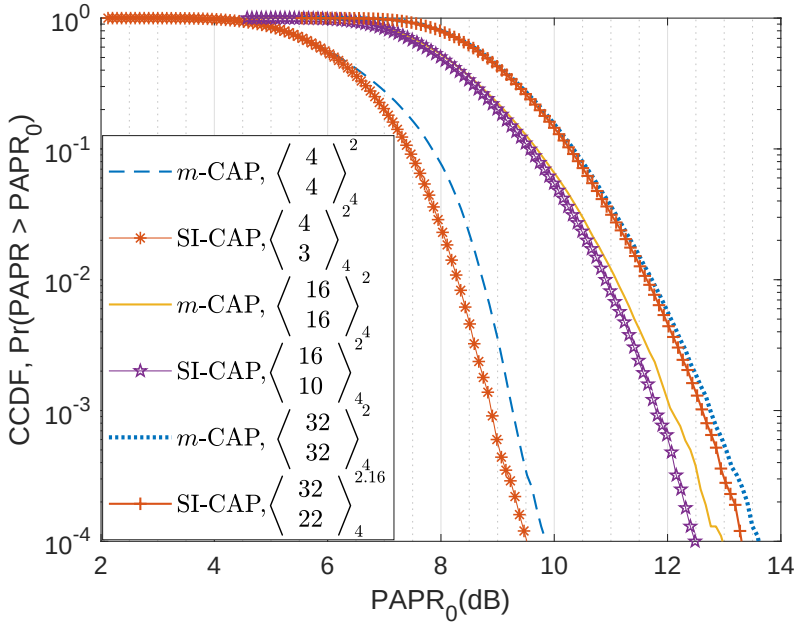

Figure 6.6: The CCDF of the PAPR of SI-CAP and m-CAP for different number of subbands and transmission efficiencies.

This means that out of every $10,000$ symbols, only 6 are likely to have their PAPR exceed 9 dB for SI-CAP as opposed to 35 for m-CAP. The PAPR of the two schemes becomes similar as N increases. However, it has been experimentally demonstrated that performance gain obtained when number of subbands is increased for m-CAP is marginal while the complexity becomes significant [125, 173]. This makes the lower PAPR exhibited by SI-CAP at lower value of N desirable.

6.4 Experimental Validation of SI-CAP Performance

The performance of the proposed SI-CAP is validated through experimental demonstrations using both VLC and SI-POF links. The illustration of the experiment set-up is shown in Fig. 6.7 with a pictorial representation shown in Fig. 6.8. For the VLC link, a high brightness blue LED (OSRAM LDCN5M) is used with a -3 dB cut-off frequency of 10.9 MHz as shown in Fig. 6.9 [174]. This VLC link introduces ISI in the transmitted symbols at high data rate due to its limited modulation bandwidth. Similarly, the SI-POF link uses a 10 m SI-POF which introduces non-linearity effect as well as ISI. A resonant-cavity LED (RCLED, HAMAMATSU L10762) whose frequency response is shown in Fig. 6.9 is employed for the

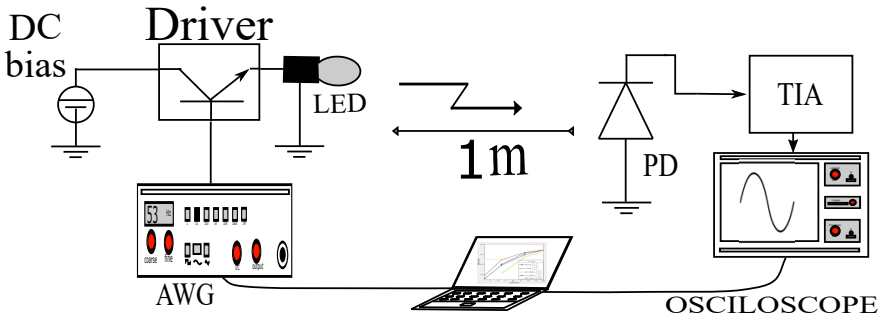

Figure 6.7: Illustration of the experimental demonstration set-up for SI-CAP.

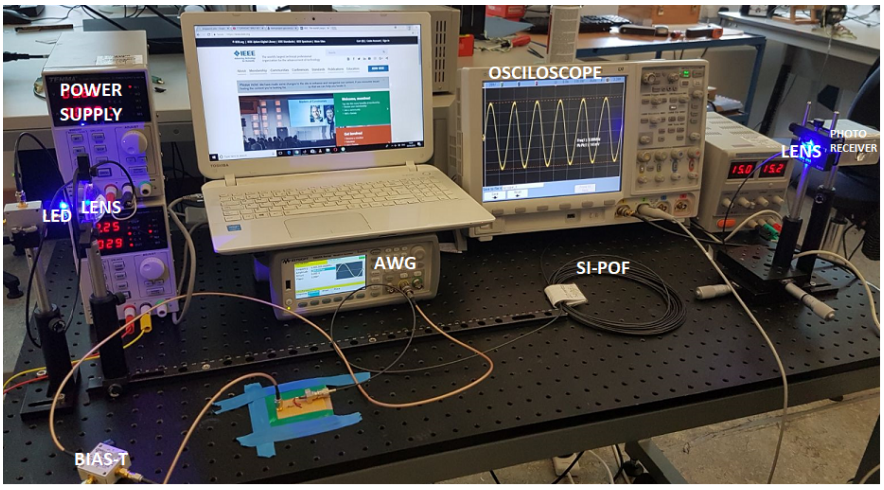

Figure 6.8: A pictorial representation of the experimental demonstration set-up in Fig. 6.7.

SI-POF demonstration [175].

Both the SI-CAP and m-CAP signals are generated offline on a computer and loaded onto an arbitrary waveform generator (AWG, Agilent 33600 series) that has a sample rate of 1 GSa/s and bandwidth of 120 MHz. The continuous waveform generated by the AWG is forwarded to a Bias-T where it is diplexed with a bias from a DC power supply to drive the optical source. Focussing lens are deployed at both the transmitting and receiving end of the VLC link to focus the data-bearing optical intensity on the receiving photodiode (PD). The PD, which is employed for both the VLC and SI-POF link, is a silicon PIN detector (THORLABS PDA10A(-EC)) with an active area of 0.8 mm^2, bandwidth of 150 MHz and a root mean square (RMS) noise of 1.5 mV [176]. It has responsivity, $\Re$, of 0.19 A/W and 0.41 A/W at the 460 nm and 660 nm of the blue LED and RCLED, respectively.

The received signal from the PD is captured in real time by an oscilloscope (Agilent 7000 B

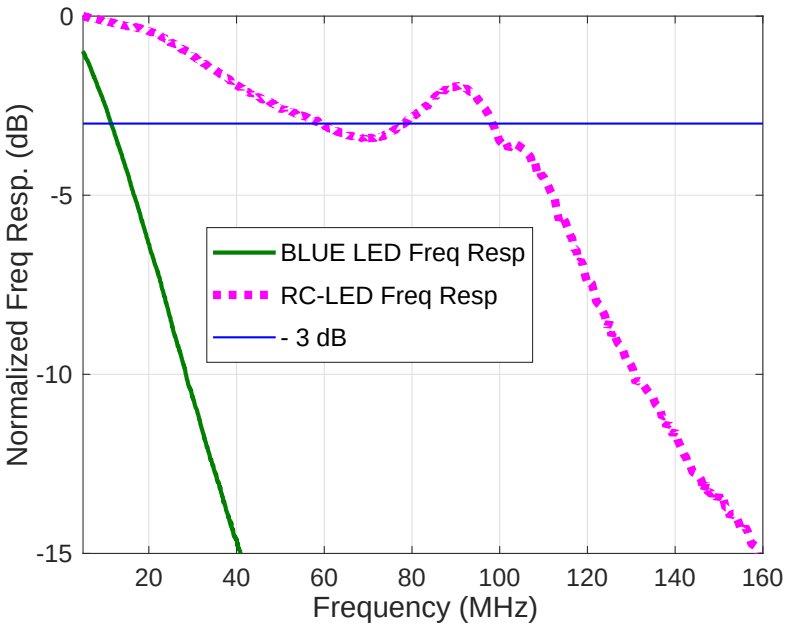

Figure 6.9: The measured normalized frequency responses of the Blue and RC-LED employed for VLC and SI-POF experimental demonstration.

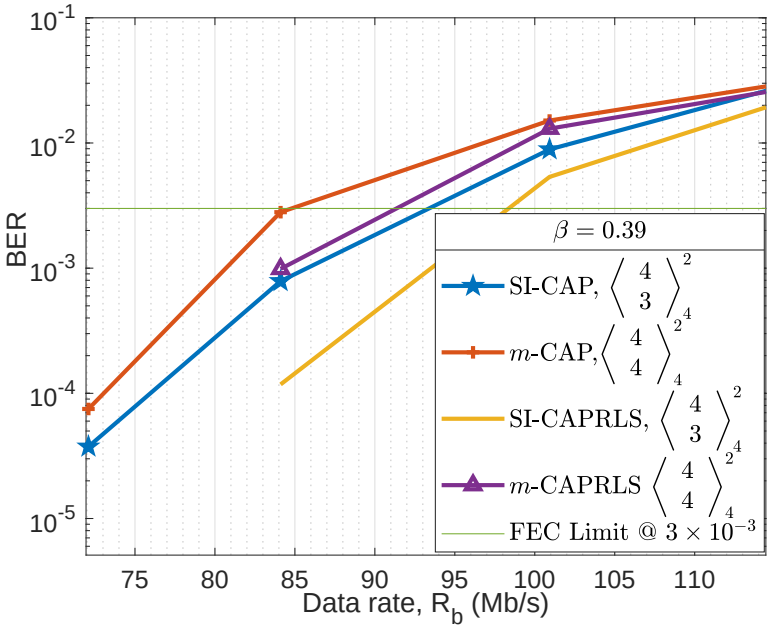

Figure 6.10: Experimental demonstration of the performance of SI-CAP and m-CAP over a VLC link with a bandwidth of 10.9 MHz and β of 0.39.

Series) with a maximum sample rate of 4 GSa/s and 1 GHz bandwidth. The signal is then processed offline using the SI-CAP and m-CAP receivers previously described. In addition, an

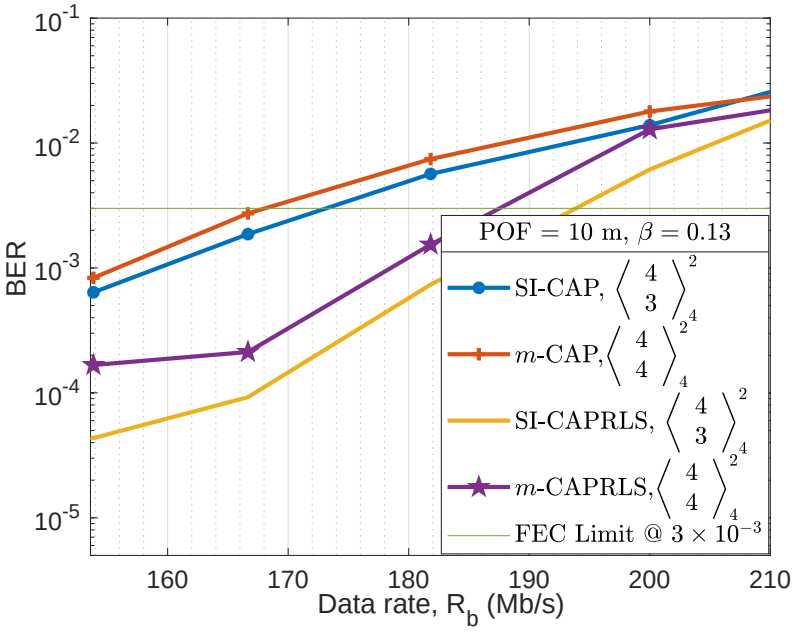

Figure 6.11: Experimental demonstration of SI-CAP and m-CAP over a 10 m SI-POF link employing RCLED with a bandwidth of 100 MHz and β of 0.13 (i.e. low SNR regime).

adaptive, symbol-spaced recursive least square (RLS) equalizer with 12 taps is implemented for the two schemes to further improve the achievable spectral efficiency.

6.4.1 Experimental Validation of SI-CAP in VLC

The performance of the two schemes in VLC system is presented in Fig. 6.10 along with the equalization results. The modulation index, β, of the transmitted signal is set at 0.39. The proposed SI-CAP has a better performance over the range of data rates investigated. At the FEC BER limit of 3×10^{-3}, the SI-CAP achieves $R_\mathrm{b} = 93.7$ Mb/s in comparison to 85 Mb/s achieved by m-CAP. This translates to data rate improvement of 8.72 Mb/s. At the same FEC limit, the RLS equalizer improves the R_b of both schemes by approximately 6.5 Mb/s with SI-CAP maintaining its performance advantage.

6.4.2 Experimental Validation of SI-CAP in SI-POF

To further show the versatility of SI-CAP, its performance is investigated in SI-POF link. The results are shown in Figs. 6.11 and 6.12 corresponding to $\beta = 0.13$ and 0.39, respectively. At $\beta = 0.13$ and the FEC BER limit, SI-CAP achieves R_b of 173 Mb/s in comparison to

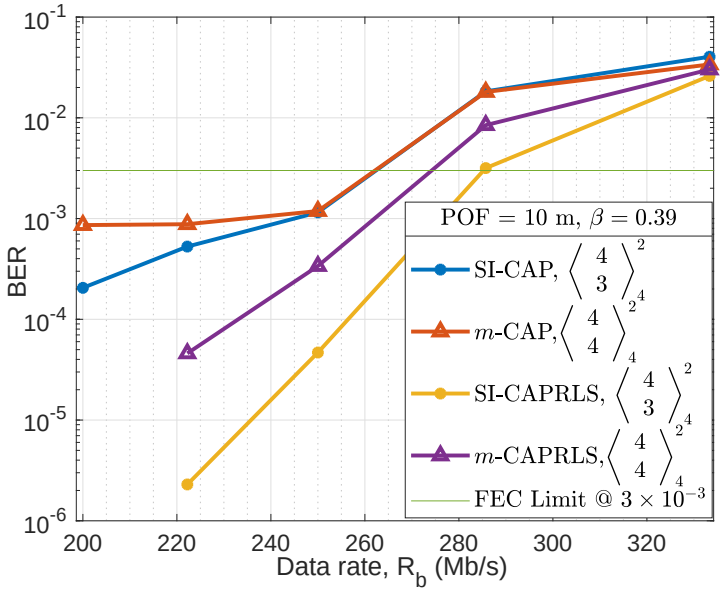

Figure 6.12: Experimental demonstration of SI-CAP and m-CAP over a 10 m SI-POF link employing RCLED with a bandwidth of 100 MHz and β of 0.39 (i.e. high SNR regime).

168 Mb/s by m-CAP. On implementation of RLS equalizer, the R_b of SI-CAP increases by 30 Mb/s while that of m-CAP increases by 18Mb/s. The performance of the two schemes are identical when the β increases to 0.39 with both achieving R_b of 262 Mb/s at the FEC BER limit. However, SI-CAP has a higher gain when RLS equalizer is applied as it achieves R_b improvement of 24 Mb/s in comparison to 12 Mb/s improvement achieved by m-CAP.

Constellation plots of the two schemes in SI-POF link are shown in Fig. 6.13 for the equalised and unequalised case with $\mathcal{T} = 2$ bpcu and $R_\mathrm{b} = 420$ Mb/s. The feedforward symbol-spaced RLS equalizer considered shows that the achievable gain of SI-CAP can be enhanced with equalization schemes. To further enhance the gain, decision feedback equalizers can also be implemented. However, these constellation plots highlight the distinct difference between SI-CAP and m-CAP signals. The plots show an extra level in the constellation of SI-CAP which corresponds to the zeros transmitted on the inactive subbands. This additional constellation point at the origin means the SI-CAP will require extra consideration when designing equalization schemes such as those with decision feedback configuration. This is because decisions on zeros, in addition to the QAM levels, will need to be fed back to the equalizer. Alternatively, different signal constellation pattern might be transmitted on the inactive subbands instead of zeros which will further enhance the transmission efficiency of

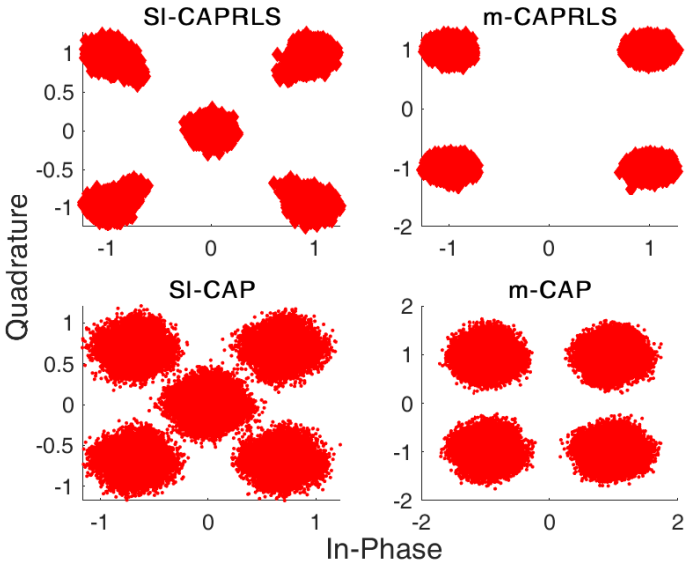

Figure 6.13: Constellation plots of the proposed SI-CAP and the conventional $m-$CAP before and after equalization in SI-POF link, $\mathcal{T} = 2$ bpcu, $R_b = 420$ Mb/s and $\beta = 0.39$.

the SI-CAP system by trading off the energy efficiency.

6.5 Summary of Chapter 6

A subband index carrierless amplitude and phase modulation scheme (SI-CAP) has been developed and investigated for optical communication systems in this chapter. The proposed SI-CAP not only modulate data symbols on the subbands of a multi-band CAP scheme, but also conveys additional information bits on the index of those subbands. A theoretical BER expression is derived for the proposed SI-CAP and validated through simulation. In addition, a new detection scheme that achieves ML solution at lower complexity is developed for the proposed SI-CAP. The SI-CAP performance is investigated for optical systems including VLC and SI-POF links through simulations and experimental demonstrations. It is shown that for the same spectral efficiency, SI-CAP requires lower SNR per bit to achieve the same BER performance as m-CAP. Alternatively, if the SNR per bit is fixed for both schemes, SI-CAP achieves a higher spectral efficiency. Furthermore, a feedforward adaptive RLS equalization scheme is implemented to further enhance the achievable gain of SI-CAP. Therefore, the superior performance of SI-CAP over the conventional m-CAP and its design flexibility make it a suitable candidate for optical communication systems.

Chapter 7

Enhanced SI-CAP (eSI-CAP) for Optical Communications Systems

The challenge in SI-CAP that is developed in chapter 6 is that the number of subbands required to achieve the same spectral efficiency as m-CAP increases as the constellation size, M, increases. This requirement results in increased complexity for SI-CAP when large constellation sizes are used. Consequently, an enhanced SI-CAP (eSI-CAP) which employs a dual constellation is developed in this chapter to address this challenge. In contrast to SI-CAP which nulls the inactive subbands by carrying no data symbols on them, eSI-CAP modulates them using symbols from a constellation other than the one employed for the active subbbands. As a result, eSI-CAP utilizes a dual distinguishable constellation $\mathcal{M}_{\mathrm{A}}$ and $\mathcal{M}_{\mathrm{B}}$ such that $\mathcal{M}_{\mathrm{A}} \cap \mathcal{M}_{\mathrm{B}} = \emptyset$ and $\mathcal{M}_{\mathrm{A}} \cup \mathcal{M}_{\mathrm{B}} = \mathcal{M}$. Thus, in addition to the index bits, the eSI-CAP modulates the active and the inactive subbands with symbols from $\mathcal{M}_{\mathrm{A}}$ and $\mathcal{M}_{\mathrm{B}}$, respectively. Therefore, eSI-CAP enhances the spectral efficiency of m-CAP for any number of subbands and constellation sizes without increasing the complexity of the resulting system.

In addition, an LCD that achieves similar BER performance as the MLD is developed for eSI-CAP. The performance gain of eSI-CAP is demonstrated in VLC and SI-POF links using theoretical analysis, simulations and experimental demonstrations.

7.1 Model Description of eSI-CAP

The proposed eSI-CAP achieves higher transmission efficiency than the conventional m-CAP by not only modulating information bits on all its subbands but also encoding additional bits on the index of those subbands. The block diagram of eSI-CAP model is shown in Fig. 7.1

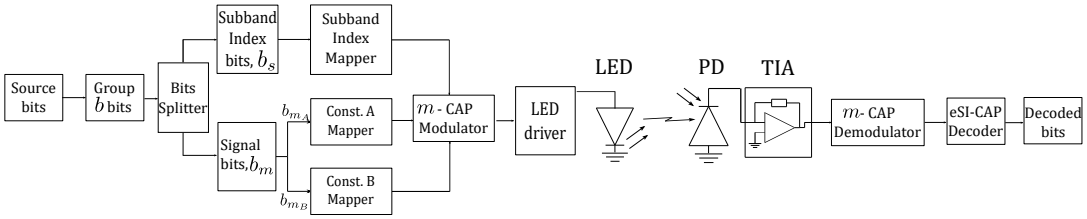

Figure 7.1: The schematic block diagram of the proposed eSI-CAP transceiver for VLC link.

for a VLC link. The stream of bits to be transmitted are grouped in blocks of b bits which is further divided into the subband index bits, b_{s} and signal bits, b_{m}. The b_{s} bits are used to select the indices of the N_{a} subbands, referred to as activated subbands, that carry symbols from constellation A ($\mathcal{M}_{\mathrm{A}}$). Unlike the SI-CAP scheme which nulls the remaining, $N_{\mathrm{b}} = N - N_{\mathrm{a}}$, unactivated subbands, the eSI-CAP modulates them with symbols drawn from constellation B ($\mathcal{M}_{\mathrm{B}}$). Thus, $b_{\mathrm{m}} = N_{\mathrm{a}}\log_2(M_{\mathrm{A}}) + N_{\mathrm{b}}\log_2(M_{\mathrm{B}})$ where M_{A} and M_{B} equal $|\mathcal{M}_{\mathrm{A}}|$ and $|\mathcal{M}_{\mathrm{B}}|$, respectively. Using the m-CAP modulator, the outputs of mappers A and B are modulated onto their corresponding subbands, as determined by b_{s} bits, before being sent over the transmission link. The received eSI-CAP signal is first passed through an m-CAP demodulator to recover the symbols on each subband and then through an eSI-CAP decoder to recover both the index and signal bits.

The BER performance of eSI-CAP is dependent on the design of its constellations $\mathcal{M}_{\mathrm{A}}$ and $\mathcal{M}_{\mathrm{B}}$. To achieve a good BER performance, the minimum Euclidean distance (MED) between the dual constellation should be similar to the separation of symbols in each constituent constellation [177]. One way to achieve this is to jointly design an $(M_{\mathrm{A}} + M_{\mathrm{B}})$-point constellation and then separate it into the individual constituents. For $M_{\mathrm{A}} = M_{\mathrm{B}} = 4$ considered in this work, Fig. 7.2 shows the optimum $(M_{\mathrm{A}} + M_{\mathrm{B}})$-point constellation under a unit average power constraint [178]. The constellation points are given in Table 7.1, where the inner and outer points have been allocated to $\mathcal{M}_{\mathrm{A}}$ and $\mathcal{M}_{\mathrm{B}}$, respectively. In comparison to its corresponding regular QAM constellation, the constellation in Fig. 7.2 has higher MED under a unit average power constraint which results in lower BER performance. Thus, it has been adopted in this work. An example of the mapping process for the proposed eSI-CAP is illustrated as follows: Consider a total subbands $N = 4$; active subbands $N_{\mathrm{a}} = 2$ and $M_{\mathrm{A}} = M_{\mathrm{B}} = 4$, then there are ${}^{N}C_{N_{\mathrm{a}}}$ possible ways of selecting the N_{a} active subbands.

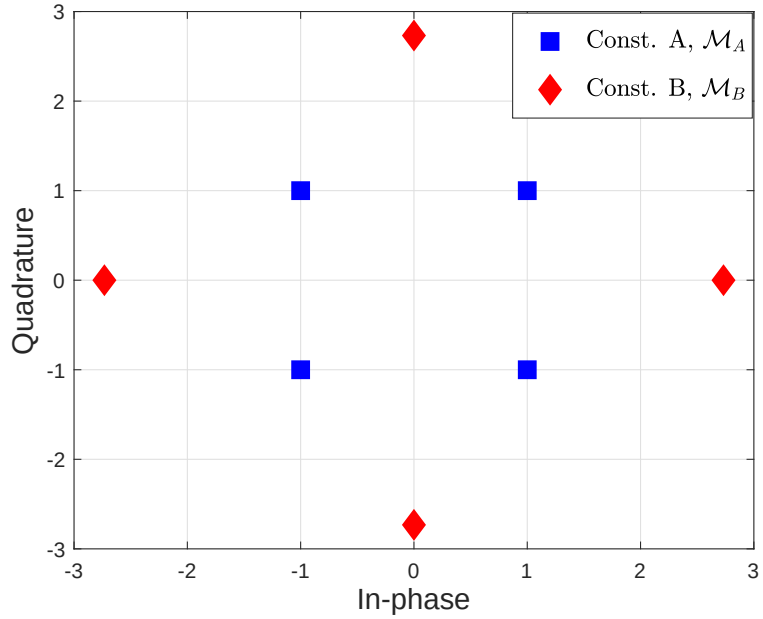

Figure 7.2: The constellation symbols of eSI-CAP showing the dual distinguishable constellation mode $\mathcal{M}_A$ and $\mathcal{M}_B$ [172].

Table 7.1: Mapping process for the proposed eSI-CAP WITH $N = 4, N_\mathrm{a} = 2$ AND $M = 4$

b_s bits	$\mathcal{S} = [\mathcal{S}_\mathrm{A}; \mathcal{S}_\mathrm{B}]$	$\log_2(M)$ bits	$\mathcal{M}_\mathrm{A}$	$\mathcal{M}_\mathrm{B}$
00	$[1, 2; 3, 4]$	00	$+1 + j$	$+(1 + \sqrt{3})$
01	$[1, 3; 2, 4]$	01	$-1 + j$	$+j(1 + \sqrt{3})$
10	$[1, 4; 2, 3]$	10	$-1 - j$	$-(1 + \sqrt{3})$
11	$[2, 3; 1, 4]$	11	$+1 - j$	$-j(1 + \sqrt{3})$

However, only $N_\mathrm{u} = 2^{\lfloor \log_2({}^{N}C_{N_\mathrm{a}}) \rfloor}$ of the possible combinations can be used to encode data bits. Thus, $N_\mathrm{u} = 4$ and $b_\mathrm{s} = \log_2(N_\mathrm{u})$. The set of selected subband indices are represented as $\mathcal{S} = \{S_{n_\mathrm{u}}\}_{n_\mathrm{u}=1}^{N_\mathrm{u}}$ as shown in Table 7.1. If bits $b =$ '1101100111' is to be transmitted, the first b_s bits, '11', is encoded in the S_{n_u} selection which is $S_4 = [2, 3; 1, 4]$ in this case. This means that subbands 2 and 3 will be modulated with symbols drawn from $\mathcal{M}_\mathrm{A}$ while subbands 1 and 4 will be modulated with symbols drawn from $\mathcal{M}_\mathrm{B}$. Still using Table 7.1, the next $N_\mathrm{a}\log_2(M_\mathrm{A})$ bits, '0110', are mapped to $\mathcal{M}_\mathrm{A}$ symbols $-1 + j$ and $-1 - j$ while the last $N_\mathrm{b}\log_2(M_\mathrm{B})$ bits, '0111′, are mapped to $\mathcal{M}_\mathrm{B}$ symbols $+j(1 + \sqrt{3})$ and $-j(1 + \sqrt{3})$. Therefore, the eSI-CAP

signal vector that is sent to the m-CAP demodulator is:

$$\mathbf{x} = \begin{bmatrix} +j(1+\sqrt{3}) & -1+j & -1-j & -j(1+\sqrt{3}) \end{bmatrix}^T. \tag{7.1}$$

The eSI-CAP configuration can be compactly denoted by $\Omega = \left\langle {}^{N}_{N_\mathrm{a}} \right\rangle^{\mathcal{T}}_{M}$, where M stands for the constellation size which is the same for both $\mathcal{M}_\mathrm{A}$ and $\mathcal{M}_\mathrm{B}$.

7.2 Analysis of eSI-CAP Scheme

The BER performance analysis of the eSI-CAP model is derived based on the maximum likelihood detection scheme (MLD). Due to the high complexity of the MLD, two other low-complexity schemes that achieve similar performance as the MLD are also reported.

7.2.1 Transmission efficiency of eSI-CAP

The transmission efficiency of eSI-CAP scheme can be expressed as:

$$\mathcal{T}_{\text{eSI-CAP}} = \frac{b_\mathrm{s} + b_\mathrm{m}}{N} \tag{7.2}$$

$$= \frac{\lfloor \log_2 \left({}^{N}C_{N_\mathrm{a}} \right) \rfloor + N_\mathrm{a} \log_2(M_\mathrm{A}) + N_\mathrm{b} \log_2(M_\mathrm{B})}{N}. \tag{7.3}$$

For SI-CAP that uses only the index modulation technique without the dual constellation, the $N_\mathrm{b}\log_2(M_\mathrm{B})$ term in (7.3) is set to zero as no data is transmitted on the 'inactive' subbands [179]. Hence, as shown in (6.3),

$$\mathcal{T}_{\text{SI-CAP}} = \frac{\lfloor \log_2 \left({}^{N}C_{N_\mathrm{a}} \right) \rfloor + N_\mathrm{a} \log_2(M)}{N}. \tag{7.4}$$

The $\mathcal{T}_{m\text{-CAP}}$ on the other hand can not exceed $\log_2(M)$ since it is independent of N. The maximum transmission efficiency that can be obtained by eSI-CAP, SI-CAP and m-CAP for $M = 4$ and 16 are compared in Fig. 7.3 for a given N. The figure shows clearly that the transmission efficiency of eSI-CAP exceeds that of m-CAP and SI-CAP for the configurations considered.

7.2.2 Power efficiency of eSI-CAP

Without power loading, the average power allocated for the conventional m-CAP is P_t/N, where P_t is the total transmitted power. However, the average power for the proposed eSI-CAP

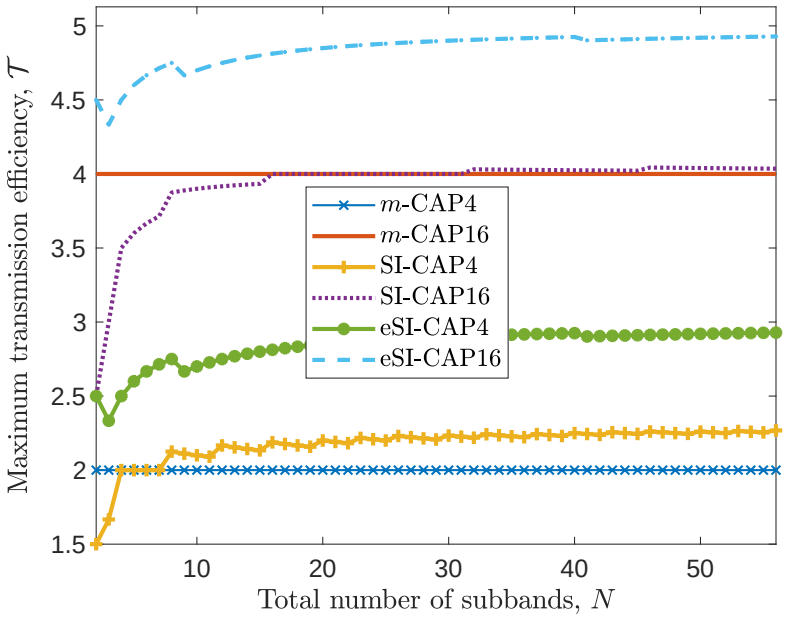

Figure 7.3: The comparison of the maximum possible transmission efficiency of eSI-CAP, SI-CAP and m-CAP for a given N and M.

is $\xi P_{\mathrm{t}}/N$ where:

$$\xi = \frac{N}{N_{\mathrm{a}}E_{\mathrm{a}} + N_{\mathrm{b}}E_{\mathrm{b}}}. \tag{7.5}$$

Both E_{a} and E_{b} respectively refers to the average energy of $\mathcal{M}_A$ and $\mathcal{M}_B$ with $\mathcal{M}$ normalized to unit average energy. Since $E_{\mathrm{b}} > E_{\mathrm{a}}$, (7.5) shows that the configuration with higher N_{a} is the most power efficient for a fixed N and $\mathcal{T}$. Intuitively, this will be the configuration with most symbols drawn from the lower-energy constellation $\mathcal{M}_A$. For example, if $N = 4$ then $N_{\mathrm{a}} = 1, 2$ and 3 all result in $\mathcal{T} = 2.5$ bpcu. However, using the constellation depicted in Fig. 7.2, the average transmitted power required for the case of $N_{\mathrm{a}} = 1, 2$ and 3 is 1.29 W, 1 W and 0.71 W, respectively. Therefore, even though the three configurations provide the same $\mathcal{T}$, the configuration with $N_{\mathrm{a}} = 3$ is the most power efficient. Hence, it can be stated that for a fixed transmission efficiency, increasing the active number of subbands results in a configuration that requires less transmitted power. The insight provided by (7.5) enables the use of optimum configuration to obtain the best performance for eSI-CAP. This will later be confirmed with simulation results and validated through an experimental demonstration.

7.2.3 Analysis of eSI-CAP BER performance with MLD

The eSI-CAP signal obtained at the output of the m-CAP demodulator, considering a line-of-sight (LOS) channel gain h, can be expressed as:

$$\mathbf{y} = \boldsymbol{\zeta}_k + \mathbf{w} \tag{7.6}$$

where $\boldsymbol{\zeta}_k = \xi \mathfrak{R} \mathcal{K} \beta h \mathbf{x}_k$. Since the eSI-CAP symbol $\{\mathbf{x}_k\}_{k=1}^{K}$ with $K = N_{\mathrm{u}} M_{\mathrm{A}}^{N_{\mathrm{a}}} M_{\mathrm{B}}^{N_{\mathrm{b}}}$ is equiprobable with probability $1/K$, the ML criterion that maximizes the probability of $\mathbf{y}$ given $\boldsymbol{\zeta}_k$ can be expressed as:

$$\hat{\mathbf{x}}_k = \arg\max_{k} p(\mathbf{y}, \boldsymbol{\zeta}_k) \tag{7.7}$$

where,

$$p(\mathbf{y}, \boldsymbol{\zeta}_k) = \frac{1}{(2\pi N_0)^{N/2}} \exp\left[-\frac{\|\mathbf{y} - \boldsymbol{\zeta}_k\|^2}{2N_0} \right] \tag{7.8}$$

The ML criteria of (7.7) can be reduced to the minimum distance criteria as:

$$\hat{\mathbf{x}}_k = \arg\min_{k} D(\mathbf{y}, \boldsymbol{\zeta}_k) \tag{7.9}$$

where the MED metric $D(\mathbf{y}, \boldsymbol{\zeta}_m)$ is expressed as:

$$D(\mathbf{y}, \boldsymbol{\zeta}_k) = \|\mathbf{y} - \boldsymbol{\zeta}_k\|^2 \tag{7.10}$$

Using the PEP, the eSI-CAP detector considers the joint detection of both the subband index combination and the transmitted symbols. The PEP for eSI-CAP is therefore derived as:

$$\begin{aligned} \mathrm{PEP}_{\text{eSI-CAP}} &= p(\mathbf{x}_k \to \tilde{\mathbf{x}}_k) \\ &= Q\left(\sqrt{\frac{(\xi \mathfrak{R} \mathcal{K} \beta)^2}{2N_0} \|h\left(\mathbf{x}_k - \tilde{\mathbf{x}}_k\right)\|^2} \right). \end{aligned} \tag{7.11}$$

The PEP of (7.11) is then used to obtain an upper bound BER expression that is shown in (7.12). The expression is obtained by considering all the possible K combinations of the eSI-CAP symbols using the union bound technique.

The computational complexity of MLD, which is of the order $\mathcal{O}(K)$, grows exponentially and becomes infeasible as the constellation size increases. In order to address this, two other lower complexity detection schemes are presented.

$$\text{BER}_{\text{eSI-CAP}} \leq \frac{1}{K\log_2(K)} \sum_{k=1}^{K} \sum_{\tilde{k}=1}^{K} \mathcal{N}_H(b_k, \tilde{b}_k) Q\left(\sqrt{\frac{(\xi \Re \mathcal{K} \beta)^2}{2N_0} \left\| h\left(\mathbf{x}_k - \tilde{\mathbf{x}}_k\right) \right\|^2} \right). \tag{7.12}$$

7.2.4 Analysis of eSI-CAP BER performance with LLR

The LLR detector considers the logarithm of the ratio of the a *posteriori* probabilities for each received subband symbol. It uses the fact that the subband symbol can either be drawn from $\mathcal{M}_A = \{s_{m_\text{a}}\}_{m_\text{a}=1}^{M_\text{A}}$ or $\mathcal{M}_B = \{s_{m_\text{b}}\}_{m_\text{b}=1}^{M_\text{B}}$. The formulation for the LLR can be stated as:

$$\chi_n = \ln\left(\frac{\sum_{m_\text{a}=1}^{M_\text{A}} \Pr(x_n = s_{m_\text{a}} | y_n)}{\sum_{m_\text{b}=1}^{M_\text{B}} \Pr(x_n = s_{m_\text{b}} | y_n)} \right) \tag{7.13}$$

where x_n and y_n respectively represent the transmitted and received symbols on the n^{th} subband. Using Baye's theorem, (7.13) can be restated as:

$$\chi_n = \ln\left(\frac{\sum_{m_\text{a}=1}^{M_\text{A}} \Pr(y_n | x_n = s_{m_\text{a}}) \Pr(x_n = s_{m_\text{a}})}{\sum_{m_\text{b}=1}^{M_\text{B}} \Pr(y_n | x_n = s_{m_\text{b}}) \Pr(x_n = s_{m_\text{b}})} \right) \tag{7.14}$$

and given the AWGN channel, the conditional probabilities can be expressed as:

$$\Pr(y_n | x_n = s_{m_\text{a}}) = \frac{1}{(2\pi N_0)^{1/2}} \exp\left[-\frac{|y_n - s_{m_\text{a}} h_n|^2}{2N_0} \right] \tag{7.15}$$

and

$$\Pr(y_n | x_n = s_{m_\text{b}}) = \frac{1}{(2\pi N_0)^{1/2}} \exp\left[-\frac{|y_n - s_{m_\text{b}} h_n|^2}{2N_0} \right]. \tag{7.16}$$

By substituting (7.15) and (7.16) in (7.14) and considering the fact that $\Pr(x_n = s_{m_\text{a}}) = N_\text{a}/NM_\text{A}$ while $\Pr(x_n = s_{m_\text{b}}) = (N - N_\text{a})/NM_\text{B}$, the LLR values for each subband can be computed as follows:

$$\begin{aligned} \chi_n = \ln\left(\frac{M_\text{B} N_\text{a}}{M_\text{A}(N - N_\text{a})} \right) + \ln\left(\sum_{m_\text{a}=1}^{M_\text{A}} \exp\left[-\frac{|y_n - s_{m_\text{a}} h_n|^2}{2N_0} \right] \right) \\ - \ln\left(\sum_{m_\text{b}=1}^{M} \exp\left[-\frac{|y_n - s_{m_\text{b}} h_n|^2}{2N_0} \right] \right). \end{aligned} \tag{7.17}$$

The LLR computations of (7.17) is prone to computational overflow which can be avoided by employing the Jacobian logarithm [170]. The computed LLR values, $\{\chi_n\}_{n=1}^{N}$, are arranged in decreasing order and the indices of the first N_a entries are taken as the activated subband index

combination. Using the already detected N_{a} indices, the remaining N_{b} indices that complete the detected $S_{n_{\mathrm{u}}}$ is easily determined as shown in Table 7.1. Thereafter, $\mathcal{M}_{\mathrm{A}}$ and $\mathcal{M}_{\mathrm{B}}$ decoders are employed to detect the symbols on the subbands in accordance with the detected $S_{n_{\mathrm{u}}}$. Because the LLR has no knowledge of the subband index combinations that are employed, it is possible to decide on some $S_{n_{\mathrm{u}}} \notin \mathcal{S}$ especially when the noise variance is high. Since this is an error event, such cases can be resolved by randomly mapping the detected combination to any of the entries in $\mathcal{S}$.

7.2.5 Analysis of eSI-CAP BER performance with LCD

The LLR detector of (7.17) requires the knowledge of noise variance and is also susceptible to computational overflow. As a result, a novel lower complexity detector is developed to address these issues. The proposed LCD employs the knowledge of $\mathcal{M}_{\mathrm{A}}$ and $\mathcal{M}_{\mathrm{B}}$, which is known to the receiver, to compute the MED between the received subband symbol and the constellation points. It then selects the most likely of the constellation symbols based on the computed values. The proposed LCD is elucidated in Algorithm 2. Using the outputs of Algorithm 2, the symbols on the active and inactive subbands can easily be detected by mapping them to the nearest symbol in $\mathcal{M}_{\mathrm{A}}$ and $\mathcal{M}_{\mathrm{B}}$, respectively. Similar to LLR, the LCD is also prone to detect some $S_{n_{\mathrm{u}}} \notin \mathcal{S}$. In such cases, the random mapping solution is also implemented.

A comparison of the LCD and LLR also shows that the LCD has lower complexity as it only computes a part of the second term in (7.17). Furthermore, the LCD dispenses with the knowledge of the noise variance and is not susceptible to computational overflow. In addition, the LCD achieves similar results with MLD especially at high SNR and it has the same order of complexity as the conventional m-CAP detector.

7.3 Simulation Results and Discussions

Computer simulations are conducted to investigate the performance of the proposed eSI-CAP. For the simulations, the electrical SNR per bit is defined as $\gamma_b = \frac{(\xi \mathfrak{R} \mathcal{K} \beta)^2}{\mathcal{T} N_0}$ where $\mathcal{T}$ is $\log_2(M)$ for m-CAP and it is as defined in (7.3) and (7.4) for eSI-CAP and SI-CAP, respectively.

The BER against SNR for the various configurations of eSI-CAP and comparison of its detection schemes is depicted in Fig. 7.4. For $N = 4$, eSI-CAP configurations using $N_{\mathrm{a}} = 1, 2$

Algorithm 2 LCD Algorithm

Require: $\mathbf{y}, \mathbf{h}, \mathcal{M}_{\mathrm{A}}, M_{\mathrm{A}}, N, N_{\mathrm{a}}, N_{\mathrm{b}}$

Ensure: $\mathcal{S}_{\mathrm{A}}$ and $\mathcal{S}_{\mathrm{B}}$ are the active and inactive subband indices, respectively;

Initialization:

$\boldsymbol{\chi} = \{\chi_{m_{\mathrm{a}}}\}_{m_{\mathrm{a}}=1}^{M_{\mathrm{A}}}$; $\boldsymbol{\lambda} = \{\lambda_n\}_{n=1}^{N}$;$\{s_{m_{\mathrm{a}}}\}_{m_{\mathrm{a}}=1}^{M_{\mathrm{A}}} = \mathcal{M}_{\mathrm{A}}$;

Note: $\{\chi_{m_{\mathrm{a}}}\}_{m_{\mathrm{a}}=1}^{M_{\mathrm{A}}} \Rightarrow \begin{bmatrix}\chi_1 & \chi_2 \cdots \chi_{M_{\mathrm{A}}}\end{bmatrix}$ and so on.

Recursion:

for $(n = 1; n \leq N; n++)$ **do**

  for $(m_{\mathrm{a}} = 1; m_{\mathrm{a}} \leq M_{\mathrm{A}}; m_{\mathrm{a}}++)$ **do**

    $\chi_{m_{\mathrm{a}}} = |y_n - h_n s_{m_{\mathrm{a}}}|^2$;

  end for

  $\lambda_n = \min_{m_{\mathrm{a}}} \{\chi_{m_{\mathrm{a}}}\}_{m_{\mathrm{a}}=1}^{M_{\mathrm{A}}}$;

end for

$\bar{\boldsymbol{\lambda}} = \{\bar{\lambda}_n\}_{n=1}^{N} = sort(\boldsymbol{\lambda})$, {sort(·) arranges the elements of (·) in an increasing order and returns their corresponding indices};

$\mathcal{S}_{\mathrm{A}} = \{\bar{\lambda}_{n_{\mathrm{a}}}\}_{n_{\mathrm{a}}=1}^{N_{\mathrm{a}}}$;

$\mathcal{S}_{\mathrm{B}} = \{\bar{\lambda}_{N-N_{\mathrm{b}}+n_{\mathrm{b}}}\}_{n_{\mathrm{b}}=1}^{N_{\mathrm{b}}}$;

return $\mathcal{S}_{\mathrm{A}}, \mathcal{S}_{\mathrm{B}}$;

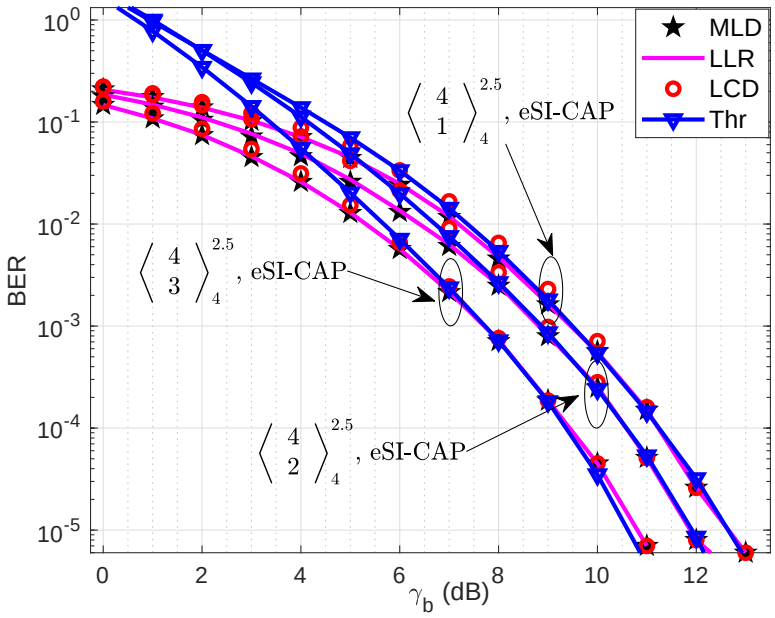

Figure 7.4: A demonstration of the optimum power-efficient eSI-CAP configuration and comparison of its detection schemes showing excellent agreement with the derived theoretical analysis.

and 3 all result in the same $\mathcal{T} = 2.5$ bpcu. However, as shown in Fig. 7.4, the configuration with $N_{\mathrm{a}} = 3$ requires an γ_b of 9.35 dB to achieve a BER of 10^{-4} compared to the cases of $N_{\mathrm{a}} = 1$

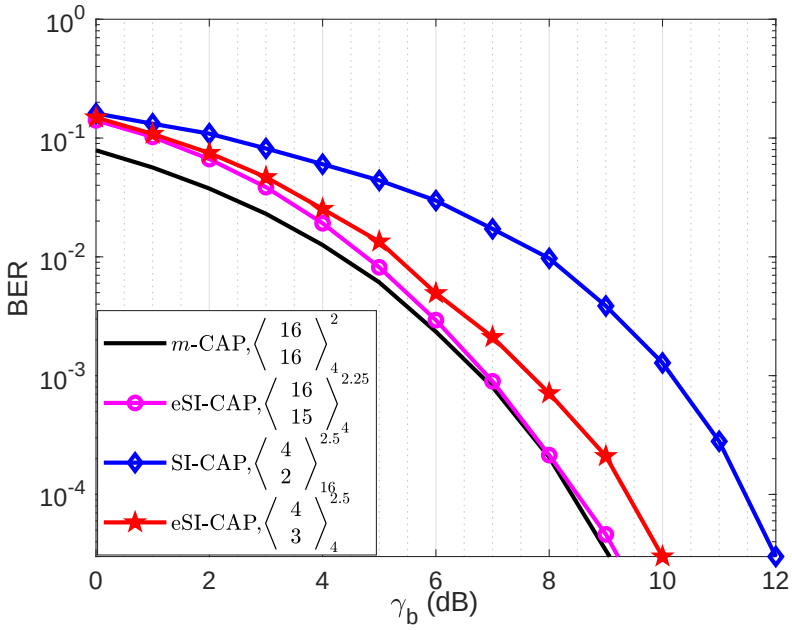

Figure 7.5: Performance comparison of eSI-CAP, SI-CAP and m-CAP schemes in AWGN channel.

and 2 which require 11.25 dB and 10.6 dB, respectively. Thus, an γ_b of $\sim$2 dB is gained by using the optimum configuration. This confirms the analysis presented in section 7.2.2. Furthermore, the LCD achieves similar performance as the LLR and MLD especially at high SNR. Therefore, LCD is the most attractive for eSI-CAP as it has the lowest complexity, is not susceptible to computational overflow and does not require knowledge of the noise variance. Also, the MLD analysis derived in (7.12) is validated and shown to have excellent agreement with the simulations. Finally, it can be inferred that the MLD analysis is valid for both LLR and LCD as they all achieve similar BER performances.

The BER performance of eSI-CAP is compared to both the conventional m-CAP and the SI-CAP in AWGN channel as shown in Fig. 7.5. Both m-CAP and eSI-CAP require an γ_b of 8.5 dB to achieve a BER of 10^{-4}. However, while m-CAP could only transmit 2 bpcu, eSI-CAP achieves 2.25 bpcu. Thus, at the same BER and SNR, eSI-CAP achieves better spectral efficiency than m-CAP. Similarly, for a fixed $\mathcal{T} = 2.5$ bpcu, eSI-CAP requires an γ_b of 9.35 dB to achieve a BER of 10^{-4} compared to 11.46 dB required by SI-CAP. Therefore, at the same $\mathcal{T}$ and BER, eSI-CAP achieves better power efficiency compared to SI-CAP.

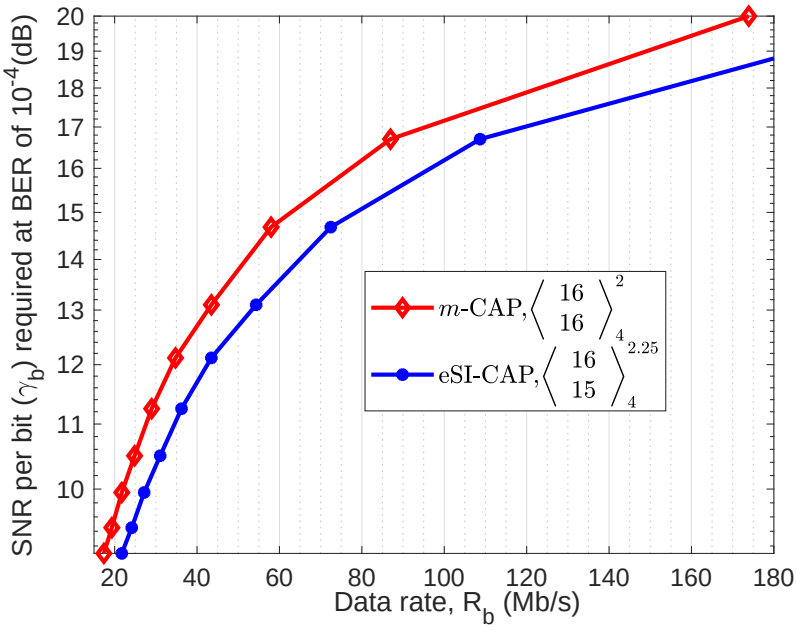

Figure 7.6: The comparison of the SNR per bit (γ_b) required by eSI-CAP and m-CAP schemes to achieve BER of 10^{-4} at varying R_b in VLC channel modelled as first-order low-pass filter with a 10 MHz 3 dB cut-off frequency.

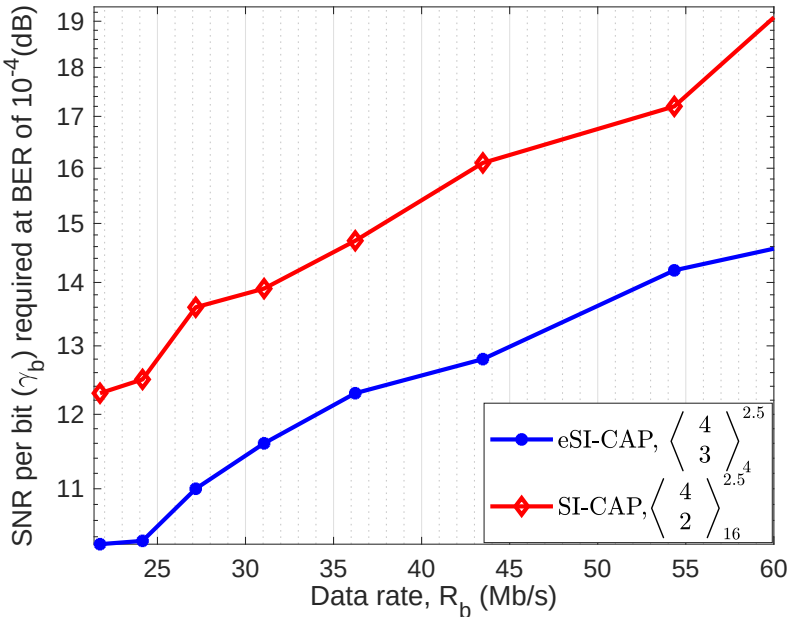

Figure 7.7: The comparison of the SNR per bit (γ_b) required by eSI-CAP and SI-CAP schemes to achieve BER of 10^{-4} at varying R_b in VLC channel modelled as first-order low-pass filter with a 10 MHz 3 dB cut-off frequency.

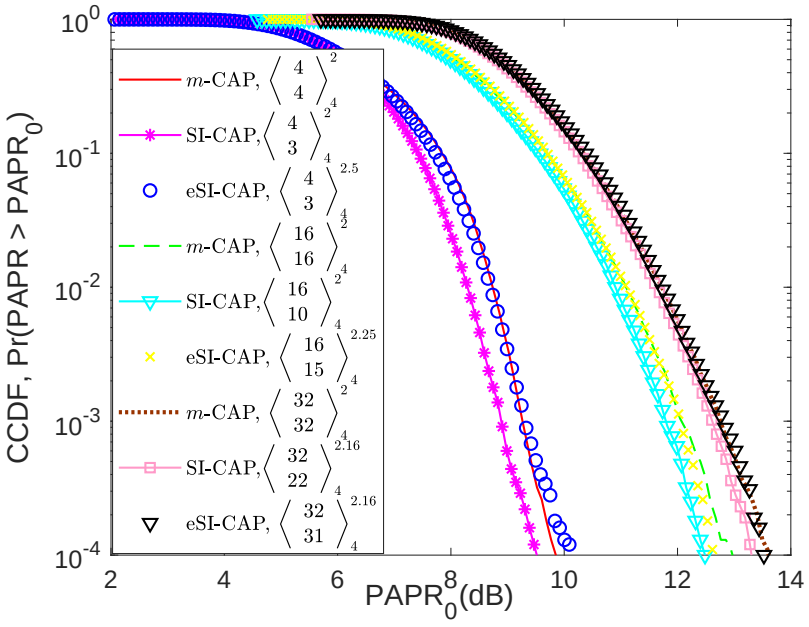

Figure 7.8: The comparison of the complimentary cumulative distribution function (CCDF) of the peak-to-average power ratio (PAPR) of eSI-CAP, SI-CAP and m-CAP for $N = 4, 16$ and 32.

The γ_b required to achieve a BER of 10^{-4} at different data rates (R_b) under the effect of VLC limited bandwidth is compared for all the schemes in Figs. 7.6 and 7.7. The effect of LED bandwidth limitation is modelled as a first-order low-pass filter with a 3 dB cut-off frequency of 10 MHz. It is shown in both figures that eSI-CAP achieves better BER performance when compared to SI-CAP and the conventional m-CAP over the range of data rates investigated. For example, when the $R_\mathrm{b} = 60$ Mb/s in Fig. 7.6, eSI-CAP requires an γ_b of 13.5 dB to achieve a BER of 10^{-4} compared to 14.8 dB required by m-CAP. Alternatively, at an γ_b of 16 dB, eSI-CAP achieves $R_\mathrm{b} = 96.5$ Mb/s at a BER of 10^{-4} compared to $R_\mathrm{b} = 77.5$ Mb/s achieved by m-CAP. With these comparisons, eSI-CAP is able to provide an γ_b gain of 1.3 dB at a fixed R_b or up to 19 Mb/s data rate improvement when the γ_b is fixed. Similarly, at $R_\mathrm{b} = 60$ Mb/s in Fig. 7.7, eSI-CAP requires an γ_b of 14.6 dB while SI-CAP requires 19 dB. When the γ_b is fixed at 15 dB, eSI-CAP achieves $R_\mathrm{b} = 66$ Mb/s compared to $R_\mathrm{b} = 37.9$ Mb/s achieved by SI-CAP. Therefore, it can be concluded that at a fixed data rate, eSI-CAP achieves better power efficiency compared to other schemes. And if the power efficiency is also fixed, eSI-CAP will achieve a better data rate for the same BER performance.

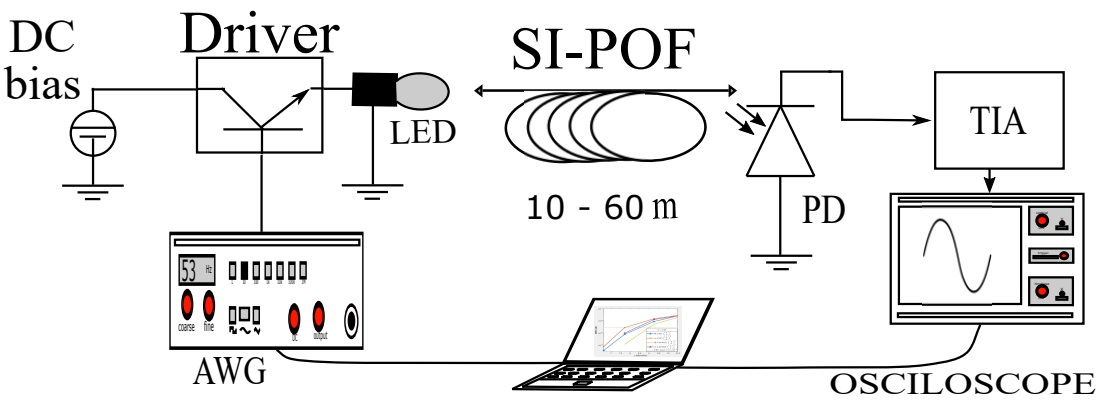

Figure 7.9: Illustration of the set-up for the experimental demonstration with SI-POF link.

The CCDF of the PAPR for all the schemes are compared in Fig. 7.8 with $N = 4, 16$ and 32. The figure shows that for small number of subbands, $N = 4$, and for any given PAPR threshold, the CCDF of SI-CAP is lower than that of both m-CAP and eSI-CAP. However, as N increases, , the CCDF plots of all the three schemes become identical. So, for $N > 4$, it can be concluded that implementing eSI-CAP does not result in PAPR penalty over the conventional m-CAP.

7.4 Experimental Validation of eSI-CAP Performance

The experimental set-up for investigating the performance of eSI-CAP in VLC link is as described in section 6.4 of chapter 6. The set-up for the experimental demonstration with an SI-POF link is depicted in Fig. 7.9 and a pictorial representation is shown in Fig. 6.8. The values of the filter parameters specified in [24] are employed for the three schemes. The signals corresponding to each of the schemes is generated on a computer before being sent to an arbitrary waveform generator (AWG, Agilent 33600 series). The continuous waveform from the AWG is fed to the LED driver with an added suitable DC bias before being used to modulate the intensity of the RC-LED [179]. The optical signal is transmitted through the SI-POF (HFBR-RUD500Z) and received by a PIN-based photo-receiver (PDA10A). A digital oscilloscope (Agilent 7000B Series) is used to capture the received electrical signal, followed by an offline post-detection processing. The response of the link can be approximated as a 4^{th}-order low-pass filter with a measured 3 dB bandwidth of 100 MHz as shown in Fig. 7.10. The system sampling rate is 500 MSa/s.

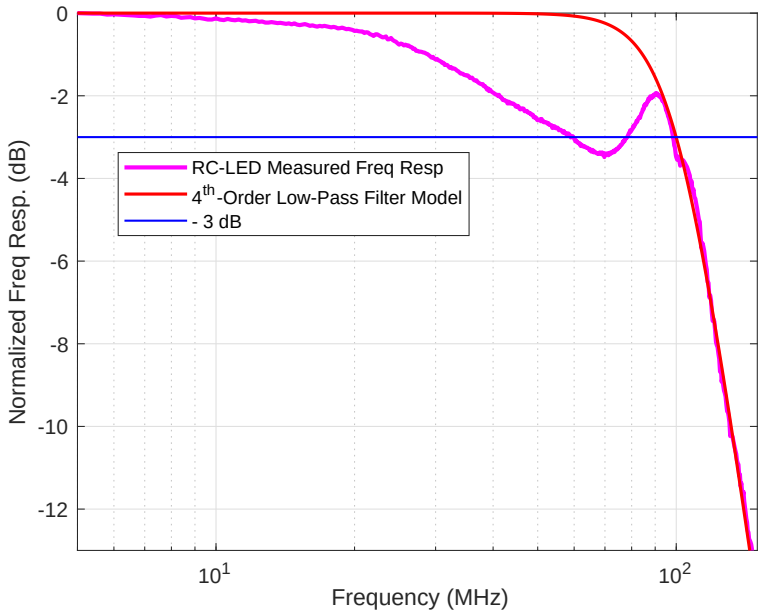

Figure 7.10: The measured normalized frequency response of the overall link fitted with a 4^{th}-order low-pass butterworth filter.

7.4.1 Experimental validation of eSI-CAP performance in VLC

The most power-efficient configuration for eSI-CAP is experimentally validated with the results shown in Fig. 7.11. The configuration with $N_{\mathrm{a}} = 3$ achieves better BER performance over the range of modulation index, β and data rates, R_{b} investigated. Specifically, at $R_{\mathrm{b}} = 153$ Mb/s and $\beta = 0.06$, the configuration with $N_{\mathrm{a}} = 3$ achieves the lowest BER at 1.5×10^{-3} compared to 4×10^{-3} and 7×10^{-3} achieved by the configurations with $N_{\mathrm{a}} = 2$ and 1, respectively. Furthermore, when the BER is fixed at 1×10^{-4} and $\beta = 0.10$, the configuration with $N_{\mathrm{a}} = 3$ achieves R_{b} of 169 Mb/s compared to 155 Mb/s and 150 Mb/s achieved by the configurations with $N_{\mathrm{a}} = 2$ and 1, respectively. At the same BER of 1×10^{-4} but higher $\beta = 0.25$, the R_{b} is 206 Mb/s, 189 Mb/s and 180 Mb/s respectively for $N_{\mathrm{a}} = 3, 2$ and 1. Therefore, for a fixed N and R_{b}, the eSI-CAP configuration with the highest N_{a} is the most power-efficient. This provides experimental validation for the simulation result of Fig. 7.4 and the analysis of section 7.2.2.

The performances of eSI-CAP and m-CAP in the VLC experimental demonstration is presented in Fig. 7.12 for varying values of R_{b} and β. The same configurations used in

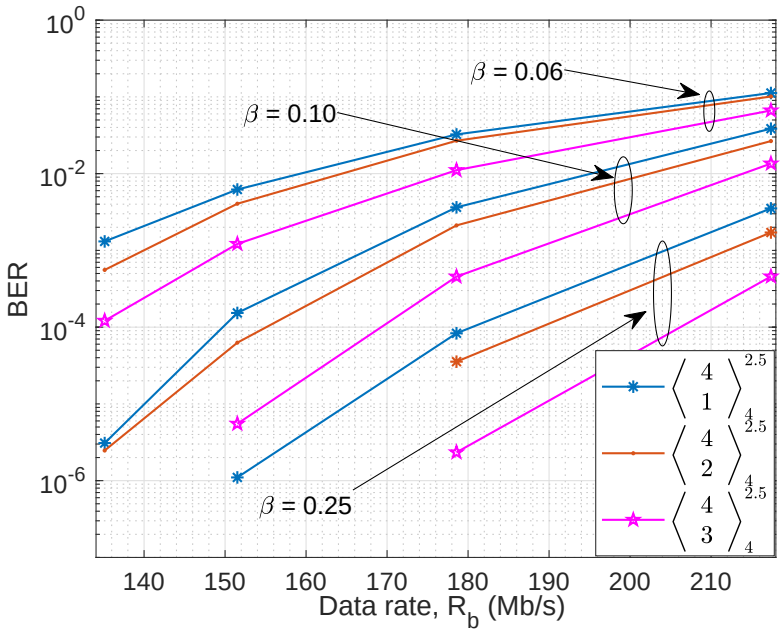

Figure 7.11: Experimental validation of the optimum power-efficient configuration for eSI-CAP in a VLC link with a 3 *dB bandwidth of* 10.9 *MHz at varying* β *and* R_b.

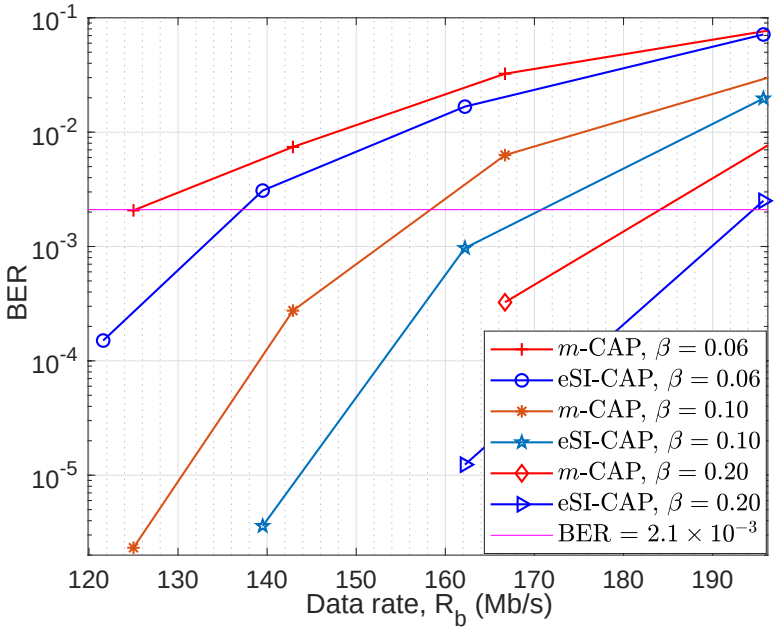

Figure 7.12: Experimental validation of the superior BER performance of eSI-CAP in VLC when compared to m*-CAP at varying modulation index,* β *and data rates,* R_b *using a commercially available LED with a link bandwidth of* 10.9 *MHz.*

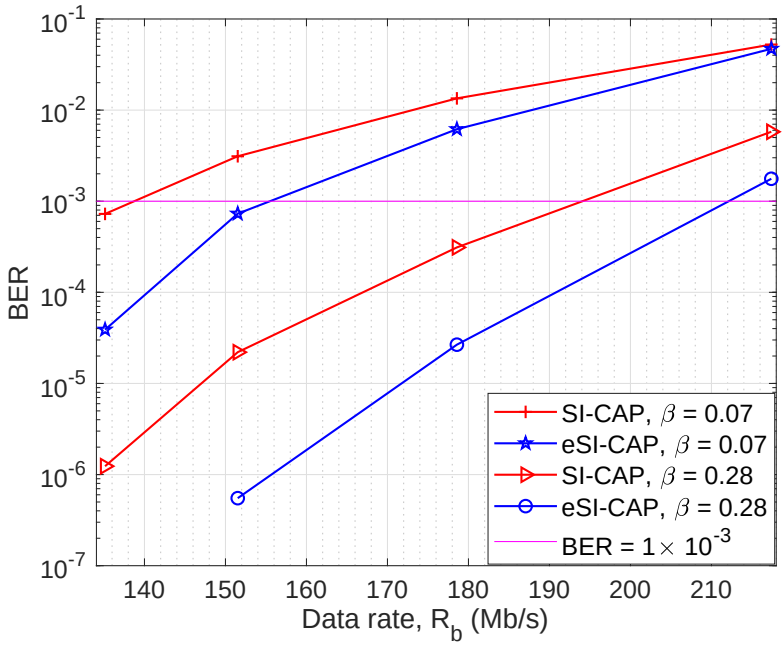

Figure 7.13: Experimental validation of the superior BER performance of eSI-CAP in VLC when compared to SI-CAP at varying modulation index, β and data rates, R_b using a commercially available LED with a link bandwidth of 10.9 *MHz.*

Fig. 7.6 is adopted for the experimental validation. Considering a BER of 2.1×10^{-3} which is lower than the FEC BER limit, the eSI-CAP outperform m-CAP for the range of R_b and β values investigated. At BER of 2.1×10^{-3} and $\beta = 0.06$, implementing eSI-CAP results in a R_b improvement of 12 Mb/s as eSI-CAP achieves R_b of 137 Mb/s compared to 125 Mb/s achieved by m-CAP. The eSI-CAP scheme maintains its advantage when the β is increased to 0.1 and 0.25 as it achieves a corresponding R_b of 171 Mb/s and 195 Mb/s compared to 159 Mb/s and 184 Mb/s achieved by m-CAP. Therefore, the eSI-CAP achieve a R_b gain of $\sim$12 Mb/s when compared to m-CAP over the range of R_b and β values investigated in the VLC experimental demonstration.

Similarly, Fig. 7.13 depicts the performance comparison of eSI-CAP and SI-CAP in the VLC experimental demonstration using the same configurations adopted in Fig. 7.7. At BER of 1×10^{-3} and $\beta = 0.07$, the eSI-CAP provides a data rate gain of 17.5 Mb/s as it achieves $R_\mathrm{b} = 157$ Mb/s compared to 139.5 Mb/s achieved by SI-CAP. When the β is increased to 0.28, the eSI-CAP maintains its advantage as it achieves R_b of 212.6 Mb/s compared to 195.1 Mb/s achieved by SI-CAP. Thus, eSI-CAP provides a R_b gain of $\sim$17.5 Mb/s when compared to

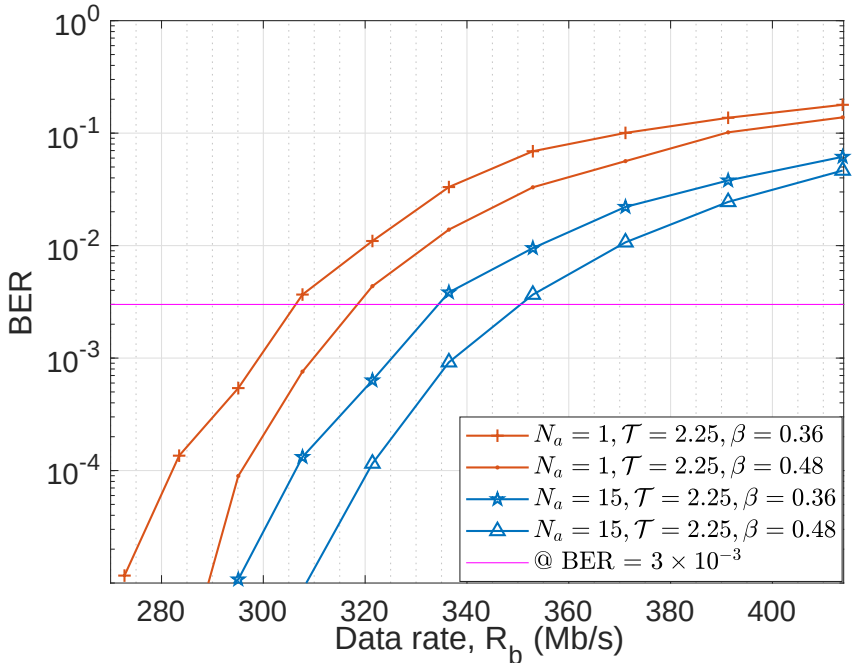

Figure 7.14: Optimum power-efficient configuration for enhanced subband index CAP (eSI-CAP) in a 10 *m SI-POF link with a measured* 3 *dB bandwidth of* 100 *MHz using different modulation index,* $\beta = [0.48, 0.36]$*,* $N = 16$*,* $N_a = [1, 15]$ *and* $M = 4$*.*

SI-CAP over the range of R_b and β values investigated in the VLC experimental demonstration. It can therefore be concluded, based on the simulation results that have been validated by the experimental demonstrations, that eSI-CAP is a very attractive scheme for VLC systems due to its performance superiority and similar complexity with SI-CAP and the conventional m-CAP schemes.

7.4.2 Experimental validation of eSI-CAP performance in SI-POF

The selection of the optimum power-efficient configuration for eSI-CAP at a fixed $\mathcal{T}$ is illustrated in Fig. 7.14 in 10 m SI-POF link for different modulation index, β. Using $N = 16$ and $M = 4$, the eSI-CAP configurations with $N_\mathrm{a} = 1$ and 15 have the same $\mathcal{T} = 2.25$. However, as shown in Fig. 7.14 at BER of 3×10^{-3} and $\beta = 0.36$, the configuration with $N_\mathrm{a} = 15$ achieves data rate, R_b, of 335 Mb/s in comparison to 306 Mb/s achieved with $N_\mathrm{a} = 1$. This leads to a R_b gain of 29 Mb/s which increases to 33 Mb/s at β of 0.48. Thus, it is found that for a fixed $\mathcal{T}$, the configuration with the highest N_a has the best BER performance and hence is the most power efficient. As a result, the configuration with $N_\mathrm{a} = 15$ has been adopted for

the SI-POF demonstration of eSI-CAP performance in subsequent results.

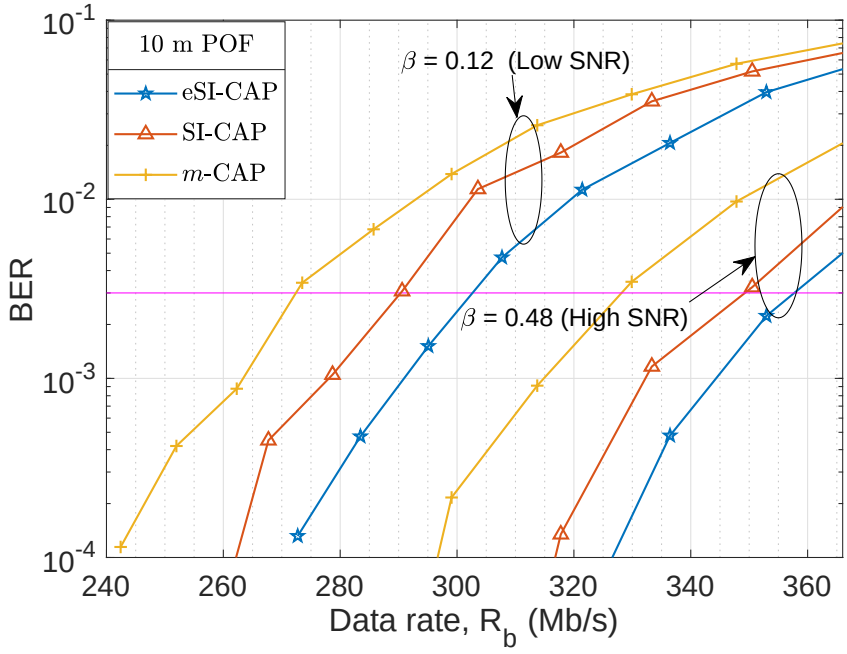

Figure 7.15: Performance comparison of the subband index schemes and m-CAP at different modulation index, β using $N = 16$ and $N_a = 15$ in 10 m SI-POF link with a measured 3 dB bandwidth of 100 MHz.

The BER performance of the subband index schemes are compared to that of the conventional m-CAP in Fig. 7.15 using $N = 16$ and $N_{\text{a}} = 15$ in 10 m SI-POF link. The figure shows the performance advantage of the subband index schemes over m-CAP and depicts the enhancement of SI-CAP by eSI-CAP. For example, at a BER of 3×10^{-3} and $\beta = 0.12$, eSI-CAP achieves R_{b} of 303 Mb/s in comparison to 291 Mb/s and 273 Mb/s achieved by SI-CAP and m-CAP, respectively. Thus, eSI-CAP has a R_{b} gain of 12 Mb/s and 30 Mb/s over SI-CAP and m-CAP, respectively. When the β is increased to 0.48 at the same BER, eSI-CAP maintains its performance advantage as it achieves R_{b} gain of 8.4 Mb/s and 30 Mb/s over SI-CAP and m-CAP, respectively. Alternatively, if the R_{b} is fixed at 336 Mb/s for all the schemes at $\beta = 0.48$, the eSI-CAP and SI-CAP achieve BER of 5×10^{-4} and 1.5×10^{-3} respectively in comparison to 5×10^{-3} achieved by m-CAP. Thus, the proposed subband index schemes achieve higher data rates for a fixed power efficiency and vice versa when compared with the conventional m-CAP. It can be seen from Table 7.2 that the subband index schemes consistently outperform the conventional m-CAP over all the range of β investigated and that

Table 7.2: The data rate achieved by each scheme below the FEC BER limit of 3×10^{-3} *in* 10 *m SI-POF link with a measured* 3 *dB bandwidth of* 100 *MHz using different modulation index (*β*),* $N = 16$ *and* $N_{\mathrm{a}} = 15$*.*

Scheme \ β	0.48	0.36	0.24	0.12	0.06
$R_{b(\text{eSI-CAP})}$ (Mb/s)	358	347	334	303	258
$R_{b(\text{SI-CAP})}$ (Mb/s)	350	331	317	291	243
$R_{b(m\text{-CAP})}$ (Mb/s)	325	317	299	273	230

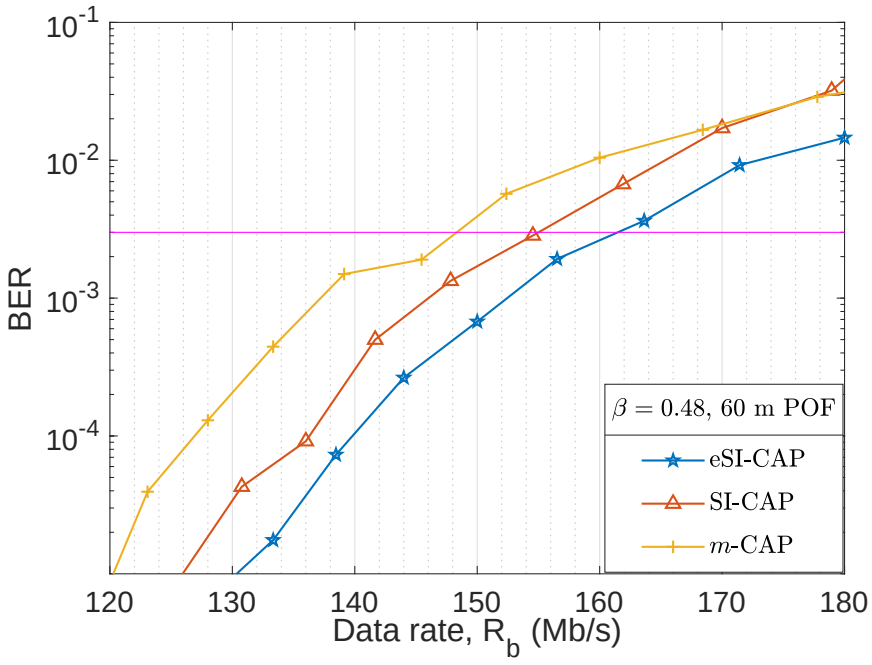

Figure 7.16: Performance comparison of the subband index schemes and m*-CAP with* $\beta = 0.48$*,* $N = 16$ *and* $N_a = 15$ *in* 60 *m SI-POF link with a measured* 3 *dB bandwidth of* 40 *MHz.*

eSI-CAP maintains its performance enhancement of SI-CAP over this range.

Finally, the performance enhancement of the subband index schemes is validated for longer SI-POF link of 60 m as shown in Fig. 7.16. The 3 dB bandwidth of the link reduces to 40 MHz from 100MHz due to the longer SI-POF length. At BER of 3×10^{-3} and $\beta = 0.48$, the eSI-CAP achieves R_{b} of 162 Mb/s in comparison to 153 Mb/s and 148 Mb/s achieved by SI-CAP and m-CAP, respectively. It is therefore concluded that the proposed subband index schemes significantly improve the spectral/power efficiency of the conventional m-CAP in short range optical data links.

7.5 Summary of Chapter 7

A novel eSI-CAP modulation scheme has been developed for SI-POF and VLC systems to address the complexity challenge in SI-CAP. The eSI-CAP not only transmit information bits by modulating the subbands of the m-CAP but also carry additional bits on the selection of the subband indices using a dual distinguishable constellations. An ML detector of the same complexity order as the m-CAP detector is developed while the optimum power-efficient configuration for eSI-CAP is also derived. The developed eSI-CAP is shown through theoretical analysis, computer simulations and experimental demonstrations to result in better performance when compared to SI-CAP and m-CAP schemes. At a fixed data rate, the eSI-CAP requires less SNR per bit to achieve a target BER thus providing higher power efficiency. Alternatively, when the SNR per bit is fixed for all the schemes, the eSI-CAP achieves a higher data rate for a target BER. The results of the experimental demonstrations in VLC and 10 m SI-POF link shows that when compared with m-CAP, eSI-CAP consistently yields a data rate improvement of between 7% and 13% for varying values of the SNR. Therefore, the eSI-CAP represents an attractive scheme for VLC and SI-POF systems as it provides low-complexity flexible design along with improving the spectral/power efficiency of the conventional m-CAP modulation scheme.

Chapter 8

Conclusions

8.1 Summary of Key Results

The overriding objective of this thesis is to improve the performance of optical communication systems, including VLC and SI-POF. In order to achieve this objective, the thesis focusses on improving the performance of CAP modulation scheme by developing novel performance-enhancing techniques. The CAP scheme is a popular physical layer technique for optical communication systems. Challenges such as low modulation bandwidth, susceptibility to timing jitter, impact of ISI, low spectral and energy efficiency as well as high computational complexity are addressed in the thesis. The techniques that are developed to address these challenges are validated using theoretical analysis, computer simulations and proof-of-concept experimental demonstrations.

To provide a solid background for the thesis, the state of the art in VLC, SI-POF and CAP modulation are reviewed in chapter 2. The detailed review shows that the use of LED as a transmitter is one of the major factors contributing to the fast adoption of VLC. Other highlighted factors include the challenge of the dwindling spectrum in RF and why the huge free spectrum in VLC can serve a complimentary or alternate solution. The proliferation of in-home, in-car and in-office applications that are employing SI-POF as a medium of communication due to its low cost and ease of installation is also mentioned. The review shows that the emergence of VLC and SI-POF is currently revolutionizing the communication landscape. The main channel models of the VLC and SI-POF systems are also presented, including their challenges. It is shown that the limited bandwidth of the LED is a major bottleneck to achieving high-speed data communication in VLC and SI-POF systems. Several

solutions such as the use of blue filtering, equalization and pre and post processing techniques are discussed in details. The use of CAP modulation technique is presented as a major approach to improving the performance of optical communication systems. The benefits of CAP such as its simple implementation and high performance in comparison to other physical layer techniques are mentioned. In conclusion, to derive the maximum benefits from the CAP scheme, the challenges facing the implementation of CAP such as its timing jitter sensitivity, low tolerance to ISI, high PAPR and complexity of its multiband version are highlighted as deserving of novel solutions.

Two novel techniques are proposed in chapter 3 to address the timing jitter sensitivity and the effect of low modulation bandwidth on the implementation of CAP modulation scheme. The 'CAP filter' synchronization technique is developed to address the timing jitter sensitivity of the CAP scheme. Simulations, analysis and experimental demonstrations show that the synchronization technique achieves perfect synchronization for CAP-based VLC systems. In comparison to the state of the art, the 'CAP filter' synchronization technique achieve similar BER and EVM at significantly lower complexity. For example, using a high-order CAP-128 in an VLC experiment over a 1 m distance, both 'CAP filter' synchronization technique and the state of the art technique achieve EVM of 15.7 dB. However, the 'CAP filter' technique utilizes only 6% of the length of the sequence that is employed for the state of the art. To further reduce the complexity of the system, FSE is employed for joint mitigation of the effects of timing jitter and low modulation bandwidth. Using the FSE removes the need for a separate synchronization block as the FSE is shown to be capable of addressing both the effects of timing jitter and low modulation bandwidth. The result of VLC experimental demonstration shows that the FSE achieves a data rate of 80 Mb/s compared to 55 Mb/s achieved by the SSE that is normally employed in the literature. Furthermore, the FSE performance is shown to be insensitive to increasing timing jitter while that of SSE degrades.

To improve the spectral and energy efficiency of the CAP-based VLC systems, the multiple LEDs that are usually deployed in VLC are employed in chapter 4 to simultaneously transmit multiple CAP signals in parallel through the spatial domain. In particular, spatial multiplexing and repetitive coding techniques are combined with the conventional CAP to improve its throughput and diversity, respectively. Using spatial multiplexing with CAP, the SM$_{ux}$-CAP

is developed that improves the throughput of the conventional CAP by a factor N_{t}. In addition, RC-CAP is also developed that significantly improve the BER performance of the conventional CAP using repetitive coding. The BER expression of both SM$_{ux}$-CAP and RC-CAP are derived using ML detector. The simulation results show that the SM$_{ux}$-CAP is most appropriate in channels with dissimilar gains while RC-CAP should be deployed in systems with closely co-located transmitters. The PFI precoding technique is then developed to address the performance degradation of SM$_{ux}$-CAP in channels with similar gains. The PFI is shown to result in 28.5 dB SNR gain when employed for SM$_{ux}$-CAP. To address the high complexity of the optimum ML detector, four low complexity detectors are investigated for SM$_{ux}$-CAP. These detectors include the ZF, MMSE, ZF-OSIC and MMSE-OSIC. It is shown that MMSE-OSIC is the best detector for SM$_{ux}$-CAP as it achieves superior performance at a moderate computational complexity. It outperforms other low complexity detectors and only has about 5 dB degradation in comparison to the practically infeasible ML detector. However, its computational complexity is an order of magnitude lower than that of the ML detector. Thus, MMSE-OSIC has the best performance-complexity trade-off for SM$_{ux}$-CAP based systems.

The challenge with SM$_{ux}$-CAP system is that the simultaneous use of all the available LEDs results in inter-channel/intersymbol interference at the receiver which degrades the system performance. To tackle this challenge, the S-CAP is developed in chapter 5 by considering the combination of spatial modulation and the conventional CAP. In contrast to the SM$_{ux}$, the S-CAP only transmits a CAP signal through one LED out of the total number of LEDs available. Its special efficiency improvement factor compared to CAP is shown to be $\log_M(MN_{\mathrm{t}})$. In addition to the bits encoded in the CAP signal, the S-CAP encodes additional information bits on the index/position of the LED that transmits the CAP signal. The BER analysis of S-CAP is also derived and its performance is investigated for both LOS and NLOS propagation. The investigation shows that S-CAP performance in LOS depends largely on three factors namely: (i) signal constellation points (SCP); (ii) the channel dissimilarity, ($|\Delta h|$); and (iii) the minimum value of the channel gains (h_{min}). While in NLOS, the τ_{rms} effect overrides the effect of h_{min}. It is found that the S-CAP performance degrades due to closely-spaced transmitting LEDs and multipath propagation that results from high order reflections. The use of PFI is found to substantially improve the S-CAP performance in LOS resulting in an SNR gain of 33.5 dB while it is ineffective in NLOS propagation. However, the

use of multiple PDs improve the performance of S-CAP in both LOS and NLOS scenarios leading to an SNR gain of 43 dB with the use of four PDs. The GS-CAP which uses multiple LEDs to transmit copies of CAP signal is further developed to improve on the S-CAP scheme. It is found that for different GS-CAP system configurations with the same spectral efficiency, the configuration with the lowest number of active LEDs results in optimum power efficiency (SNR) and BER performance.

The problem with the SM$_{ux}$-CAP and S-CAP techniques is the requirement for sufficient separation between transmitting LEDs and receiving PDs to achieve good BER performance. So as alternative to using the spatial domains, the suband domains is explored in chapter 6 to improve on the performance of CAP modulation. The index modulation technique is combined with m-CAP to develop SI-CAP. The SI-CAP only transmits data bits on some selected subbands of m-CAP. Additional bits are then encoded on the selection of which subbands to modulate with data bits while the rest are nulled, that is no data symbols are modulated on them. The BER analysis of SI-CAP is derived based on MLD and its performance is investigated in both VLC and SI-POF. The derived BER expression is validated using computer simulations. Two low complexity detectors are then developed to address the computational complexity of the MLD. It is shown that the two detectors achieve similar BER performance as MLD at significantly low complexity. The performance of SI-CAP and m-CAP are compared using simulation and experimental demonstrations. It is shown that SI-CAP achieves SNR gain of 1 dB over m-CAP in AWGN channel. When the performance is compared in VLC systems, SI-CAP achieves an SNR gain of 2.2 dB. The performance gain of SI-CAP is validated using experimental demonstration for both VLC and SI-POF channels. The SI-CAP also maintains its performance advantage when RLS equalizers are employed to improve performance. It is found that for a fixed data rate, the SI-CAP requires lower SNR per bit to achieve the same BER performance as the m-CAP. Alternatively, when the SNR per bit is fixed for both schemes, SI-CAP achieves higher data rate at a target BER.

However, a challenge arises with increasing constellation size in SI-CAP. It is noted that the number of subbands required to achieve the same spectral efficiency as m-CAP increases as the constellation size, M, increases in SI-CAP. This requirement results in increased complexity for SI-CAP when large constellation sizes are used. As a result, an enhanced

SI-CAP (eSI-CAP) is developed in chapter 7 to address this challenge. The eSI-CAP addresses the challenge by modulating all the subbands of m-CAP with data symbols from a dual distinguishable constellations. In addition, it encodes information bits on the index of the subbands. This ensure that eSI-CAP achieves higher spectral efficiency than SI-CAP and m-CAP without increasing complexity as the constellation size increases. The BER performance analysis of eSI-CAP is derived using the MLD and validated through simulation and experimental demonstrations. To further reduce complexity, a low complexity detector is developed for eSI-CAP that achieves similar BER performance as the MLD. The results also show that eSI-CAP outperform SI-CAP and m-CAP for varying values of modulation index considered in VLC and SI-POF channels. The results of the experimental demonstrations in VLC and 10 m SI-POF link shows that when compared with m-CAP, eSI-CAP consistently yields a data rate improvement of between 7% and 13% for varying values of the SNR. A comparison of the schemes' PAPR shows that beyond $N > 4$, all the schemes exhibit similar PAPR. Thus, eSI-CAP is a low-complexity technique that improves the data rate of the conventional m-CAP modulation.

8.2 Limitation

The main limitation of the various techniques that are proposed in this thesis pertains to their complexities. The ML receiver is not scalable as its computational complexity increases exponentially with increasing system parameters. This makes the implementation of ML receiver infeasible for real-time applications. As a result, low-complexity receivers have been designed for the proposed techniques in the thesis which result in compromising performance for reduced complexity. Hence, further research is required to develop receivers that are suitable for real-time applications in terms of their complexities while having similar or comparable performance to the ML receiver.

8.3 Future Direction

The techniques that have been developed in this theses are by no means exhaustive and based on the results, there are several considerations that merit further investigations. Some of these considerations are further discussed as future work to be carried out.

Theoretical quantification of channel impairments: Theoretical analysis quantifying the effect of timing jitter in CAP as well as the effect of multipath remains open research issues. Similarly, the analytical quantification of the effects of signal clipping and LED non-linearity also remain outstanding research problem, especially in view of the high PAPR of the m-CAP scheme. The effect of a non-linear system on a multi-carrier input signal can be modelled as an attenuation of the signal plus a non- Gaussian clipping noise component using the central limit and Bussgang theorem [180]. But whether this characterization can be extended to the m-CAP scheme requires some investigation, considering its use of RRC filter and the fact that only a few subbands are implemented.

Analysis incorporating NLOS and timing jitter effects: The BER performance analysis for spatial and MIMO CAP as well as SI-CAP all assumed perfect synchronization and line-of-sight (LOS) conditions. These analyses can be extended further to obtain BER expressions that incorporate the effects of non LOS and timing jitter. Such analyses will enable a more accurate evaluation of the effects of NLOS and timing jitter on the techniques that have been developed in the theses.

Hybrid of spatial and subband indexing techniques: Considering the performance gain of the S-CAP and SI-CAP, a hybrid system can also be developed that combines the two techniques. This means that the SI-CAP, rather than the CAP signal, is transmitted through multiple LEDs. This will combine the advantages of both the spatial and subband index modulations and results in further enhancement of the CAP modulation technique.

Real time implementation: Field programmable gate array (FPGA) development is a promising area of research and provides a means of achieving real-time implementation (RTI) of CAP modulation. There has not been much work done on RTI of CAP in the literature compared to other competing schemes [181–183]. The possibility of operating at the Nyquist sampling rate offered by m-CAP modulation might be an advantage in hardware implementation, especially for the design of analogue-to-digital converter (ADC) and digital-to-analogue converter (DAC) at high data rates [24]. Other parameters of considerable importance will be the bit resolution and the previously highlighted timing jitter. While a CAP system, being a single carrier, requires low bit resolution [89], m-CAP will require higher bit resolution as more subbands are added. Furthermore, the computational cost and power

requirements will put significant constraints on the hardware realization and will be crucial in its design. Overall, RTI of CAP on FPGA will enable thorough analysis of the various issues concerning CAP system and the required hardware resources.

References

[1] H. Haas, "LiFi is a paradigm-shifting 5G technology," *Reviews in Physics*, vol. 3, pp. 26 – 31, 2018.

[2] D. Karunatilaka, F. Zafar, V. Kalavally, and R. Parthiban, "LED based indoor visible light communications: State of the art," *IEEE Communications Surveys Tutorials*, vol. 17, no. 3, pp. 1649–1678, thirdquarter 2015.

[3] H. Haas, L. Yin, Y. Wang, and C. Chen, "What is LiFi?" *Journal of Lightwave Technology*, vol. 34, no. 6, pp. 1533–1544, March 2016.

[4] Z. Ghassemlooy, W. Popoola, and S. Rajbhandari, *Optical Wireless Communications: System and Channel Modelling with MATLAB*, 1st ed. Boca Raton, FL, USA: CRC Press, Inc., 2012.

[5] M. Figueiredo, L. N. Alves, and C. Ribeiro, "Lighting the wireless world: The promise and challenges of visible light communication," *IEEE Consumer Electronics Magazine*, vol. 6, no. 4, pp. 28–37, Oct 2017.

[6] S. H. Yu, O. Shih, H. M. Tsai, N. Wisitpongphan, and R. D. Roberts, "Smart automotive lighting for vehicle safety," *IEEE Communications Magazine*, vol. 51, no. 12, pp. 50–59, December 2013.

[7] K. O. Akande, P. A. Haigh, and W. O. Popoola, "On the implementation of carrierless amplitude and phase modulation in visible light communication," *IEEE Access*, pp. 1–1, 2018.

[8] H. Le Minh *et al.*, "100-Mb/s NRZ visible light communications using a postequalized white LED," *IEEE Photonics Technology Letters*, vol. 21, no. 15, pp. 1063–1065, 2009.

[9] K. H. Lee and S. W. R. Lee, "Process development for yellow phosphor coating on blue light emitting diodes (LEDs) for white light illumination," in *2006 8th Electronics Packaging Technology Conference*, Dec 2006, pp. 379–384.

[10] H. L. Minh, D. O'Brien, G. Faulkner, L. Zeng, K. Lee, D. Jung, and Y. Oh, "High-speed visible light communications using multiple-resonant equalization," *IEEE Photonics Technology Letters*, vol. 20, no. 14, pp. 1243–1245, July 2008.

[11] J. Grubor, S. C. J. Lee, K. D. Langer, T. Koonen, and J. W. Walewski, "Wireless high-speed data transmission with phosphorescent white-light LEDs," in *33rd European Conference and Exhibition of Optical Communication - Post-Deadline Papers (published 2008)*, Sept 2007, pp. 1–2.

[12] C. W. Chow, C. H. Yeh, Y. Liu, and Y. F. Liu, "Digital signal processing for light emitting diode based visible light communication," *IEEE Photon. Soc. Newslett.*, vol. 26, no. 5, pp. 9–13, October 2012.

[13] G. Stepniak, M. Schüppert, and C. A. Bunge, "Advanced modulation formats in phosphorous LED VLC links and the impact of blue filtering," *Journal of Lightwave Technology*, vol. 33, no. 21, pp. 4413–4423, Nov 2015.

[14] G. Stepniak, M. Schüppert, and C.-A. Bunge, "8 - polymer-optical fibres for data transmission," in *Polymer Optical Fibres*, C.-A. Bunge, T. Gries, and M. Beckers, Eds. Woodhead Publishing, 2017, pp. 217 – 310.

[15] O. Ziemann, J. Krauser, P. E. Zamzow, and W. Daum, *POF Handbook: Optical Short Range Transmission Systems*. Berlin, Heidelberg: Springer-Verlag, 2008.

[16] O. Ziemann, P. E. Zamzow, J. Krauser, W. Daum, W. Daumeister, and E. Al, *POF-Polymer Optical Fibers for Data Communication*. Berlin, Heidelberg: Springer-Verlag, 2002.

[17] I. N. Osahon, S. Rajbhandari, and W. O. Popoola, "Performance comparison of equalization techniques for SI-POF multi-gigabit communication with PAM- M and device non-linearities," *Journal of Lightwave Technology*, vol. 36, no. 11, pp. 2301–2308, June 2018.

[18] I. N. Osahon, M. Safari, and W. O. Popoola, "10-Gb/s transmission over 10-m SI-POF with M-PAM and multilayer perceptron equalizer," *IEEE Photonics Technology Letters*, vol. 30, no. 10, pp. 911–914, May 2018.

[19] Y. Wang, L. Tao, X. Huang, J. Shi, and N. Chi, "8-Gb/s RGBY LED-based WDM VLC system employing high-order CAP modulation and hybrid post equalizer," *IEEE Photonics Journal*, vol. 7, no. 6, pp. 1–7, Dec 2015.

[20] Y. Wang, X. Huang, L. Tao, J. Shi, and N. Chi, "4.5-Gb/s RGB-LED based WDM visible light communication system employing CAP modulation and RLS based adaptive equalization," *Opt. Express*, vol. 23, no. 10, pp. 13 626–13 633, May 2015.

[21] Y. Wang, X. Huang, L. Tao, and N. Chi, "1.8-Gb/s WDM visible light communication over 50-meter outdoor free space transmission employing CAP modulation and receiver diversity technology," in *2015 Optical Fiber Communications Conference and Exhibition (OFC)*, March 2015, pp. 1–3.

[22] S. Lin, J. B. Wang, J. Y. Wang, J. Wang, and M. Chen, "Low-timing-sensitivity waveform design for carrierless amplitude and phase modulation in visible light communications," *IET Optoelectronics*, vol. 9, no. 6, pp. 317–324, 2015.

[23] A. H. Abdolhamid and D. A. Johns, "A comparison of CAP/QAM architectures," in *Proceedings of the 1998 IEEE International Symposium on Circuits and Systems, 1998. ISCAS'98.*, vol. 4. IEEE, 1998, pp. 316–316.

[24] M. I. Olmedo, T. Zuo, J. B. Jensen, Q. Zhong, X. Xu, S. Popov, and I. T. Monroy, "Multiband carrierless amplitude phase modulation for high capacity optical data links," *Journal of Lightwave Technology*, vol. 32, no. 4, pp. 798–804, Feb 2014.

[25] P. A. Haigh *et al.*, "Multi-band carrier-less amplitude and phase modulation for bandlimited visible light communications systems," *IEEE Wireless Communications*, vol. 22, no. 2, pp. 46–53, April 2015.

[26] G. . Im, D. B. Harman, G. Huang, A. V. Mandzik, M. . Nguyen, and J. . Werner, "51.84 Mb/s 16-CAP ATM LAN standard," *IEEE Journal on Selected Areas in Communications*, vol. 13, no. 4, pp. 620–632, May 1995.

[27] J. Gao, Y. H. Leung, and V. Sreeram, "Digital filters for carrierless amplitude and phase receivers," in *Proceedings of IEEE Region 10 International Conference on Electrical and Electronic Technology. TENCON 2001 (Cat. No.01CH37239)*, vol. 2, 2001, pp. 575–579 vol.2.

[28] B. R. Saltzberg, "Comparison of single-carrier and multitone digital modulation for ADSL applications," *IEEE Communications magazine*, vol. 36, no. 11, pp. 114–121, 1998.

[29] W. O. Popoola, Z. Ghassemlooy, and B. G. Stewart, "Pilot-assisted PAPR reduction technique for optical OFDM communication systems," *Journal of Lightwave Technology*, vol. 32, no. 7, pp. 1374–1382, 2014.

[30] G. Stepniak and J. Siuzdak, "Experimental investigation of PAM, CAP and DMT modulations efficiency over a double-step-index polymer optical fiber," *Optical Fiber Technology*, vol. 20, no. 4, pp. 369 – 373, 2014.

[31] K. Zhong *et al.*, "Experimental study of PAM-4, CAP-16, and DMT for 100 Gb/s short reach optical transmission systems," *Opt. Express*, vol. 23, no. 2, pp. 1176–1189, Jan 2015.

[32] A. G. Bell, W. G. Adams, Tyndall, and W. H. Preece, "Discussion on "the photophone and the conversion of radiant energy into sound"," *Journal of the Society of Telegraph Engineers*, vol. 9, no. 34, pp. 375–383, 1880.

[33] P. M. Pattison, M. Hansen, and J. Y. Tsao, "LED lighting efficacy: Status and directions," *Comptes Rendus Physique*, vol. 19, no. 3, pp. 134 – 145, 2018.

[34] G. Pang, T. Kwan, C.-H. Chan, and H. Liu, "LED traffic light as a communications device," in *Proceedings 199 IEEE/IEEJ/JSAI International Conference on Intelligent Transportation Systems (Cat. No.99TH8383)*, Oct 1999, pp. 788–793.

[35] Y. Tanaka, S. Haruyama, and M. Nakagawa, "Wireless optical transmissions with white colored LED for wireless home links," in *11th IEEE International Symposium on Personal Indoor and Mobile Radio Communications. PIMRC 2000. Proceedings (Cat. No.00TH8525)*, vol. 2, Sept 2000, pp. 1325–1329 vol.2.

[36] J. Söderberg, "Free space optics in the czech wireless community: Shedding some light on the role of normativity for user-initiated innovations," *Science, Technology, & Human Values*, vol. 36, no. 4, pp. 423–450, 2011.

[37] H. Burchardt, N. Serafimovski, D. Tsonev, S. Videv, and H. Haas, "VLC: Beyond point-to-point communication," *IEEE Communications Magazine*, vol. 52, no. 7, pp. 98–105, July 2014.

[38] P. A. Haigh, F. Bausi, H. L. Minh, I. Papakonstantinou, W. O. Popoola, A. Burton, and F. Cacialli, "Wavelength-multiplexed polymer LEDs: Towards 55 Mb/s organic visible light communications," *IEEE Journal on Selected Areas in Communications*, vol. 33, no. 9, pp. 1819–1828, Sept 2015.

[39] S.-H. Yang, H.-S. Kim, Y.-H. Son, and S.-K. Han, "Reduction of optical interference by wavelength filtering in RGB-LED based indoor VLC system," in *16th Opto-Electronics and Communications Conference*, July 2011, pp. 551–552.

[40] P. A. Haigh, Z. Ghassemlooy, S. Rajbhandari, and I. Papakonstantinou, "Visible light communications using organic light emitting diodes," *IEEE Communications Magazine*, vol. 51, no. 8, pp. 148–154, August 2013.

[41] P. A. Haigh, Z. Ghassemlooy, S. T. Le, F. Bausi, H. L. Minh, F. Cacialli, and I. Darwazeh, "Organic visible light communications: Methods to achieve 10 Mb/s," in *2017 IEEE Photonics Conference (IPC)*, Oct 2017, pp. 553–554.

[42] H. Chen, Z. Xu, Q. Gao, and S. Li, "A 51.6 Mbps experimental VLC system using a monochromic organic LED," *IEEE Photonics Journal*, vol. PP, no. 99, pp. 1–1, 2017.

[43] M. S. Islim, R. X. Ferreira, X. He, E. Xie, S. Videv, S. Viola, S. Watson, N. Bamiedakis, R. V. Penty, I. H. White, A. E. Kelly, E. Gu, H. Haas, and M. D. Dawson, "Towards 10 Gb/s orthogonal frequency division multiplexing-based visible light communication using a GaN violet micro-LED," *Photon. Res.*, vol. 5, no. 2, pp. A35–A43, Apr 2017.

[44] R. X. G. Ferreira, E. Xie, J. J. D. McKendry, S. Rajbhandari, H. Chun, G. Faulkner, S. Watson, A. E. Kelly, E. Gu, R. V. Penty, I. H. White, D. C. O'Brien, and M. D. Dawson, "High bandwidth GaN-based micro-LEDs for multi-Gb/s visible light communications," *IEEE Photonics Technology Letters*, vol. 28, no. 19, pp. 2023–2026, Oct 2016.

[45] J. J. D. McKendry, R. P. Green, A. E. Kelly, Z. Gong, B. Guilhabert, D. Massoubre, E. Gu, and M. D. Dawson, "High-speed visible light communications using individual pixels in a micro

light-emitting diode array," *IEEE Photonics Technology Letters*, vol. 22, no. 18, pp. 1346–1348, Sept 2010.

[46] R. Baets, D. Delbeke, R. Bockstaele, and P. Bienstman, "Resonant-cavity light-emitting diodes: a review," in *Proceedings of SPIE (Light-emitting Diodes:Research, Manufactering, and Applications VII)*, E. Schubert, H. Yao, K. Linden, and D. McGraw, Eds., 2003, pp. 74–86.

[47] J. Vucic, C. Kottke, S. Nerreter, A. Buttner, K. . Langer, and J. W. Walewski, "White light wireless transmission at 200+Mb/s net data rate by use of discrete-multitone modulation," *IEEE Photonics Technology Letters*, vol. 21, no. 20, pp. 1511–1513, Oct 2009.

[48] A. M. Khalid, G. Cossu, R. Corsini, P. Choudhury, and E. Ciaramella, "1-Gb/s transmission over a phosphorescent white LED by using rate-adaptive discrete multitone modulation," *IEEE Photonics Journal*, vol. 4, no. 5, pp. 1465–1473, Oct 2012.

[49] F. M. Wu, C. T. Lin, C. C. Wei, C. W. Chen, H. T. Huang, and C. H. Ho, "1.1-Gb/s white-LED-based visible light communication employing carrier-less amplitude and phase modulation," *IEEE Photonics Technology Letters*, vol. 24, no. 19, pp. 1730–1732, Oct 2012.

[50] X. Huang, S. Chen, Z. Wang, J. Shi, Y. Wang, J. Xiao, and N. Chi, "2.0-Gb/s visible light link based on adaptive bit allocation OFDM of a single phosphorescent white LED," *IEEE Photonics Journal*, vol. 7, no. 5, pp. 1–8, Oct 2015.

[51] H. Chun, S. Rajbhandari, G. Faulkner, D. Tsonev, E. Xie, J. J. D. McKendry, E. Gu, M. D. Dawson, D. C. O'Brien, and H. Haas, "LED based wavelength division multiplexed 10 Gb/s visible light communications," *Journal of Lightwave Technology*, vol. 34, no. 13, pp. 3047–3052, July 2016.

[52] A. Burton, S. Zvanovec, Z. Ghassemlooy, P. A. Haigh, I. Darwazeh, and H. L. Minh, "Investigation of WDM VLC using standard 5 mm RGB LEDs," in *2018 11th International Symposium on Communication Systems, Networks Digital Signal Processing (CSNDSP)*, July 2018, pp. 1–6.

[53] G. Cossu, W. Ali, R. Corsini, and E. Ciaramella, "Gigabit-class optical wireless communication system at indoor distances (1.5 – 4 m)," *Opt. Express*, vol. 23, no. 12, pp. 15 700–15 705, Jun 2015.

[54] D. Tsonev, H. Chun, S. Rajbhandari, J. J. D. McKendry, S. Videv, E. Gu, M. Haji, S. Watson, A. E. Kelly, G. Faulkner, M. D. Dawson, H. Haas, and D. O'Brien, "A 3-Gb/s single-LED OFDM-based wireless VLC link using a gallium nitride μLED," *IEEE Photonics Technology Letters*, vol. 26, no. 7, pp. 637–640, April 2014.

[55] C. Shen, T. K. Ng, J. T. Leonard, A. Pourhashemi, H. M. Oubei, M. S. Alias, S. Nakamura, S. P. DenBaars, J. S. Speck, A. Y. Alyamani, M. M. Eldesouki, and B. S. Ooi,

"High-modulation-efficiency, integrated waveguide modulator–laser diode at 448 nm," *ACS Photonics*, vol. 3, no. 2, pp. 262–268, 2016.

[56] Y.-C. Chi, D.-H. Hsieh, C.-T. Tsai, H.-Y. Chen, H.-C. Kuo, and G.-R. Lin, "450-nm GaN laser diode enables high-speed visible light communication with 9-Gbps QAM-OFDM," *Opt. Express*, vol. 23, no. 10, pp. 13 051–13 059, May 2015.

[57] D. Tsonev, S. Videv, and H. Haas, "Towards a 100 Gb/s visible light wireless access network," *Opt. Express*, vol. 23, no. 2, pp. 1627–1637, Jan 2015.

[58] M. T. Sajjad, P. P. Manousiadis, H. Chun, D. A. Vithanage, S. Rajbhandari, A. L. Kanibolotsky, G. Faulkner, D. O'Brien, P. J. Skabara, I. D. W. Samuel, and G. A. Turnbull, "Novel fast color-converter for visible light communication using a blend of conjugated polymers," *ACS Photonics*, vol. 2, no. 2, pp. 194–199, 2015.

[59] D. A. Vithanage, A. L. Kanibolotsky, S. Rajbhandari, P. P. Manousiadis, M. T. Sajjad, H. Chun, G. E. Faulkner, D. C. O'Brien, P. J. Skabara, I. D. W. Samuel, and G. A. Turnbull, "Polymer colour converter with very high modulation bandwidth for visible light communications," *J. Mater. Chem. C*, vol. 5, pp. 8916–8920, 2017.

[60] S. Rajbhandari, J. J. D. McKendry, J. Herrnsdorf, H. Chun, G. Faulkner, H. Haas, I. M. Watson, D. O'Brien, and M. D. Dawson, "A review of gallium nitride LEDs for multi-gigabit-per-second visible light data communications," *Semiconductor Science and Technology*, vol. 32, no. 2, p. 023001, 2017.

[61] J. M. Kahn and J. R. Barry, "Wireless infrared communications," *Proceedings of the IEEE*, vol. 85, no. 2, pp. 265–298, Feb 1997.

[62] O. Kharraz and D. Forsyth, "Performance comparisons between PIN and APD photodetectors for use in optical communication systems," *Optik - International Journal for Light and Electron Optics*, vol. 124, no. 13, pp. 1493 – 1498, 2013.

[63] N. Saha, M. S. Ifthekhar, N. T. Le, and Y. M. Jang, "Survey on optical camera communications: challenges and opportunities," *IET Optoelectronics*, vol. 9, no. 5, pp. 172–183, 2015.

[64] E. Sarbazi, M. Safari, and H. Haas, "Statistical modeling of single-photon avalanche diode receivers for optical wireless communications," *IEEE Transactions on Communications*, vol. 66, no. 9, pp. 4043–4058, Sept 2018.

[65] F.-M. Wu, C.-T. Lin, C.-C. Wei, C.-W. Chen, Z.-Y. Chen, and H.-T. Huang, "3.22-Gb/s WDM visible light communication of a single RGB LED employing carrier-less amplitude and phase modulation," in *2013 Optical Fiber Communication Conference and Exposition and the National Fiber Optic Engineers Conference (OFC/NFOEC)*, March 2013, pp. 1–3.

[66] Y. Li, M. Safari, R. Henderson, and H. Haas, "Optical OFDM with single-photon avalanche diode," *IEEE Photonics Technology Letters*, vol. 27, no. 9, pp. 943–946, May 2015.

[67] B. Fahs, M. Romanowicz, and M. M. Hella, "A Gbps building-to-building VLC link using standard CMOS avalanche photodiodes," *IEEE Photonics Journal*, vol. 9, no. 6, pp. 1–9, Dec 2017.

[68] P. Luo, M. Zhang, Z. Ghassemlooy, H. L. Minh, H. M. Tsai, X. Tang, and D. Han, "Experimental demonstration of a 1024-QAM optical camera communication system," *IEEE Photonics Technology Letters*, vol. 28, no. 2, pp. 139–142, Jan 2016.

[69] T. Yamazato, I. Takai, H. Okada, T. Fujii, T. Yendo, S. Arai, M. Andoh, T. Harada, K. Yasutomi, K. Kagawa, and S. Kawahito, "Image-sensor-based visible light communication for automotive applications," *IEEE Communications Magazine*, vol. 52, no. 7, pp. 88–97, July 2014.

[70] C.-W. Chen, C.-W. Chow, Y. Liu, and C.-H. Yeh, "Efficient demodulation scheme for rolling-shutter-patterning of CMOS image sensor based visible light communications," *Opt. Express*, vol. 25, no. 20, pp. 24 362–24 367, Oct 2017.

[71] W.-C. Wang, C.-W. Chow, L.-Y. Wei, Y. Liu, and C.-H. Yeh, "Long distance non-line-of-sight (nlos) visible light signal detection based on rolling-shutter-patterning of mobile-phone camera," *Opt. Express*, vol. 25, no. 9, pp. 10 103–10 108, May 2017.

[72] S. Collins, D. C. O'Brien, and A. Watt, "High gain, wide field of view concentrator for optical communications," *Opt. Lett.*, vol. 39, no. 7, pp. 1756–1759, Apr 2014.

[73] *A comparative study of optical concentrators for visible light communications*, vol. 10128, 2017.

[74] R. Mulyawan, H. Chun, A. Gomez, S. Rajbhandari, G. Faulkner, P. P. Manousiadis, D. A. Vithanage, G. A. Turnbull, I. D. W. Samuel, S. Collins, and D. O'Brien, "MIMO visible light communications using a wide field-of-view fluorescent concentrator," *IEEE Photonics Technology Letters*, vol. 29, no. 3, pp. 306–309, Feb 2017.

[75] P. P. Manousiadis, S. Rajbhandari, R. Mulyawan, D. A. Vithanage, H. Chun, G. Faulkner, D. C. O'Brien, G. A. Turnbull, S. Collins, and I. D. Samuel, "Wide field-of-view fluorescent antenna for visible light communications beyond the étendue limit," *Optica*, vol. 3, no. 7, pp. 702–706, Jul 2016.

[76] J. Armstrong, R. J. Green, and M. D. Higgins, "Comparison of three receiver designs for optical wireless communications using white LEDs," *IEEE Communications Letters*, vol. 16, no. 5, pp. 748–751, May 2012.

[77] J. M. Kahn, R. You, P. Djahani, A. G. Weisbin, B. K. Teik, and A. Tang, "Imaging diversity receivers for high-speed infrared wireless communication," *IEEE Communications Magazine*, vol. 36, no. 12, pp. 88–94, Dec 1998.

[78] G. Yun and M. Kavehrad, "Spot-diffusing and fly-eye receivers for indoor infrared wireless communications," in *1992 IEEE International Conference on Selected Topics in Wireless Communications*, June 1992, pp. 262–265.

[79] A. H. Azhar, T. Tran, and D. O'Brien, "Demonstration of high-speed data transmission using MIMO-OFDM visible light communications," in *2010 IEEE Globecom Workshops*, Dec 2010, pp. 1052–1056.

[80] F. R. Gfeller and U. Bapst, "Wireless in-house data communication via diffuse infrared radiation," *Proceedings of the IEEE*, vol. 67, no. 11, pp. 1474–1486, Nov 1979.

[81] K. Lee, H. Park, and J. R. Barry, "Indoor channel characteristics for visible light communications," *IEEE Communications Letters*, vol. 15, no. 2, pp. 217–219, February 2011.

[82] H. L. Minh, D. O'Brien, G. Faulkner, L. Zeng, K. Lee, D. Jung, and Y. Oh, "80 Mbit/s visible light communications using pre-equalized white LED," in *2008 34th European Conference on Optical Communication*, Sept 2008, pp. 1–2.

[83] J. Vucic, C. Kottke, S. Nerreter, K. Langer, and J. W. Walewski, "513 Mbit/s visible light communications link based on DMT-modulation of a white LED," *Journal of Lightwave Technology*, vol. 28, no. 24, pp. 3512–3518, Dec 2010.

[84] B. S. Krongold, K. Ramchandran, and D. L. Jones, "Computationally efficient optimal power allocation algorithm for multicarrier communication systems," in *ICC '98. 1998 IEEE International Conference on Communications. Conference Record. Affiliated with SUPERCOMM'98 (Cat. No.98CH36220)*, vol. 2, June 1998, pp. 1018–1022 vol.2.

[85] L. Zeng, D. O'Brien, H. Le-Minh, K. Lee, D. Jung, and Y. Oh, "Improvement of date rate by using equalization in an indoor visible light communication system," in *2008 4th IEEE International Conference on Circuits and Systems for Communications*, May 2008, pp. 678–682.

[86] T. Komine and M. Nakagawa, "Fundamental analysis for visible-light communication system using LED lights," *IEEE Transactions on Consumer Electronics*, vol. 50, no. 1, pp. 100–107, Feb 2004.

[87] H. Elgala, R. Mesleh, and H. Haas, "A study of led nonlinearity effects on optical wireless transmission using ofdm," in *2009 IFIP International Conference on Wireless and Optical Communications Networks*, April 2009, pp. 1–5.

[88] J. Armstrong and A. J. Lowery, "Power efficient optical OFDM," *Electronics Letters*, vol. 42, no. 6, pp. 370–372, March 2006.

[89] J. Armstrong, "OFDM for optical communications," *Journal of Lightwave Technology*, vol. 27, no. 3, pp. 189–204, Feb 2009.

[90] ——, "Peak-to-average power reduction for OFDM by repeated clipping and frequency domain filtering," *Electronics Letters*, vol. 38, no. 5, pp. 246–247, Feb 2002.

[91] C. W. Chow, C. H. Yeh, Y. F. Liu, and P. Y. Huang, "Mitigation of optical background noise in light-emitting diode (led) optical wireless communication systems," *IEEE Photonics Journal*, vol. 5, no. 1, pp. 7 900 307–7 900 307, Feb 2013.

[92] C. Chang, Y. Su, U. Kurokawa, and B. I. Choi, "Interference rejection using filter-based sensor array in VLC systems," *IEEE Sensors Journal*, vol. 12, no. 5, pp. 1025–1032, May 2012.

[93] K. C. Kao and G. A. Hockham, "Dielectric-fibre surface waveguides for optical frequencies," *Proc. Inst. Electric. Eng.3. Radio Commun. Eng.*, vol. 113, pp. 1151–1158, 1966.

[94] G. Keiser, *Optical fiber communications; 2nd ed.*, ser. McGraw-Hill electrical and electronic engineering series. New York, NY: McGraw-Hill, 1991.

[95] E. F. Schubert, N. E. J. Hunt, R. J. Malik, M. Micovic, and D. L. Miller, "Temperature and modulation characteristics of resonant-cavity light-emitting diodes," *Journal of Lightwave Technology*, vol. 14, no. 7, pp. 1721–1729, July 1996.

[96] M. Atef, R. Swoboda, and H. Zimmermann, "Real-time 1.25-Gb/s transmission over 50-m SI-POF using a green laser diode," *IEEE Photonics Technology Letters*, vol. 24, no. 15, pp. 1331–1333, Aug 2012.

[97] C. Gimeno, C. Sánchez-Azqueta, E. Guerrero, J. Aguirre, C. Aldea, and S. Celma, "Single-chip receiver for 1.25 Gb/s over 50-m SI-POF," *IEEE Photonics Technology Letters*, vol. 27, no. 11, pp. 1220–1223, June 2015.

[98] X. Li, N. Bamiedakis, J. Wei, J. J. D. McKendry, E. Xie, R. Ferreira, E. Gu, M. D. Dawson, R. V. Penty, and I. H. White, "μLED-based single-wavelength bi-directional POF link with 10 Gb/s aggregate data rate," *Journal of Lightwave Technology*, vol. 33, no. 17, pp. 3571–3576, Sept 2015.

[99] J. B. D. Soole and H. Schumacher, "InGaAs metal-semiconductor-metal photodetectors for long wavelength optical communications," *IEEE Journal of Quantum Electronics*, vol. 27, no. 3, pp. 737–752, March 1991.

[100] S. Loquai, F. Winkler, S. Wabra, E. Hartl, B. Schmauss, and O. Ziemann, "High-speed, large-area POF receivers for fiber characterization and data transmission $\geq$10-Gb/s based on MSM-photodetectors," *Journal of Lightwave Technology*, vol. 31, no. 7, pp. 1132–1137, April 2013.

[101] D. L. Rogers, "Integrated optical receivers using MSM detectors," *Journal of Lightwave Technology*, vol. 9, no. 12, pp. 1635–1638, Dec 1991.

[102] *Spectrally efficient polymer optical fiber transmission*, vol. 7960, 2011.

[103] S. Werzinger and C.-A. Bunge, "Statistical analysis of intrinsic and extrinsic coupling losses for step-index polymer optical fibers," *Opt. Express*, vol. 23, no. 17, pp. 22 318–22 329, Aug 2015.

[104] C. Zerna, J. Sundermeyer, A. Fiederer, N. Verwaal, B. Offenbeck, and N. Weber, "Integrated PAM2 decision feedback equalizer for gigabit ethernet over standard SI-POF using red LED," in *36th European Conference and Exhibition on Optical Communication*, Sept 2010.

[105] H. Li, X. Chen, B. Huang, D. Tang, and H. Chen, "High bandwidth visible light communications based on a post-equalization circuit," *IEEE Photonics Technology Letters*, vol. 26, no. 2, pp. 119–122, Jan 2014.

[106] S. He, G. Ren, Z. Zhong, and Y. Zhao, "M-ary variable period modulation for indoor visible light communication system," *IEEE Communications Letters*, vol. 17, no. 7, pp. 1325–1328, July 2013.

[107] S. H. Lee, K. Ahn, and J. K. Kwon, "Multilevel transmission in dimmable visible light communication systems," *Journal of Lightwave Technology*, vol. 31, no. 20, Oct 2013.

[108] X. Li, N. Bamiedakis, X. Guo, J. J. D. McKendry, E. Xie, R. Ferreira, E. Gu, M. D. Dawson, R. V. Penty, and I. H. White, "Wireless visible light communications employing feed-forward pre-equalization and PAM-4 modulation," *Journal of Lightwave Technology*, vol. 34, no. 8, pp. 2049–2055, April 2016.

[109] R. Kruglov, S. Loquai, C. Bunge, M. Schueppert, J. Vinogradov, and O. Ziemann, "Comparison of PAM and CAP modulation schemes for data transmission over SI-POF," *IEEE Photonics Technology Letters*, vol. 25, no. 23, pp. 2293–2296, Dec 2013.

[110] X. Li, J. L. Wei, N. Bamiedakis, R. V. Penty, and I. H. White, "Avalanche photodiode enhanced PAM-32 5 Gb/s LED-POF link," in *2014 The European Conference on Optical Communication (ECOC)*, Sept 2014, pp. 1–3.

[111] R. Mesleh, H. Elgala, and H. Haas, "On the performance of different OFDM based optical wireless communication systems," *IEEE/OSA Journal of Optical Communications and Networking*, vol. 3, no. 8, pp. 620–628, August 2011.

[112] S. Loquai, R. Kruglov, O. Ziemann, J. Vinogradov, and C. Bunge, "10 Gbit/s over 25 m plastic optical fiber as a way for extremely low-cost optical interconnection," in *2010 Conference on Optical Fiber Communication (OFC/NFOEC), collocated National Fiber Optic Engineers Conference*, March 2010, pp. 1–3.

[113] G.-H. Im, D. Harman, G. Huang, A. Mandzik, M.-H. Nguyen, and J.-J. Werner, "51.84 Mb/s 16-CAP ATM LAN standard," *IEEE Journal on Selected Areas in Communications*, vol. 13, no. 4, pp. 620–632, 1995.

[114] K. Gentile, "The care and feeding of digital pulse-shaping filters," *RF DESIGN*, vol. 25, no. 4, pp. 50–58, Oct 2002.

[115] S. Long, M. A. Khalighi, M. Wolf, Z. Ghassemlooy, and S. Bourennane, "Performance of carrier-less amplitude and phase modulation with frequency domain equalization for indoor visible light communications," in *2015 4th International Workshop on Optical Wireless Communications (IWOW)*, Sept 2015, pp. 16–20.

[116] P. A. Haigh *et al.*, "A multi-CAP visible-light communications system with 4.85-b/s/Hz spectral efficiency," *IEEE Journal on Selected Areas in Communications*, vol. 33, no. 9, pp. 1771–1779, Sept 2015.

[117] P. A. Haigh, P. Chvojka, S. Zvanovec, Z. Ghassemlooy, S. T. Le, T. Kanesan, E. Giacoumidis, N. J. Doran, I. Papakonstantinou, and I. Darwazeh, "Experimental verification of visible light communications based on multi-band CAP modulation," in *2015 Optical Fiber Communications Conference and Exhibition (OFC)*, March 2015, pp. 1–3.

[118] P. A. Haigh *et al.*, "Multi-band carrier-less amplitude and phase modulation for highly bandlimited visible light communications-invited paper," in *2015 International Conference on Wireless Communications Signal Processing (WCSP)*, Oct 2015, pp. 1–5.

[119] F. Sjöberg, "A VDSL tutorial," Luleå tekniska universitet, Tech. Rep., 2000, godkänd; 2000; 20070912 (margjo).

[120] M. A. Khalighi, S. Long, S. Bourennane, and Z. Ghassemlooy, "PAM- and CAP-based transmission schemes for visible-light communications," *IEEE Access*, vol. 5, pp. 27 002–27 013, 2017.

[121] A. Shalash and K. K. Parhi, "Comparison of discrete multitone and carrierless AM/PM techniques for line equalization," in *Circuits and Systems, 1996. ISCAS'96., Connecting the World., 1996 IEEE International Symposium on*, vol. 2. IEEE, 1996, pp. 560–563.

[122] G. Stepniak, L. Maksymiuk, and J. Siuzdak, "Experimental comparison of PAM, CAP, and DMT modulations in phosphorescent white LED transmission link," *IEEE Photonics Journal*, vol. 7, no. 3, pp. 1–8, June 2015.

[123] F. M. Wu *et al.*, "Performance comparison of OFDM signal and CAP signal over high capacity RGB-LED-based WDM visible light communication," *IEEE Photonics Journal*, vol. 5, no. 4, pp. 7 901 507–7 901 507, Aug 2013.

[124] J. Wei, L. Geng, D. Cunningham, R. Penty, and I. White, "Gigabit NRZ, CAP and optical OFDM systems over POF links using LEDs," *Optics express*, vol. 20, no. 20, pp. 22 284–22 290, 2012.

[125] J. L. Wei, C. Sanchez, and E. Giacoumidis, "Fair comparison of complexity between a multi-band CAP and DMT for data center interconnects," *Opt. Lett.*, vol. 42, no. 19, pp. 3860–3863, Oct 2017.

[126] Y. Wang, X. Huang, L. Tao, J. Shi, and N. Chi, "4.5-Gb/s RGB-LED based WDM visible light communication system employing CAP modulation and rls based adaptive equalization," *Optics express*, vol. 23, no. 10, pp. 13 626–13 633, 2015.

[127] Y. Wang, L. Tao, X. Huang, J. Shi, and N. Chi, "Enhanced performance of a high-speed WDM CAP64 VLC system employing Volterra series-based nonlinear equalizer," *IEEE Photonics Journal*, vol. 7, no. 3, pp. 1–7, June 2015.

[128] Y. Wang, L. Tao, Y. Wang, and N. Chi, "High speed WDM VLC system based on multi-band CAP64 with weighted pre-equalization and modified CMMA based post-equalization," *IEEE Communications Letters*, vol. 18, no. 10, pp. 1719–1722, Oct 2014.

[129] F.-M. Wu, C.-T. Lin, C.-C. Wei, C.-W. Chen, Z.-Y. Chen, and H.-T. Huang, "3.22-Gb/s WDM visible light communication of a single RGB LED employing carrier-less amplitude and phase modulation," in *2013 Optical Fiber Communication Conference and Exposition and the National Fiber Optic Engineers Conference (OFC/NFOEC)*, March 2013, pp. 1–3.

[130] G. Stepniak and J. Siuzdak, "Transmission beyond 2 Gbit/s in a 100 m SI-POF with multilevel CAP modulation and digital equalization," in *2013 Optical Fiber Communication Conference and Exposition and the National Fiber Optic Engineers Conference (OFC/NFOEC)*, March 2013, pp. 1–3.

[131] F.-M. Wu, C.-T. Lin, C.-C. Wei, C.-W. Chen, H.-T. Huang, and C.-H. Ho, "1.1-Gb/s white-LED-based visible light communication employing carrier-less amplitude and phase modulation," *IEEE photonics technology letters*, vol. 24, no. 19, pp. 1730–1732, 2012.

[132] A. N. Pinto, J. R. F. da Rocha, , and G. P. Agrawal, "Optical versus electrical dispersion compensation: role of timing jitter," *Journal of Lightwave Technology*, vol. 24, no. 1, pp. 387–395, Jan 2006.

[133] J. O'Reilly, J. da Rocha, and K. Schumacher, "Optical fiber direct detection receivers optimally tolerant to jitter," *IEEE Transactions on Communications*, vol. 34, no. 11, pp. 1141–1147, November 1986.

[134] K. Schumacher and J. J. O'Reilly, "Power penalty due to jitter on optical communication systems," *Electronics Letters*, vol. 23, no. 14, pp. 718–719, July 1987.

[135] A. V. T. Cartaxo and A. A. de Albuquerque, "Jitter in the square synchroniser on direct detection optical communications. part 1: theoretical analysis," *IEE Proceedings - Optoelectronics*, vol. 141, no. 4, pp. 209–219, Aug 1994.

[136] K. O. Akande and W. O. Popoola, "Synchronization of carrierless amplitude and phase modulation in visible light communication," in *2017 IEEE International Conference on Communications Workshops (ICC Workshops)*, May 2017, pp. 156–161.

[137] J. Gao and Y. H. Leung, "A new adaptive equalizer for carrierless amplitude and phase (CAP) receivers," in *Proceedings of the 1999 IEEE International Symposium on Circuits and Systems, 1999. ISCAS '99.*, vol. 3, Jul 1999, pp. 90–93 vol.3.

[138] P. A. Haigh, P. Chvojka, S. Zvanovec, Z. Ghassemlooy, and I. Darwazeh, "Analysis of Nyquist pulse shapes for carrierless amplitude and phase modulation in visible light communications," *Journal of Lightwave Technology*, vol. 36, no. 20, pp. 5023–5029, Oct 2018.

[139] P. A. Haigh and I. Darwazeh, "Demonstration of reduced complexity multi-band CAP modulation using Xia-pulses in visible light communications," in *2018 Optical Fiber Communications Conference and Exposition (OFC)*, March 2018, pp. 1–3.

[140] I. L. Thng, A. Cantoni, and Y. H. Leung, "Low timing sensitivity receiver structures for CAP," *IEEE Transactions on Communications*, vol. 48, no. 3, pp. 396–400, 2000.

[141] S. Daumont, B. Rihawi, and Y. Lout, "Root-raised cosine filter influences on PAPR distribution of single carrier signals," in *3rd International Symposium on Communications, Control and Signal Processing, 2008. ISCCSP 2008.*, March 2008, pp. 841–845.

[142] R. H. Barker, "Group synchronizing of binary digital sequences," *In Communication Theory*, pp. 273–287, London, Butterworth, 1953.

[143] F. Penna, R. Garello, and M. A. Spirito, "Probability of missed detection in eigenvalue ratio spectrum sensing," in *2009 IEEE International Conference on Wireless and Mobile Computing, Networking and Communications*, Oct 2009, pp. 117–122.

[144] K. Werfli *et al.*, "Multi-band carrier-less amplitude and phase modulation with decision feedback equalization for bandlimited VLC systems," in *4th International Workshop on Optical Wireless Communications (IWOW), 2015*, Sept 2015, pp. 6–10.

[145] Y. Wang and N. Chi, "Investigation of advanced pre- and post-equalization schemes in high-order CAP modulation based high-speed indoor VLC transmission system," in *Society of Photo-Optical Instrumentation Engineers (SPIE) Conference Series*, vol. 10019, oct 2016, p. 100190C.

[146] J. G. Proakis, "Adaptive equalization for TDMA digital mobile radio," *IEEE Transactions on Vehicular Technology*, vol. 40, no. 2, pp. 333–341, 1991.

[147] K. O. Akande, P. A. Haigh, and W. O. Popoola, "Joint equalization and synchronization for carrierless amplitude and phase modulation in visible light communication," in *2017 13th International Wireless Communications and Mobile Computing Conference (IWCMC)*, June 2017, pp. 876–881.

[148] A. H. Sayed, *Adaptive Filters*. Wiley-IEEE Press, 2008.

[149] J. R. Treichler, I. Fijalkow, and C. Johnson, "Fractionally spaced equalizers," *IEEE Signal Processing Magazine*, vol. 13, no. 3, pp. 65–81, 1996.

[150] N. W. K. Lo, D. D. Falconer, and A. U. H. Sheikh, "Adaptive equalization for co-channel interference in a multipath fading environment," *IEEE Transactions on Communications*, vol. 43, no. 2/3/4, pp. 1441–1453, Feb 1995.

[151] E. Ip and J. M. Kahn, "Digital equalization of chromatic dispersion and polarization mode dispersion," *Journal of Lightwave Technology*, vol. 25, no. 8, pp. 2033–2043, Aug 2007.

[152] P. A. Haigh, Z. Ghassemlooy, S. Rajbhandari, and E. Leitgeb, "A 100 Mb/s visible light communications system using a linear adaptive equalizer," in *19th European Conference on Networks and Optical Communications - (NOC 2014),*, June 2014, pp. 136–139.

[153] W. O. Popoola, E. Poves, and H. Haas, "Error performance of generalised space shift keying for indoor visible light communications," *IEEE Transactions on Communications*, vol. 61, no. 5, pp. 1968–1976, 2013.

[154] M. Safari and M. Uysal, "Do we really need OSTBCs for free-space optical communication with direct detection?" *IEEE Transactions on Wireless Communications*, vol. 7, no. 11, pp. 4445–4448, November 2008.

[155] P. W. Wolniansky, G. J. Foschini, G. D. Golden, and R. A. Valenzuela, "V-BLAST: an architecture for realizing very high data rates over the rich-scattering wireless channel," in *1998 URSI International Symposium on Signals, Systems, and Electronics. Conference Proceedings (Cat. No.98EX167)*, Sep 1998, pp. 295–300.

[156] J. G. Proakis, *Digital Communications, (4th Ed)*. New York: McGraw-Hill, 2001.

[157] J. Jeganathan, A. Ghrayeb, and L. Szczecinski, "Spatial modulation: optimal detection and performance analysis," *IEEE Communications Letters*, vol. 12, no. 8, pp. 545–547, Aug 2008.

[158] K. Cho and D. Yoon, "On the general BER expression of one-and two-dimensional amplitude modulations," *IEEE Transactions on Communications*, vol. 50, no. 7, pp. 1074–1080, 2002.

[159] C. Wang, E. K. S. Au, R. D. Murch, W. H. Mow, R. S. Cheng, and V. Lau, "On the performance of the MIMO zero-forcing receiver in the presence of channel estimation error," *IEEE Transactions on Wireless Communications*, vol. 6, no. 3, pp. 805–810, March 2007.

[160] Y. Jiang, M. K. Varanasi, and J. Li, "Performance analysis of ZF and MMSE equalizers for MIMO systems: An in-depth study of the high SNR regime," *IEEE Transactions on Information Theory*, vol. 57, no. 4, pp. 2008–2026, April 2011.

[161] J. R. Barry *et al.*, "Simulation of multipath impulse response for indoor wireless optical channels," *IEEE Journal on Selected Areas in Communications*, vol. 11, no. 3, pp. 367–379, Apr 1993.

[162] T. Fath and H. Haas, "Performance comparison of MIMO techniques for optical wireless communications in indoor environments," *IEEE Transactions on Communications*, vol. 61, no. 2, pp. 733–742, 2013.

[163] D. Wubben, R. Bohnke, V. Kuhn, and K. D. Kammeyer, "MMSE extension of V-BLAST based on sorted QR decomposition ," in *2003 IEEE 58th Vehicular Technology Conference. VTC 2003-Fall (IEEE Cat. No.03CH37484)*, vol. 1, Oct 2003, pp. 508–512 Vol.1.

[164] J. Benesty, Y. Huang, and J. Chen, "A fast recursive algorithm for optimum sequential signal detection in a BLAST system," *IEEE Transactions on Signal Processing*, vol. 51, no. 7, pp. 1722–1730, July 2003.

[165] M. D. Renzo, H. Haas, A. Ghrayeb, S. Sugiura, and L. Hanzo, "Spatial modulation for generalized MIMO: Challenges, opportunities, and implementation," *Proceedings of the IEEE*, vol. 102, no. 1, pp. 56–103, Jan 2014.

[166] X. Zhang, S. Dimitrov, S. Sinanovic, and H. Haas, "Optimal power allocation in spatial modulation OFDM for visible light communications," in *2012 IEEE 75th Vehicular Technology Conference (VTC Spring)*, May 2012, pp. 1–5.

[167] W. O. Popoola and H. Haas, "Demonstration of the merit and limitation of generalised space shift keying for indoor visible light communications," *Journal of Lightwave Technology*, vol. 32, no. 10, pp. 1960–1965, May 2014.

[168] H. G. Olanrewaju, J. Thompson, and W. O. Popoola, "On spatial pulse position modulation for optical wireless communications," in *2016 IEEE Photonics Society Summer Topical Meeting Series (SUM)*, July 2016, pp. 44–45.

[169] W. O. Popoola, "Merits and limitations of spatial modulation for optical wireless communications," in *2013 2nd International Workshop on Optical Wireless Communications (IWOW)*, Oct 2013, pp. 152–156.

[170] E. Başar, U. Aygölü, E. Panayırcı, and H. V. Poor, "Orthogonal frequency division multiplexing with index modulation," in *2012 IEEE Global Communications Conference (GLOBECOM)*, Dec 2012, pp. 4741–4746.

[171] E. Basar, "Orbital angular momentum with index modulation," *IEEE Transactions on Wireless Communications*, vol. 17, no. 3, pp. 2029–2037, March 2018.

[172] T. Mao, Z. Wang, Q. Wang, S. Chen, and L. Hanzo, "Dual-mode index modulation aided OFDM," *IEEE Access*, vol. 5, pp. 50–60, 2017.

[173] P. A. Haigh, E. Hugues-Salas, and J. Wei, "On the performance of increasing subcarrier order in multi-band carrier-less amplitude and phase modulation for short haul optical links," in *Asia Communications and Photonics Conference*. Optical Society of America, 2017, p. S4B.6.

[174] O. O. Semiconductors, *OSLON SX Datasheet*, Nov. 2012, ver 1.1.

[175] Hamamatsu, *Resonant cavity LED for POF data communication*, Feb. 2016.

[176] Thorlabs, *Si Amplified Fixed Gain Detector*, Sept. 2017, rev. J.

[177] Q. Wang, T. Mao, and Z. Wang, "Index modulation-aided OFDM for visible light communications," in *Visible Light Communications*, J.-Y. Wang, Ed. Rijeka: InTech, 2017, ch. 4.

[178] G. Foschini, R. Gitlin, and S. Weinstein, "Optimization of two-dimensional signal constellations in the presence of Gaussian noise," *IEEE Transactions on Communications*, vol. 22, no. 1, pp. 28–38, January 1974.

[179] K. O. Akande and W. O. Popoola, "Subband index carrierless amplitude and phase modulation for optical communications," *Journal of Lightwave Technology*, vol. 36, no. 18, pp. 4190–4197, Sept 2018.

[180] S. Dimitrov, S. Sinanovic, and H. Haas, "Clipping noise in OFDM-based optical wireless communication systems," *IEEE Transactions on Communications*, vol. 60, no. 4, pp. 1072–1081, April 2012.

[181] Y. Mao, X. Jin, W. Liu, C. Gong, and Z. Xu, "Demonstration of real-time CAP transceivers with hybrid digital equalization for visible light communication," in *Asia Communications and Photonics Conference*. Optical Society of America, 2017, p. M1G.4.

[182] J. Shi, X. Huang, Y. Wang, and N. Chi, "Real-time bi-directional visible light communication system utilizing a phosphor-based LED and RGB LED," in *2014 Sixth International Conference on Wireless Communications and Signal Processing (WCSP)*, Oct 2014, pp. 1–5.

[183] C.-H. Yeh, Y.-L. Liu, and C.-W. Chow, "Real-time white-light phosphor-LED visible light communication (VLC) with compact size," *Optics express*, vol. 21, no. 22, pp. 26 192–26 197, 2013.